10-24-2018

Development of Polymer-Based In-Plane Nanopore for DNA Sequencing

Zheng Jia
Louisiana State University and Agricultural and Mechanical College

DEVELOPMENT OF POLYMER-BASED IN-PLANE NANOPORE FOR DNA SEQUENCING

A Dissertation

Submitted to the Graduate Faculty of the
Louisiana State University and
Agricultural and Mechanical College
in partial fulfillment of the
requirements for the degree of
Doctor of Philosophy

in

The Department of Mechanical Engineering

by
Zheng Jia
B.Eng., Beihang University, 2013
December 2018

To my parents,

Mr. Junjie Jia and Mrs. Shuying Cheng,

my girlfriend Miss Fen Yang

and lovely friends

Acknowledgments

I would like to acknowledge the support and guidance from my major professor, Dr. Sunggook Park, who gave me an interesting topic to study and taught me how to be a good researcher and a good supervisor by setting an example with his own conduct. I would like to acknowledge the support and guidance from my graduate committee, Dr. Steven A. Soper, Dr. Michael C. Murphy, Dr. Dorel Moldovan. Dr. Jin-Woo Choi and Dr. Michal Brylinski who is acting as the Dean's representative.

I would like to acknowledge the P41 Center for BioModular Multiscale Systems for Precision Medicine (P41EB020594) from the National Institutes of Health. Thanks to my colleagues, CBM^2 members, KU and UNC team members, especially Dr. Junseo Choi, who helped me a lot during my study, as a good colleague and a good friend.

Table of Contents

Abstract

Mechanically robust solid-state nanopores have the potential to be the next generation DNA sensing platforms. However, mass production and limited base-calling accuracy are the hurdles for solid-state nanopore based DNA sensing. In order to solve these problems, a polymer dual-nanopore device fabricated via high throughput nanoimprint lithography (NIL) was proposed to sequence DNA by time-of-flight (ToF) measurement. As a proof of concept, this study presents mononucleotides discrimination via ToF measurement using polymer in-plane dual-nanopore device.

First, fabrication of polymer in-plane nanopore with controllable dimensions was studied in consideration of experimental conditions and materials selection. Then, surface charge density effect on DNA translocation through in-plane nanopore was studied numerically and experimentally using fabricated nanopore devices on PEGDA, PMMA and COC. λ-DNA sensing was only observed in PEGDA device with a surface charge density lower than the threshold surface charge density predicted by COMSOL simulation.

With demonstrated single molecule sensing ability, mononucleotides were introduced to PEGDA dual-nanopore with 500 nm flight tube and discriminated under various conditions. At pH 8.0, mononucleotides were driven by eletrophoretic motion and their ToF was in a decreasing order of dGMP > dAMP > dCMP > dTMP. At pH 10.0, mononucleotides were driven by electroosmotic flow (EOF) due to a higher surface charge density on nanochannel walls and ToF was in the same order as pH 8.0 with an average identification accuracy of 55%. Dual-nanopore device with 1 μm flight tube was then used to improve the average identification accuracy to 75%. Finally, dGMP and dTMP in a mix solution were dicriminated by their ToF difference.

Chapter 1. Introduction

1.1 General background

In 2015, President Obama announced the "Precision Medicine" project, which aims to provide individual patients personalized medical treatment, especially for genetic related diseases, for example, cancer. In order to achieve this goal, we have to collect genetic information not only from single patient but millions of people to build up a database. However, it is not an easy work. Here are some facts: it took the Human Genome Project (HGP) 10 years to sequence a single human genome. Today, even with the latest technology, it still takes several days and couple thousands of dollars to do the same thing. DNA sequencing is still far from a routine clinical application. We desperately need a faster and cheaper sequencing platform and nanopores are the promising tools.

A nanopore is a nanoscale opening with high sensitivity. Over the past thirty years, nanopore-based DNA sequencing platforms have drawn increasing attention due to their label free, long-read and low cost features. The sequencing mechanism is straightforward: a negatively charged DNA molecule is driven toward a nanopore filled with conductive electrolyte under an external electric field and ionic current through the nanopore is measured at the same time; when the DNA molecule is present in the nanopore, ion transport is temporarily blocked, which leads to a measurable ionic current change; biological information of DNA molecule can be revealed by analyzing the ionic current data. In recent years, many works have been done to improve the performance of nanopore-based DNA sequencing platforms. However, large-scale device fabrication, precise DNA motion control and high base-calling accuracy are still the three main hurdles for practical application of nanopore-based DNA sequencer. In order to overcome these drawbacks, we present the development of polymer-based in-plane dual-nanopore device for DNA sequencing via time-of-flight (ToF) measurement.

1.2 Goals and objectives of this study

The goal of this study is to develop a new DNA sequencing platform, a polymer-based in-plane dual-nanopore device to discriminate deoxy-nucleoside monophosphates (dNMPs). The in-plane dual nanopore device is fabricated on polymer materials via high throughput nanoimprint lithography (NIL), which solves the mass fabrication problem. DNA is sequenced base by base after digestion by enzyme, therefore DNA motion is precisely controlled by enzyme activity (which is not the focus of this work). When a released DNA base passes through two pores, it triggers two current change signals and the time delay between two signals indicates the base's mobility. The four DNA bases A, T, G and C are distinguished by their mobility difference in addition to current drop and dwelling time, which enhances the base-calling accuracy.

This study has three objectives: the first is to present the fabrication of dual-nanopore device with controllable pore size on polymer substrates via NIL; the second is to demonstrate DNA sensing and dNMPs discrimination ability using fabricated device; and the third objective is to study DNA/dNMPs translocation mechanism and optimize system performance by manipulating factors such as the device design, buffer system and polymer surface properties.

1.3 Outline of manuscript

This manuscript has seven chapters and the brief overview of each chapter is shown below.

Chapter 1 serves as an introduction and states the goal and objectives of this study.

Chapter 2 is a review of DNA sequencing technologies, from widely used next generation DNA sequencing (NGS) technologies to the third generation DNA sequencing (TGS) technologies with single molecule resolution. Among TGS technologies, nanopore-based DNA sequencing technology is promising due to its label-free, long-read and low cost features. Four emerging nanopore-based sensing companies are also introduced to provide some insights for academic

research. From the evolution of nanopore-based sequencing technologies, we find mass production, single base resolution and DNA motion control are still three main hurdles, especially for solid-state nanopores. In order to solve these problems, we propose to fabricate polymer in-plane dual-pore device for DNA sequencing by time of flight (ToF) measurement.

Chapter 3 focuses on how to make polymer-based nanopore device via NIL and how to control the nanopore dimensions. The fabrication process consists of four steps: Si master mold fabrication, UV-resin mold replication, imprinting and thermal bonding. Nanopore dimensions are initially defined by Si master mold via FIB milling bitmap mode. High replication fidelity is required for UV resin mold fabrication and polymer substrate imprinting by selecting UV-resin properly. Nanopore dimensions can be further reduced by reflow process during thermal bonding.

Chapter 4 serves as a proof of concept by demonstrating single molecule sensing ability of polymer in-plane nanopore. λ-DNA was successfully translocated and detected by polymer in-plane single nanopore device. Besides, DNA translocation dynamics was studied by considering surface charge density of polymer materials. A COMSOL continuum model was first built to predict the threshold surface charge density for DNA translocation. In order to verify simulated results, DNA translocation was confirmed optically and electrically in nanopore device with surface charge density lower than the predicted surface charge density. Based on experimental results, we expect to detect mononucleotides by in-plane nanopore device with smaller pore size.

Chapter 5 demonstrates mononucleotides (dGMP, dAMP, dCMP and dTMP) detection and discrimination using polymer based dual-nanopore devices. There are several factors which affect the measured ToF and sensing resolution: pH of the buffer system, flight tube length and driving voltage. Such factors were studies and discussed based on experimental results. Besides,

mononucleotides translocation mechanism through in-plane nanopore was discussed with the help of COMSOL simulation.

Chapter 6 presents surface charge density reduction of polymer substrates by using multivalent salts. For mononucleotides translocation, although they are not like λ-DNA with flexible, long chain, we still observed pile-up issue in front of nanopore. In order to solve this issue, we tried to manipulate substrates' surface charge by introducing multivalent metal-containing salt. Bivalent salt $MgCl_2$ and trivalent salt $AlCl_3$ were studied by comparing their surface charge density reduction efficiency for COC, PMMA and PEGDA nanofluidic devices.

Chapter 7 provides an outline for future work, which will be helpful to get a better knowledge of the mechanism of biomolecule translocation through in-plane nanopore and to improve the sensing platform resolution: (1) DNA translocation kinetics through in-plane nanopore: in-plane nanopore is different with traditional solid-state nanopore, till today, there is no study focusing on the DNA translocation kinetics through in-plane nanopore by considering factors such as diffusion, entropy barrier, effective driving force, selective transport and DNA length; (2) Signal/nanopore correlation: determining which peak from which pore to assist data collection. Possible solutions could be designing dual pore with different dimension or using three-electrode system. (3) ToF data analysis: provide some insights for designing software for ToF data analysis.

Chapter 2. Nanopore-Based DNA Sequencing Technologies

2.1 Introduction: Evolution of DNA sequencing technologies

DNA molecules contain important genomic information and a full understanding of such information would inspire early diagnosis and precision medicine discovery [1-4]. In order to reveal the genomic information in DNA molecules, the Human Genome Project (HGP) was launched in 1990. And the first draft of human genome sequence was completed in 2001. It was a great but labor-intensive work due to the Sanger sequencing method used at that time. Four years later, the high throughput next generation sequencing (NGS) platform Roche/454 was introduced, followed by the Illumina system and the Ion Torrent system [4]. Since then, the cost of DNA sequencing decreased dramatically and in 2014 Illumina claimed to achieve "the $1000 genome" goal set by National Institutes of Health (NIH) [5].

Though the NGS platforms are making whole genome sequencing routine, they still have some drawbacks. First of all, the cost reduction comes from the huge capital investment on expensive high-performance sequencer. For example, the $1000-per-genome cost calculation for Illumina's Hiseq X Ten system is based on the use of ten systems over four years, which is a total investment of $ 82 million for capital and running costs. Secondly, due to the lack of single molecule sequencing ability, all the NGS platforms rely on PCR amplification to generate enough signal, but the PCR process can introduce inaccuracy in the sequencing [4, 6]. In order to overcome such drawbacks, third generation sequencing (TGS) platforms with different sensing mechanisms have been developed by Helicos BioSciences Corporation, Pacific Biosciences and Oxford Nanopore Technologies since 2010. Compared with NGS platforms, TGS platforms have single molecule sequencing ability, so the PCR process is no longer needed and they can perform DNA sequencing with longer reads, shorter times and lower costs.

Among all of the TGS platforms, the nanopore-based DNA sequencer is unique and the most promising. For nanopore-based DNA sequencing, natural DNA without any manipulation can be sequenced while driven through the nanopore under a certain voltage bias. In the early 1990s, Daniel Branton and David Deamer conceived the idea of using a biological nanopore (α-hemolysin) for DNA sequencing [7]. In the paper they published in 1996, they successfully detected homopolymers of RNA by measuring the ionic current [8]. Since then, biological nanopores have become an emerging and promising tool for DNA sequencing. In 2012 Oxford Nanopore Technologies (ONT) released their first portable DNA sequencer MinION and they started to ship their devices to users for tests in 2014. According to the phase 2 data released by the company in 2017, this $1000 sequencer achieves a single read accuracy of 97% for a 2D experiment [9]. Though this accuracy is still insufficient for real medical applications, it is reasonable to believe that it will have better performance with further improvement on DNA motion control and base-calling software. Meanwhile, Oxford Nanopore Technologies collaborate with solid-state nanopore researchers, trying to overcome the hurdles for solid-state nanopore's application to DNA sequencing [10, 11]. In the long term, solid-state nanopores would be a good alternative to biological nanopores due to their superior mechanical, chemical and thermal stability, and the potential to reduce the cost further [12].

In the beginning of this chapter, NGS and TGS technologies and the leading companies were summarized. Then we focused on the traditional nanopore-based technologies, and the achievements and challenges were summarized and discussed. In the last part, we propose a single molecule sequencing method based on time of flight (TOF) measurement. In this way, four mononucleotides, dAMP, dTMP, dGMP, dCMP can be distinguished by TOF (mobility) in

addition to ionic current drop and dwell time. If combined with exonuclease, DNA molecules can be sequenced in real-time, base by base after digestion [13].

2.1.1 Next generation sequencing (NGS) technologies

One main purpose of the HGP was to reveal 'life's instruction book' by whole genome sequencing [14]. However, due to the limitations of Sanger sequencing, the genome information researchers got from HGP was not enough to provide guidance to medical application. In order to achieve the initial goal, much more DNA samples need to be sequenced in a much faster and less expensive way [1, 14]. In 2004, 454 Life Sciences (acquired by Roche in 2007 and shut down by Roche in 2013) introduced the first commercial NGS platform Genome Sequencer FLX [15]. NGS platforms are still the main force for DNA sequencing in academia and genetic service companies.

Though the detection mechanism varies, all NGS platforms follow a similar wash-and-scan process. Before this process, thousands of short DNA strands are immobilized on the flow cell (Illumina genome sequencer) or amplification beads (Roche/454 FLX pyrosquencer, Applied Biosystems SOLiD sequencer and Ion Torrent sequencer) to create strands or clusters by PCR, which amplifies the signals generated [16]. Four nucleotides are then introduced (nucleotides probes for SOLiD) for incorporation and the signals generated during the synthesis reaction are scanned. Residual reagents are washed away and the wash-and-scan process is repeated until the reaction ends. A summary of four widely used NGS platforms and their comparison with Sanger sequencing are shown in Table 2.1 and Table 2.2. More information related to NGS platforms' sequencing mechanism, performance comparison and cost analysis can be found in Ref. [15-19].

Table 2.1. Summary of four wide spread NGS technologies

Platform	Current company	Initial company	Sequencing mechanism	Claim to fame [17]
Roche/454	Roche (shut down by Roche in 2013)	454	Synthesis (pyrosequencing)	First Next-Gen Sequencer, Long reads
Illumina	Illumina	Solexa	Synthesis	First short-read sequencer; current leader in advantages
SOLiD	ThermoFisher Scientific	Applied Biosystems	Ligation	Second short-read sequencer; low error rates
Ion Torrent	ThermoFisher Scientific	Ion Torrent	Synthesis (H^+ detection)	First Post-light sequencer; first system <$100 000

Table 2.2. Comparison of NGS platforms and Sanger sequencing platforms

Sequencer	Roche/454 GS FLX [17, 18]	Illumina HiSeq 2500 v4 [17, 18]	SOLiD 5500xl [17, 18]	Ion Torrent Proton [17, 18]	Sanger 3730xl [16]
Read length	700 bp	100 bp (SE)	75 bp (SE)	Up to 200 bp (SE)	400 ~ 900 bp
Error profile	0.1%, indel	0.1 %, substitution	≤0.1%, A-T bias	1%, indel	99.999%
Reads	1 M	3 G	1.4 B	60 ~ 80 M	-
Time/run	23 Hours	5 Days	10 Days	2 ~ 4 Hours	20 Min ~ 3Hours
Cost/ Million bases	$10	$0.045	$0.13	$0.08	$2400
Advantage	Read length, fast	High throughput	Accuracy	Fast, optical free	High quality, long read
Disadvantage	High cost, low throughput	Short read assembly	Short read assembly	Error rate [19]	High cost, low throughput

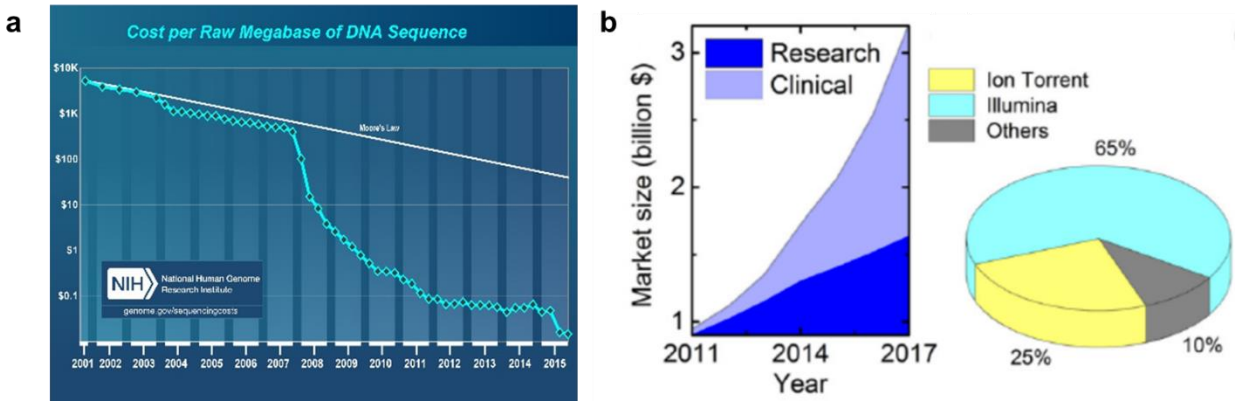

Figure 2.1. (a) Sequencing cost per Million bases. Wetterstrand KA. DNA Sequencing Costs: Data from the NHGRI Genome Sequencing Program (GSP) Available at: www.genome.gov/sequencingcostsdata. Accessed 08/20/2017 (b) DNA sequencing market size and shares using NGS platforms.

In the sequencing market, cost is the key to winning. From Table 2.2, it is clear that NGS platforms reduce the sequencing cost dramatically (from $2400 per million bases to as low as

$0.08) due to their high throughput. The competition in NGS platfroms almost came to an end when Roche shut down its R&D for the FLX sequencer. As reported in Figure 2.1(b), Illumina, Ion Torrent and Qiagen (a German company focusing more on NGS platform clinical applications) are the remaining players in this game [18]. Among the platforms mentioned above, Ion Torrent is unique due to its state-of-art semiconductor technology. Electrical signal detection has higher efficiency and also reduces the hardware (laser, CCD camera) and reagent cost. In fact, the time cost and reagent expense can be reduced further if the PCR step and wash-and-scan process can be avoided. To achieve this, single molecule real time sequencing ability is the step in the right direction [4, 6, 20].

2.1.2 Third-generation sequencing (TGS) technologies

There is considerable work to define the TGS technologies in different ways [6, 21, 22]. Here we consider TGS technologies to be capable of single molecule sequencing and long reads. With single molecule sequencing ability, TGS platforms skip the PCR process which is required by all previous technologies. Therefore, longer reads, shorter sample preparation times, lower error rates and lower costs can be achieved [4, 6]. Single molecule sequencing ability can be achieved in three ways: (1) optical detection of DNA synthesis with fluorescence labeled nucleotides as building blocks (Helicos Biosciences Corporation and Pacific Biosciences); (2) nanopore-based DNA sequencing (Oxford Nanopore Technologies, Genia, acquired by Roche in 2014 and IBM); (3) direct imaging DNA molecules with advanced microscopy technologies (ZS Genetics, Halcyon Molecular) [4, 6].

Helicos Biosciences was the first company to launch a commercially available sequencer with single molecule sequencing ability. Its sequencing process (wash-and-scan) is similar to Illumina's platform, but without any bridge PCR amplification. However, its short read length,

high error rate (3-4%) and high cost prevented its final success and the company filed for bankruptcy in 2012 [4, 6, 22].

Pacific Biosciences with its single-molecule real-time (SMRT) sequencing technology is now the leading force (less than 10%, see Figure 2.1(b)) [18] in the sequencing market competing with well-developed NGS platforms. Zero-mode waveguide (ZMW) technology makes real-time sequencing possible [6, 23]. With this technology, DNA strands can be sequenced base by base in real time with a high signal to noise level, which saves running time and cost per run as well.

In 2014, Oxford Nanopore Technologies released their first commercially available biological nanopore-based portable DNA sequencer. Its fluorescence-free, long read, low cost and portability features make it a promising candidate for the fourth generation DNA sequencing technologies. Details about the mechanism, development and challenges of nanopore-based sequencing are discussed below. A summary and comparison of TGS platforms is shown in Table 2.3.

Table 2.3. Comparison of TGS platforms (HiliScope and Illumina Synthetic Long-read are not considered as TGS platforms here, shown for comparison)

Sequencer	Pacific Biosciences Sequel [24]	Oxford Nanopore MinION [24]	HeliScope [6]	Illumina Synthetic Long-read
Read length	8 ~12 K bp	Up to 200 K bp	Up to 55 bp	~ 100 K bp
Error profile	NA	7.5% for 2D “pass” read	3 ~ 5%	0.1 %, substitution
Reads	~ 350000	>100,000	NA	3 G
Time/run	0.5 ~ 6 Hours	Up to 48 Hours	Up to 8 Days	5 Days
Cost/Million bases	NA	$ 0.75	NA	$ 1
Advantage	Long read	Longer read, fluorescence-free	Single molecule sequencing	High throughput
Disadvantage	Fluorescence needed	Error rate	Short read length Wash-and-scan process	PCR needed, fluorescence needed

2.2 Nanopore-based DNA sequencing: toward the fourth generation

The idea of using nanopore as sensor for DNA sequencing was proposed by Daniel Branton and David Deamer in the early 1990s [7, 25]. In 1996, they demonstrated the detection of homopolymers of RNA by measuring the ionic current [8]. Their results indicated nanopores could be a promising tool for DNA sequencing. During the past two decades, more than 900 papers have been published related to this area [26]. The landmark for nanopore-based DNA sequencing was the launch of ONT's first commercial available biological nanopore-based DNA sequencer MinION in 2012. It has made impressive achievements with five years' further development [9, 27, 28].

The principle for nanopore-based sensing technology originated from the Coulter counter. Charged biomolecules are driven through a nanopore filled with conductive electrolyte by a bias voltage. When the biomolecules pass through the nanopore, they can trigger electric signals, which are related to their physical and chemical properties. By statistical studies on the amplitude and duration of these signals, different biomolecules can be distinguished. For DNA sequencing, if the four nucleotides A, T, G, C can be distinguished when they pass through the pore then the DNA strand is sequenced.

Though the sequencing principle is straightforward, there are two long-standing hurdles for nanopore-based DNA sequencing technologies: (1) fast translocation speed of DNA; (2) single base resolution from the recorded signal [10, 29]. Recent advances in nanopore-based sequencing technologies to overcome such challenges are reviewed by the nanopore type, sequencing approach (strand sequencing, exonuclease-sequencing and sequencing by synthesis) [30] and detection modality (ion current, tunneling current, conductance) [31].

2.2.1 Biological nanopores

2.2.1.1 Biological nanopore types

Biological nanopores are pore-forming proteins, which can be found naturally in cell membranes acting as ion or molecular transport channels. Mass production of biological nanopores has been achieved by employing standard biology techniques. The purified products have homogeneous well-defined pore sizes and they can be modified easily with advanced biology techniques. There are three commonly used biological nanopores: α-hemolysin, MspA and Phi 29, α-hemolysin and MspA nanopores are usually used for DNA sequencing.

These protein nanopores are usually set in non-conductive lipid bilayer to form the reservoir-pore-reservoir configuration for DNA sequencing. The lipid bilayer is fragile and not stable at extreme working conditions [11, 32]. One alternative is to use a non-conductive polymer membrane as a supporting substrate, which has been used in ONT's MinION sequencer. The summary and comparison of these biological nanopores are shown in Table 2.4.

Table 2.4. Summary and comparison of three commonly used biological nanopores

Nanopore type	Structure and dimensions of the nanopore [33]	Working conditions	Supporting substrate	Molecules detected
α-hemolysin	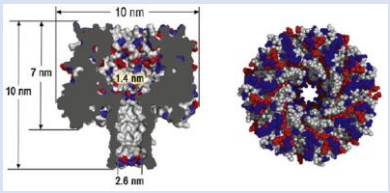	Less than 100°C, pH 2 ~ 12 [34]	Lipid bilayer Self-assemble	ssDNA, RNA, small molecules
MspA	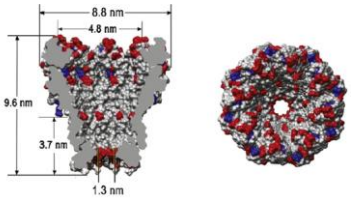	Maintain at 100°C For 30 min, pH 0 ~14 [35]	Lipid bilayer Self-assemble	ssDNA, RNA

(table continued)

Nanopore type	Structure and dimensions of the nanopore [33]	Working conditions	Supporting substrate	Molecules detected
Phi 29	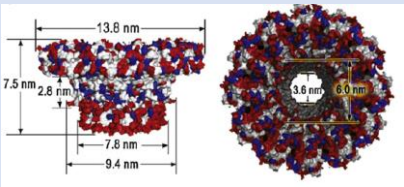	NA	Lipid bilayer Two-step approach required [33]	ssDNA, dsDNA, peptides and possibily small proteins

2.2.1.2 DNA sequencing by biological nanopores

DNA can be sequenced by biological nanopores using three approaches: (1) strand sequencing, (2) exonuclease-sequencing, (3) sequencing by synthesis. For all three approaches, ionic current is the detection signal.

2.2.1.2.1 Strand sequencing

Single strand DNA is driven through biological nanopore under bias voltage and the presence of a DNA molecule in the pore leads to temporary ionic current change. By analyzing the ionic current change, DNA sequence can be determined. In order to achieve this, there are three requirements [10, 36]: (1) single strand DNA should be threaded into nanopore with high efficiency; (2) the motion of single strand DNA should be slow enough to make sure single nucleotides can be detected; (3) the nanopore should have enough sensitivity to distinguish single nucleotides using the ionic current change.

DNA capture rate can be enhanced by manipulating the surface charge on the biological nanopore walls [37, 38]. As illustrated in Figure 2.2, negative charges on the nanopore walls introduce an electroosmotic flow (EOF) opposite to the DNA motion direction, which reduces the capture rate and increases the drag force during translocation. By adding positive charge point mutations to the biological nanopores, DNA capture rate can be increased even with low driving voltages.

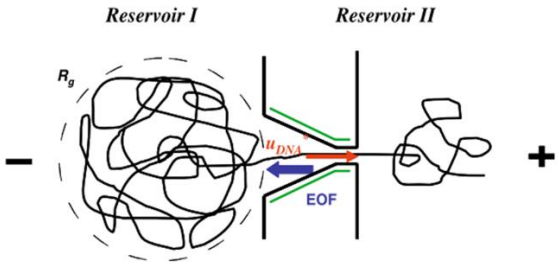

Figure 2.2. Double strand DNA translocation through nanopore. Driving force by electric field and drag force by EOF are two main forces affecting DNA translocation.

Fast translocation speeds (3,000-50,000 nt/ms) [39] are challenge for DNA strand sequencing. DNA motion can be controlled in several ways, such as protein motors (DNA exonucleases and DNA polymerases), driving voltage and electrolyte viscosity. For biological nanopores strand sequencing, DNA translocation can be controlled well by polymerase motor. As shown in Figure 2.3, DNA polymerase from Phi 29 can process DNA at a rate of one nucleotide every ten milliseconds or slower when it extends DNA primer to synthesis [40, 41]. ONT uses a similar mechanism for their commercial MinION sequencer [28].

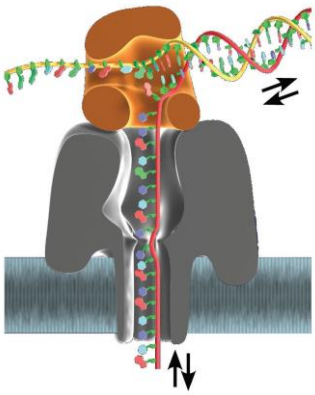

Figure 2.3. Stranding sequencing with motion control by Phi 29 DNA polymerase (brown). An α-hemolysin (grey) is inserted in a lipid bilayer and the DNA substrate (red backbone) is inserted into the pore by an electric field and polymerase activity.

For strand sequencing, high sensitivity means that the nanopore should be small and thin enough to ensure both spatial and longitudinal resolution. Four nucleotides can be discriminated with high accuracy by modified α-hemolysin [42, 43] (shown in Figure 2.4(a)) and MpsA

nanopores [44, 45], but it is impossible to produce a simple 1-base/ 1-current output. Several bases make contributions to the ionic current change [10, 36] and special algorithms are needed to analyze the data.

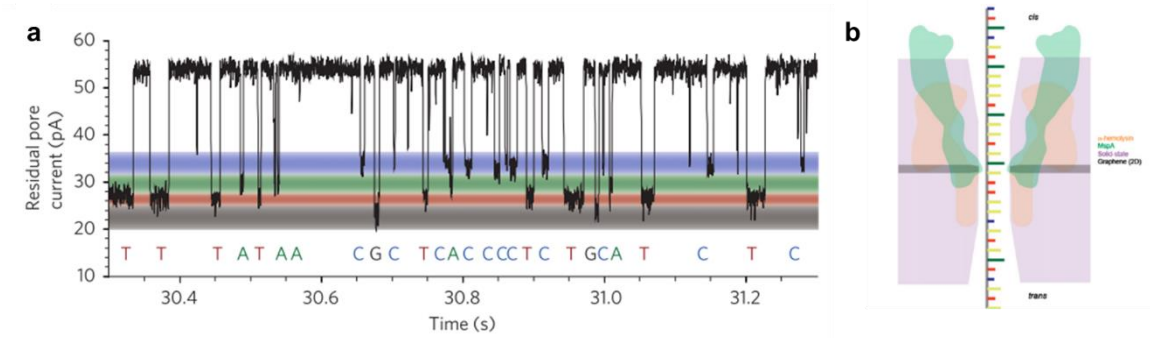

Figure 2.4. (a) Single-channel recording from the WT(M113R/N139Q)6(M113R/N139Q/L135C)1- am6amDP1bCD pore showing dGMP, dTMP, dAMP and dCMP discrimination, with coloured bands (three standard deviations from the centre of the individual Gaussian fits) added to represent the residual current distribution for each nucleotide. (b) An illustration comparing the relative seized of α- hemolysin (αHL) (orange), MspA (green), solid-state (purple), and graphene nanopores (gray).

2.2.1.2.2 Exonuclease-sequencing

As presented in Figure 2.5, Bayley et al. [46] demonstrated four nucleotides released by exonuclease can be distinguished by a modified α-hemolysin nanopore. Compared with strand sequencing, exonuclease-sequencing can produce 1 base/ 1 current output, which makes the data analysis straight forward. But untill now, no data has been shown regarding DNA sequencing with this method and there are still some challenges to overcome: (1) the enzyme should remain active under a strong electric field and high salt concentration [47, 48]; (2) the enzyme digestion rate should be more controllable [30, 31, 49]; (3) the enzyme location should be close to the nanopore mouth in order to ensure all nucleotides can be captured and detected through the nanopore [46, 48]. Several simulation works have been published to facilitate the design of the enzyme-nanopore complex with 100% capture rates [50, 51] and more experimental work is needed to improve this approach.

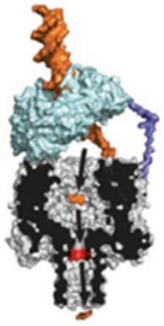

Figure 2.5. Exonuclease-sequencing. An exonuclease (pale blue) attached to the top of an α-hemolysin pore through a genetically encoded (deep blue), or chemical, linker sequentially cleaves dNMPs (gold) off the end of a DNA strand (in this case, one strand of a double-stranded DNA).

2.2.1.2.3 Sequencing by synthesis

As shown in Figure 2.6 (a) and Figure 2.6 (b), Genia (acquired by Roche in 2014) offers an alternative way to sequence single DNA strands by combining the advantages of strand sequencing and exonuclease-sequencing. A DNA polymerase is attached directly to a wild type α-hemolysin nanopore mouth and nucleotides with unique PEG tags pass through the nanopore during DNA synthesis [30]. In this way, template DNA motion is controlled by the DNA polymerase and one tagged nucleotide makes a contribution to the ionic current change at one time.

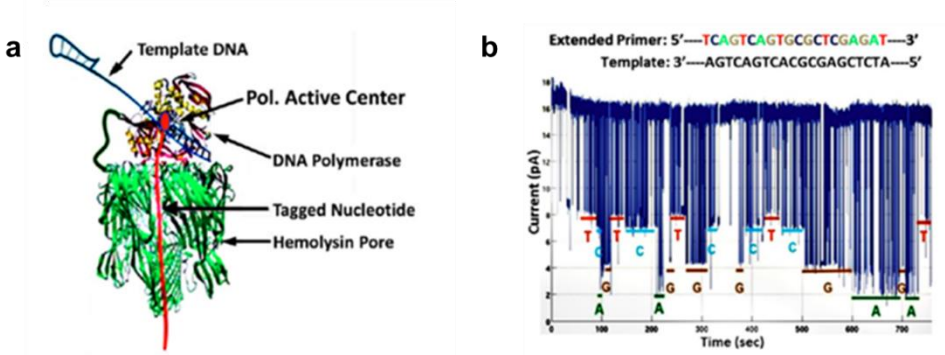

Figure 2.6. (a) Sequencing by synthesis. (b) Long sequence read from nanopore array. During the sequencing, a nucleotide appears to be captures several times before the incorporation of the next nucleotide. Such stuttering can be reduced by changing experimental conditions.

Their preliminary result (shown in Figure 2.6(b)) is promising but there is still significant optimization work to do. Reaction conditions need to be optimized to prevent the "stuttering" issue (the same nucleotide passed the nanopore several times) and base call accuracy can be increased further by polymer tag development.

2.2.2 Solid-state nanopores

With the help of advanced micro/nano fabrication technologies, the first solid-state nanopore with single-nanometer precision was reported in 2001 [52], and since then the popularity of solid-state nanopores is growing. Compared with biological nanopores, solid-state nanopores have several advantages: (1) solid-state nanopores have tunable sizes from sub-nanometer to tens of nanometers for different applications; (2) solid-state nanopores are mechanically robust and stable under various electrolyte concentrations, pH and temperature conditions; (3) solid-state nanopores can be chemically modified and integrated with sophisticated electronics.

In this section, different types of solid-state nanopores, their fabrication technique, and recent practice/challenges toward DNA sequencing by solid-state nanopores are summarized.

2.2.2.1 Solid-state nanopore types

2.2.2.1.1 Si based nanopores

SiO_2 and Si_3N_4 nanopores are the most commonly used and studied solid-state nanopores. Such nanopores are drilled on very thin (20- 30 nm) low-stress SiO_2 and Si_3N_4 film deposited on Si substrates by electron beam or ion beam, as demonstrated in Figure 2.7.

In 2001 Golovchenko et al. from Harvard first demonstrated the fabrication of synthetic nanopores by ion beam sculpting process [52]: materials on the surface was sputtered away by an ion beam to form a nanometer scale pore at the bottom of the resulting bowl shaped cavity. A feedback system monitors the pore size in real time by counting the transmitted ions. Furthermore,

their experiments indicated nanopores could enlarge or shrink dependent on temperature, cycle time and ion flux [52].

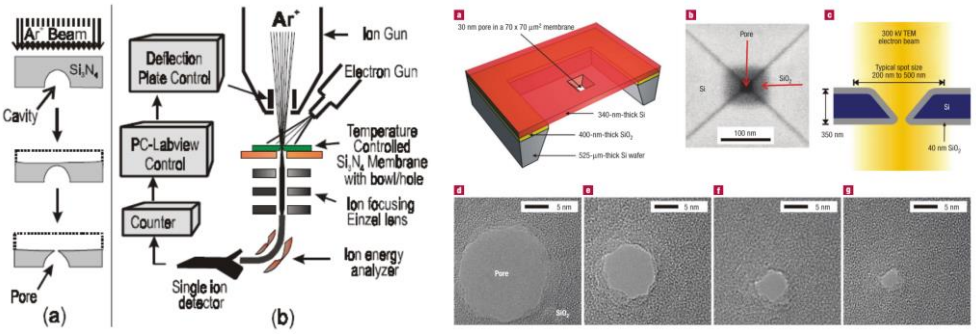

Figure 2.7. (a) Solid-nanopore fabrication by ion sculpting process. (b) Solid-state nanopore fabrication by standard silicon processing and transmission electron microscopy (TEM).

In 2003 Dekker et al. from Delft proposed an alternative approach based on standard silicon processing and transmission electron microscopy (TEM). During this process, a small pre-defined SiO_2 nanopore (smaller than membrane thickness) was fabricated by wet etching or direct TEM then the nanopore size could be reduced further because SiO_2 flows and reshapes near the pore when exposed to high intensity electron beam drilling [53, 54]. Compared with ion sculpting, this approach allows more precise specification of pore size, which can be monitored easily by TEM imaging in real-time [55]. The cross-section of the nanopore fabricated by this method is hour-glass shaped as obtained from microscopy tomography [54]. The total resistance of such solid-state nanopore is modeled as a sum of channel resistance and access resistance [56].

2.2.2.1.2 Al_2O_3 nanopore

Compared with Si based nanopores, Al_2O_3 nanopores have better performance in terms of noise level, DNA capture and DNA motion control [25]. Al_2O_3 nanopore can be manufactured on metal oxide membranes using the same method as Si based nanopores. Such nanopores could reduce the DNA translocation speed by enhancing the electrostatic and hydrodynamic interaction

between DNA and nanopore [57]. An alternative approach is to deposit Al_2O_3 on Si based nanopores with atomic layer deposition (ALD) system. The thin Al_2O_3 layer could decreases the nanopore size further, reduce the 1/f noise level and increase the DNA capture rate due to the positive surface charge on the wall [58].

2.2.2.1.3 Solid-State nanopores with embedded nanogap electrode

For solid-state nanopore based DNA sequencing, DNA motion control is still a main challenge. One possible way to slow down DNA translocation speed is to locate one pair of electrodes with nanogap directly at the nanopore aperture [59]. These transverse electrodes can be used to sequence DNA by measuring the tunneling current during DNA translocation. Early work on DNA imaging by scanning tunneling microscopy (STM) demonstrated that the four dNMPs have their own distinct tunneling current signatures [60, 61]. Kawai and coworkers demonstrated dNMPs and oligomers can be sequenced by nanogap Au electrode in a free solution [62, 63]. No data has been reported regarding DNA sequenced by tunneling current while driven through nanopores by an electric field.

The bottleneck for this method is the low throughput device fabrication. The nanogap electrodes can be fabricated by traditional e-beam lithography [59, 64] or by mechanical/electrical breakdown [62, 63]. The nanopore is usually drilled right in between the electrodes by the ion beam or e-beam. Also, nanogap electrodes can be damaged during experiments [59, 64].

2.2.2.1.4 Monolayer nanopores

Compared with the nanopores mentioned above, monolayer nanopores are very thin (thickness ~ 0.335 nm), which is close to the gap between two adjacent base pairs. Thus, high longitudinal resolution can be achieved if monolayer nanopores are used for DNA strand sequencing. Monolayer nanopores can be fabricated from graphene [65], BN and MoS_2 [39] by TEM drilling. Figure 2.8 presents another promising monolayer, graphene based nanopore. Schneider et al. detected double stranded DNA via a graphene nanopore [65] and later they modified the graphene nanopore with a hydrophilic layer coating to prevent the clogging during translocation [66]. One more advantage of the graphene nanopore is that DNA strand can be sequenced by both ionic current and tunneling current (conductance) due to the electrical properties of the graphene. Several simulation works have been published related to dynamic and electronic transport properties of DNA/nucleotides translocating through graphene nanopores, but no experimental data has been published [67-71].

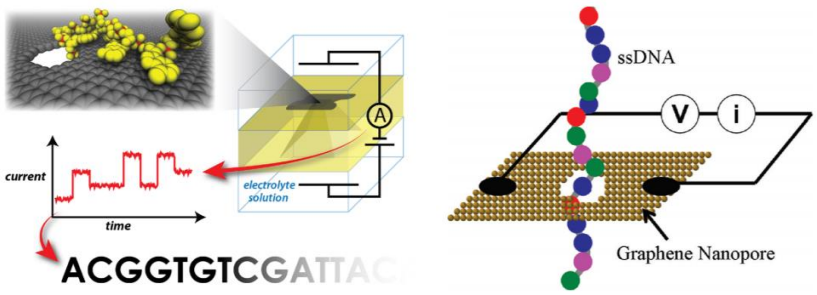

Figure 2.8. (a) DNA sequencing by graphene nanopore, ionic current measurement scheme. (b) DNA sequencing by graphene nanopore, tunneling current measurement scheme.

In a recently published paper, Feng et al. identified four single nucleotides in a MoS_2 nanopore [39]. This is the first experiment to show single nucleotides identification in solid-state nanopore by measuring the ionic current. This work indicates DNA can be sequenced by MoS_2

nanopores in the same way as biological nanopores (stranding sequencing and exonuclease-sequencing) did.

2.2.2.2 Challenges for DNA sequencing by solid-state nanopores

For solid-state nanopores DNA sequencing, most research focused on strand sequencing approach, either by ionic current measurement or tunneling current measurement. Here, we focus on the current challenges for DNA strand sequencing in solid-state nanopores. Though dNMPs detectability has been demonstrated by solid-state nanopores [39, 63], single base resolution, DNA motion control and nanopore size variations are still three main challenges for solid-state nanopore sequencing.

2.2.2.2.1 Single base resolution

Si based nanopores are the most commonly used solid-state nanopores and their fabrication technologies are well developed [72]. Small nanopores with size comparable to biological nanopores are drilled on SiO_2 or Si_3N_4 membranes with tens of nanometer thickness. Compared with the distance between adjacent DNA base pairs, such long nanopores have poor longitudinal resolution for strand sequencing. There are several methods to reduce the membrane thickness such as e-beam [73], ion beam [74] and plasma thinning [75]. The cross-section shape of the drilled nanopore can be controlled by electron beam size. As illustrated in Figure 2.9, with electron beam becomes wider, the nanopore cross-section profile changes from cylindrical shape to a compressed hourglass shape [55], which has a shorter pore length. However, these passive methods cannot solve the resolution issue completely.

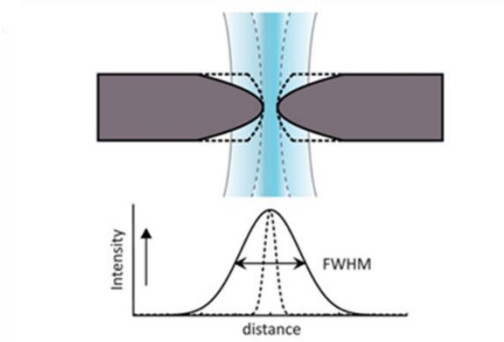

Figure 2.9. Si nanopore cross-section profile chages from cylinder shape to hour glass shape, depending on electron beam spot size.

An alternative way is to fabricate nanopores in monolayer material such as graphene, BN and MoS_2 as we discussed above. dNMPs detection has been demonstrated in MoS_2 nanopores [39] but no DNA sequencing data have been published.

2.2.2.2.2 DNA motion control

For a double stranded DNA (dsDNA), the typical translocation speed in a solid-state nanopore is about 30 base pairs per microsecond under a few hundred millivolts, which is beyond the capability of current data acquisition systems [10, 76, 77]. There are two major approaches to control long DNA translocation through solid-state nanopores: (1) nanopore surface modification and adjustment of experimental condition for voltage-driven DNA translocation (2) protein motor controlled DNA ratcheting.

For voltage-driven DNA translocation, the translocation velocity of dsDNA can be expressed as [76]:

$$\upsilon = \varepsilon \frac{\zeta_d - \zeta_w}{\eta} E, \quad (1)$$

where ε is the dielectric constant of the electrolyte, η the viscosity of the electrolyte, ζ_d and ζ_w the zeta potentials on the DNA and pore surfaces respectively, and E the biasing electric field. Based on Equation 2.1, DNA translocation speed can be slowed down by increasing the frictional force

during DNA translocation, adjusting the zeta potentials on the DNA and nanopore surfaces or reducing the electric field.

Table 2.5. Forces affecting double-stranded DNA translocation.

Force	Magnitude
F_u^* (Muthukumar 1999)	~0.01 pN
F_u^* (Odijk 1983)	0.67 pN
F_u^* (Klushin et al. 2008)	1.9 pN
F_r^* (Prinsen et al. 2009)	0.083 pN
F_{blob1}^* (Storm et al. 2005b)	7.86 pN
F_{blob2}^*	~0.1 pN
F_e^*	113 pN
F_d^*	83.5 pN

According to Table 2.5, electrophoretic driving force and hydrodynamic drag force are the two main forces affecting DNA translocation. By increasing the buffer solution viscosity, the DNA translocation velocity can be reduced. It was demonstrated dsDNA translocation velocity was reduced 5 to 6 times in a 1:1 glycerol-water mixture [77]. MD simulation shows ssDNA translocation velocity can be reduced 10 times in a 1:2 glycerol-water solution [76]. In addition to the hydrodynamic friction force, contact friction between a DNA molecule and nanopore surface can reduce the DNA translocation velocity further. Hydrophilic self-assembled monolayer (SAM) coatings can slow down DNA translocation velocity and increase capture rate by enhancing the interaction between dsDNA and Si_3N_4 nanopore [78].

Zeta potential of a charged surface is determined by its surface charge density [79]. Effective surface charge density of dsDNA is affected by electrolyte concentration. According to MD simulation results, for mono- or di-valent electrolyte, dsDNA translocation speed decreases with increasing ion concentration [76]. Surface charge density of solid-state nanopore walls can be tailored by chemical surface modification or controlled by integrated gate electrode [80]. Negative surface charges introduce EOF, which slows down DNA translocation.

Low electric field is preferred to slow down DNA translocation but the driving voltage should be higher than a certain threshold value to ensure efficient DNA capture. As presented in

Figure 2.10, MD simulation shows ssDNA can be trapped within nanopore by alternating bias electric field [81] and single base resolution can be achieved by precise bias voltage control. An alternative is to trap DNA within a DNA transistor device [82]. MD simulation shows ssDNA can be ratcheted through a nanopore one nucleotide at a time. The challenge for this method is metal layer thickness control, cutting-edge fabrication techniques such as atomic layer deposition (ALD) are required.

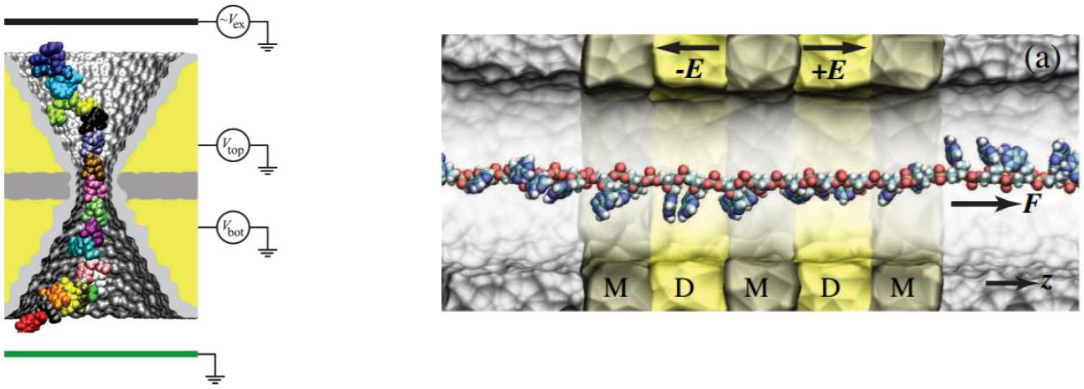

Figure 2.10. MD simulation of DNA trapped within nanopore with embedded alternative electrodes.

Ratcheting ssDNA through nanopore has been realized by attaching a Phi-29 DNA polymerase at α-haemolysin nanopore mouth. Similar idea can be applied to solid-state nanopores. However, no experimental data have been released regarding this method. One possible reason is that locating enzymes precisely at solid-state nanopore mouth is challenging. Also, for both polymerase and exonuclease assist DNA motion control, the most important thing is to find suitable enzymes which can keep active under nanopore measurement conditions. Moreover, for exonuclease assisted DNA motion control, 100% detection efficiency is required for released nucleotides.

2.2.2.2.3 Nanopores size variations

With the help of advanced biological technologies, well-defined biological nanopore dimension can be produced on a large-scale. On the contrary, solid-state nanopores are fabricated using low throughput methods and the nanopores sizes could be different. Since the ionic current blockage is sensitive to nanopore size, robust sequencing of DNA with high base calling accuracy is hard to achieve with such variation.

One way to overcome pore size variation effect on detection accuracy is to distinguish different biomolecules by their mobility instead of their current blockade signature. Pedone and co-workers introduced a pore-cavity-pore (PCP) device to study the escape behavior of nanoparticles and DNA [83, 84]. A smaller Si_3N_4 nanopore (~ 50 nm diameter), a pyramidal cavity and a larger Si nanopore (~ 160 nm diameter) were fabricated as analyte entrance, trap and exit. Fluorescence labeled λ-DNA molecules were electrically driven through the Si nanopore and trapped the in pyramidal cavity after turning off the external electric field. The trapped DNA molecule can escape by diffusion from the Si nanopore in several seconds, which was observed by fluorescence microscopy.

Jacobson et al., fabricated an in-plane dual-nanopore device on a Si substrate to detect hepatitis B virus (HBV) capsids [85]. The device consisted of two nanopores (50 nm wide, 50 nm deep and 40 nm long and a 2 μm long flight tube. When single HBV capsid is driven through the two nanopores, it triggered ionic current blockades with downward or upward peaks on current-time trace) in series. By analyzing peak-to-peak time duration, electrophoretic mobility of analyte was calculated and different analytes can be distinguished based on that.

2.3 Emerging nanopore-based sensing companies

The idea of using nanopores for biomolecules sensing can be traced back to the 1990s. After more than 20 years of research and development, the challenges of DNA sequencing by biological nanopores have been overcome by academic laboratories [28, 36]. One milestone for nanopore-based sensing technologies is the launching of Oxford Nanopore's first portable DNA sequencer MinION in 2014 and since then many emerging companies are working on delivering maturing nanopore technologies for routine clinical application. In this section, we introduce four companies and their products, which provide some insights for academic researchers. Oxford Nanopore Technologies (ONT) and Genia Technologies are companies working on biological nanopores. Two Pore Guys and iZON Science are working on Si-based nanopores and polymer-based, respectively. More information about emerging companies in this field can be found on https://www.thenanoporesite.com/companies.html.

2.3.1 Oxford Nanopore Technologies (ONT)

Oxford Nanopore Technologies was founded in 2005 and initially worked on exonuclease-sequencing [36, 86]. The company abandoned this approach in mid-2011 [46] due to an arbitration proceeding initiated by Illumina (San Diego). The company transferred its focus to strand sequencing after having support from academic laboratories. In 2012, the company announced the success of DNA strand sequencing using nanopores and two years later they launched the first commercial USB type nanopore sequencer MinION. With four years development, the accuracy of a 2D read can reach up to 97% [9]. Methylation [87] and structural variatians [88] in cancer can also be detected. With its long read, portability and affordable features, many groups have used ONT devices for their own research (even in Antarctic Valleys) and reported device performance

for its further improvement [89-91]. In addition to DNA sequencing, ONT has expanded its application and service to RNA sequencing, protein sensing, and water testing.

Figure 2.11. Portable, USB-size MinION from ONT (https://nanoporetech.com/products/minion); Schematic image showing DNA sequencing by biological nanopore, dsDNA (orange), adapter (green), nanopore (blue) and lipid layer (grey).

As shown in Figure 2.11, each ONT device contains hundreds of biological nanopores. Prior to sequencing, an adapter is ligated to DNA, which facilitate DNA capture and motion control. Upon captured by nanopore, DNA is fed through by the adapter (enzyme) on millisecond time scale. Though DNA motion is well-controlled by the enzyme, multiple bases make contribution to current output, therefore special base-calling software [28, 92] is required to decode the current change data.

In the long term, ONT keeps seeking for new materials including mutant, adapter and nanopore materials to improve their device performance. They are collaborating with researchers to study solid-state nanopores, hybrid nanopores, integrated sensors and graphene nanopores.

2.3.2 Genia Technologies

After shutting down 454 Life Sciences, Roche returned to the sequencing game by acquiring Genia Technologies in 2014. As mentioned above, Genia developed the sequence by synthesis (SBS) approach as shown in Figure 2.6. DNA polymerase is attached to a nanopore (α HL-polymerase complex) and nucleotides with different PEG tags are detected during

incorporation. Genia published one paper in PNAS [30] in 2016, demonstrating their technology by sequencing short length DNAs. Since then, no data or report has been released.

2.3.3 Two Pore Guys (TPG)

Unlike ONT and Genia, Two Pore Guys uses Si-based nanopores for biomolecule sensing. Due to the limitations of solid-state nanopores, for example thickness, it seems the company will not use Si-based nanopore for sequencing directly, but for sensing variations or DNA motion control. As shown in Figure 2.12, a nanowire electrode is integrated in between two pores as a sensor for DNA sequencing. No DNA sequencing data have been released using this TPG device, while some initial data with DNA variation for cancer were reported on their website.

Figure 2.12. Video clip from TPG YouTube channel, demonstrating their technology (https://www.youtube.com/watch?v=0g-9BlNW9uo). DNA motion is regulated by controlling bias voltage applied through two nanopores and therefore ample time is available for sequencing.

2.3.4 iZON Science

iZON is a fast-growing company focusing more on larger objectives (> 100 nm) sensing, such as nanoparticles and extracellular vesicles. Unlike previous companies using nanopores with fixed sizes, iZON Science invented its unique tunable resistive pulse sensing (TRPS) technology. Compared with traditional nanopores with fixed pore size, resizable elastomeric thermoplastic polyurethane (TPU) based nanopores can improve the sensitivity and resolution of systems for discriminating nanoparticle suspensions [93, 94]. As illustrated in Figure 2.13, nanopore size is

controlled by stretching “S” and analytes are fed through nanopore by both applied voltage “V” and pressure “P”. All these parameters are required to be optimized several times to achieve an accurate analysis with high resolution. By analyzing the current blockade magnitude, dwell time and frequency, analytes information of size, surface charge (zeta potential) and concentration can be collected.

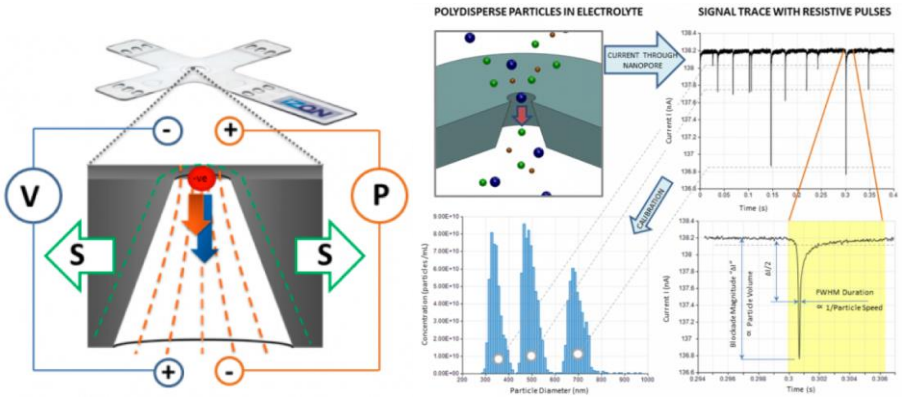

Figure 2.13. Consumable iZON nanopore with tunable pore size and sensing mechanism. (http://izon.com/how-trps-works/)

2.4 DNA sequencing by time of flight (ToF) measurement

After reviewing the evolution of DNA sequencing technologies and current nanopore-based sensing platforms, we find that over the long term, solid-state nanopores could be good alternatives to biological nanopores for sensing applications. However, it is still challenging for solid-state nanopores to sequence DNA due to low-through put device fabrication, nanopore size variation and limited resolution. In order to overcome the challenges mentioned above, we propose to sequence DNA base by base using ToF measurement with a polymer based in-plane dual-nanopore device. The detection process consists of two steps, DNA digestion and single nucleotide detection. Exonuclease immobilization and solid phase DNA digestion have been demonstrated on polymer post arrays by preliminary experiments [95]. In this work, we focus on the second step, single nucleotide discrimination.

Compared with traditional solid-state nanopores fabricated by e-beam or ion beam drilling, polymer based in-plane nanopores can be fabricated by high throughput nanoimprint lithography (NIL) on different polymer substrates with good replication fidelity [96]. Compared with vertical type nanopores on thin membrane, an in-plane nanopore device can be easily handled, especially for fluorescence observation. The sequencing mechanism is similar to HBV capsids detection by in-plane dual-nanopore device demonstrated by the Jacobson group [97]. Enzyme digested single nucleotides (1 nucleotide per 1-2 ms) are electrically driven through two sub-5 nm size (equivalent diameter) nanopores with 0.5-1 μm spacing. The four nucleotides are distinguished by their time-of-flight values with current blockade and dwell time data serving as supporting information.

2.5 References

1. Collins, F.S. and H. Varmus, *A new initiative on precision medicine.* New England Journal of Medicine, 2015. **372**(9): p. 793-795.

2. Bianchi, D.W., et al., *DNA sequencing versus standard prenatal aneuploidy screening.* New England Journal of Medicine, 2014. **370**(9): p. 799-808.

3. Gonzalez de Castro, D., et al., *Personalized cancer medicine: molecular diagnostics, predictive biomarkers, and drug resistance.* Clinical Pharmacology & Therapeutics, 2013. **93**(3): p. 252-259.

4. Ozsolak, F., *Third-generation sequencing techniques and applications to drug discovery.* Expert opinion on drug discovery, 2012. **7**(3): p. 231-243.

5. Sheridan, C., *Illumina claims [dollar] 1,000 genome win*. 2014, Nature Research.

6. Schadt, E.E., S. Turner, and A. Kasarskis, *A window into third-generation sequencing.* Human molecular genetics, 2010. **19**(R2): p. R227-R240.

7. Deamer, D., *Nanopore analysis of nucleic acids bound to exonucleases and polymerases.* Annual review of biophysics, 2010. **39**: p. 79-90.

8. Kasianowicz, J.J., et al., *Characterization of individual polynucleotide molecules using a membrane channel.* Proceedings of the National Academy of Sciences, 1996. **93**(24): p. 13770-13773.

9. Jain, M., et al., *MinION Analysis and Reference Consortium: Phase 2 data release and analysis of R9. 0 chemistry.* F1000Research, 2017. **6**.

10. Maitra, R.D., J. Kim, and W.B. Dunbar, *Recent advances in nanopore sequencing.* Electrophoresis, 2012. **33**(23): p. 3418-3428.

11. Dekker, C., *Solid-state nanopores.* Nat Nanotechnol, 2007. **2**(4): p. 209-15.

12. Venkatesan, B.M. and R. Bashir, *Nanopore sensors for nucleic acid analysis.* Nature nanotechnology, 2011. **6**(10): p. 615-624.

13. Zwolak, M. and M. Di Ventra, *Colloquium: Physical approaches to DNA sequencing and detection.* Reviews of Modern Physics, 2008. **80**(1): p. 141.

14. Hayden, E.C., *The $1,000 genome.* Nature, 2014. **507**(7492): p. 294.

15. Shendure, J. and H. Ji, *Next-generation DNA sequencing.* Nat Biotechnol, 2008. **26**(10): p. 1135-45.

16. Liu, L., et al., *Comparison of next-generation sequencing systems.* BioMed Research International, 2012. **2012**.

17. Glenn, T.C., *Field guide to next-generation DNA sequencers.* Molecular ecology resources, 2011. **11**(5): p. 759-769.

18. Steinbock, L. and A. Radenovic, *The emergence of nanopores in next-generation sequencing.* Nanotechnology, 2015. **26**(7): p. 074003.

19. Salipante, S.J., et al., *Performance comparison of Illumina and ion torrent next-generation sequencing platforms for 16S rRNA-based bacterial community profiling.* Applied and environmental microbiology, 2014. **80**(24): p. 7583-7591.

20. Pettersson, E., J. Lundeberg, and A. Ahmadian, *Generations of sequencing technologies.* Genomics, 2009. **93**(2): p. 105-111.

21. Heather, J.M. and B. Chain, *The sequence of sequencers: the history of sequencing DNA.* Genomics, 2016. **107**(1): p. 1-8.

22. Lee, H., et al., *Third-generation sequencing and the future of genomics.* BioRxiv, 2016: p. 048603.

23. Eid, J., et al., *Real-time DNA sequencing from single polymerase molecules.* Science, 2009. **323**(5910): p. 133-138.

24. Goodwin, S., J.D. McPherson, and W.R. McCombie, *Coming of age: ten years of next-generation sequencing technologies.* Nature Reviews Genetics, 2016. **17**(6): p. 333-351.

25. Feng, Y., et al., *Nanopore-based fourth-generation DNA sequencing technology.* Genomics Proteomics Bioinformatics, 2015. **13**(1): p. 4-16.

26. Haque, F., et al., *Solid-State and Biological Nanopore for Real-Time Sensing of Single Chemical and Sequencing of DNA.* Nano Today, 2013. **8**(1): p. 56-74.

27. Mikheyev, A.S. and M.M. Tin, *A first look at the Oxford Nanopore MinION sequencer.* Mol Ecol Resour, 2014. **14**(6): p. 1097-102.

28. Jain, M., et al., *The Oxford Nanopore MinION: delivery of nanopore sequencing to the genomics community.* Genome biology, 2016. **17**(1): p. 239.

29. Schneider, G.F. and C. Dekker, *DNA sequencing with nanopores.* Nature biotechnology, 2012. **30**(4): p. 326-328.

30. Fuller, C.W., et al., *Real-time single-molecule electronic DNA sequencing by synthesis using polymer-tagged nucleotides on a nanopore array.* Proceedings of the National Academy of Sciences, 2016. **113**(19): p. 5233-5238.

31. Carson, S. and M. Wanunu, *Challenges in DNA motion control and sequence readout using nanopore devices.* Nanotechnology, 2015. **26**(7): p. 074004.

32. Kawano, R., et al., *A Polymer-Based Nanopore-Integrated Microfluidic Device for Generating Stable Bilayer Lipid Membranes.* Small, 2010. **6**(19): p. 2100-2104.

33. Haque, F., et al., *Solid-state and biological nanopore for real-time sensing of single chemical and sequencing of DNA.* Nano today, 2013. **8**(1): p. 56-74.

34. Kang, X.f., et al., *Single protein pores containing molecular adapters at high temperatures.* Angewandte Chemie International Edition, 2005. **44**(10): p. 1495-1499.

35. Consortium, C.T., *The nature and identification of quantitative trait loci: a community's view.* Nature reviews. Genetics, 2003. **4**(11): p. 911.

36. Bayley, H., *Nanopore sequencing: from imagination to reality.* Clinical chemistry, 2015. **61**(1): p. 25-31.

37. Maglia, G., et al., *Enhanced translocation of single DNA molecules through α-hemolysin nanopores by manipulation of internal charge.* Proceedings of the National Academy of Sciences, 2008. **105**(50): p. 19720-19725.

38. Butler, T.Z., et al., *Single-molecule DNA detection with an engineered MspA protein nanopore.* Proc Natl Acad Sci U S A, 2008. **105**(52): p. 20647-52.

39. Feng, J., et al., *Identification of single nucleotides in MoS2 nanopores.* Nat Nanotechnol, 2015. **10**(12): p. 1070-6.

40. Cherf, G.M., et al., *Automated forward and reverse ratcheting of DNA in a nanopore at 5-A precision.* Nature biotechnology, 2012. **30**(4): p. 344-348.

41. Lieberman, K.R., et al., *Processive replication of single DNA molecules in a nanopore catalyzed by phi29 DNA polymerase.* Journal of the American Chemical Society, 2010. **132**(50): p. 17961-17972.

42. Astier, Y., O. Braha, and H. Bayley, *Toward single molecule DNA sequencing: direct identification of ribonucleoside and deoxyribonucleoside 5 '-monophosphates by using an engineered protein nanopore equipped with a molecular adapter*. Journal of the American Chemical Society, 2006. **128**(5): p. 1705-1710.

43. Venkatesan, B.M. and R. Bashir, *Nanopore sensors for nucleic acid analysis.* Nat Nanotechnol, 2011. **6**(10): p. 615-24.

44. Manrao, E.A., et al., *Reading DNA at single-nucleotide resolution with a mutant MspA nanopore and phi29 DNA polymerase.* Nature biotechnology, 2012. **30**(4): p. 349-353.

45. Manrao, E.A., et al., *Nucleotide discrimination with DNA immobilized in the MspA nanopore.* PloS one, 2011. **6**(10): p. e25723.

46. Clarke, J., et al., *Continuous base identification for single-molecule nanopore DNA sequencing.* Nat Nanotechnol, 2009. **4**(4): p. 265-70.

47. McGinn, S., et al., *New technologies for DNA analysis–a review of the READNA Project.* New biotechnology, 2016. **33(**3): p. 311-330.

48. Reiner, J.E., et al., *The effects of diffusion on an exonuclease/nanopore-based DNA sequencing engine.* The Journal of chemical physics, 2012. **137**(21): p. 214903.

49. van Oijen, A.M., et al., *Single-molecule kinetics of λ exonuclease reveal base dependence and dynamic disorder.* Science, 2003. **301**(5637): p. 1235-1238.

50. Sampath, G., *DNA sequencing with stacked nanopores and exonuclease: A simulation - based analysis.* Electrophoresis, 2016. **37**(17-18): p. 2429-2434.

51. Brady, K.T. and J.E. Reiner, *Improving the prospects of cleavage-based nanopore sequencing engines.* The Journal of chemical physics, 2015. **143**(7): p. 08B608_1.

52. Li, J., et al., *Ion-beam sculpting at nanometre length scales.* Nature, 2001. **412**(6843): p. 166.

53. Storm, A.J., et al., *Fabrication of solid-state nanopores with single-nanometre precision.* Nat Mater, 2003. **2**(8): p. 537-40.

54. Keyser, U.F., et al., *Nanopore tomography of a laser focus.* Nano letters, 2005. **5**(11): p. 2253-2256.

55. van den Hout, M., et al., *Controlling nanopore size, shape and stability.* Nanotechnology, 2010. **21**(11): p. 115304.

56. Kowalczyk, S.W., et al., *Modeling the conductance and DNA blockade of solid-state nanopores.* Nanotechnology, 2011. **22**(31): p. 315101.

57. Venkatesan, B.M., et al., *DNA sensing using nanocrystalline surface-enhanced Al2O3 nanopore sensors.* Advanced functional materials, 2010. **20**(8): p. 1266-1275.

58. Chen, P., et al., *Atomic layer deposition to fine-tune the surface properties and diameters of fabricated nanopores.* Nano letters, 2004. **4**(7): p. 1333-1337.

59. Healy, K., et al., *Fabrication and characterization of nanopores with insulated transverse nanoelectrodes for DNA sensing in salt solution.* Electrophoresis, 2012. **33**(23): p. 3488-3496.

60. Chang, S., et al., *Electronic signatures of all four DNA nucleosides in a tunneling gap.* Nano letters, 2010. **10**(3): p. 1070-1075.

61. Xu, M., et al., *Conductance of single thiolated poly (GC)-poly (GC) DNA molecules.* Applied Physics Letters, 2005. **87**(8): p. 083902.

62. Tsutsui, M., et al., *Single-molecule sensing electrode embedded in-plane nanopore.* Scientific reports, 2011. **1**.

63. Tsutsui, M., et al., *Identifying single nucleotides by tunnelling current.* Nat Nanotechnol, 2010. **5**(4): p. 286-90.

64. Gierhart, B.C., et al., *Nanopore with transverse nanoelectrodes for electrical characterization and sequencing of DNA.* Sensors and Actuators B: Chemical, 2008. **132**(2): p. 593-600.

65. Schneider, G.F., et al., *DNA translocation through graphene nanopores.* Nano Lett, 2010. **10**(8): p. 3163-7.

66. Schneider, G.F., et al., *Tailoring the hydrophobicity of graphene for its use as nanopores for DNA translocation.* Nat Commun, 2013. **4**: p. 2619.

67. Prasongkit, J., et al., *Transverse conductance of DNA nucleotides in a graphene nanogap from first principles.* Nano letters, 2011. **11**(5): p. 1941-1945.

68. Nelson, T., B. Zhang, and O.V. Prezhdo, *Detection of nucleic acids with graphene nanopores: ab initio characterization of a novel sequencing device.* Nano letters, 2010. **10**(9): p. 3237-3242.

69. Avdoshenko, S.M., et al., *Dynamic and electronic transport properties of DNA translocation through graphene nanopores.* Nano letters, 2013. **13**(5): p. 1969-1976.

70. Wells, D.B., et al., *Assessing graphene nanopores for sequencing DNA.* Nano letters, 2012. **12**(8): p. 4117-4123.

71. Prasongkit, J., et al., *Theoretical study of electronic transport through DNA nucleotides in a double-functionalized graphene nanogap.* The Journal of Physical Chemistry C, 2013. **117**(29): p. 15421-15428.

72. Miles, B.N., et al., *Single molecule sensing with solid-state nanopores: novel materials, methods, and applications.* Chemical Society Reviews, 2013. **42**(1): p. 15-28.

73. Rodríguez-Manzo, J.A., et al., *DNA translocation in nanometer thick silicon nanopores.* ACS nano, 2015. **9**(6): p. 6555-6564.

74. Hall, A.R., *In situ thickness assessment during ion milling of a free-standing membrane using transmission helium ion microscopy.* Microscopy and Microanalysis, 2013. **19**(3): p. 740-744.

75. Wanunu, M., et al., *Rapid electronic detection of probe-specific microRNAs using thin nanopore sensors.* Nature nanotechnology, 2010. **5**(11): p. 807-814.

76. Luan, B., G. Stolovitzky, and G. Martyna, *Slowing and controlling the translocation of DNA in a solid-state nanopore.* Nanoscale, 2012. **4**(4): p. 1068-1077.

77. Fologea, D., et al., *Slowing DNA translocation in a solid-state nanopore.* Nano letters, 2005. **5**(9): p. 1734-1737.

78. Wang, D., et al., *Regulating the transport of DNA through biofriendly nanochannels in a thin solid membrane.* Sci Rep, 2014. **4**: p. 3985.

79. Behrens, S.H. and D.G. Grier, *The charge of glass and silica surfaces.* The Journal of Chemical Physics, 2001. **115**(14): p. 6716-6721.

80. He, Y., et al., *Gate manipulation of DNA capture into nanopores.* Acs Nano, 2011. **5**(10): p. 8391-8397.

81. Sigalov, G., et al., *Detection of DNA sequences using an alternating electric field in a nanopore capacitor.* Nano letters, 2008. **8**(1): p. 56-63.

82. Luan, B., et al., *Base-by-base ratcheting of single stranded DNA through a solid-state nanopore.* Physical review letters, 2010. **104**(23): p. 238103.

83. Pedone, D., et al., *A Pore− Cavity− Pore Device to Trap and Investigate Single Nanoparticles and DNA Molecules in a Femtoliter Compartment: Confined Diffusion and Narrow Escape.* Nano letters, 2011. **11**(4): p. 1561-1567.

84. Pedone, D., et al., *Fabrication and electrical characterization of a pore–cavity–pore device.* Journal of Physics: Condensed Matter, 2010. **22**(45): p. 454115.

85. Harms, Z.D., et al., *Nanofluidic devices with two pores in series for resistive-pulse sensing of single virus capsids.* Analytical chemistry, 2011. **83**(24): p. 9573-9578.

86. Brown, C.G. and J. Clarke, *Nanopore development at Oxford Nanopore.* Nature biotechnology, 2016. **34**(8): p. 810.

87. Simpson, J.T., et al., *Detecting DNA methylation using the oxford nanopore technologies MinION sequencer.* bioRxiv, 2016: p. 047142.

88. Norris, A.L., et al., *Nanopore sequencing detects structural variants in cancer.* Cancer biology & therapy, 2016. **17**(3): p. 246-253.

89. Laver, T., et al., *Assessing the performance of the oxford nanopore technologies minion.* Biomolecular detection and quantification, 2015. **3**: p. 1-8.

90. Johnson, S.S., et al., *Real-time DNA sequencing in the Antarctic dry valleys using the Oxford Nanopore sequencer.* Journal of biomolecular techniques: JBT, 2017. **28**(1): p. 2.

91. Weirather, J.L., et al., *Comprehensive comparison of Pacific Biosciences and Oxford Nanopore Technologies and their applications to transcriptome analysis.* F1000Research, 2017. **6**.

92. Loman, N.J. and A.R. Quinlan, *Poretools: a toolkit for analyzing nanopore sequence data.* Bioinformatics, 2014. **30**(23): p. 3399-3401.

93. Vogel, R., et al., *Quantitative sizing of nano/microparticles with a tunable elastomeric pore sensor.* Analytical chemistry, 2011. **83**(9): p. 3499-3506.

94. Willmott, G. and P. Moore, *Reversible mechanical actuation of elastomeric nanopores.* Nanotechnology, 2008. **19**(47): p. 475504.

95. Oliver-Calixte, N.J., et al., *Immobilization of lambda exonuclease onto polymer micropillar arrays for the solid-phase digestion of dsDNAs.* Analytical chemistry, 2014. **86**(9): p. 4447-4454.

96. Wu, J., et al., *Complete plastic nanofluidic devices for DNA analysis via direct imprinting with polymer stamps.* Lab on a Chip, 2011. **11**(17): p. 2984-2989.

97. Harms, Z.D., et al., *Nanofluidic devices with two pores in series for resistive-pulse sensing of single virus capsids.* Anal Chem, 2011. **83**(24): p. 9573-8.

Chapter 3. Fabrication of Thermoplastic-Based In-Plane Nanopores[1]

3.1 Introduction: Fabrication of thermoplastic-based nanofluidic devices via NIL by using UV-resin mold

Nanofluidic devices such as nanopores, nanoslits, nanochannels, and nanopipets are fluidic devices with at least one dimension less than 100 nm [1-3]. Such small length scale leads to unique transport phenomena, which are affected by surface charge, ion-current rectification and entropy barriers [3]. Therefore, nanofluidic devices are useful tools in applications of sample preconcentration [4, 5], nanofluidice diodes and transistors [6-8], ion and biomolecule sieving [9, 10] and single molecule analysis [11-15]. With developments in nanofabrication technologies, nanofluidic devices can be fabricated by sophisticated but expensive e-beam lithography (EBL) [16-18] or focus ion beam (FIB) milling [19-21] on inorganic materials such as Si and quartz. In recent years, thermoplastic based nanofluidic devices have drawn increasing attention due to their large scale fabrication potential via nanoimprint lithography (NIL) [22-24]. Thermoplastics such as poly(methylmethacrylate) (PMMA), polycarbonate (PC), polyethylene terephthalate (PET) and cyclic olefin copolymer (COC) are made of linear or branched polymers with high molecular weights and high Young's moduli. Unlike amorphous elastomers, nanoscale patterns on imprint mold can be transferred to thermoplastic resists by direct imprint with negligible deformation [25-27], as shown in Figure 3.1(a).

[1] Part of this chapter was reprinted by permission (copyright IOP Publishing, all rights reserved) from "Selection of UV Resins for Nanostructured Mold for Thermal-NIL" published in Nanotechnology, Volume 29, Number 36, on 29 June 2018, by Zheng Jia, Junseo Choi and Sunggook Park.

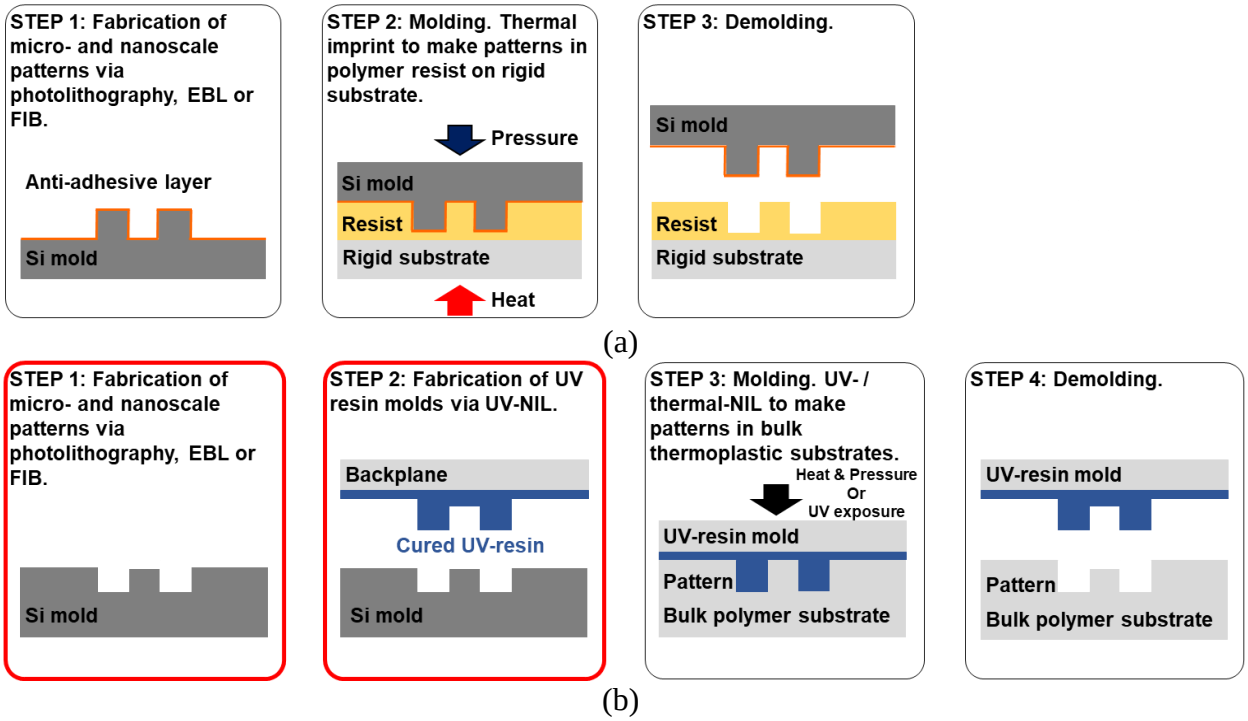

Figure 3.1. (a) Thermal-NIL to generate micro- and nanoscale patterns on thermoplastic resists coated on rigid substrate by using Si master mold. The whole process consists three steps: master mold fabrication, molding and demolding. (b) Thermal-NIL to generate micro- and nanoscale patterns on bulk thermoplastic substrates using UV-resin mold. The whole process consists four steps: master mold fabrication, UV-resin mold fabrication, molding and demolding.

Typical NIL consists of two main steps: molding and demolding. Imprint molds for NIL are usually made of hard materials (such as Si and quartz) with a high Young's moduli in order to achieve sufficient replication fidelity. Lifetime of these molds is critical for NIL throughput and it is affected by both the molding and demolding processes. In the molding step, an imprint mold is pressed into a thin layer of resist or bulk polymer substrate under pressure and heat (thermal-NIL) or with UV exposure (UV-NIL). For thermal-NIL, imprint molds need to be replaced after ~ 50 repeated imprints due to damage caused by high pressures and heating-cooling cycles [28]. In the demolding process, the imprint mold is released from the hardened substrates with replicated patterns. In order to assist demolding, an anti-adhesive layer is usually coated on the mold surface [24, 29]. However, the durability of the commonly used fluorinated silane has a lifetime of less than 100 consecutive imprints [24, 28, 30]. The issues mentioned above limit the use of hard mold

for NIL but they can be solved by using imprint mold made of UV-curable resins. There are three advantages to mold thermoplastic substrates by using UV-resin molds: (1) original master molds can be preserved by using replicated UV-resin molds; (2) UV-resin molds can be used many times because of the crosslink formed polymer networks [31] and (3) UV-resin molds have excellent demolding features due to their similar thermal expansion coefficient with thermoplastic substrates and lower Young's moduli [27, 31]. UV-resin molds can be replicated from an original master mold (usually Si) via UV-NIL, as illustrated in Figure 3.1(b). By utilizing UV-resin molds, the goal to fabricate nanofluidic devices in large scale and with low cost can be accomplished.

In this section, we summarize recent advances in fabrication of thermoplastic-based nanofluidic devices via thermal-NIL using UV-resin molds. The whole fabrication process is investigated, including fabrication of Si master mold, fabrication of UV-resin mold, thermal-NIL, surface modification and device assembling. For each fabrication step, we focus on the solutions to overcome current challenges by proper selection of materials and experimental conditions.

3.1.1 Fabrication of Si master mold

A good imprint mold should meet two basic requirements: well-defined structures and good demolding features [24, 29]. Nanofluidic devices can be fabricated directly on various rigid substrates via different methods, and such methods can be applied to rigid imprint mold fabrication. Photolithography, EBL and IBL are three primary methods to generate nanoscale patterns in rigid substrates [25]. In this section, we focus on how to fabricate high-resolution Si master mold via photolithography, EBL and IBL. Figure 3.2 shows schematic images representing these methods. Other nanofabrication methods such as interference lithography (IL), sphere lithography (SL), scanning probe lithography (SPL) and edge lithography (EL) are well documented in Ref. [25, 28, 32].

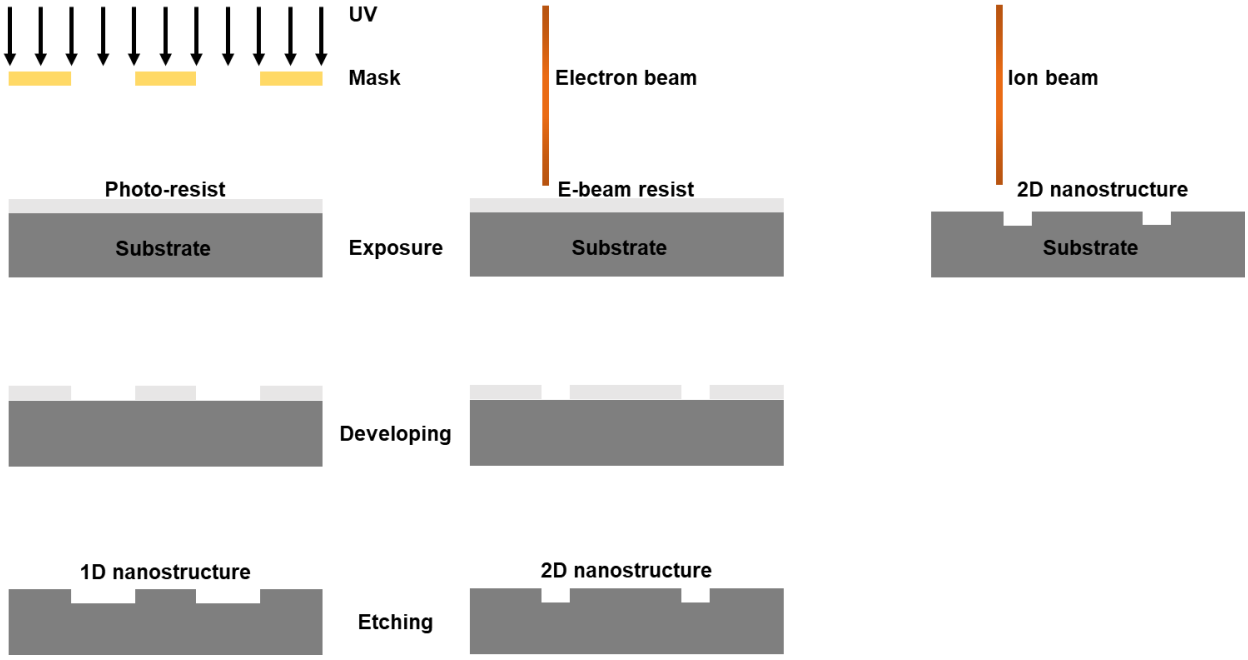

Figure 3.2. Schematic images of three commonly used nano-fabrication techniques: (a) photolithography, (b) maskless electron beam lithography (EBL), and (c) maskless and resist-free ion beam lithography (IBL).

3.1.1.1 Photolithography

Photolithography is widely used in semiconductor industry for large-scale fabrication. As presented in Figure 3.2 (a), a thin layer of photo-sensitive material (photo-resist) is first coated on target substrates and then exposed to UV light through a photo-mask with predefined patterns. Such pattern can also be written on the resist layer by a UV laser writer [25]. After developing and etching, desirable structures are formed in target substrates. In academia, resolution of conventional photolithography ranges from 1 μm to 3 μm [25, 33], which is limited by the diffraction of light. Therefore, photolithography is only suitable to fabricate one dimensional nanostructures (nanoslits) by controlling the etching depth. Nanoslits with depth ranging from 40 nm to 100 nm can be fabricated by this method [32]. Resolution below 100 nm can be achieved

with advanced photolithography techniques by changing the light source to deep UV, extreme UV or X-rays and using diamond masks [25, 34].

3.1.1.2 Electron Beam lithography (EBL)

Compared with photolithography, EBL is a maskless method and provides better resolution due to the much smaller wavelength of the electron beam [25, 32, 35]. Nanoscale patterns can be written directly on e-beam sensitive resist coated on target substrates and transferred to these substrates through developing and etching process or developing, lift-off and etching process [24]. For high resolution EBL, very thin layer of resist is required to minimize electron scattering effect (indicated in Figure 3.3 (a)) [36]. As EBL resolution approaches to sub-10 nm region, resist/developer selection and post exposure fabrication process are the keys to achieve well-defined structures, especially for dense patterns [36-38]. Here, we introduce two high resolution resists for rigid imprinting mold fabrication.

Polymethyl methacrylate (PMMA) is the most commonly used positive resist (at low exposure doses) for EBL [25, 36]. Previously established 10 nm limit for the width of isolated line pattern defined by EBL can be surpassed by using ultrasonic agitation during development [39]. In addition to isolated patterns, 30-nm dense arrays can be fabricated using pure IPA as developer with ultrasonic [37]. One disadvantage of developing using ultrasonic is the distortion and destruction of small structures [36]. An alternative to increase EBL resolution is to develop with cold developers (4-10 °C) [40].

Compared with positive resists, negative resists tend to have less bias [41]. Hydrogen silsesquioxane (HSQ) is an advanced negative resist for EBL with high resolution, high etching resistance and the ability to check EBL performance under scanning electron microscope (SEM) without metal coating [42, 43]. Sub-10 nm isolated line patterns can be achieved by using alkaline

solutions to increase resist dissolution rated instead of commonly used tetramethyl ammonium hydroxide (TMAH) [42, 44]. Besides, HSQ can be used as imprinting mold due to its good adhesion on Si substrate [36].

In addition to fabricate rigid imprinting mold directly, electron beam can be used to tailor predefined Si master mold with protrusion features via electron-beam-induced etching (EBIE) [45]. Jacobson et al. demonstrated in-plane nanopore size reduction in width and depth by EBIE [45]. Dimension changes were confirmed by ionic measurement of replicated h-PDMS devices, in addition to AFM measurements.

3.1.1.3 Ion beam lithography (IBL)

Compared with EBL, IBL (also known as focused ion beam (FIB) milling) is a resist-free process and nanoscale patterns can be directly written on target substrates by heavier ion with higher energy and less scattering [25]. Besides, more complicated 3D structures can be fabricated by IBL using grayscale bitmap[46], for example, tapered inlet structure with depth gradient to reduce entropy barrier for DNA capture from microchannel [23, 47]. Both EBL and IBL are time consuming and expensive for large-scale fabrication due to their serial writing nature.

Resolution of IBL is determined by the combination of ion source selection, scan method selection, beam parameter selection and processing parameter selection [48]. Details regarding how these factors affect milling quality can be found in Ref. [48-50]. Though the beam spot size can be less than 10 nm (for a Ga^+ source), it is still challenging to fabricate patterns having comparable size by direct milling [21, 49]. Moreover, nanoscale patterns milled directly by FIB have ridges along pattern edges due to re-deposition and swelling (shown in Figure 3.3(b)), which can affect device bonding [21, 50]. Milling through a sacrificial layer (metal layer thicker than 100 nm) can help to achieve smaller feature size (sub-10 nm) and smooth top surface [21, 25]. Figure

3.3(c) shows the schematic diagram of metal-assisted milling and smooth Si top surface after metal layer removal.

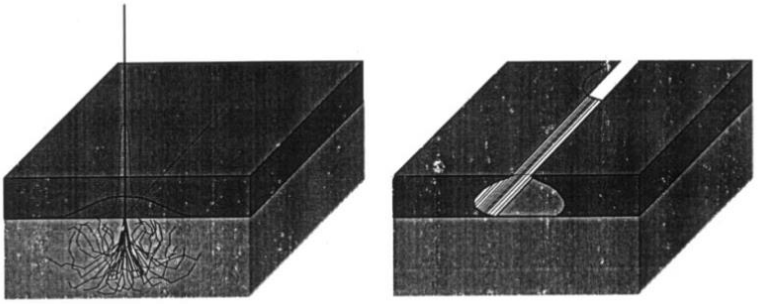

(a)

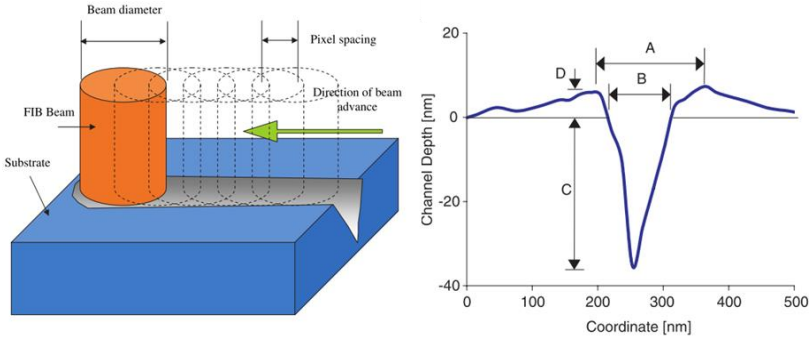

(b)

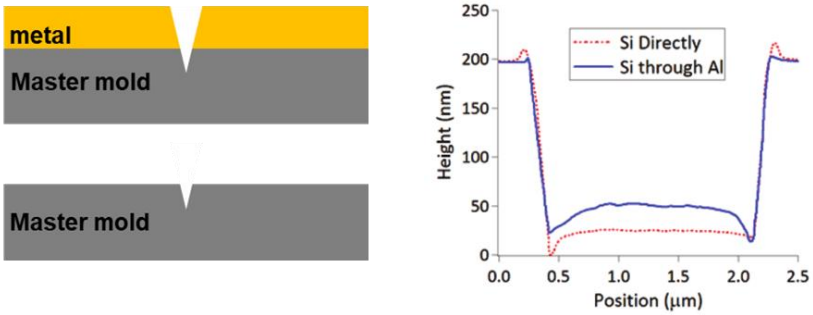

(c)

Figure 3.3. (a) Schematic diagram of electron beam injection into resist with scattering (left) and cross-section of exposed area after developing (right). Thin resist layer is required to compensate beam scattering. (b) Schematic diagram of FIB milling (left) and AFM measurement of single pass milled line pattern(right). Ridge structures can be found at structure mouth due to re-deposition. (c) Schematic diagram of metal-assisted FIB milling to achieve small structure and prevent ridge structures during milling (left). AFM measurement of nanochannel milled into Si with/without metal layer protection. Re-deposition was eliminated with metal layer protection.

3.1.2 Fabrication of UV-resin mold

UV-resin molds are replicated from rigid mold (usually Si) fabricated by techniques mentioned above via UV-NIL (or called step-and-flash imprint lithography (SFIL) in some literature) [28], as illustrated in Figure 3.4(a). First, UV-resin solution is dropped on Si master mold and then a substrate is put on top of resin solution as a supporting backplane (if non-transparent substrates are used as backplanes, transparent mold such as quartz is required as original master mold). A UV-resin solution usually consists of resin monomer (base) and a small portion of a photoinitiator and/or a cross-linking agent. It is also noteworthy that a flexible substrate is preferred due to its better demolding feature and better conformal contact with substrates for thermal-NIL [24, 28, 51]. Next, a low pressure or finger pressing is applied to remove residual resin solution and air bubbles. After curing, UV-resin mold is released from Si mold along pattern direction to avoid distortion and collapse.

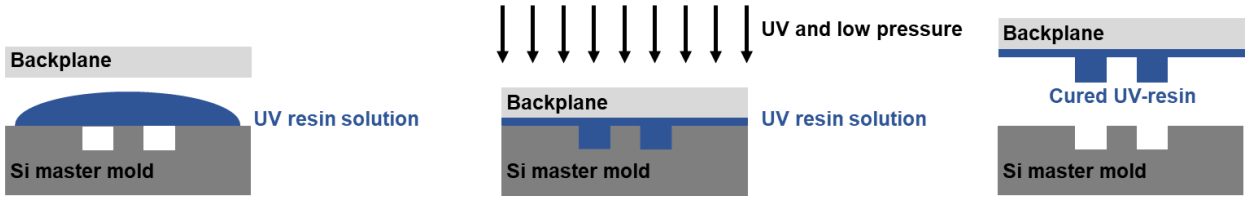

(a)

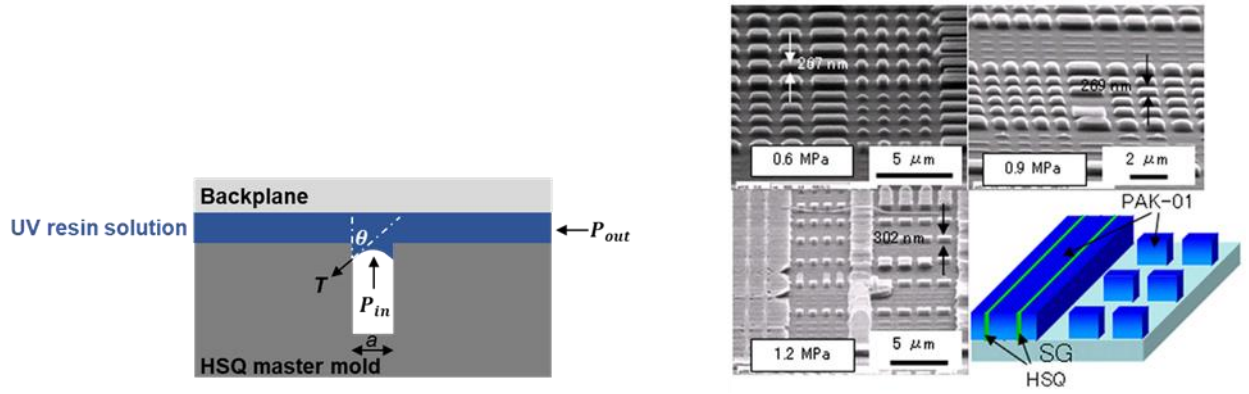

(b)

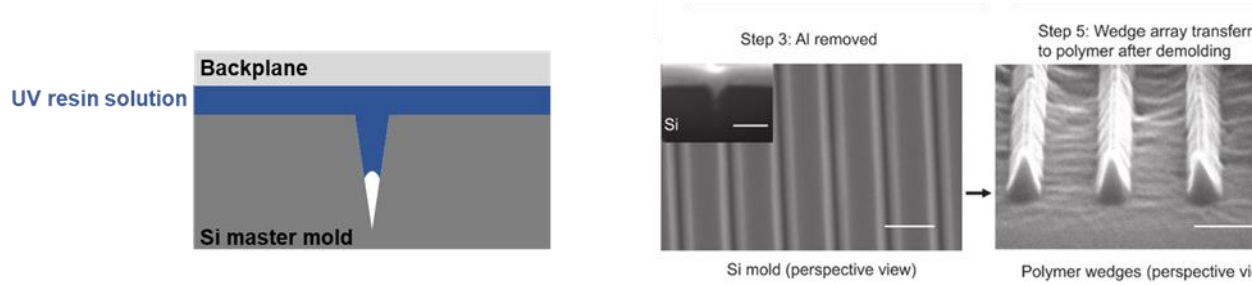

(c)

Figure 3.4. (a) UV-resin mold fabrication process. (b) UV-resin filling into midair HSQ mold with hydrophobic coating [52]. For master mold with low surface energy, a minimum 1.2 MPa pressure is needed to achieve a good filling. (c) UV-resin filling into confined sharp-tip Si master mold generated by metal-assisted FIB milling [53]. Filling into sub-30 nm cavities is difficult due to the comparable length scale to monomer size and increased viscosity. Scale bar: 500 nm.

3.1.2.1 UV-resin filling

One basic but important consideration for all UV-resin molds is their replication fidelity from Si master mold. Good replication fidelity is achieved by complete filling of UV-resin solution into Si master mold. Most Si master molds have one-side open patterns, therefore UV-resin filling problem is always coupled with air trapping issue. We first summarize the work related to air

bubble formation and elimination then discuss UV-resin filling in consideration of UV-resin solution physical properties, master mold surface properties and experimental conditions.

Considering the cost of vacuum chamber, UV-NIL is usually conducted in poor vacuum environment [54, 55]. Air bubbles can be formed and trapped at mold/resin interface. Trapped air prevents UV-resin filling into Si master mold, especially for isolated patterns and thin residual UV-resin layer. Air bubble formation and elimination was extensively studied by experiments and simulations for dispensing-based nanoimprint lithography (D-NIL) and the findings can be applied to other UV-NIL methods [54, 56, 57]. There are two mechanisms for air bubble formation during D-NIL: feature pinning and resists droplets encircling [55]. For thick residual UV-resin layer case, air bubbles formed in both ways can be eliminated within few seconds and the dissolution time is dependent on initial air bubble size, imprinting pressure and air solubility. For thin residual UV-resin layer case, air bubbles can't be removed easily. Simulation results indicated a maximum 60% UV-resin filling rate for a 140 nm wide and 140 nm deep structure with trapped air [54]. Instead of operating under vacuum environment, complete UV-resin filling can be achieved by utilizing condensable 1,1,1,3,3-pentafluoropropane (PTF) as ambient gas [54, 56, 57].

If trapped air is no longer a critical issue, filling of a UV-resin into nanostructures in the Si master mainly depends on the interfacial properties between the resin and the nanostructures, and the nanostructure geometry [53, 58]. Properties of a UV-resin is determined by the physical and chemical properties of the monomer. A governing equation is obtained by considering the equilibrium of force at the UV-resin solution– air interface illustrated in Figure 3.4(b),

$$P_{in} * a = P_{out} * a + 2T \cos\theta \quad (1)$$

where P_{in} is the pressure in cavity, P_{out} is the pressure in solution, T is surface tension (energy), θ is contact angle and a is channel width. According to Equation 3.1, UV-resin with high surface

energy and low viscosity can fill cavities in Si master mold by capillary force. Filling behavior of UV-resin was studied independently using midair structure, which allows trapped air to escape easily [52]. Commercial available UV-resin PAK-01 mold was replicated from HSQ master mold with and without anti-adhesive layer. Experimental results indicated a pressure of 1.2 MPa was required to achieve a good replication fidelity for master mold with anti-adhesive (hydrophobic) coating due to its lower surface energy [52].

As shown in Figure 3.4 (c), UV-resin filling in sub-30 nm region is challenging, for example, sharp-tip master mold fabricated metal-assisted FIB milling. Increased resin solution viscosity and the comparable length scale to monomer size are the two possible reasons [58, 59]. UV-resin viscosity in confined structures was studied by shear resonance measurement [59]. The experiment results indicated compared with bare polyurethane based resin losing its fluidity when confined in a 30 nm gap, the same resin with fluorine-containing monomers maintained its fluidity even when confined in a gap smaller than 15 nm. UV-resin filling into sub-20 nm structure was also studied by using porous anodic aluminum oxide (AAO) film as mold. Experimental results indicated UV-resin filling into small recesses was improved by the presence of hydroxy groups in the aliphatic di(meth)acrylate monomers [58].

3.1.2.2 Commonly used UV-resin molds

As NIL molds, well replicated UV-resin molds should be possessed of a good demolding feature and sufficient Young's modulus (especially for thermal NIL). Acrylate-based UV-resins and fluorine-containing UV-resins are the most commonly used imprint mold material.

Commercially available poly-urethane acrylate (PUA) based resin with low surface energy and high Young's modulus (hundreds of megapascals) is suitable for thermal-NIL [51]. Homemade tripropyleneglycol diacrylate (TPGDA) based resin has sufficient Young's modulus

and low viscosity. Sub-30 nm nanochannel can be replicated and imprinted into bulk thermoplastic substrates using TPGDA mold [23, 31, 60, 61]. Compared with acrylate-based UV resins, fluorine-containing UV resins have better demolding feature due to relative low surface energy. For example, Teflon AF 2400 has a Young's modulus of 1.6 GPa and a surface energy of 15.6 dyn cm^{-1}. Therefore, it can be used as mold for thermal and UV-NIL over many imprint cycles without any surface treatment [62]. Physical properties of these three UV resin are summarized in Table 3.1.

Table 3.1. Physical properties of three commonly used UV resins. Physical properties of PUA resin are obtained from supplier's (PUA511RM, Minuta technology) MSDS. Physical properties of TPGDA and Telflon AF 2400 are obtained from Ref. 61 [61] and Ref. 63 [63], respectively. No viscosity data of TPGDA is available, and its viscosity is lower than PUA based on our observation during experiment.

UV-resin	Molecular weight of monomer (g/mol)	Viscosity of UV-resin solution (cps)	Young's modulus of cured UV-resin (MPa)	Surface energy of cured UV-rein (mN/m)
PUA	600-6000 [64]	241.4	4771	24.76
TPGDA [61]	300	NA Lower than PUA	698	63
Teflon AF 2400 [63]	300000 (gyration radius: 23 nm)	NA	1600	15.6

In summary, UV-resin selection is important for NIL, in order to achieve a high replication fidelity and a good durability. Factors such as subsequent molding method (thermal-NIL or UV-NIL), structure geometry and UV-resin properties should be fully considered.

3.1.3 Thermal-NIL into thermoplastic substrates

Elastomeric materials, for example, polydimethylsiloxane (PDMS) have been widely used for microfluidic devices fabrication via soft lithography [65, 66]. However, nanoscale fabrication in elastomeric materials suffers from structure deformation and collapse [25, 27, 33]. Unlike elastomeric materials, nanofluidic devices can be fabricated by direct molding into thermoplastic

resists coated on rigid substrates or bulk thermoplastic substrates [25, 27, 67]. There are three advantages of using thermoplastic as substrates for nanofluidic devices: (1) nanoscale patterns can be molded into thermoplastic with high replication fidelity via high throughput, low cost fabrication techniques such as NIL and injection molding [25, 68]; (2) high optic transparency [27, 69] and low dielectric noise [67] features of thermoplastics are favorable for optical observation and electrical measurement, respectively; (3) surface properties of thermoplastics can be modified for different application accordingly [70, 71].

3.1.3.1 Commonly used thermoplastic substrates and their imprint/demolding conditions

Poly(methylmethacrylate) (PMMA) and polycarbonate (PC) are the most commonly used rigid thermoplastic substrates for thermal-NIL with features of low cost, good optic transparency and excellent electric properties [70, 72, 73]. Polyethylene terephthalate (PET) with high transparency and flexibility is usually introduced as substrates for depositing metallic or as UV-resin mold backplane [51, 74, 75]. PET itself is another ideal material for thermal-NIL with its low thermal expansion coefficient and low glass transition temperature features [74, 76]. Cyclic olefin copolymer (COC) is an emerging thermoplastic with excellent optical properties and good chemical resistance. COC substrates with a wide range of glass transition temperature are available from manufactures for different applications [69]. Nanoscale patterns imprinted on these four thermoplastic substrates are presented in Figure 3.5. And in Table 3.2, we summarize the physical properties of these commonly used thermoplastic substrates, such as glass transition temperature, T_g; coefficient of thermal expansion (CET) and surface charge density or zeta potential.

Table 3.2. Physical properties and imprint/demolding conditions for PMMA, PC, PET and COC substrates.

Thermoplastic	T_g (°C) [27]	Linear CTE (α) (ppm °C^{-1}) [27]	Surface charge (mC/m^2) / zeta potential (mV)	Imprint/demolding conditions
PMMA	100−122	70−150	-40.5/ -59.8 (O_2 plasma treated) [77]	130 °C, 20 bar, 5 min for PMMA with TPGDA mold/ demolding at 70 °C [23].
PC	145−148	60−70	NA/ ∼-35 [72]	180 °C, 50 bar, 30 s for PC (T_g= 150 °C) with SiO_2 mold/ demolding at 125 °C [78].
PET	69−78	48−78	NA/ ~ 38 [72]	95 °C, 2 MPa, 100 s for PET (T_g= 71.3°C) with Si mold/ demolding at 55 °C [79].
COC	70−155	60−80	-59.9/ NA (UV/O_3 treated) [80]	125 °C, 1.91 MPa, 2 min for TOPAS 5010 (T_g = 108 °C) with TPGDA mold/ NA [80].

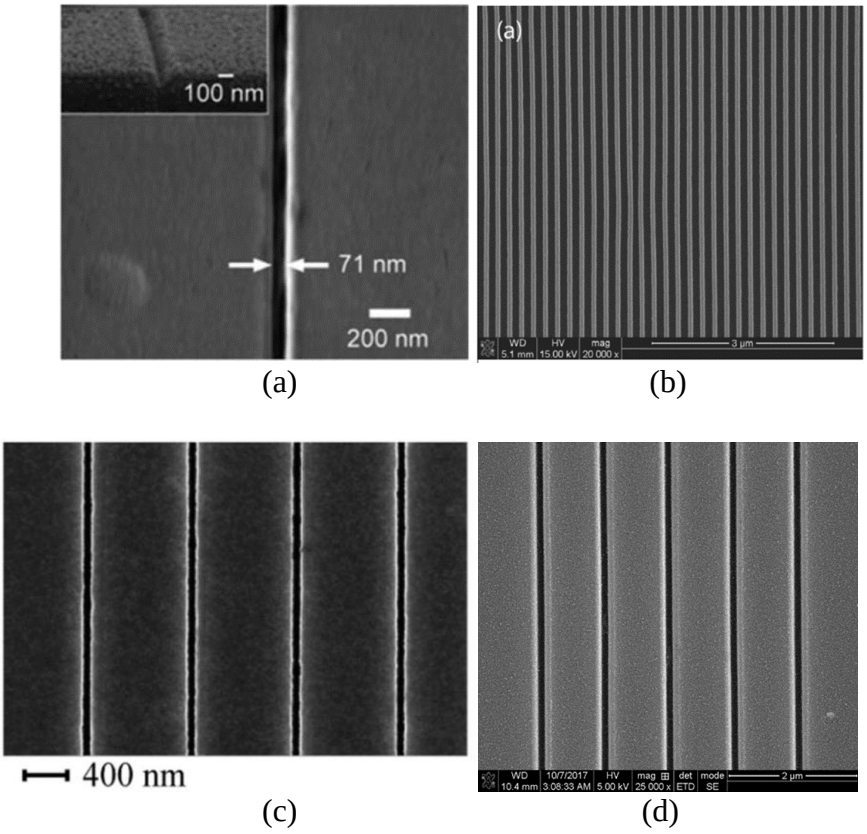

Figure 3.5. SEM images of nanopatterns imprinted in commonly used thermoplastic substrates. (a) Nanochannel imprinted in 125 mm thick PMMA using TPGDA mold. (b) 200 nm period gratings imprinted in 0.2 mm flexible PC substrate using SiO_2 mold. (c) Nanochannels imprinted in 0.25 mm PET foil using Si mold. (d) Nanochannels imprinted in 125 mm thick COC using PUA mold.

3.1.3.2 Experimental conditions for thermal-NIL

Thermal-NIL consists of two steps: molding and demolding. And it can be conducted in a commercial nanoimprinter [23], a hot embossing machine [80] or a home-made imprint chamber [81, 82]. Imprint and demolding conditions for commonly used thermoplastic are also summarized in Table 3.2. In the molding step, high pressure is applied to press a UV-resin mold into a thermoplastic substrate, which is heated above its T_g, for enough time. Similar to UV-NIL, thermal-NIL is a flow-and-fill process and the replication fidelity is determined by the combination of imprint pressure, temperature and time. In order to find the optimal conditions, thermal-NIL process has been investigated through numerical simulations [83, 84]. An imprint temperature of 30-50 °C higher than the polymer substrate's T_g and an imprint pressure of $\sim$ 500 to 200000 KN/m^{-2} are typical working conditions for thermal-NIL [73, 85].

Subsequent demolding step is critical to thermal-NIL because most structural damages of imprinted patterns occur during this step [27, 86-88]. During demolding, imprint mold and substrate are cooled down to a demolding temperature, which is lower than the substrate's T_g. Then imprint mold is released from substrate by overcoming chemical and mechanical interactions between mold and substrate. As shown in Figure 3.6 (a), such interactions include thermal stress generated due to mismatch of thermal expansion in mold/substrate during cooling step, adhesion at mold/substrate interface and sidewall friction[86, 87]. Demolding failure will occur when the stress at mold/substrate interface during demolding becomes larger than the yield strength (σ_Y) of the substrate [27, 86]. Therefore, a low demolding force is favorable in order to achieve a defect-tolerant demolding. Demolding force is dependent on demolding temperature and the interfacial properties between mold and substrate. Optimal demolding temperatures were reported for hard mold released from PMMA resist (60 °C for Al mold [87] and 70 °C for Si mold [86]), PC resists

(100 °C for Al mold [87]) and PET sheet (55 °C for Si mold). As we mentioned early, the use of UV-resin mold can also reduce thermal stress because of its similar thermal expansion with thermoplastic substrate [23]. However, optimal demolding temperatures for UV-resin molds released from bulk thermoplastic substrates haven't been reported yet.

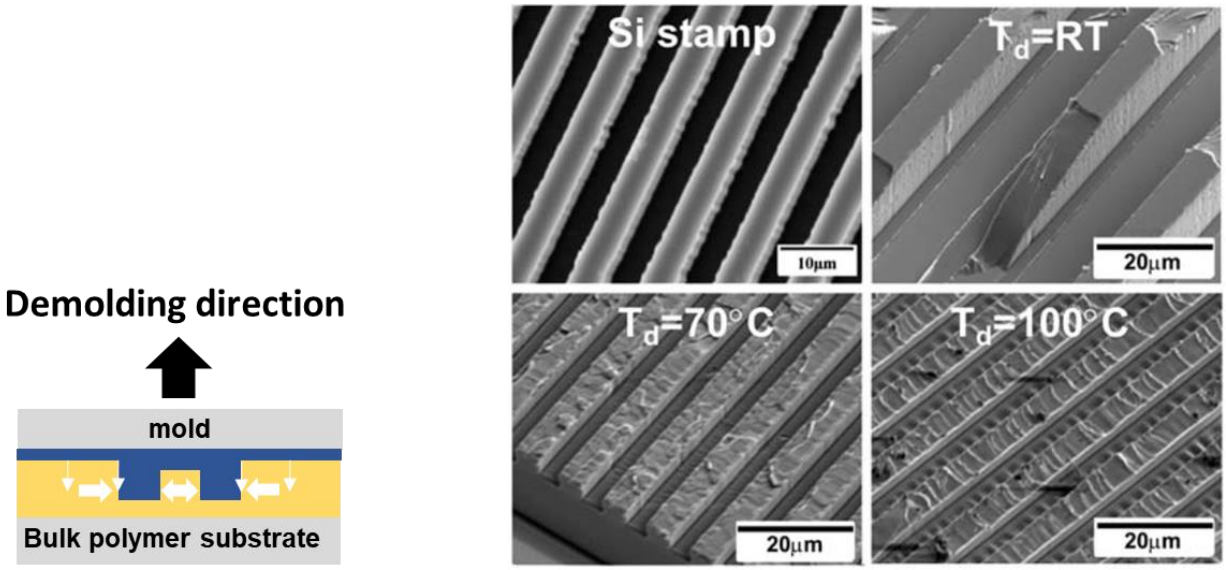

(a) (b)

Figure 3.6. (a) Thermal stress, adhesion at mold/substrate interface and friction from sidewall are the factors affecting imprint mold release. (b) Imprinted PMMA resist after Si mold released at different temperature. An optimal demolding temperature is required to avoid structure damage.

An alternative to reduce demolding force is to coat an anti-adhesive layer on imprint mold [24]. Experimental results indicate hydrophobic silane coating on Si can reduce adhesion at mold/substrate during demolding from PMMA resist [29]. Such a good demolding feature can also be achieved by using UV-resin mold having low surface energy. In this way, surface treatment on Si master mold is no longer required [24, 62].

3.1.4 Surface modification of imprinted substrates and device assembling

After imprinting, proper surface modification is usually required for substrates and cover sheets in order to assist device assembling [85, 89, 90] or/and device performance [91-93]. Since some device assembling techniques (for example, thermal fusion bonding) require surface modification prior to bonding, we first introduce surface modification methods for thermoplastic based nanofluidic devices and then discuss device assembling techniques.

3.1.4.1 Surface modification

Hydrophobic nature of the pristine polymer substrate surface is the main problem for polymer based nanofluidic devices [71, 91, 93]. Therefore, the substrate surface must be activated first to achieve a good wettability, to prevent hydrophobic binding with analytes or to serve as anchor for attaching different functional molecules [71, 92, 94, 95]. Thermoplastic devices can be simply activated by O_2 plasma or UV/O_3 treatment while maintaining its bulk properties [94, 96-99].

Surface characteristics of polymer substrate after modification are usually examined by water contact angle measurement, electroosmotic flow (EOF) measurement, X-ray photoelectron spectroscopy (XPS). When polymer is treated with O_2 plasma, polar functional groups (carboxyl, carbonyl, carbonate, etc.) are introduced to polymer surface [96, 99], as illustrated in Figure 3.7(a). Similarly, carboxyl groups can also be formed when the polymer is exposed to 254-nm UV light (optimal wavelength [98]) in air [71, 96, 98]. Such functional groups improve the wetting property of polymer substrates by increasing surface energy [80, 99] and the modified hydrophilic surface prevents non-specific binding with analytes such as proteins and cells [100, 101]. In addition to surface activation, O_2 plasma and UV/O_3 treatment (associated with covalent modification if

necessary) can control electroosmotic flow (EOF) strength by tailoring surface charge density of polymer surface [77].

Though O_2 plasma and UV/O_3 treatment provide a simple way to modify polymer surface, they both suffer from hydrophobic recovery, especially for O_2 plasma treated samples [92, 102]. Recovery time is dependent on treatment method, treatment duration and storage conditions [92, 100]. O_2 plasma treated surface undergoes recovery within several hours, while UV/O_3 treated surface can retain hydrophilic up to weeks [100]. In general, dehumidified and low temperature conditions are favorable for sample storage [92, 103, 104]. An alternative way to achieve stable hydrophilic polymer surface is covalent modification, for example, grafting poly-ethylene glycol (PEG) or coating polyvinyl alcohol (PVA) on O_2 plasma or UV/O_3 treated samples through complex chemical reactions [101, 105, 106].

3.1.4.2 Device assembling

Thermal fusion bonding is the most commonly used method for microfluidics devices sealing [85, 107]. As presented in Figure 3.7(a), during thermal bonding, imprinted substrates and cover plate are brought into contact and heated above their T_g. With well controlled pressure, temperature and time, interdiffusion of polymer chains on both surfaces leads to a strong bonding. Thermal fusion bonding for nanofluidic devices is challenging (especially for low aspect ratio patterns) due to structure deformation at high bonding temperature, which is required due to the low surface energy of pristine polymer substrates [90, 108]. Therefore, surface modification is required in order to achieve low temperature thermal bonding. As mentioned above, O_2 plasma and UV/O_3 treatment increase polymer surface energy and generate a thin layer at top surface with lower T_g (compared with the bulk) [85, 101]. O_2 plasma-assisted thermal bonding of PMMA, COC and PC based devices were reported and shown in Figure 3.7(b) for nanoslits at moderate

temperature with minor deformation [85]. Moreover, bonding temperature can be reduced further via hybrid bonding with low T_g COC cover sheet (cover sheet are activated by O_2 plasma or UV/O_3 prior to bonding). Bonding between PMMA (T_g= 105 °C, as substrate)/ COC (T_g= 75 °C, as cover) substrates and COC (T_g= 108 °C, as substrate)/ COC (T_g= 75 °C, as cover) was accomplished at 70 °C [80]. Thermal bonding conditions for commonly used thermoplastic substrates and corresponding surface modification methods are shown in Table 3.3.

Table 3.3. Thermal bonding conditions for commonly used thermoplastic substrates.

Substrate	Cover sheet	Surface modification	Bonding conditions
PMMA (T_g= 105 °C)	PMMA (Tg= 105 °C) [85] COC (Tg= 75 °C) [80]	O_2 plasma for cover & substrate O_2 plasma for cover only	87 °C, 160 kPa for 30 min 70 °C, 680 kPa for 15 min
PC (T_g= 150 °C)	PC (Tg= 150 °C) [85]	O_2 plasma for cover & substrate	130 °C, 370 kPa for 30 min
PET (T_g= 71.3°C)	PET (Tg= 71.3 °C) [79]	O_2 plasma for cover & substrate	69 °C, 200 kPa for 30 min
COC (T_g= 134 °C) COC (T_g= 108 °C)	COC (Tg= 134 °C) [85] COC (Tg= 75 °C) [80]	O_2 plasma for cover & substrate O_2 plasma for cover only	115 °C, 370 kPa for 30 min 70 °C, 680 kPa for 15 min

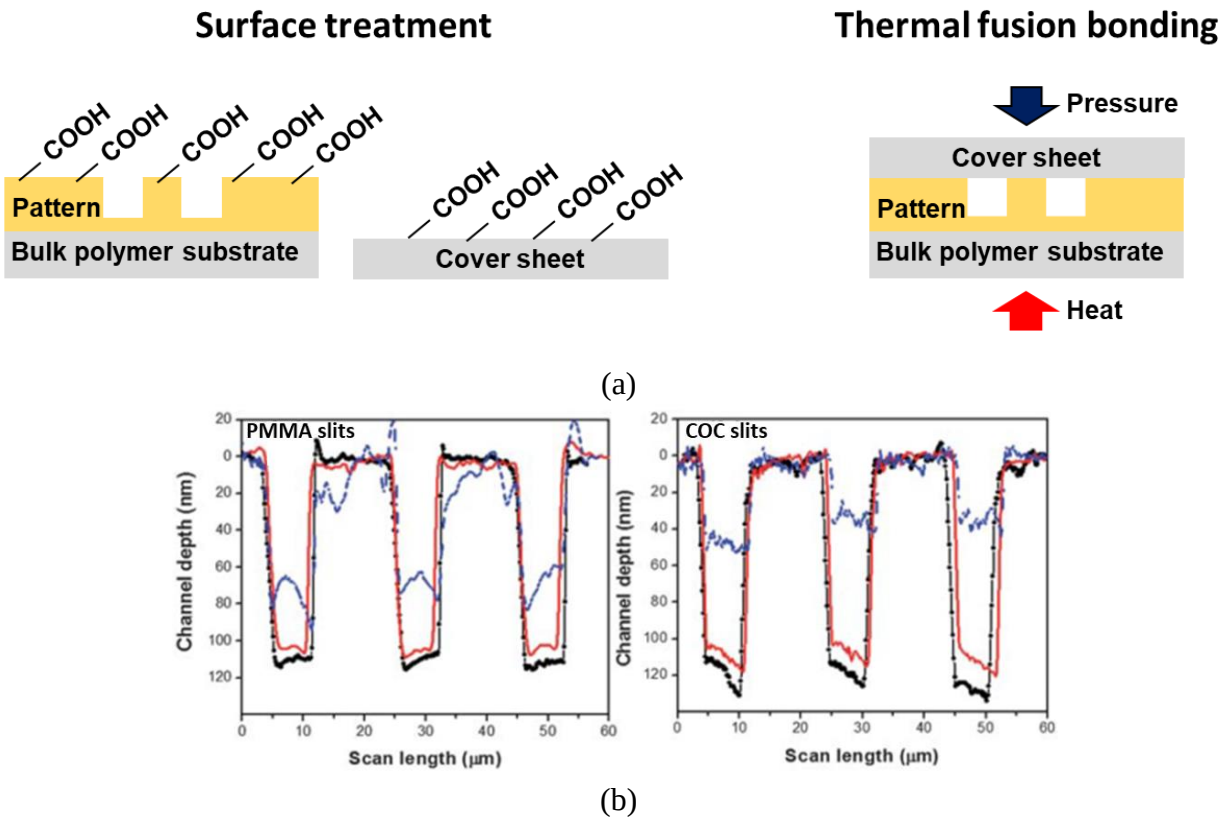

Figure 3.7. Surface treatment and device assembling by thermal fusion bonding. (a) Carboxyl groups are formed on imprinted substrate and cover sheet after O_2 plasma and UV/O_3 treatment. Modified cover sheet and substrate are bonded under optimal temperature and pressure. (b) Moderate temperature is favorable for nanofluidic device bonding in order to avoid deformation. Blue-dashed line represent slits depth following thermal fusion bonding at 107 °C for PMMA and at 130 °C for COC slits; red solid line is the depth of the slits following thermal fusion bonding at 87 °C and 115 °C of oxygen plasma treated substrate and cover plate for PMMA and COC, respectively; and the black-circle line is the nanoslits following molding, but not subjected to thermal fusion bonding [85].

3.1.5 Summary

NIL is a well-developed tool to fabricate polymer-based nanofluidic devices in large scale and with low cost. Compared with traditionally used hard imprint molds, the use of UV-resin molds can increase production throughput and facilitate the demolding process of thermal-NIL. In this section, we focus on the fabrication of thermoplastic based nanofluidic devices via NIL using UV-resin mold. Bottleneck of each fabrication step was studied and the corresponding solutions

were summarized from literature. Proper selection of materials and appropriate experimental conditions are the keys to achieve high-resolution NIL with sufficient replication fidelity. The tips and conditions discussed here will be applied to in-plane nanopore device fabrication for DNA sequencing as presented below.

3.2 Experiments

3.2.1 Fabrication of Si master mold via FIB

The Si master molds used in this study were fabricated by standard photolithography and wet etching for the access microchannels, and by FIB for the nanostructures connecting the microchannels (including inlet/outlet, pillar array structure and nanochannel/nanopore). The FIB machine, FEI Quanta 3D Dual Beam, is located at LSU shared instrument facility (SIF). An accelerating voltage of 30 kV, and beam current values ranging from 10 pA to 5 nA are used depending on the structure size. Usually a beam current of 10 pA is chosen used for nanochannel/nanopore, 0.1 nA to 0.5 nA for pillar array and 1 nA to 5 nA for inlet/outlet. Different milling modes (rectangular mode, cleaning cross-section mode and bitmap mode) are chosen accordingly. Pt deposition mode is used to coat metal layer locally, protecting sample surface while cutting cross-section. For metal-assisted FIB milling, Cr or Al layer is etched away by commercial etchant (Cr etchant, purchased from Sigma-Aldrich; Al etchant, purchased from Transene).

3.2.2 Fabrication of UV-resin molds via UV-NIL

UV-resin molds are fabricated via UV-NIL, as presented in Figure 3.4(a). UV-resin solution was first dropped on the Si master mold, then a thin polymer sheet (250 μm PET from Goodfellow, coated with an adhesion layer) was put on top of the resin solution and used as a supporting backplane. Residual resin solution and air bubbles were gently squeezed out by finger pressing. The sandwich-like structure was put in a commercial nanoimprinter (Eitre6, Obducat) and UV-NIL was performed at a UV lamp power of 1.8 W/cm^2 for 20 s. After UV curing, the molded UV-resin/PET substrate was demolded from the Si master along the nanochannel direction. Usually TPGDA resin molds are used to imprint into PMMA and COC substrates, MD 700 resin molds are used to imprint into PEGDA coated on PMMA substrate.

3.2.3 Fabrication of complete polymer nanofluidic device via NIL and bonding

Polymer nanofluidic devices were produced by UV- or thermal-NIL into three different polymer substrates: PEGDA (MW = 200, Sigma-Aldrich), PMMA (ePlastics) and COC (COC6013, T_g=142 °C, TOPAS) as shown in Figure 3.1(a). In order to cure, PEGDA was exposed to flash-type UV light (250-400 nm) for 1 min at an intensity of ~1.8 W/cm^2 after adding 1 wt% of the UV initiator (2,2-dimethoxy-2-phenylacetophenone, Sigma-Aldrich). PMMA and COC were thermally imprinted at 135 °C, 3.5 MPa and 160 °C, 5 MPa for 15 min, respectively.

In order to enhance wetting of the nanopore device and reduce hydrophobic interaction between DNA and the nanopore wall, the patterned substrates (except for PEGDA) and cover sheets were modified to become hydrophilic by O_2 plasma prior to bonding [70, 109].
For bonding at 70 °C, 1 MPa for 15 min, a low T_g thin COC sheet (COC8007, T_g=78 °C, TOPAS) was used as the cover plate for all three nanopore substrates. The use of a low T_g cover plate minimize the deformation of the nanostructured substrate [80, 85]. Details on the device fabrication can be found in our previous work [23, 80, 110].

3.3 Results and discussion

3.3.1 Si master mold with well-defined small nanopore

As discussed above, IBL is a maskless and resist-free technique to generate imprint mold. For our research, we use FIB bitmap mode to fabricate in-plane nanopore on Si as original mold. For all nanopore based sensing platforms, precise control of nanopore size is the key to achieve high signal to noise ratio. Therefore, in this section we focus on how to produce well-defined nanopore structure via FIB milling.

There are several FIB milling modes for different application, no matter which mode is chosen, a good focus and astigmatism correction is always required. Figure 3.8 shows nanochannel and pillar array milled with and without a good focus respectively.

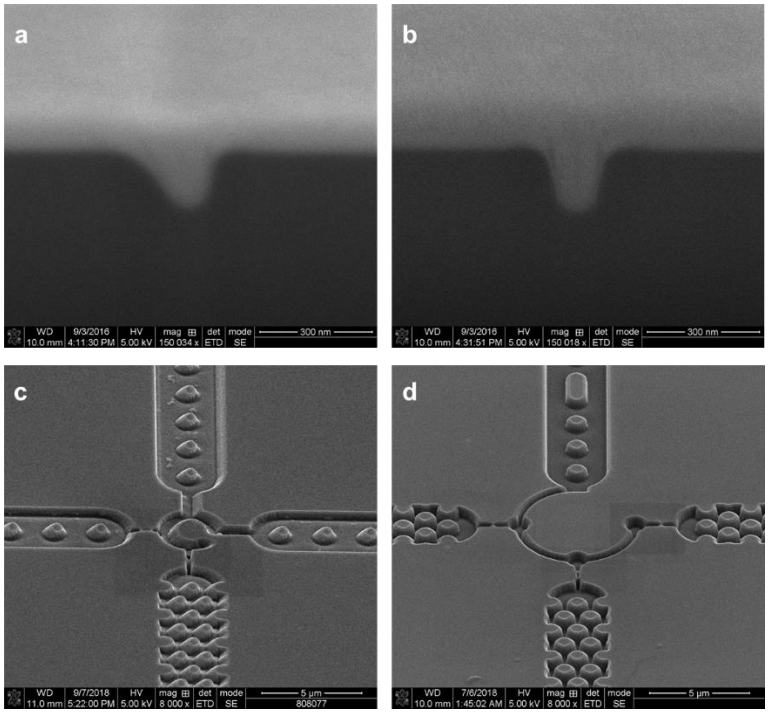

Figure 3.8. (a) and (b) 150 nm width nanochannel milled by FIB without and with good focusing, 30 kV, 10 pA; (c) and (d) Pillar array milled by FIB without and with good focusing, 30 kV, 0.1 nA.

3.3.1.1 Nanopore dimension control by milling time

FIB bitmap mode is usually used to mill complex structures [46, 47]. In bitmap mode, scan dwell time for each pixel is defined by gray scale color. Which means, milled part is denoted as white color and un-milled part is denoted as dark color in bitmap. The bitmap we use to fabricate in-plane nanopore is presented in Figure 3.9. In between two triangles, we draw a short long single pixel line, which is going to be milled as in-plane nanopore. Theoretically, the width of the nanopore is dependent on the ion beam spot size. For nanopore milling, we usually used 10 pA as ion beam current (10 nm spot size), which can provide enough brightness and contrast for focusing, and form small spot size at the same time. The depth of the nanopore can be simply controlled by milling time therefore we first discuss nanopore dimension control by milling time.

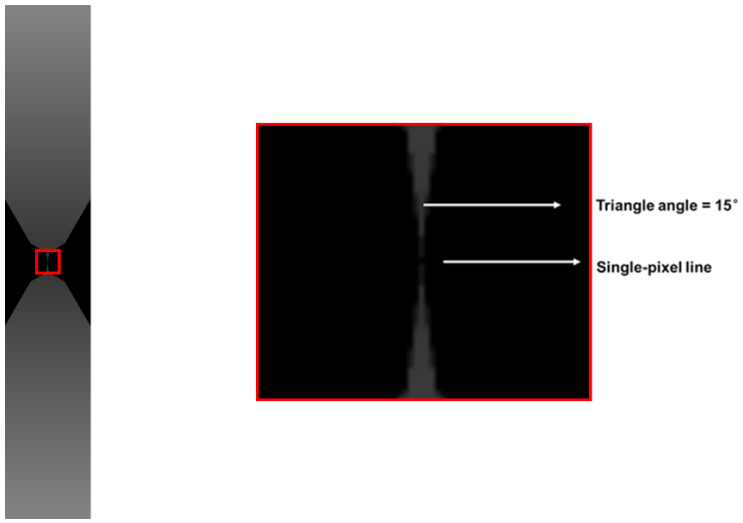

Figure 3.9. Bitmap used for nanopore milling via FIB.

Bitmap containing two pores are used for FIB milling by FEI Quanta 3D dual beam machine, at 30 KV, 10 pA with various time. For deep nanopores, their depth can be measured by SEM; while for shallow nanopores, their depth can be measured by AFM. As shown in Figure 3.10, nanopore becomes deeper as milling time increases and sub- 10 nm nanopore (in depth) can be fabricated by controlling milling time.

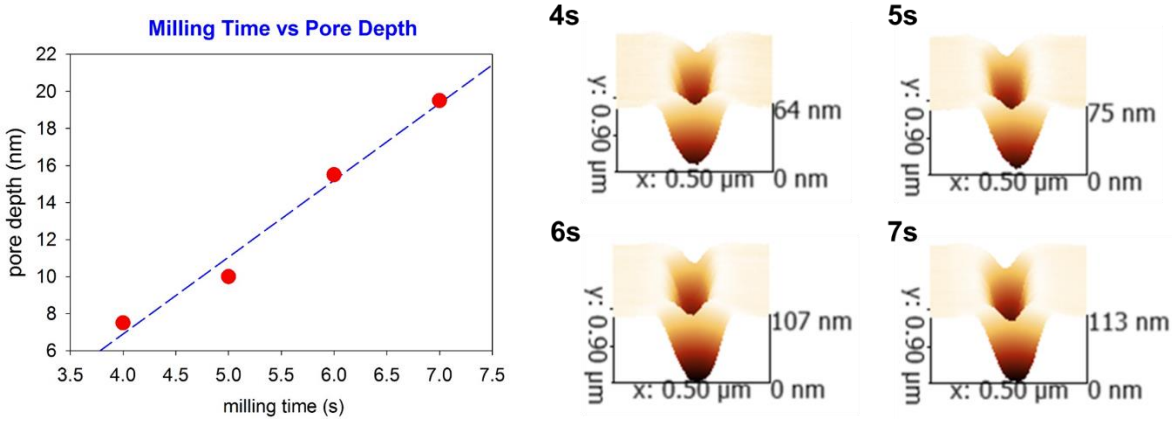

(a) (b)

Figure 3.10. (a) Nanopore depth is linear to FIB milling time. Nanopore depth value is obtained by averaging two pore depth values from AFM measurement. (b) AFM measurement of two nanopore milled for various time.

3.3.1.2 Nanopore dimension control by bitmap design

For dual-pore device fabrication, we put two nanopore in a single bitmap file for FIB milling in order to avoid the misalignment of different bitmaps. Sometimes, we need to have nanopores with different dimensions to facilitate data processing. For example, if so many DNA molecules pass through two identical pores, they will trigger similar current change signals from two pores. Therefore, it will be troublesome to define paired peaks (ToF). In order to solve this problem, we can put nanopores with different design in a single bitmap file. Figure 3.11 shows nanopore geometry (depth) can be controlled by changing the triangle angles. For the same milling time, nanopore with smaller angle is milled less compared with nanopore with larger angle.

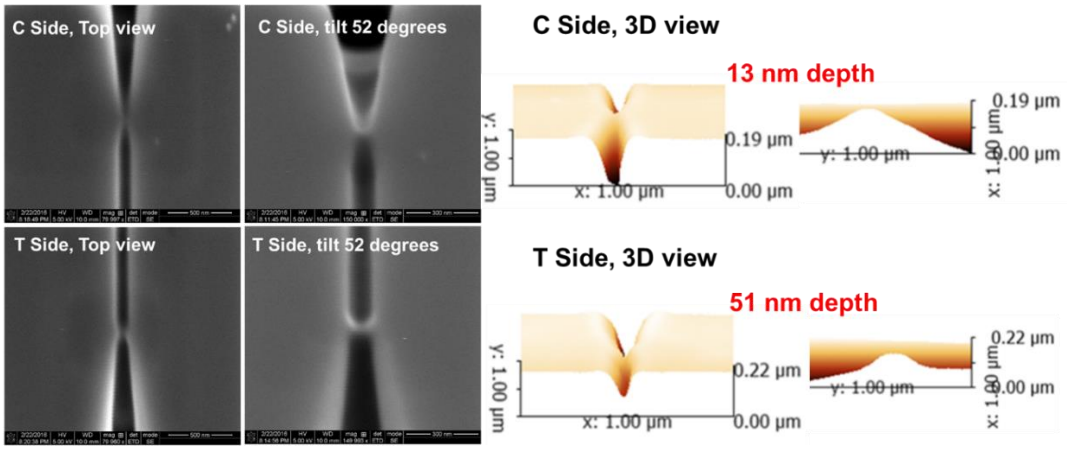

(a) (b)

Figure 3.11. SEM images of nanopores with different triangle angles: "C" side 15° and "T" side 60°. (b) AFM measurement of nanopores with different triangle angles.

3.3.1.3 Nanopore dimension control by metal-assisted FIB milling

As can be seen in Figure 3.12(a), in-plane nanopore milled directly into Si is 1-D nanopore, which means the nanopore width can't controlled well. In order to fabricate nanopore with both small width and depth, we tried metal-assisted FIB milling. Metal-assisted FIB milling was used to fabricate sub- 20 nm nanochannels on rigid substrate [21, 80] as illustrated in Figure 3.12(b). Over

100 nm thick metal layer (usually Al or Cr) is coated on rigid substrate as sacrificial layer. The coated metal layer can help to confine the width of milled structure and it also assists the focusing process during operation. Figure 3.12(c) shows nanopore fabricated by metal-assisted FIB milling through 65 nm thickness Cr layer. Prior to metal removing, the milled nanopore has a width similar to the connecting nanochannel and a depth of 79 nm. After metal removal, nanopore width is narrowed down to 23 nm, which is much smaller than the width of connecting nanochannels. Nanopore depth is 15 nm, which is confirmed by measuring the copied PUA resin mold. Though the small pore can be replicated well, the copied connecting channels usually have some defects, which may be due to in-complete UV-resin filling. UV-resin filling issue for sharp-tip structures is discussed in the next section.

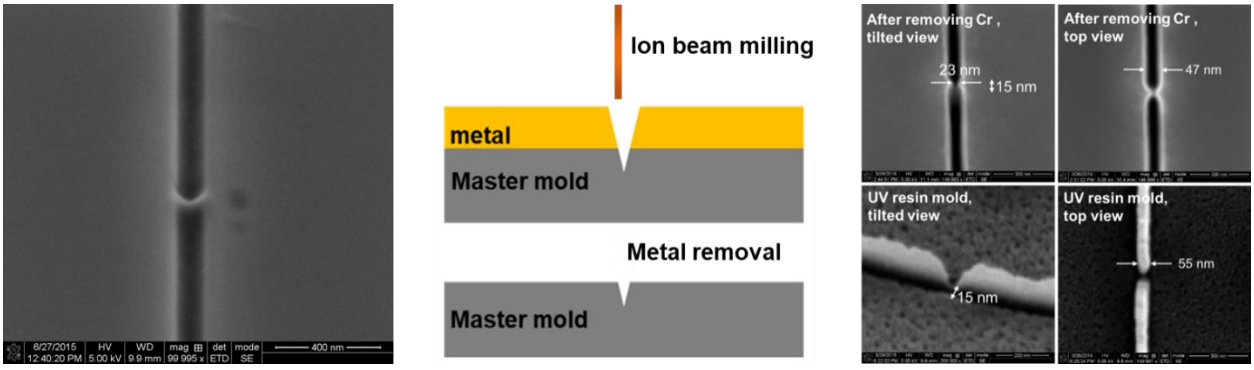

(a) (b) (c)

Figure 3.12. (a) Typical 1-D nanopore milled directly on Si substrate; (b) Schematic image showing metal-assist FIB milling process; (c) 2-D nanopore by metal-assisted FIB milling (using unmodified bitmap in Fig. x with 100 nm connecting nanochannel), Si master mold after metal removal and replicated PUA resin stamp.

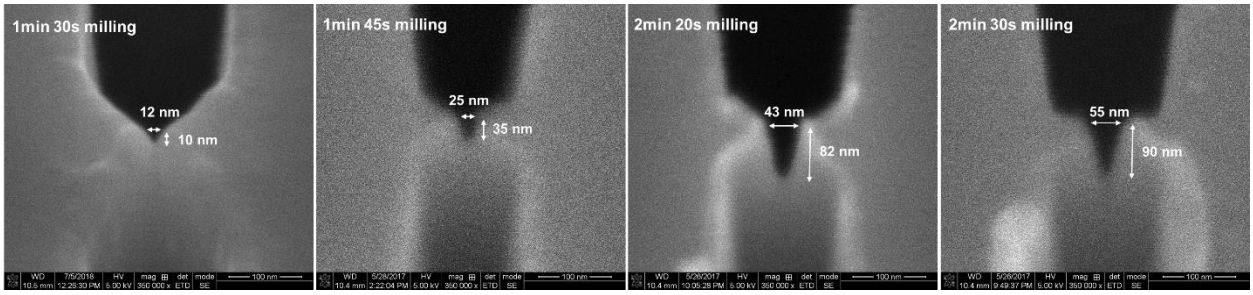

Figure 3.13. FIB milled Si master mold with 150 nm Al layer coating for different time (using modified bitmap with wider connecting nanochannels to facilitate UV-resin filling, explained and shown below), after metal removal in Al etchant.

Moreover, SEM images in Figure 3.13 show Al-coated Si master (150 nm, TELIC, CA) mold milled for different time, as milling time increases, width and depth of 2-D nanopore increase. It should be noted the quality of metal-assisted FIB milling is dependent on the homogeneity of the metal layer coating and subsequent metal removal process, which is not presented here.

In summary, sub-15 nm nanopore (both width and depth) can be fabricated by well controlling FIB milling time, bitmap design and using metal as sacrificial layer.

3.3.2 Replication fidelity and thermal-NIL performance of UV-resin molds

For thermal-NIL using UV-resin mold, the key is to fabricate UV-resin molds with high replication fidelity. Here, the term “replication fidelity” has two meanings: the replication fidelity of UV resin mold from original Si mold and the replication fidelity for nanostructures imprinted in thermoplastic substrate by using UV-resin mold. The former one requires a good UV-resin filling property while the latter one requires a UV-resin mold processing high Young’s modulus. In the section, we first studied the replication fidelity of four commonly used UV-resins: home-made tripropyleneglycol diacrylate (TPGDA) based UV resin and polypropyleneglycol diacrylate (PPGDA) based UV resin, and commercially available poly-urethane acrylate (PUA) based UV resin and fluorine-containing UV resin (MD 700). Then we studied their performance in the

subsequent thermal-imprint step. The physical properties of these UV-resins are shown in Table. 3.4.

Table 3.4**.** Physical properties of UV resins used in this study. Physical properties of TPGDA and PPGDA resin are obtained from Ref. [61]. No viscosity data of these two resin solutions is available, and their viscosity is lower than PUA and MD 700 based on our observation during experiments. Physical properties of PUA and MD 700 are obtained from supplier's MSDS.

UV-resin	Molecular weight of monomer (g/mol)	Viscosity of UV resin Solution (cps)	Young's modulus of cured UV resin (MPa)	Surface energy of cured UV resin (mN/m)
TPGDA [61]	300	NA lower than PUA and MD700	698	63
PPGDA [61]	900	NA lower than PUA and MD 700	65	60
PUA	600-6000 [64]	241.4	4771	24.76
MD 700	1600	850	10.5	12.7 [111]

3.3.2.1 Replication fidelity of UV-resin molds

Usually, it is difficult for UV-resin to fill into high aspect ratio nanostructures directly milled by FIB or small structures by metal-assisted FIB milling (as presented in Figure 3.4(c) and Figure 3.12 (c)). Therefore, UV-resin filling behavior is studied by replicating from a Si master with nanostructures having different aspect ratio, as shown in Figure 3.13. For each UV-resin, five mold were replicated from original Si mold via UV-NIL in an Obducat nanoimprinter (1.8 W/cm^2 for 20 s), followed by steps shown in Figure 3.4(b).

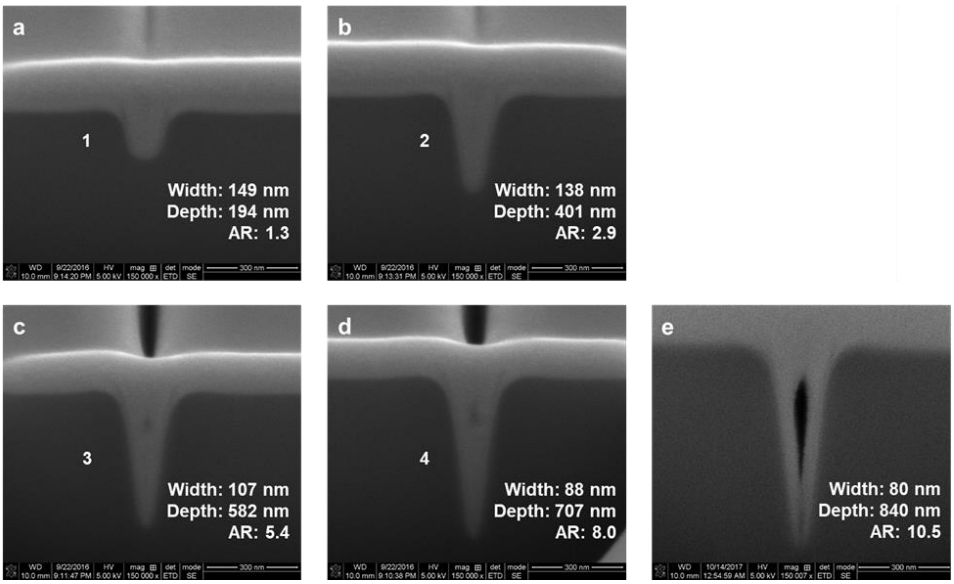

Figure 3.14. SEM images of cross-sectional profiles of nanochannels on the Si master with different aspect ratio. Nanochannels were milled by FIB rectangular mode, with 100 nm fixed width and depth ranging from 100 nm to 500 nm. When milled deeper by FIB, nanochannel profile changes from U-shaped to sharp tip V-shaped, which makes UV-resin solution hard to fill at the very bottom. SEM images were taken with a tilt angle of 52°. In this study, nanochannel width is defined as the width at half-depth of the channel, unless otherwise specified.

Replication fidelity of copied UV-resin molds was then inspected via SEM, as presented in Figure 3.15. For nanochannels with the lowest aspect ratio, all UV-resin molds were well replicated with good replication fidelity. For nanochannels with higher aspect ratios, however, saw-tooth shaped defects were clearly observed on top of the replicated protrusions in PUA and MD 700 resin molds, which is indicative of incomplete filling into the bottom of the sharp V-shaped nanochannels.

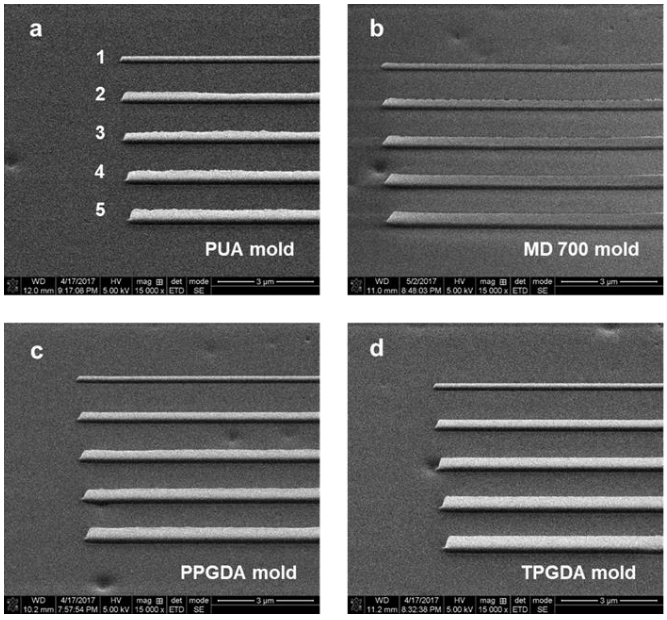

Figure 3.15. SEM images of replicated UV resin molds by UV-NIL from a Si master. Nanochannel depth increases from top to bottom as indicated by number in the image. The numbers 1-5 correspond to nanochannels 1-5 in Fig. 14. For low surface energy resins with high monomer molecular weight (PUA and MD 700), saw-tooth defects are seen for the replicated nanoprotrusions from deeper nanochannels due to incomplete resin filling. The SEM images were taken with a tilt angle of 52°.

In order to quantitatively evaluate the replication fidelity in the fabrication of UV-resin molds from the Si master, we define "UV-resin filling ratio" as the ratio of a protrusion height in the resin mold to the corresponding nanochannel depth in the Si master. The filling ratio for different UV-resins was plotted as a function of nanochannel depth in Figure 3.16 (a). Overall, the UV-resin filling ratio decreases as the nanochannel depth increases, showing obviously that it is difficult to fill a UV-resin into deeper nanochannels. The filling ratios among the four resins studied are in the decreasing order of TPGDA resin > PPGDA resin > PUA resin > MD 700 resin, where TPGDA resin is the best candidate for replicating sharp nanostructures by UV-NIL. The higher filling ratios of TPGDA and PPGDA resins over those of the other two resins are attributed to the combined effect of the higher surface energy and the small sizes of the resin monomers, as illustrated in Figure 3.15 (b). Comparing TPGDA and PPGDA which have similar surface energies

of 63 and 60 mN/m, respectively, the filling ratio of PPGDA is significantly lower than that of TPGDA, which can be attributed to TPGDA's smaller monomer size. Comparing PUA and MD 700 resins, the viscosity of MD 700 resin is significantly higher than that of PUA resin and thus one may expect that MD 700 resin would be more difficult to fill nanostructures. However, our results show that the PUA resin has the lowest filling ratio. This indicates that the molecular size of the UV-resin monomer, together with surface energy, is a critical factor in determining the filling into nanoscale structures. Even though PUA and MD 700 resins have been used as imprinting molds due to respectively the high Young's modulus and the low surface energy [51, 112], our results indicate that they are not the appropriate candidates for UV-resin molds replication from sharp nanochannels having a channel width less than ~ 100 nm.

However for nanochannels with ~ 200 nm and 300 nm FIB setting widths, the replicated PUA molds have better replication fidelity as shown in Figure 3.17. The results indicate that each UV-resin has its own limit regarding the smallest feature size to achieve good replication fidelity, which should be an important consideration in selecting materials for resin molds and during device design. Therefore, in order to facilitate UV-resin filling into Si mold fabricated by metal-assisted milling, we modified the bitmap with wider connecting nanochannels. Modified bitmap, Si master mold after metal removal and imprint nanopore on COC substrate are shown in Figure 3.18.

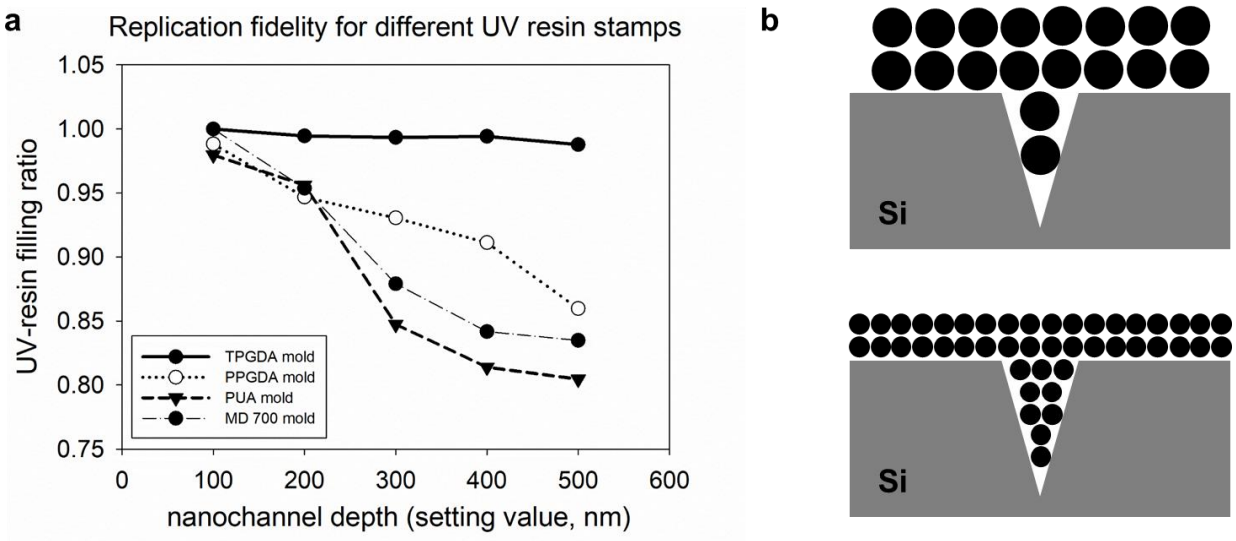

Figure 3.16. (a) UV-resin filling ratio, which represents the replication fidelity, of different UV-resin molds from Si master mold during UV-NIL. In general, the UV-resin filling ratio decreases as the nanochannel depth increases. TPGDA mold with the smallest monomer size shows the highest filling ratio. (b) Schematic image of monomers with different sizes filling into sharp nanostructures, showing that UV-resins with smaller monomers show better filling into sharp nanostructures.

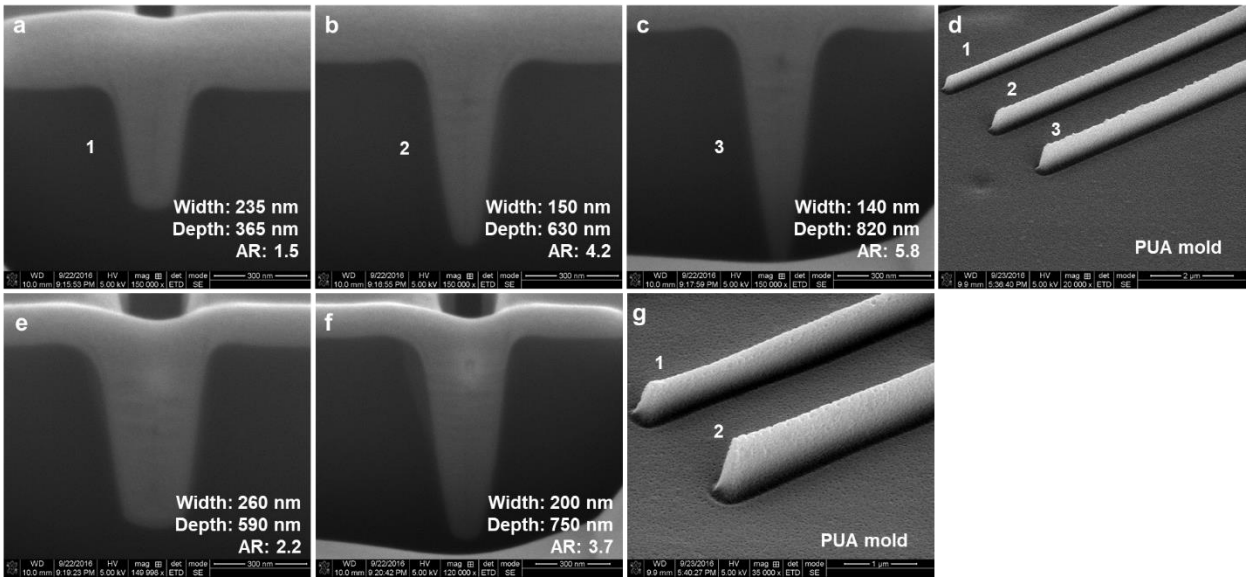

Figure 3.17. Top: (a-c) Cross-sectional profiles of 200 nm width (FIB milling setting value) nanochannels with different channel depth; (d) Replicated PUA resin mold having a replication limit for 200 nm width sharp nanochannels of 4 (aspect ratio). Bottom: (e-f) Cross-sectional profiles of 300 nm width (FIB milling setting value) nanochannels with different channel depth; (g) Replicated PUA resin mold having a replication limit for 200 nm width sharp nanochannels of 3.7 (aspect ratio).

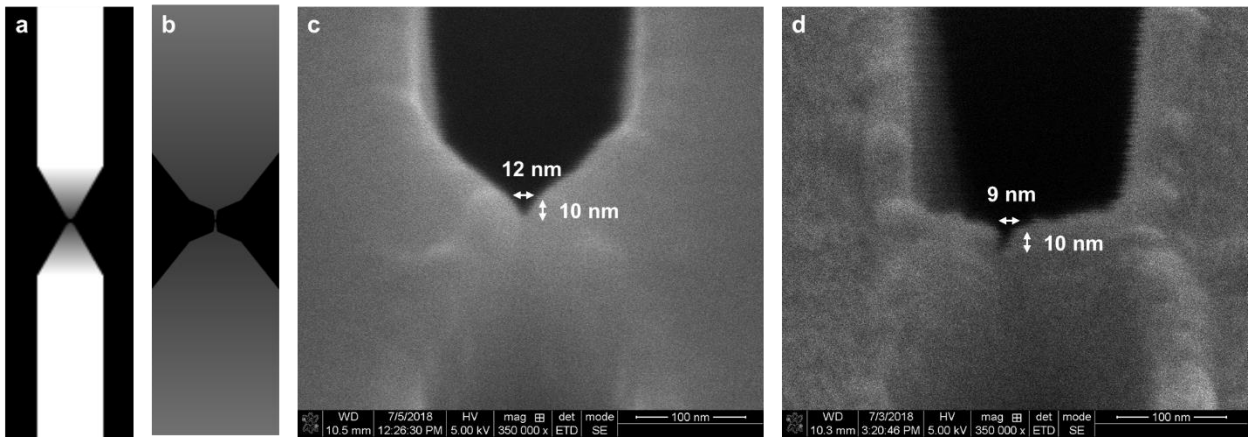

Figure 3.18. (a) Original bitmap for single nanopore milling with 100 nm connecting nanochannel. (b) Modified bitmap for single-nanopore milling with 250 nm connecting nanochannel to facilitate UV resin filling; (b) Si master mold milled through 150 nm Al layer for 1 min 30s after metal removal; (c) Nanopore imprinted on COC 6013.

3.3.2.2 Thermal-NIL performance of UV-resin molds

The performance of the UV-resin molds in thermal-NIL were tested using the resin molds replicated from the Si master mold with low aspect ratio nanochannels, which ensures a complete resin filling. Thermal imprinting was performed into COC substrates (T_g= 142 °C) with the TPGDA, PUA and MD 700 resin molds (imprint condition: 160 °C, 50 bar for 10 min). SEM images of the Si master mold and imprinted COC substrates with those resin molds are shown in Figure 3.19. Top-view SEM images only showed that nanochannels were well transferred to COC substrates. However, dimensional changes were clearly seen with cross-sectional SEM images. Overall, the imprinted nanochannels on COC substrates possessed larger channel widths and smaller channel depths when compared with those of the original Si mold. The dimensional variations for the widths and depths were in a decreasing order of MD 700 (35%, 11%) > TPGDA (23%, 7%) > PUA (8%, 1%), which was consistent with the order of their Young's modulus values. Based on our previous work, the dimensional variation of the molded structures from TPGDA or PPGDA resin stamps is due to the mold deformation during thermal NIL process [23]. In that work, the variations of the width and depth for a 100 nm wide nanochannel imprinted in poly(methyl methacrylate) (PMMA) with a TPGDA resin mold were 22.5% and 28%, respectively. Despite such variations, the mold deformation was fully recovered after demolding because of the presence of crosslinks in the cured UV-resin [23]. For nanochannels imprinted in COC substrates in this work, larger dimensional changes in the lateral direction than those in the longitudinal direction were observed, which is different from the PMMA imprinting (imprinting conditions: 130°C, 30 bar for 5 min) results in the previous work. This may be attributed to a higher imprinting temperature for imprinting COC substrates, which results in a higher thermal stress and thus larger lateral shrinkage upon cooling.

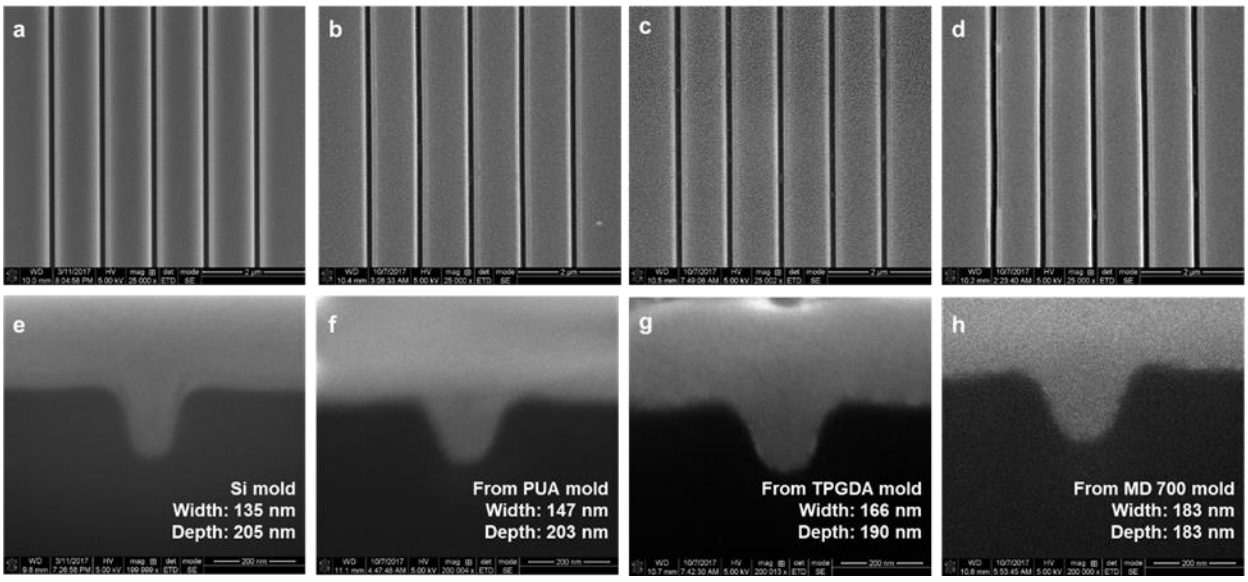

Figure 3.19. SEM images of the Si master (a, e) and imprinted COC substrates (b-c and f-h) from different UV-resin molds replicated from the Si master: top-view images (a-d) and their cross-sectional profiles (e-h). The thermal NIL performance of a UV-resin mold was determined by measuring the cross-sectional profile of the imprinted nanochannel.

In summary, we have studied the replication fidelity of four different UV-resin molds from sharp nanostrucrures during UV-NIL and their performance in thermal-NIL. UV-resin molds made from a lower molecular weight monomer and with a higher surface energy showed better replication fidelity due to the good resin filling into the mold structures in Si. For thermal-NIL with resin molds, the Young's modulus of the cured resin was a critical material parameter to achieve good replication fidelity.

3.3.3 Imprinted polymer nanopores and dimensions control via thermal bonding

3.3.3.1 Imprinted polymer nanopores

In previous sections, we have demonstrated our ability to fabricate Si master mold having in-plane nanopore structures and the ability to fabricate UV-resin mold with high replication fidelity. In this section, we present the fabrication of thermoplastic-based in-plane nanopore devices by using UV-resin mold having single-nanopore structure. SEM images of original Si mold and imprinted nanopores on different polymer substrates are shown in Figure 3.20 .

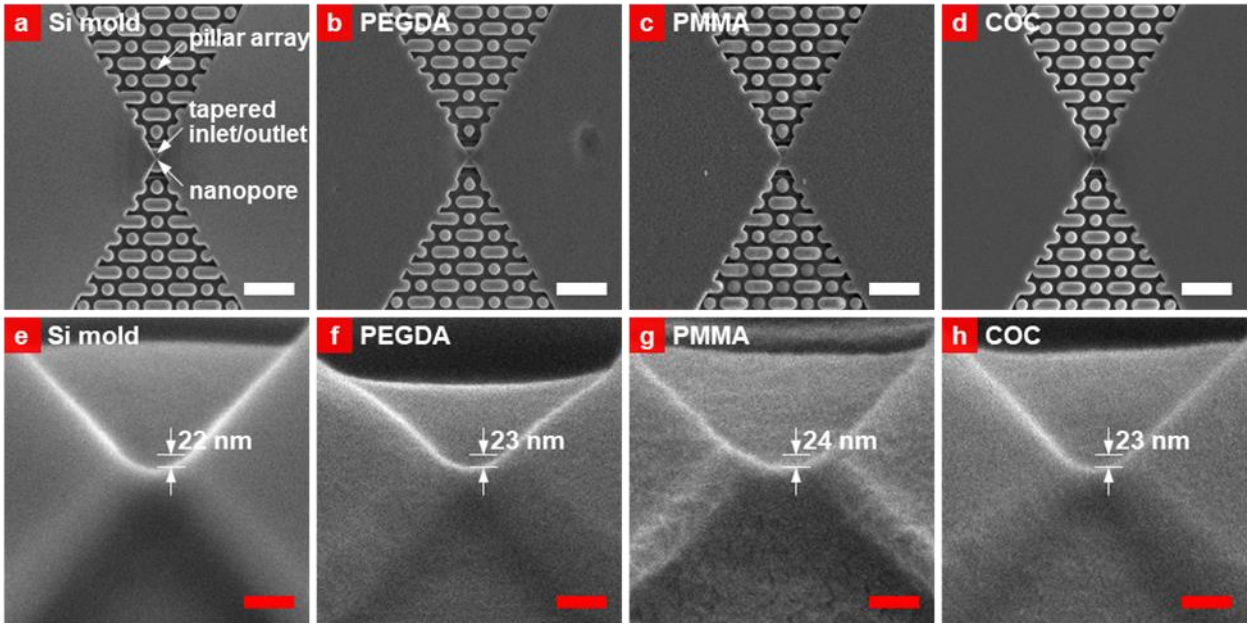

Figure 3.20. SEM images of Si master mold (a, e) and imprinted in-plane nanopore on PEGDA (b, f), PMMA (c, g) and COC (d, h) substrates. Nanopillar arrays with 300 nm gap and tapered inlet/outlet are designed to pre-stretch DNA. Images were taken under 5 kV, 5.9 pA by FEI Quanta 3D instrument. Despite deposition of a 4 nm Au/Pd layer on polymer chips to avoid charging effect, the nanopore feature on PMMA substrate was deformed (enlarged and bent) under high magnification by electron beams (g). Compared with original Si master mold, all imprinted nanopores have good replication fidelity. Scale bars, 3 μm in white and 100 nm red.

For polymer-based nanopore devices, we choose poly(ethylene glycol) diacrylate (PEGDA), poly(methyl methacrylate) (PMMA) and cyclic olefin copolymer (COC) as substrates. PEGDA substrates have anti-biofouling feature and they are imprinted via UV-NIL by using MD 700 mold. PMMA and COC are commonly used thermoplastic substrates with good optical

properties and they are imprinted via thermal-NIL by using TPGDA mold. In comparison with the original Si mater, imprinted nanopores have good replication fidelity. FIB milled and imprinted in-plane nanopores have parabolic shape and their equivalent circular pore diameter can be calculated from pore width and depth measured on SEM images, resulting in 25 ± 5.3 nm diameter. To make actual fluidic devices, all imprinted samples were treated with O_2 plasma except PEGDA samples and bonded with O_2 plasma treated COC cover sheets [80]. These hybrid devices are denoted as PEGDA-COC, PMMA-COC and COC-COC below. In order to estimate their pore sizes after thermal bonding, these devices were filled with 1 M KCl for conductance measurement. As indicated in Table. 5, their conductance values are close to each other. Based on Figure 3.21, the estimated pore size is 10 ± 3.7 nm. However, the value was dissimilar to one calculated roughly by SEM measurement. It is because of two reasons: (1) pore size reduction during thermal bonding process and (2) the inaccuracy and difficulty to measure in-plane nanopore size by SEM.

Table 3.5. Conductance of bonded single-pore devices with 1M KCl under 1V

Device	PEGDA-COC	PMMA-COC	COC-COC
Conductance (nS)	147 ± 30	157 ± 21	144 ± 25

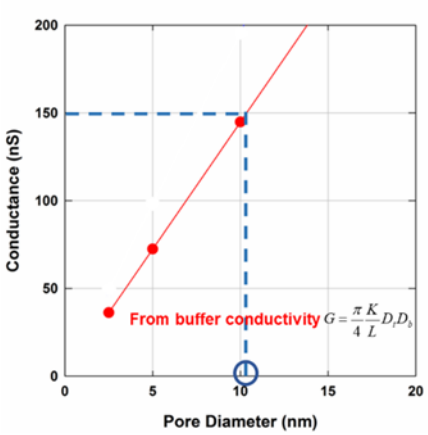

Figure 3.21. Equivalent nanopore diameter verse nanopore conductance [113] (filled with 1M KCl as electrolyte).

3.3.3.2 Nanopore dimensions control by thermal bonding conditions

As presented above, nanopore size was decreased after thermal bonding process and such phenomenon can be utilized to reduce nanopore size from its original dimensions in Si master mold. In order to study how bonding conditions can affect nanopore size after thermal bonding, we used a higher T_g COC (COC7010, Tg = 110°C) as cover sheet instead of low T_g COC8007. A Si master mold containing a 57 nm equivalent diameter nanopore was copied to COC with high replication fidelity as shown in Figure 3.22.

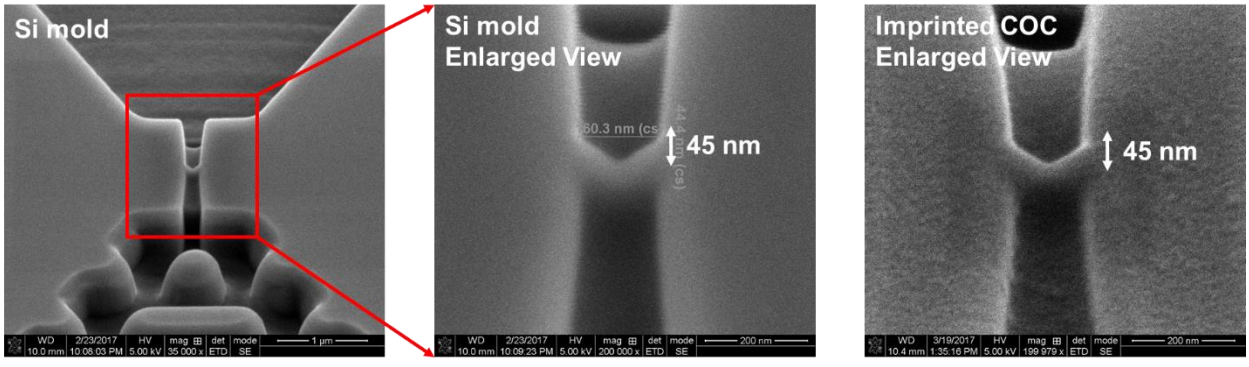

Figure 3.22. Left: Si master mold used for nanopore size reduction study; Middle: Close view of 57 nm equivalent diameter nanopore (45 nm is measured nanopore depth); Right: Nanopore structure imprinted on COC6013.

After O_2 plasma treatment, imprinted COC6013 substrates were bonded with COC7010 covers at 100°C, 105°C and 110°C, 1 MPa for 15 min. Nanopore size after thermal bonding was examined by ionic current measurement. Conductance values of nanopore are shown in Table 3.6 and from the results we can conclude the nanopore size reduces as bonding temperature increases. Around 10 nm diameter nanopore can be produced from a 57 nm diameter nanopore in Si mold with 110°C as bonding temperature.

Table 3.6. Conductance values of nanopore bonding at different temperature.

Bonding temperature	Conductance (nS)	Corresponding pore diameter (nm)
100°C	90 ± 23	40 ± 6
105°C	62 ± 16	10 ± 4
110°C	47 ± 10	10 ± 2

3.4 Conclusion

In this chapter, we demonstrated the fabrication of thermoplastic-based in-plane nanopore devices. By proper selecting materials and experimental conditions, sub-10 nm equivalent diameter in-plane nanopores can be fabricated on PEGDA, PMMA and COC substrates. In next chapter, we will used these devices for DNA sensing applications.

3.5 References

1. Sparreboom, W., A. van den Berg, and J.C. Eijkel, *Principles and applications of nanofluidic transport.* Nature nanotechnology, 2009. **4**(11): p. 713.

2. Abgrall, P. and N.T. Nguyen, *Nanofluidic devices and their applications.* Analytical chemistry, 2008. **80**(7): p. 2326-2341.

3. Haywood, D.G., et al., *Fundamental studies of nanofluidics: nanopores, nanochannels, and nanopipets.* Analytical chemistry, 2014. **87**(1): p. 172-187.

4. Wang, Y.-C., A.L. Stevens, and J. Han, *Million-fold preconcentration of proteins and peptides by nanofluidic filter.* Analytical chemistry, 2005. **77**(14): p. 4293-4299.

5. Kovarik, M.L. and S.C. Jacobson, *Integrated nanopore/microchannel devices for ac electrokinetic trapping of particles.* Analytical chemistry, 2008. **80**(3): p. 657-664.

6. Ali, M., et al., *Logic gates using nanofluidic diodes based on conical nanopores functionalized with polyprotic acid chains.* Langmuir, 2009. **25**(20): p. 11993-11997.

7. Cheng, L.-J. and L.J. Guo, *Nanofluidic diodes.* Chemical Society Reviews, 2010. **39**(3): p. 923-938.

8. Vlassiouk, I., T.R. Kozel, and Z.S. Siwy, *Biosensing with nanofluidic diodes.* Journal of the American Chemical Society, 2009. **131**(23): p. 8211-8220.

9. Cabodi, M., S.W. Turner, and H.G. Craighead, *Entropic recoil separation of long DNA molecules.* Analytical chemistry, 2002. **74**(20): p. 5169-5174.

10. Kaji, N., et al., *Separation of long DNA molecules by quartz nanopillar chips under a direct current electric field.* Analytical chemistry, 2004. **76**(1): p. 15-22.

11. Foquet, M., et al., *DNA fragment sizing by single molecule detection in submicrometer-sized closed fluidic channels.* Analytical Chemistry, 2002. **74**(6): p. 1415-1422.

12. Mannion, J. and H. Craighead, *Nanofluidic structures for single biomolecule fluorescent detection.* Biopolymers, 2007. **85**(2): p. 131-143.

13. Menard, L.D., et al., *A device for performing lateral conductance measurements on individual double-stranded DNA molecules.* ACS nano, 2012. **6**(10): p. 9087-9094.

14. Storm, A.J., et al., *Fast DNA translocation through a solid-state nanopore.* Nano Letters, 2005. **5**(7): p. 1193-1197.

15. Harms, Z.D., et al., *Nanofluidic devices with two pores in series for resistive-pulse sensing of single virus capsids.* Analytical chemistry, 2011. **83**(24): p. 9573-9578.

16. Yasui, T., et al., *DNA separation in nanowall array chips.* Analytical chemistry, 2011. **83**(17): p. 6635-6640.

17. Nam, S.-W., et al., *Sub-10-nm nanochannels by self-sealing and self-limiting atomic layer deposition.* Nano letters, 2010. **10**(9): p. 3324-3329.

18. Liu, S., et al., *Controlled deformation of Si3N4 nanopores using focused electron beam in a transmission electron microscope.* Nanotechnology, 2011. **22**(11): p. 115302.

19. Chen, P., et al., *Probing single DNA molecule transport using fabricated nanopores.* Nano letters, 2004. **4**(11): p. 2293-2298.

20. Li, H.-W., et al., *Focused ion beam fabrication of silicon print masters.* Nanotechnology, 2003. **14**(2): p. 220.

21. Menard, L.D. and J.M. Ramsey, *Fabrication of sub-5 nm nanochannels in insulating substrates using focused ion beam milling.* Nano letters, 2010. **11**(2): p. 512-517.

22. Chou, S.Y., P.R. Krauss, and P.J. Renstrom, *Imprint of sub-25 nm vias and trenches in polymers.* Applied physics letters, 1995. **67**(21): p. 3114-3116.

23. Wu, J., et al., *Complete plastic nanofluidic devices for DNA analysis via direct imprinting with polymer stamps.* Lab on a Chip, 2011. **11**(17): p. 2984-2989.

24. Guo, L.J., *Nanoimprint lithography: methods and material requirements.* Advanced materials, 2007. **19**(4): p. 495-513.

25. Sobolev, K. and F. Sanchez, *Nano-engineered Concrete.* Encyclopedia of Nanotechnology, 2012: p. 1530-1538.

26. Chou, S.Y., P.R. Krauss, and P.J. Renstrom, *Nanoimprint lithography.* Journal of Vacuum Science & Technology B: Microelectronics and Nanometer Structures Processing, Measurement, and Phenomena, 1996. **14**(6): p. 4129-4133.

27. Chantiwas, R., et al., *Flexible fabrication and applications of polymer nanochannels and nanoslits.* Chemical Society Reviews, 2011. **40**(7): p. 3677-3702.

28. Gates, B.D., et al., *New approaches to nanofabrication: molding, printing, and other techniques.* Chemical reviews, 2005. **105**(4): p. 1171-1196.

29. Amirsadeghi, A., et al., *The role of hydrophobic silane coating on Si stamps in nanoimprint lithography.* Journal of Applied Physics, 2017. **121**(4): p. 044909.

30. Colburn, M., et al. *Step and flash imprint lithography: a new approach to high-resolution patterning*. in *Emerging Lithographic Technologies III*. 1999. International Society for Optics and Photonics.

31. Wu, J., et al., *Polymer Stamps for Imprinting Nanopatterns in Polymer Substrate.* Journal of nanoscience and nanotechnology, 2015. **15**(1): p. 471-474.

32. Xia, D., J. Yan, and S. Hou, *Fabrication of nanofluidic biochips with nanochannels for applications in DNA analysis.* Small, 2012. **8**(18): p. 2787-2801.

33. Qin, D., Y. Xia, and G.M. Whitesides, *Soft lithography for micro-and nanoscale patterning.* Nature protocols, 2010. **5**(3): p. 491.

34. Wang, L., et al., *Nano-Crystalline diamond films for x-ray lithography mask*, in *Lithography*. 2010, InTech.

35. Duan, C., W. Wang, and Q. Xie, *Fabrication of nanofluidic devices.* Biomicrofluidics, 2013. **7**(2): p. 026501.

36. Grigorescu, A. and C. Hagen, *Resists for sub-20-nm electron beam lithography with a focus on HSQ: state of the art.* Nanotechnology, 2009. **20**(29): p. 292001.

37. Vieu, C., et al., *Electron beam lithography: resolution limits and applications.* Applied surface science, 2000. **164**(1-4): p. 111-117.

38. Broers, A., A. Hoole, and J. Ryan, *Electron beam lithography—Resolution limits.* Microelectronic Engineering, 1996. **32**(1-4): p. 131-142.

39. Chen, W. and H. Ahmed, *Fabrication of 5–7 nm wide etched lines in silicon using 100 keV electron-beam lithography and polymethylmethacrylate resist.* Applied physics letters, 1993. **62**(13): p. 1499-1501.

40. Hu, W., et al., *Sub-10 nm electron beam lithography using cold development of poly (methylmethacrylate).* Journal of Vacuum Science & Technology B: Microelectronics and Nanometer Structures Processing, Measurement, and Phenomena, 2004. **22**(4): p. 1711-1716.

41. Tseng, A.A., et al., *Electron beam lithography in nanoscale fabrication: recent development.* IEEE Transactions on electronics packaging manufacturing, 2003. **26**(2): p. 141-149.

42. Grigorescu, A., et al., *10 nm lines and spaces written in HSQ, using electron beam lithography.* Microelectronic Engineering, 2007. **84**(5-8): p. 822-824.

43. Yang, H., et al., *Low-energy electron-beam lithography of hydrogen silsesquioxane.* Microelectronic engineering, 2006. **83**(4-9): p. 788-791.

44. Namatsu, H., et al., *Three-dimensional siloxane resist for the formation of nanopatterns with minimum linewidth fluctuations.* Journal of Vacuum Science & Technology B: Microelectronics and Nanometer Structures Processing, Measurement, and Phenomena, 1998. **16**(1): p. 69-76.

45. Perry, J.M., Z.D. Harms, and S.C. Jacobson, *3D Nanofluidic Channels Shaped by Electron-Beam-Induced Etching.* Small, 2012. **8**(10): p. 1521-1526.

46. Anzalone, P.A., J.F. Mansfield, and L.A. Giannuzzi, *DualBeam Milling and Deposition of Complex Structures Using Bitmap Files and Digital Patterning.* Microscopy and Microanalysis, 2004. **10**(S02): p. 1154.

47. Cao, H., et al., *Gradient nanostructures for interfacing microfluidics and nanofluidics.* Applied Physics Letters, 2002. **81**(16): p. 3058-3060.

48. Kim, C.-S., S.-H. Ahn, and D.-Y. Jang, *Developments in micro/nanoscale fabrication by focused ion beams.* Vacuum, 2012. **86**(8): p. 1014-1035.

49. Latif, A., *Nanofabrication using focused ion beam*. 2000, University of Cambridge.

50. Tseng, A.A., *Recent developments in micromilling using focused ion beam technology.* Journal of Micromechanics and Microengineering, 2004. **14**(4): p. R15.

51. Suh, D., S.J. Choi, and H.H. Lee, *Rigiflex lithography for nanostructure transfer.* Advanced materials, 2005. **17**(12): p. 1554-1560.

52. Taniguchi, J., et al., *Filling behavior of UV nanoimprint resin observed by using a midair structure mold.* Microelectronic Engineering, 2009. **86**(4): p. 676-680.

53. Kannegulla, A. and L.-J. Cheng, *Metal assisted focused-ion beam nanopatterning.* Nanotechnology, 2016. **27**(36): p. 36LT01.

54. Matsui, S., et al., *Breakthrough achievement in nanoimprint lithography using PFP condensable gas.* Journal of Photopolymer Science and Technology, 2014. **27**(1): p. 61-72.

55. Liang, X., et al., *Air bubble formation and dissolution in dispensing nanoimprint lithography.* Nanotechnology, 2006. **18**(2): p. 025303.

56. Wang, Q., et al., *Real-time full-area monitoring of the filling process in molds for UV nanoimprint lithography using dark field illumination.* Journal of Vacuum Science & Technology B, Nanotechnology and Microelectronics: Materials, Processing, Measurement, and Phenomena, 2012. **30**(6): p. 06FB13.

57. Youn, S.-W., et al., *Control of Resin Filling and Pattern Quality of Ultraviolet Nanoimprint Lithography in Pentafluoropropane and Helium Ambient.* Japanese Journal of Applied Physics, 2013. **52**(6S): p. 06GJ07.

58. Nakagawa, M., et al., *Size-Dependent Filling Behavior of UV-Curable Di (meth) acrylate Resins into Carbon-Coated Anodic Aluminum Oxide Pores of around 20 nm.* ACS applied materials & interfaces, 2016. **8**(44): p. 30628-30634.

59. Shimazaki, Y., et al., *Reduction in Viscosity of Quasi-2D-Confined Nanoimprint Resin through the Addition of Fluorine-Containing Monomers: Shear Resonance Study.* ACS applied materials & interfaces, 2013. **5**(16): p. 7661-7664.

60. Uba, F.I., et al., *Surface charge, electroosmotic flow and DNA extension in chemically modified thermoplastic nanoslits and nanochannels.* Analyst, 2015. **140**(1): p. 113-126.

61. Amirsadeghi, A., *Developing Defect-tolerant Demolding Process in Nanoimprint Lithography*. 2013.

62. Khang, D.-Y. and H.H. Lee, *Sub-100 nm patterning with an amorphous fluoropolymer mold.* Langmuir, 2004. **20**(6): p. 2445-2448.

63. Zhang, H. and S.G. Weber, *Teflon AF materials*, in *Fluorous chemistry*. 2011, Springer. p. 307-337.

64. Kunwong, D., N. Sumanochitraporn, and S. Kaewpirom, *Curing behavior of a UV-curable coating based on urethane acrylate oligomer: the influence of reactive monomers.* Sonklanakarin Journal of Science and Technology, 2011. **33**(2): p. 201.

65. Persson, F. and J.O. Tegenfeldt, *DNA in nanochannels—directly visualizing genomic information.* Chemical Society Reviews, 2010. **39**(3): p. 985-999.

66. Moonen, P.F., I. Yakimets, and J. Huskens, *Fabrication of transistors on flexible substrates: from mass-printing to high-resolution alternative lithography strategies.* Advanced materials, 2012. **24**(41): p. 5526-5541.

67. Fanzio, P., et al., *DNA detection with a polymeric nanochannel device.* Lab on a Chip, 2011. **11**(17): p. 2961-2966.

68. McCormick, R.M., et al., *Microchannel electrophoretic separations of DNA in injection-molded plastic substrates.* Analytical Chemistry, 1997. **69**(14): p. 2626-2630.

69. Nunes, P.S., et al., *Cyclic olefin polymers: emerging materials for lab-on-a-chip applications.* Microfluidics and nanofluidics, 2010. **9**(2-3): p. 145-161.

70. Chen, Y., L. Zhang, and G. Chen, *Fabrication, modification, and application of poly(methyl methacrylate) microfluidic chips.* Electrophoresis, 2008. **29**(9): p. 1801-14.

71. Prakash, S., M. Karacor, and S. Banerjee, *Surface modification in microsystems and nanosystems.* Surface Science Reports, 2009. **64**(7): p. 233-254.

72. Kirby, B.J. and E.F. Hasselbrink, *Zeta potential of microfluidic substrates: 2. Data for polymers.* Electrophoresis, 2004. **25**(2): p. 203-213.

73. Juang, Y.J., L.J. Lee, and K.W. Koelling, *Hot embossing in microfabrication. Part I: Experimental.* Polymer Engineering & Science, 2002. **42**(3): p. 539-550.

74. Cecchini, M., et al., *High-resolution poly (ethylene terephthalate)(PET) hot embossing at low temperature: thermal, mechanical, and optical analysis of nanopatterned films.* Langmuir, 2008. **24**(21): p. 12581-12586.

75. Liao, W.-c. and S.L.-C. Hsu, *A novel liquid thermal polymerization resist for nanoimprint lithography with low shrinkage and high flowability.* Nanotechnology, 2007. **18**(6): p. 065303.

76. Yin, Z., L. Sun, and H. Zou, *Numerical analysis on PET demolding stage in thermal nanoimprinting lithography.* Microsystem Technologies, 2017. **23**(4): p. 899-905.

77. Uba, F.I., et al., *Surface charge, electroosmotic flow and DNA extension in chemically modified thermoplastic nanoslits and nanochannels.* Analyst, 2015. **140**(1): p. 113-26.

78. Meng, F., et al., *Fabrication and characterization of bilayer metal wire-grid polarizer using nanoimprint lithography on flexible plastic substrate.* Microelectronic Engineering, 2011. **88**(10): p. 3108-3112.

79. Yin, Z., et al., *Fabrication of two dimensional polyethylene terephthalate nanofluidic chip using hot embossing and thermal bonding technique.* Biomicrofluidics, 2014. **8**(6): p. 066503.

80. Uba, F.I., et al., *High process yield rates of thermoplastic nanofluidic devices using a hybrid thermal assembly technique.* Lab on a Chip, 2015. **15**(4): p. 1038-1049.

81. Chen, J. and K. Sun, *Enhancement of the light conversion efficiency of silicon solar cells by using nanoimprint anti-reflection layer.* Solar Energy Materials and Solar Cells, 2010. **94**(3): p. 629-633.

82. Kim, J.K., et al., *Fabrication of ZrO2 nanopatterns for biomimetic antireflection by thermal nanoimprint lithography.* Microelectronic Engineering, 2012. **100**: p. 12-15.

83. Hirai, Y., et al., *Study of the resist deformation in nanoimprint lithography.* Journal of Vacuum Science & Technology B: Microelectronics and Nanometer Structures Processing, Measurement, and Phenomena, 2001. **19**(6): p. 2811-2815.

84. Kim, N.W., K.W. Kim, and H.-C. Sin, *Finite element analysis of low temperature thermal nanoimprint lithography using a viscoelastic model.* Microelectronic Engineering, 2008. **85**(9): p. 1858-1865.

85. Chantiwas, R., et al., *Simple replication methods for producing nanoslits in thermoplastics and the transport dynamics of double-stranded DNA through these slits.* Lab on a Chip, 2010. **10**(23): p. 3255-3264.

86. Park, S., et al., *Demolding temperature in thermal nanoimprint lithography.* Applied Physics A, 2009. **97**(2): p. 395-402.

87. Dirckx, M.E. and D.E. Hardt, *Analysis and characterization of demolding of hot embossed polymer microstructures.* Journal of Micromechanics and Microengineering, 2011. **21**(8): p. 085024.

88. Saha, B., et al., *Replication performance of Si-N-DLC-coated Si micro-molds in micro-hot-embossing.* Journal of Micromechanics and Microengineering, 2010. **20**(4): p. 045007.

89. Vlachopoulou, M., et al., *A low temperature surface modification assisted method for bonding plastic substrates.* Journal of Micromechanics and Microengineering, 2008. **19**(1): p. 015007.

90. Tennico, Y.H., et al., *Surface modification-assisted bonding of polymer-based microfluidic devices.* Sensors and Actuators B: Chemical, 2010. **143**(2): p. 799-804.

91. Chen, Y., L. Zhang, and G. Chen, *Fabrication, modification, and application of poly (methyl methacrylate) microfluidic chips.* Electrophoresis, 2008. **29**(9): p. 1801-1814.

92. Vesel, A. and M. Mozetic, *Surface modification and ageing of PMMA polymer by oxygen plasma treatment.* Vacuum, 2012. **86**(6): p. 634-637.

93. Kovach, K.M., et al., *The effects of PEG-based surface modification of PDMS microchannels on long-term hemocompatibility.* J Biomed Mater Res A, 2014. **102**(12): p. 4195-205.

94. Liu, J., et al., *Surface-modified poly (methyl methacrylate) capillary electrophoresis microchips for protein and peptide analysis.* Analytical chemistry, 2004. **76**(23): p. 6948-6955.

95. Venkatesan, B.M., et al., *DNA Sensing using Nano-crystalline Surface Enhanced Al(2)O(3) Nanopore Sensors.* Adv Funct Mater, 2010. **20**(8): p. 1266-1275.

96. ONeil, C.E., et al., *Interrogating Surface Functional Group Heterogeneity of Activated Thermoplastics Using Super-Resolution Fluorescence Microscopy.* Analytical chemistry, 2016. **88**(7): p. 3686-3696.

97. Wei, S., et al., *Photochemically patterned poly (methyl methacrylate) surfaces used in the fabrication of microanalytical devices.* The Journal of Physical Chemistry B, 2005. **109**(35): p. 16988-16996.

98. McCarley, R.L., et al., *Resist-free patterning of surface architectures in polymer-based microanalytical devices.* Journal of the American Chemical Society, 2005. **127**(3): p. 842-843.

99. Chai, J., et al., *Wettability interpretation of oxygen plasma modified poly (methyl methacrylate).* Langmuir, 2004. **20**(25): p. 10919-10927.

100. Lin, T.-Y., T.T. Pfeiffer, and P.B. Lillehoj, *Stability of UV/ozone-treated thermoplastics under different storage conditions for microfluidic analytical devices.* RSC advances, 2017. **7**(59): p. 37374-37379.

101. Yu, H., et al., *Low temperature and deformation-free bonding of PMMA microfluidic devices with stable hydrophilicity via oxygen plasma treatment and PVA coating.* RSC Advances, 2015. **5**(11): p. 8377-8388.

102. Occhiello, E., et al., *Hydrophobic recovery of oxygen-plasma-treated polystyrene.* Polymer, 1992. **33**(14): p. 3007-3015.

103. Butler, T.Z., et al., *Single-molecule DNA detection with an engineered MspA protein nanopore.* Proc Natl Acad Sci U S A, 2008. **105**(52): p. 20647-52.

104. Morent, R., et al., *Study of the ageing behaviour of polymer films treated with a dielectric barrier discharge in air, helium and argon at medium pressure.* Surface and Coatings Technology, 2007. **201**(18): p. 7847-7854.

105. Llopis, S.L., J. Osiri, and S.A. Soper, *Surface modification of poly (methyl methacrylate) microfluidic devices for high-resolution separations of single-stranded DNA.* Electrophoresis, 2007. **28**(6): p. 984-993.

106. Bi, H., et al., *Deposition of PEG onto PMMA microchannel surface to minimize nonspecific adsorption.* Lab Chip, 2006. **6**(6): p. 769-75.

107. Tsao, C.-W. and D.L. DeVoe, *Bonding of thermoplastic polymer microfluidics.* Microfluidics and Nanofluidics, 2009. **6**(1): p. 1-16.

108. Tsao, C., et al., *Low temperature bonding of PMMA and COC microfluidic substrates using UV/ozone surface treatment.* Lab on a Chip, 2007. **7**(4): p. 499-505.

109. Schneider, G.F., et al., *Tailoring the hydrophobicity of graphene for its use as nanopores for DNA translocation.* Nat Commun, 2013. **4**: p. 2619.

110. Jia, Z., J. Choi, and S. Park, *Selection of UV Resins for Nanostructured Molds for Thermal-NIL.* Nanotechnology, 2018.

111. Cho, H., et al., *Replication of flexible polymer membranes with geometry-controllable nano-apertures via a hierarchical mould-based dewetting.* Nature communications, 2014. **5**: p. 3137.

112. Con, C., et al., *Thermal nanoimprint lithography using fluoropolymer mold.* Microelectronic Engineering, 2012. **98**: p. 246-249.

113. Scopece, P., et al., *Conical nanopore membranes: solvent shaping of nanopores.* Nanotechnology, 2006. **17**(15): p. 3951.

Chapter 4. Surface Charge Density Dependent DNA Translocation Through Polymer In-Plane Nanopores

4.1 Introduction: DNA translocation through solid-state nanopores

For nanopore-based sequencing platforms, DNA translocation is a basic and fundamental experiment to test the platform's performance. dsDNA, ssDNA and even methylated DNA with different chain length have been translocated through solid-state nanopores [1-7] and these biomolecules can be detected electrically and optically. For electrical detection, device chamber is filled with conductive electrolyte (usually high concentration KCl solution) solution as shown in Figure 4.1(a). Negatively charged DNA molecules are driven through nanopore by external electric field and at the same time ionic current is measured by high bandwidth voltage-clamp. When DNA molecule travels into the pore, it blocks ions transport temporarily. If nanopore size is comparable to DNA size, a current drop signal will be generated and recorded. Biological information of the molecules can be revealed by analyzing the signal shape, size, duration and frequency [1, 5, 7, 8]. Although electrical detection of DNA by nanopore has advantages such as label-free and high efficiency, it is hard to conduct electrical detection with multiple pores. While optical observation provides the probability to analyze DNA translocation with high throughput [9]. For optical observation, fluorescence signal from translocated DNA is recorded by camera. During recording more than one DNA molecules are driven to nanopore, in order to increase signal to noise ratio and capture the right molecule, additional optical component is needed (for example, zero-mode waveguide) [10]. Since our ultimate goal is to sequence DNA using in-plane nanopore without any fluorescence label, we focus on the researches related to DNA electrical detection by solid-state nanopore, which can serve as reference for our work.

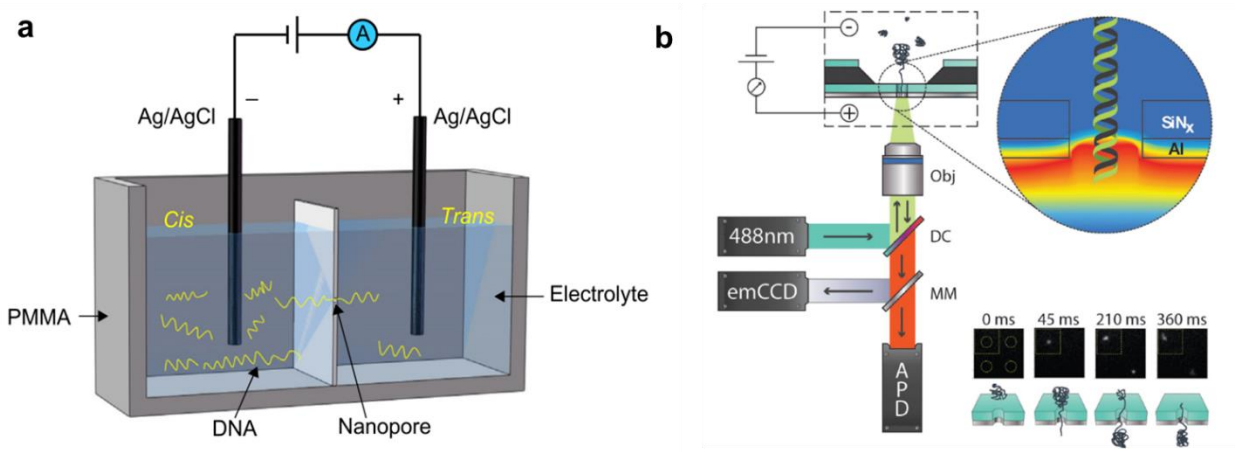

Figure 4.1. (a) Schematic image of DNA sensing setup by ionic current measurement. (b) Schematic diagram of optical observation setup for DNA translocation. A thin Al layer is coated on Si_3N_4 nanopore as waveguide (top right). Fluorescence signal of translocated DNA is captured by camera.

The structure of this chapter is described as follows. In the beginning of this chapter, we review DNA translocation kinetics through traditional vertical type solid-state nanopore. For vertical nanopore, diffusion and entropy are the limits to efficient DNA capture. Long chain DNA translocation is in diffusion limit regime and short chain DNA translocation is in entropy barrier limit regime. Study of translocation kinetics helps us to have a better understanding of DNA translocation phenomenon through in-plane nanopore. Then we summarize the solid-state nanopore DNA translocation event data, by correlating current change and dwelling time with translocated DNA configuration, molecule length, driving voltage and electrolyte concentration. Such information helps us to analyze our data from in-plane nanopore. Based on the knowledge from solid-state nanopore, we performed DNA translocation through polymer based in-plane nanopores. Prior to translocation experiments, surface charge density effect on DNA translocation was studied by COMSOL simulation. Effective driving force for dsDNA translocation was simulated with various surface charge densities and nanopore sizes. For a 10 nm diameter nanopores, the threshold surface charge density for DNA translocation was determined as -50 mC/m^2. In order to validate the simulation results, λ-DNA translocation was conducted in

nanopores imprinted on poly(ethylene glycol) diacrylate (PEGDA), poly(methyl methacrylate) (PMMA) and cyclic olefin copolymer (COC) substrates with their surface charge densities (absolute value) in an increasing order (PEGDA > PMMA > COC). Both fluorescence observation (1× TE buffer) and ionic current (1× TE buffer) measurement confirmed the simulation results that translocation of λ-DNA molecules only occurred in PEGDA based nanopore with a surface charge density of -24.1 mC/m^2. In order to compare with λ-DNA translocation data obtained from solid-state nanopore, ionic current was recorded for λ-DNA translocation through PEGDA based nanopore filled with 1 M KCl.

4.1.1 DNA translocation kinetics

Efficient DNA capture is a basic but challenging requirement for all nanopore-based sequencing platforms [11-14]. Therefore, it is necessary to study DNA translocation kinetics in order to increase the DNA capture rate. As illustrated in Figure 4.2, there are three main steps for polymer chain translocation: drift diffusion, capture, and translocation [15]. When DNA molecules are far from nanopore, their movement are dominated by drift due to weak extending electric field and diffusion arising from collision with solvent molecules [15, 16]. Once the molecule enters the capture zone, it moves toward the nanopore mouth and never goes back. The term "capture radius", r^* is usually used to define the size of the capture zone. A higher r^* value indicates more molecules will be delivered to nanopore and the theoretical DNA capture rate based on r^* denotes as R_c^{diff}. However, capture radius is not the only term determines capture rate. This's because translocation stage requires the molecule to overcome an entropy (free energy) barrier by putting its chain end into the pore first. Once the end of DNA chain enters the pore, it will be pulled through nanopore by an effective driving force. Based on Kramers theory, DNA capture rate can be calculated based on the barrier height as R_c^{bar} [16]. If $R_c^{diff} > R_c^{bar}$, DNA capture is in diffusion

limit regime, otherwise it is in barrier regime. Here, we first study DNA translocation kinetics by in diffusion limit regime and barrier regime. Then, we discuss the forces related to DNA translocation. We want to find the main factors affecting DNA translocation and optimize them for our device.

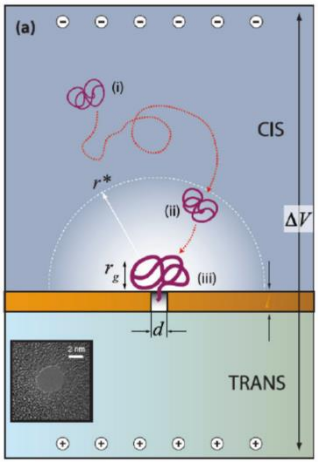

Figure 4.2. Schematic image of DNA translocation through solid-state nanopore: (i) drift diffusion, (ii) capture, (iii) translocation.

4.1.1.1 Diffusion limit regime

4.1.1.1.1 Diffusion limit capture rate, R_c^{diff} and capture radius r^*

As mentioned above, if entropy barrier for translocation can be overcome easily, any molecule enters capture zone will be translocated without time delay. Then DNA capture process is limited by diffusion and the DNA capture rate, R_c^{diff}, is given by the classical Smoluchowski theory [11, 16, 17]

$$R_c^{diff} = 2\pi D r^*, \tag{1}$$

where D is diffusion coefficient. So the key is to find capture radius and there are two ways to derive r^*.

r^* can be calculated from its definition. As absorption radius, r^* is the distance DNA molecule can travel within its longest relaxing time, from cis chamber toward nanopore [11, 13]. The longest relaxing time τ_z is given by the Zimm relaxing time [18, 19]

$$\tau_z = \int_0^{r^*} \frac{dr}{V_{DNA}(r)} \tag{2}$$

$$\tau_z \approx 0.3 \frac{\eta R_g^3}{kT}, \tag{3}$$

where $V_{DNA}(r)$ is DNA local velocity, η is solution viscosity, R_g is the gyration radius of the polymer. $V_{DNA}(r)$ consists of three components, diffusion velocity, V_{diff}, drift velocity, V_{dr}, and convection velocity, V_c and it can be estimated as

$$V_{DNA} = V_{dr} + V_{diff} + V_c \approx -\mu_{DNA} E - \frac{D_{DNA}}{R_a} + V_{EOF}, \tag{4}$$

where μ_{DNA} and D_{DNA} are electrophoretic mobility and diffusion coefficient of DNA molecule, and V_c is estimated as EOF velocity [11]. r^* can be calculated by substituting Equation 4.4 to Equation 4.2. Usually, diffusion term can be neglected compared with the other two terms.

r^* can also be calculated from work by stall force. Recent researches indicate DNA capture is influenced by a weak but nonuniform electric field extending out of the pore, as shown in Figure 4.3. We denote the potential associated with this field as $U(r)$ [2, 16, 20]. $U(r)$ can be estimated by an access resistance model [16, 20-22]

$$U(r) = \frac{d^2}{8lr} \Delta U, \tag{5}$$

where d is nanopore diameter, l is nanopore length, r is distance from nanopore and ΔU is the applied driving voltage.

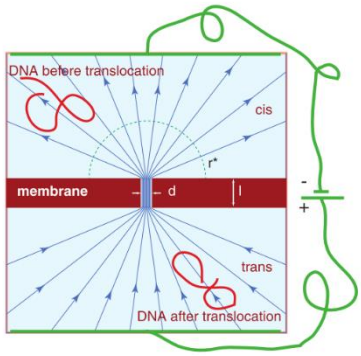

Figure 4.3. Electric filed outside nanopore and inside nanopore. Electric filed inside nanopore is strong due to large potential drop. Electric field extending out of the pore is weak but affects DNA translocation into capture zone.

The probability of moving DNA molecule from on location to another in the field $U(r)$ should be proportional to $\exp[-W/k_BT]$, where W is the minimal work needed to move DNA molecule between two points and k_B is Bolztmann constant. And the critical condition for this situation is $W\ (r^*) \sim k_BT$. To be minimal, the driving force should be equal to the stall force at every moment. Based on this assumption, we get

$$W(r) = \frac{\mu k_B T}{D} U(r). \tag{6}$$

Derivation details can be found in Ref. 17. Thus,

$$U(r^*) = \frac{D}{\mu} \tag{7}$$

$$r^* = \frac{d^2\mu}{8lD}\Delta U, \tag{8}$$

Substituting Equation 4.8 to Equation 4.1, we have

$$R_c^{diff} = \frac{\pi d^2 \mu}{4l}\Delta U. \tag{9}$$

From Equation 4.9, we know for diffusion limit DNA capture, the capture rate is proportional to driving voltage. Though DNA chain length has effect on diffusion coefficient, for diffusion limit capture, DNA molecules with different size have the same capture rate.

In addition to the method mentioned above to derive DNA capture rate in diffusion limit regime, capture rate derivation is also discussed in Ref. 12 and Ref. 29.

In Ref. 12, DNA capture rate is determined by definition, numbers of molecules delivered into capture zone per unit time.

$$R_c^{diff} = 2\pi(r^*)^2 c_0 V_{DNA}(r^*) \tag{10}$$

where c_0 is DNA bulk concentration far from nanopore, $V_{DNA}(r^*)$ is DNA local velocity at capture radius edge and r^* can be calculated from Equation 4.2 and 4.4. From Equation 4.10, we can find DNA capture rate can be enhanced by increasing capture radius and molecule speed moving toward nanopore.

In Ref. 29, DNA capture rate (DNA flux) is calculated by considering diffusion, drift and entropy barrier (for diffusion limit regime only, entropy barrier effect is neglected)

$$J(x,t) = -D\frac{\partial c}{\partial t} - c\mu\frac{\partial U(x)}{\partial x} - cD\frac{\partial F(x)}{k_B T \partial x}, \tag{11}$$

where $F(x)$ is entropy barrier height. The three terms on the right represent the contributions from diffusion, drift and entropy barrier. In summary, $J_{diff} \sim \frac{c}{N^{0.6}}$ and $J_{drift} \sim cU$.

Though these models are built based on different theories, for diffusion limit regime, they all show a DNA capture rate linear to driving voltage, which is in good agreement with experimental results [5, 15, 23] as shown in Figure 4.4(a) and (b). For long chain DNA or DNA translocation under high bias voltage, translocation is in diffusion limit regime. Next, we are going to discuss how to increase DNA capture rate for diffusion limit translocation.

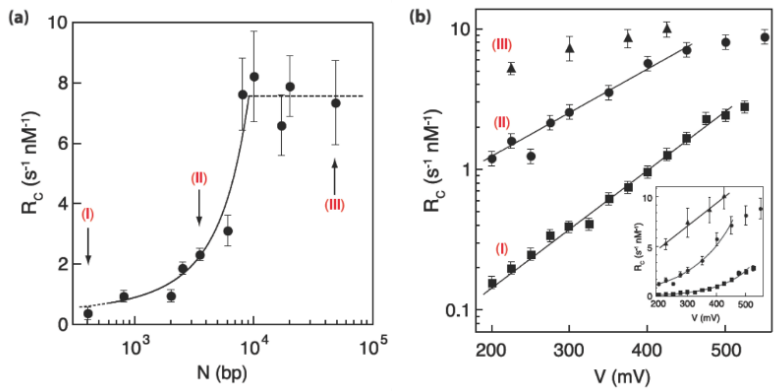

Figure 4.4. (a) DNA capture rate dependent on molecule size (300 mV as driving voltage). For long chain molecules, DNA capture rate is independent of molecule size. For short chain molecules, DNA capture rate is size dependent. (b) DNA capture rate dependent on driving voltage. For long chain molecules, DNA translocation is in diffusion regime with its capture rate linear to driving voltage. For short chain molecules, DNA translocation is in barrier limit regime with its capture exponential to driving voltage.

4.1.1.1.2 Solutions to increase R_c^{diff}

As discussed above, for DNA translocation in a symmetric buffer system (same salt concentration in both cis and trans chamber), capture rate increases along with driving voltage independent of molecule size. Obviously, DNA capture rate can be increased by applying higher driving voltage. However, higher driving voltage also leads to faster DNA translocation speed, which is not favorable for strand DNA sequencing [11, 24, 25].

Though driving voltage has impact on DNA capture rate as shown in Equation 4.9 and Figure 4.4(b), the intrinsic "driving force" comes from the extending electric field at nanopore mouth. Electric field at cis side nanopore mouth *U(r)* can be enhanced by salt gradient, as illustrated in Figure 4.5(a). With salt gradient present, a higher electric field along nanopore is required to keep conservation of the electrical current. Furthermore, positive net charges are accumulated around pore mouth because of tuned electric field. Stronger *U(r)* together with cationic EOF increase DNA capture radius and molecule velocity toward nanopore [5, 11]. DNA capture rate is increased based on Equation 4.10. Meanwhile, DNA translocation dwelling time

increases based on the experimental results in Ref. 11, which can be attributed to EOF generated from enriched K^+ along DNA chain and nanopore surface. By using salt solution with concentration gradient, high DNA capture rate and slow DNA translocation can be achieved simultaneously.

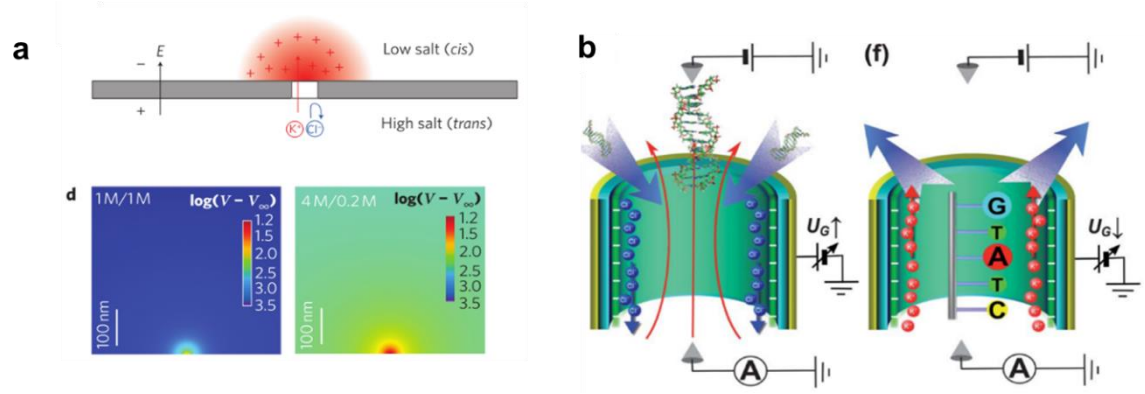

Figure 4.5. (a) Schematic image showing *U(r)* enrichment and positive charge accumulation at cis side nanopore mouth with salt concentration gradient present; (b) DNA capture controlled by gate voltage, high gate voltage introduce positive surface charge and cationic EOF, which helps DNA capture. While, low gate voltage introduce negative surface charge and anionic EOF, which slow down DNA translocation.

As mentioned above, DNA capture rate can be enhanced by increasing capture radius and molecule velocity toward nanopore. From Equation 4.2 and 4.4, we find EOF velocity has impact on DNA capture radius and translocation velocity. Therefore, DNA capture can be enhanced by manipulating nanopore internal surface charge. Internal surface charge of biological nanopore can be manipulated by advanced biological technology [26, 27]. For commonly used SiO_2 and Si_3N_4 nanopores, surface charge on nanopore wall can be tuned by Al_2O_3 layer coating [14, 28]. However, it is not easy to control nanopore size after additional layer coating. An alternative way to control surface charge is by integrating gate electrodes on nanopore wall, as illustrated in Figure 4.5(b). High gate voltage is applied during DNA capture process to enhance DNA capture by cationic EOF. Low gate voltage is applied during DNA translocation to reduce DNA translocation speed

by anionic EOF. Several simulation work has been done regarding this method but few experimental data has been reported because of the device complexity [11, 29, 30].

4.1.1.2 Barrier limit regime

Once DNA molecules are delivered to nanopore mouth, translocation process begins. Translocation process is composed of three steps: (1) chain end localization, (2) nucleation and (3) threading. During translocation, coiled DNA molecules have to overcome entropy barriers arising from conformational change, electrostatic interaction between distribution of ionic clouds and solvent molecules [31, 32]. DNA translocation through nanopore with high entropy barrier is in barrier limit regime. Because delivered molecules need some time [33] (several attempts) to overcome the barrier and the required time is longer than its travel time into capture zone, $R_c^{diff} > R_c^{bar}$. Let's first take a look at the origin of such barrier and then discuss how the barrier affect DNA capture.

4.1.1.2.1 Origin of entropy barrier and barrier height

Schematic images of DNA translocation process and free energy landscape corresponding to the process are illustrates in Figure 4.6(a) and (b). During translocation, DNA chain has to overcome two entropy barriers, associating with localization step and threading step, respectively. Since the first barrier is larger, in this work we study the barrier associated with the first step (from stage A to stage B in Figure 4.6(a)) [31].

For vertical type nanopore, molecules delivered to nanopore mouth are in coiled state as illustrated in Figure 4.6(a). Prior to translocation, it requires DNA to put its chain end into nanopore. In order to achieve this, DNA chain end has to overcome an entropy barrier. As discussed above, though there are many factors make contribution to this barrier, it mainly comes

from DNA chain conformational change [31]. Therefore, we can say DNA chain conformational change is the main resource for entropy barrier during DNA translocation.

From the standpoint of statistical mechanics, we can explain the origin of entropy barrier [34]. Neglecting intrachain electrostatic, DNA molecules can be treated as Gaussian chain with N segments having no surface charge. Entropy of DNA chain can be calculated from Boltzmann equation

$$S = k_B lnP(r1, r2), \tag{13}$$

where P is a the probability of two DNA chain ends at position $r1$ and $r2$, repectively. At stage A, DNA chain has two free ends with an entropy P_A. At stage B, DNA chain has one end free and one end fixed at nanopore mouth with entropy P_B. Without external electric field, the probability of one chain fixed and one chain free is lower than two chain ends free. In other words, DNA chain has to overcome an entropy barrier ΔS

$$\Delta S = k_B(lnP_A - P_B), \tag{14}$$

to achieve stage B. Details regarding the derivation and calculation of Equation 4.13 and 4.14 can be found in Ref. 33.

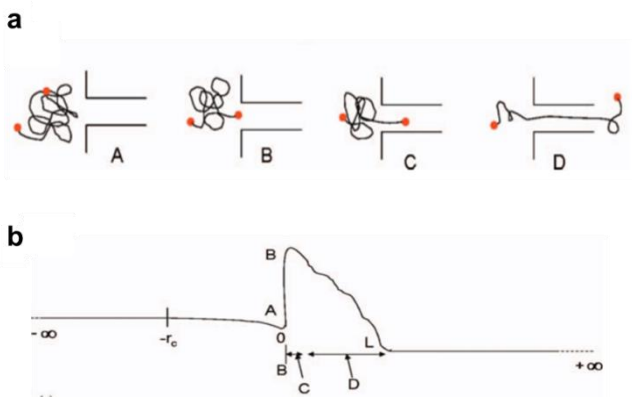

Figure 4.6. (a) Three stages for translocation step. (b) Free energy landscape.

4.1.1.2.2 Free energy barrier and free barrier effect on DNA capture rate

Entropy barrier change is part of free energy change. Assuming temperature is constant, free energy change ΔF increases with entropy decrease, as shown in Figure 4.6(b)

$$\Delta F = \Delta H - T\Delta S. \tag{15}$$

With external electric field, DNA chain increase energy ΔH by putting chain end at nanopore mouth,

$$\Delta H = q_{eff}\Delta U \tag{16}$$

where q_{eff} is effective surface charge of DNA chain end at nanopore mouth and ΔU is applied driving voltage. Based on Equation 4.15 and 4.16, increasing driving voltage is one method to reduce translocation free energy barrier [13, 32]. Free energy change can be calculated by self-consistent-field theory (SCFT) and the value ΔF is found to decrease with molecule length (segment number N) [31]

$$\Delta F \sim \frac{k_B T}{N^{\alpha}},\ \alpha \cong 0.2 \pm 0.1. \tag{17}$$

Which means long chain molecules have lower free energy barrier during translocation and this has been proved by experimental results [2, 16, 32].

Moreover, based on Kramers theory, barrier limited DNA capture rate should be proportional to $\exp(\frac{\Delta F}{k_B T})$ [2, 11, 16, 20]. For DNA translocation in vertical nanopores, high free energy barrier reduces capture rate but usually it can be overcome by applying higher voltage. Besides, free energy barrier is the reason for threshold driving voltage in translocation experiment [32].

To conclude, we discuss the origin of the translocation barrier during DNA translocation through vertical nanopore. For free energy barrier calculation, external electric filed only affects enthalpy change and entropy change is calculated from conformational change (without electric

field). It is rather difficult to evaluate free energy barrier precisely, therefore EOF effect is not included in discussion. Free energy barrier height is simply proportional to $\frac{k_B T}{N^{\alpha}}$. DNA capture rate in barrier limit regime is exponential to this barrier height.

4.1.1.3 Forces affecting DNA translocation

Another factor affect DNA translocation through nanopore is the forces, including electrophoretic driving force and viscous drag force. After DNA putting its chain end into nanopore, there should be enough effective driving force to pull DNA chain through nanopore. Here we summarize and compare forces affecting DNA translocation. Details related to force calculation can be found in Ref. 36.

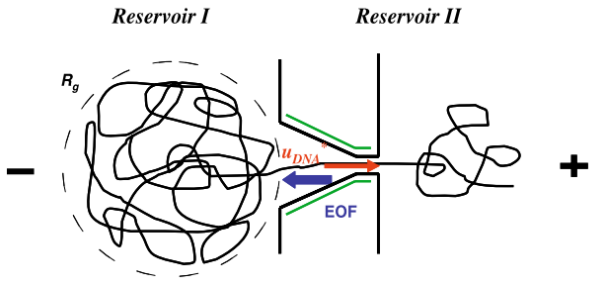

Figure 4.7. Schematic image of DNA translocation through negatively charged nanopore. Under electric field. DNA moving direction is opposite to EOF direction.

Under electric field, negatively charged DNA chain is subject to electrophoretic driving force F_e, moving toward Reservoir II shown in Figure 4.7. Commonly used nanopore materials have negative charges on the wall, which induces EOF opposite to DNA moving direction. Frictional force due to relative motion between bulk fluid flow and DNA chain is the main source for drag force. Drag force is composed of three components: viscous drag force acting on DNA inside nanopore, F_d, viscous drag force acting on DNA outside nanopore, F_{blob1} and F_{blob2} and uncoiling/recoiling forces acting on DNA during translocation, F_u and F_r [35]. Summary and comparison of these forces is present in Table 4.1.

Table 4.1. Comparison of forces affecting DNA translocation. 16.5 kbps dsDNA translocation through 10 nm diameter nanopore under 120 mV [35]. F_d is measured with DNA immobilized (DNA velocity equal to 0) [36].

Force	Magnitude
F_u^* (Muthukumar 1999)	~0.01 pN
F_u^* (Odijk 1983)	0.67 pN
F_u^* (Klushin et al. 2008)	1.9 pN
F_r^* (Prinsen et al. 2009)	0.083 pN
F_{blob1}^* (Storm et al. 2005b)	7.86 pN
F_{blob2}^*	~0.1 pN
F_e^*	113 pN
F_d^*	83.5 pN

Forces related to DNA translocation have been studied experimentally and numerically [29, 36-38]. Optical tweezer was used to measure effective driving force during DNA translocation. Effective driving force was found only 20%~30% of total electrophoretic driving force as shown in Table 4.1. This difference was first attributed to charge reduction by Manning condensation [32, 36, 39] without considering hydrodynamic force caused by EOF. Later, researches attributed this phenomenon to hydrodynamic drag force caused by EOF [37, 40]. In order words, low surface charge is good for DNA translocation in terms of effective driving force.

4.1.2 DNA translocation events

We have summarized the DNA translocation kinetics through nanopore and now it's the time to analyze DNA translocation data: current change and dwelling time. Experimental results from previous studies are summarized here as reference for our work.

4.1.2.1 Current change

As discussed before, when DNA molecule is present in nanopore, it triggers a current change signal. By analyzing current change signals, we can get information regarding DNA translocation configuration, molecules sizes and so on. dsDNA molecules are commonly used to

test solid-state nanopore performance and here we focus on current change data from dsDNA translocation experiments.

4.1.2.1.1 Current decrease and current enhancement

Though high concentration KCl (for example 1M) solution is commonly used as electrolyte for DNA translocation detection, low concentration KCl solution is usually added to TE buffer in order to increase signal to noise ratio and avoid weakening the binding strength between dye molecules and DNA backbones [41, 42]. Therefore, it is worthy to study current change signals with different salt concentration. Dekker et al. found current change signal due to DNA translocation is electrolyte concentration dependent (as shown in Figure 4.8) based on different mechanism [5]. Here we briefly summarize their results and details can be found in Ref. 5.

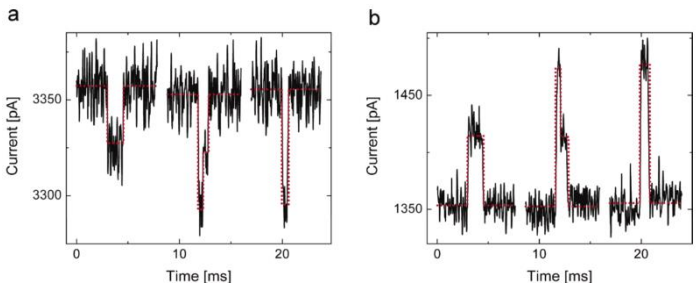

Figure 4.8. Current change signals for DNA translocation in (a) 500 mM KCl and (b) 150 mM KCl solution. DNA translocation leads to current decrease in high electrolyte concentration environment and current increase in low electrolyte concentration environment.

They explained their experimental results by exploring the mechanism for current change due to DNA translocation. With DNA present in the pore, there are two effects on ionic current: (1) obviously, ion transport will be blocked temporarily, which tends to reduce ionic current value and (2) negatively charged DNA molecule also brings counter-ions into nanopore, which increases the ion carriers number in nanopore and therefore tends to increase ionic current value. Combing two factors together, they got an equation to express conductance (ionic current) change (for certain pore size) , ΔG, due to DNA translocation

$$\Delta G = \frac{1}{L_{pore}}\left(-\frac{\pi}{4}{d_{DNA}}^2(\mu_{K^+} + \mu_{Cl^-})n_{KCl}e\ + \mu^*_{K^+}q^*_{l,DNA}\right) \quad (18)$$

where d_{DNA} (2.2 nm) is DNA chain diameter, μ_{K^+} and μ_{Cl^-} are electrophoretic mobility of K^+ and Cl^- ions, n_{KCl} is bulk KCl solution, $\mu^*_{K^+}$ is effective electrophoretic mobility of K^+ moving along with DNA chain, $q^*_{l,DNA}$ is effective surface charge on DNA per unit length.

From Equation 4.18, we can see the second term (current increase) will be dominant when KCl concentration is low. Based on their work, the critical concentration is close to 400 mM. Though their work explains current change due to DNA translocation well, Ramsey et al. reported lateral current increase events during DNA translocation under low salt concentration [43]. For the discussion below, we study the current decrease signal induced by DNA translocation in high concentration electrolyte.

4.1.2.1.2 DNA translocation mode and current decrease signals

Now we will take a look at current decrease signals and analyze signal shape and signal amplitude.

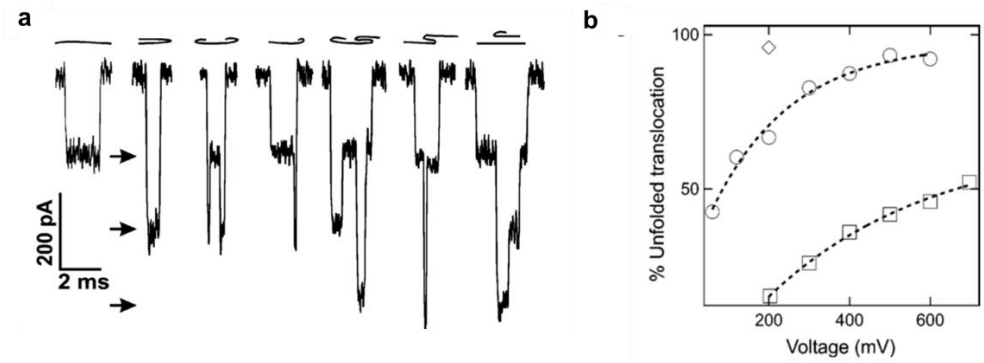

Figure 4.9. (a) Different λ-DNA configuration when translocation through nanopore and their corresponding current decrease signals. (b) Unfloded event rate vs driving voltage for DNA molecules with different length. Squares represent λ-DNA, circles for 10 kbp and diamonds for 3 kbp.

Branton et al. observed various current drop signals shown in Figure 4.9 and they attributed this difference to DNA configuration during translocation. Unfolded DNA results in small current

drop and long dwelling time. While for folded DNA, folded part leads to high current drop (peaks within current drop signals) and shorter dwelling time. Moreover, higher driving voltage can increase unfolded event rate, which can be attributed to high electric filed to overcome entropic forces [44].

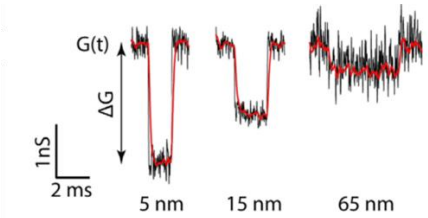

Figure 4.10. Current change signals for DNA translocation through nanopores with different sizes.

For DNA translocation in high salt concentration environment, when DNA is present in nanopore, it blocks ion transport temporarily and current drop signal will be measured. Current drop amplitude indicates the ratio between biomolecules size and nanopore diameter. Generally speaking, for nanopore with fixed size, current drop amplitude increase as molecule size increases; for certain biomolecules, current drop amplitude decreases as nanopore size increase, as shown in Figure 4.10. DNA sequencing (mononucleotides discrimination) based on current drop difference has been demonstrated for biological nanopores and MoS_2 solid-state nanopore [27, 45-48]. Moreover, damaged or methylated DNA molecules can be detected by solid-state nanopore based on current drop amplitude change due to geometry difference [3].

4.1.2.1.3 Conductance change model for DNA translocation

Dekker et al. studied the conductance model for solid-state nanopore and current drop amplitude for DNA translocation [22, 37] by considering access resistance and nanopore geometry. Cross-section of Si based synthetic nanopores are hourglass shaped, and to simplify the problem, we consider cylinder shape nanopore. Conductance of cylinder shape nanopore, G, in high salt

concentration (neglecting contribution from surface charge density) can be simply expressed as [5]:

$$G = \sigma \frac{\pi d^2}{4l}, \tag{19}$$

where σ is bulk salt solution conductivity, d is nanopore diameter and l is membrane thickness (nanopore length). Conductance change due to DNA translocation, ΔG, can be calculated by substituting Equation 4.20 and 4.21 into Equation 4.19:

$$\Delta G = G_{open\ pore} - G_{with\ DNA} = G(d) - G(d_{with\ DNA}) \tag{20}$$

$$d_{with\ DNA} = \sqrt{d^2 - d_{DNA}^2} \tag{21}$$

$$\Delta G = \sigma \frac{\pi d_{DNA}^2}{4l}. \tag{22}$$

However, this simple model doesn't fit conductance values experimentally determined for larger nanopores as shown in Figure 4.11(a). Moreover, it can't explain nanopore size dependent conductance change with DNA translocation as shown in Figure 4.10 and Figure 4.11(b). Therefore, an improved model considering access resistance [49, 50] is proposed to predict nanopore conductance and conductance change due to DNA translocation.

$$G = \sigma \left[\frac{4l}{\pi d^2} + \frac{1}{d}\right]^{-1} \tag{23}$$

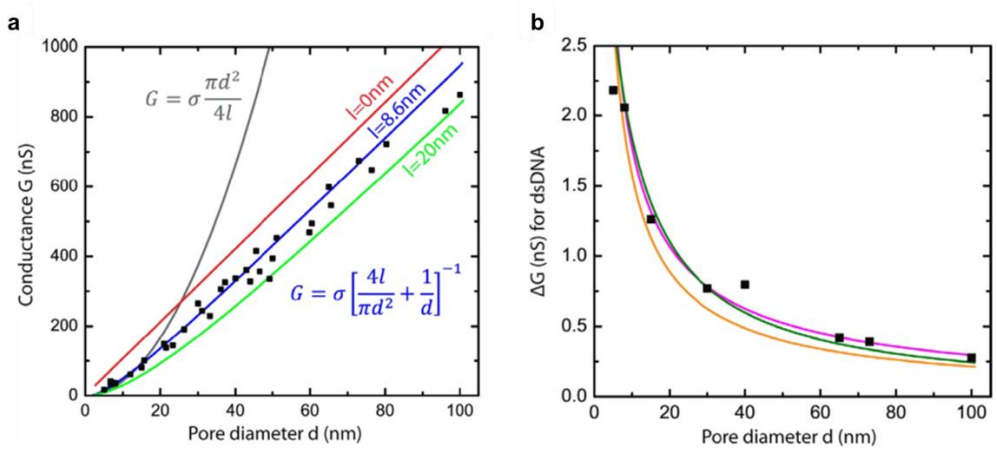

Figure 4.11 (a) Experimental data for nanopore (drilled on 20 nm thickness Si_3N_4 membrane) conductance versus nanopore diameter. Grey line, prediction based on simple model. Red line, blue line and green line are predictions based on conductance model including access resistance. Different l values are chosen for curve fitting and l = 8.6 nm fits the data well due to the hourglass shaped nanopore cross-section. (b) Experimental determined ΔG verse nanopore diameter. Solid lines are predictions by improved model based on different nanopore geometry. (Green line is simple cylinder nanopore).

4.1.2.2 Dwelling time

Current drop signal reveals DNA lateral dimension, while dwelling time indicates DNA molecule length. Unfolded translocation events are usually used for analyzing DNA translocation dwelling time [44, 51, 52]. Analyzed dwelling time information can be used to distinguish DNA molecules with different chain length as shown in Figure 4.12. We will summarize experimental results regarding dwelling time for different chain length DNA translocation and briefly discuss the factors affect dwelling time.

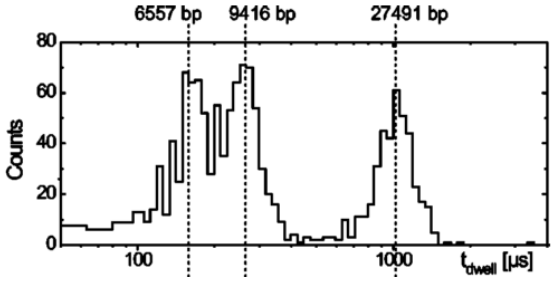

Figure 4.12. DNA fragments identification from a mixture of DNA molecules based on dwelling time.

DNA molecules with different length have been translocated through solid-state nanopore and their corresponding dwelling time, t_d, is dependent on molecule length as shown in Figure 4.13(a) and (b). Figure 4.13(a) shows dwelling time data and DNA length fit a power-law curve, $t_d \sim L^{\alpha}$. While Fig. 13(b) indicates dwelling time is proportional to DNA length. Dwelling time can be calculated from a simple equation,

$$t_d = K \frac{\eta L_{DNA}}{\lambda V} \tag{24}$$

assuming electrophoretic driving force is balanced by hydrodynamic drag force, where η is the viscosity of the solution, λ and L_{DNA} are the linear charge density and length of the DNA molecule, respectively, V is applied driving voltage and K is a constant accounting for complex issues for this simple model [53].

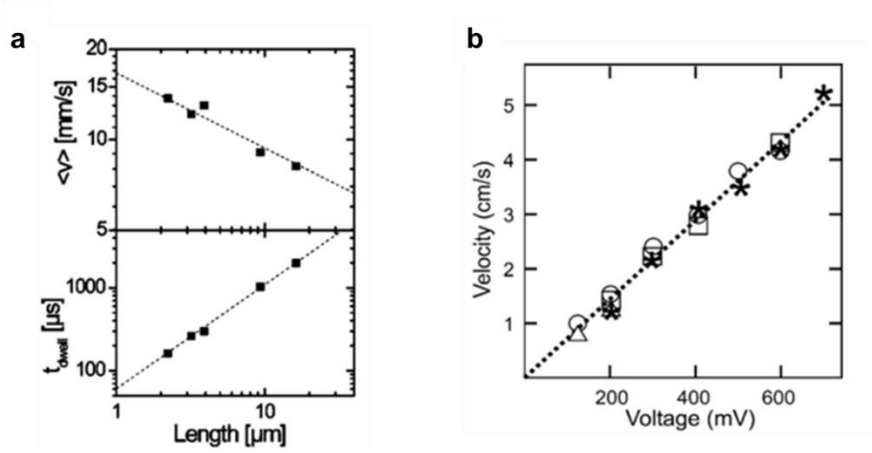

Figure 4.13(a) Dwelling time and translocation speed verse DNA molecule length. (b) DNA translocation speed verse driving voltage. Squares (48.5 kbp), circles (10 kbp), and diamonds (3 kbp) have similar translocation speed, which mean dwelling time is dependent on molecule length.

In summary, for single-file translocation, dwelling time is an important criterion to distinguish DNA molecules with different chain length.

Typical dsDNA translocation speed in solid-state nanopore is 30 bases per microsecond (10 mm/s) [52, 53], which is much faster than that for α-hemolysin pore with a speed of 1 base per microsecond. Therefore, it is necessary to study the factors affecting dwelling time. For solid-state

nanopore, dwelling time can be controlled by adjusting electrolyte viscosity as demonstrated in Ref. 53.

4.2 Experiments

Surface charge density of nanopore walls plays a critical role in DNA translocation in nanopore-based sensing platforms. This section studied the effect of surface charge density on the capture of double-stranded (ds) DNA molecules into a polymer in-plane nanopore numerically and experimentally. For negatively charged DNA and nanopore walls, electrophoretic driving force (F_{EP}) under an electric field is opposed by the viscous drag force by electroosmotic flow (F_{EOF}). Focus was given on the capture stage from the nanopore mouth into the nanopore by placing a rod-like DNA at the nanopore mouth rather than inside the nanopore. As the surface charge density of the nanopore wall becomes more negative, F_{EOF} exceeds F_{EP} beyond a threshold surface charge density, $\sigma_{threshold}$, where DNA molecules cannot be driven through the nanopore via electrophoretic motion. We first simulated the effective driving force (F_{eff}) for the translocation of a dsDNA through an in-plane nanopore with different sizes and surface charge densities.

$$F_{eff} = F_{EP} - F_{EOF} \tag{25}$$

Simulation results were then validated by λ-DNA translocation experiments performed in nanopore devices having different surface charge density values.

4.2.1 Effective driving force simulation

As shown in Figure 4.14, a 2-D axisymmetric dimensional model was built in COMSOL 5.0 (COMSOL, Inc.) to investigate the effect of surface charge density on F_{eff} for DNA translocation [29, 54]. We assume that a dsDNA is partially pre-stretched by a nanopillar array and reaches the nanopore mouth. Thus, the DNA molecule can be modeled as a 2 nm diameter cylinder. Since the electric field is strong near nanopore mouth, the end of the cylinder near the

nanopore makes a major contribution to F_{eff} [35]. In our model, we placed a 30 nm long cylinder (which is shorter than dsDNA persistence length, 50 nm) with no velocity in front of the nanopore to calculate F_{EOF} and F_{EP}. F_{eff} was obtained by Equation 4.25. For the negatively charged DNA, we used the DNA's bare surface charge density of -0.15 C/m^2 (2e per base pair) [38, 40, 55].

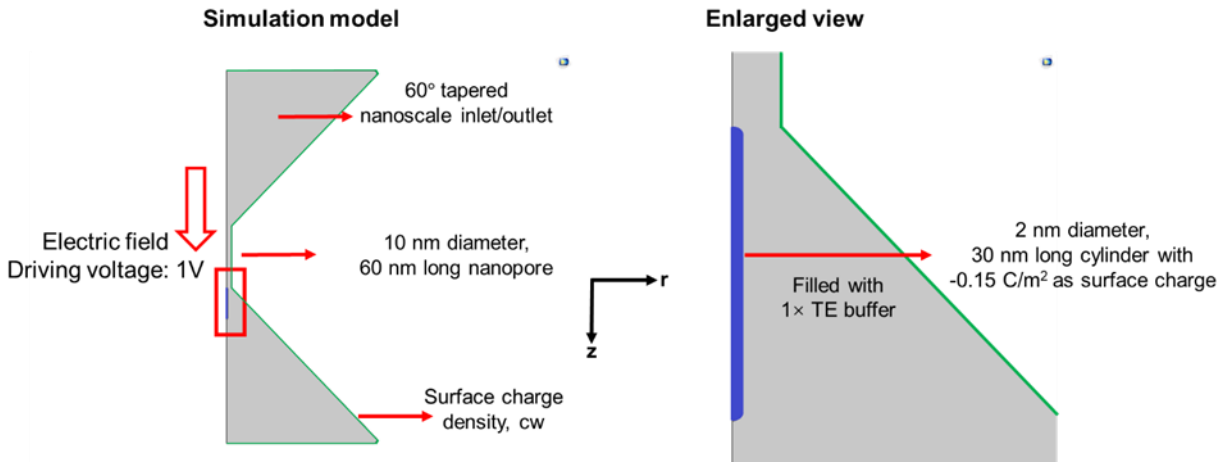

Figure 4.14. COMSOL simulation model. DNA molecule, nanopore wall, tapered inlet/outlet walls are shown in color for illustration.

For most DNA translocation simulation, KCl solution was the common electrolyte [54, 56, 57]. In our experiment, we used 1× TE buffer (Sigma-Aldrich, containing 10 mM Tris-HCl, 1mM EDTA, pH 8.0) as electrolyte for both fluorescence observation and electrical measurement. For COMSOL simulation, therefore, we used 10 mM Tris-HCl concentration as the KCl concentration, making sure that they have the same Debye length (ionic strength). All parameters for COMSOL simulation are shown in Table 4.2.

Table 4.2. COMSOL simulation parameters.

Parameter	Value	Definition
D1	1.95e-9[m^2/s]	Diffusivity of K^+
D2	2.03e-9[m^2/s]	Diffusivity of Cl^-
z1	1	Valence of K^+
z2	-1	Valence of Cl^-
F	96485.3415[C/mol]	Faraday Constant
R0	8.314472[J/K/mol]	Gas Constant
T	300[K]	Temperature
eps0	8.854187817e-12[F/m]	Permittivity of vacuum
eps_r	80	Relative permittivity of fluid
eps_d	3.9	Relative permittivity of nanopore
eta	1.0e-3[Pa*s]	Fluid viscosity
rho	1e3[kg/m^3]	Fluid density
V0	1[V]	Applied voltage
cp	-0.15[C/m^2]	Surface charge density of DNA
cw	-0.076[C/m^2]	Surface charge density of nanopore
c0	10[mol/m^3]	Electrolyte concentration
a	1e-9[m]	DNA radius

4.2.2 Fabrication of polymer in-plane nanopore devices

In order to verify the simulation results, DNA translocation experiments were designed and conducted using polymer nanopore devices with different surface charge densities. Previous studies show that the surface charge density of O_2 plasma treated COC substrates is higher than that of O_2 plasma treated PMMA [58, 59]. Also, poly-ethylene glycol (PEG) is a well-known coating material to suppress EOF on a target surface [60, 61]. Therefore, in this study we chose PEGDA, PMMA and COC as substrates for device fabrication and their fabrication details can be found in chapter 3. For all imprinted substrates, we used O_2 plasma treated COC sheets as cover plate for bonding at 70°C, 1 MPa for 15 min [58]. These hybrid devices are denoted as PEGDA-COC, PMMA-COC and COC-COC, respectively.

4.2.3 Surface charge density measurement

Nanofluidic devices with an array of nanochannels with the width and height of 154 and 203 nm, respectively, were used to measure surface charge density of different polymer substrates.

SEM images of the Si master and imprinted polymer nanochannel substrates used for the surface charge density measurements are shown in Figure 4.15.

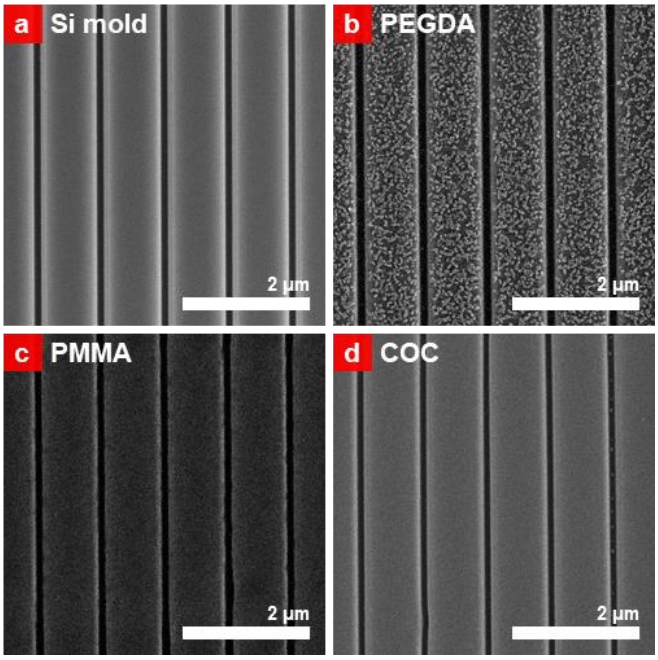

Figure 4.15. SEM images of nanochannel devices for surface charge density calculation and surface charge density calculation results; (a) Si master mold, (b) UV imprinted nanochannels on PEGDA substrate, (c) thermal imprinted nanochannels on PMMA substrate, and (d) thermal imprinted nanochannels on COC substrate.

Conductance through these nanochannel arrays at each KCl concentration was determined by measuring I-V curves using Axopatch 200B (Molecular Devices). The measurement was repeated for different salt concentrations ranging from 10^{-6} M to 1 M. The current-voltage measurements were performed after the baseline current became stable during current-time measurement. 10 devices were measured for each substrate material. At high salt concentration the nanochannel conductance is dependent on the salt concentration while at low salt concentration the conductance is governed by surface charge density on the wall [59, 62, 63]. The effective surface charge density, σ_s^*, of a nanochannel substrate can be obtained from the transition point between these two regimes, c_t, based on Equation 4.26,

$$\sigma_s = \frac{10^3 N_A * e * w * h * 2\mu_{opp} * c_t}{(w+h)(\mu_{K^+} + \mu_{Cl^-})} \quad (26)$$

where μ_{K^+} and μ_{Cl^-} are the ion mobilities of K^+ and Cl^- ions, N_A is Avogadro's number, w, L and h are the nanochannel width, length and height, respectively, μ_{opp} is the mobility of the counterion.

4.2.4 Optical and electrical detection of λ-DNA translocation

Prior to introducing DNA molecules, all devices were filled with 1 M KCl solution (Sigma-Aldrich) containing 1x TE (Sigma-Aldrich), pH 8.0 at room temperature and ionic current (conductance) across the nanopore was measured via Axopatch 200B (Molecular Devices) to make sure that all testing devices have similar pore sizes. The nanopore size was determined by comparing the measured conductance through the nanopore with the simulated conductance for a given nanopore size [5, 22]. The average ionic current prior to introducing DNA molecules was 150 ± 31 nA under 1 V, which equals to 150 ± 31 nS in conductance. The estimated equivalent nanopore diameter was 10.3 ± 3.3 nm (see Figure 3.21).

Then, 1 M KCl solution containing 1x TE was replaced to 1× TE buffer (Sigma-Aldrich) and a solution of 5 ng/μL double-strand λ-DNA (New England BioLabs) stained with YOYO-1 dye (ThermoFisher Scientific) was added to the cis side of the microchannel. Pt electrodes were used to drive DNA molecules with a commercial power supply (BK Precision DC power supply 1735). The DNA movement was observed under a fluorescence microscope (Olympus IX70) with a 100× oil immersion objective (Olympus). Fluorescence images and videos were captured by a CCD camera (Photon Max, Princeton Instruments).

Immediately after fluorescence observation, we used the same nanopore device for electrical detection of DNA translocation by using same 1× TE buffer as electrolyte. In order to reduce the noise level, the device was kept in a homemade Faraday cage during electrical

measurement. Ag/AgCl electrodes were placed in inlet/outlet reservoirs to drive stained DNA molecules. Ionic transient current signal was recorded at a sampling rate of 250 kHz and low-pass filtered at 10 kHz.

4.3 Results and discussion

4.3.1. Effective driving force simulation

DNA molecules can be driven into a nanopore by electrophoretic motion only when the surface charge density of the nanopore wall is less negative than $\sigma_{threshold}$ due to a lower hydrodynamic drag force caused by weaker EOF [37, 38]. $\sigma_{threshold}$ of the nanopore device can be predicted by performing COMSOL simulation on the electrokinetic behavior of a DNA molecule in the nanopore device with different surface charge density values [36, 38]. Our structural model consists of an in-plane nanopore with 10 nm diameter and 60 nm length connected to a tapered inlet and outlet structure. The surface charge density of the entire device wall varied from -20 to -80 mC/m^2. To simulate F_{eff} of a rod-like, double-stranded λ-DNA molecule into an in-plane nanopore, a cylindrical rod with a diameter of 2 nm and the surface charge density of -0.15 C/m^2 [38, 40] was placed at the nanopore mouth. This initial DNA location assumes that one of the DNA chain ends was pre-stretched and approached the nanopore mouth. 1× TE buffer was chosen as electrolyte in consideration of the subsequent fluorescence observation. Figure 4.14 shows the axisymmetric structural model and boundary conditions used for the simulation. It should be noted that this model is similar to the in-plane nanopore structure used for experimental verification. With the model, F_{EP} and F_{EOF} were calculated by solving the coupled Poisson-Nernst-Planck (PNP) equations, which gives F_{eff} from Equation 4.25. Details regarding the simulation model and parameters used can be found in the experimental section and in Table 4.2.

Figure 4.16 shows F_{EOF} and F_{EP} exerting on the DNA molecule surface placed in front of a 10 nm pore as a function of surface charge density of the nanopore wall. It should be reminded that F_{EOF} and F_{EP} correspond to the force in the direction of the nanopore axis. F_{EOF} was obtained by contour integration of $F_{EOF,iz}$ around the DNA contour surface, $F_{EOF} = \oint F_{EOF,iz}$, where $F_{EOF,iz}$ is the hydrodynamic drag force at a given DNA surface. As shown in Figure 4.16(a), F_{EOF} increases as the surface charge density of the nanopore wall becomes more negative. Figure 4.16(b) shows the spatial distribution of the simulated EOF velocity in the direction of the nanopore axis for three representative surface charge density values of -20 mC/m^2, -30 mC/m^2 and -80 mC/m^2, respectively. More negative surface charge density leads to a higher EOF velocity against the electrophoretic motion of the molecule.

On the other hand, as shown in Figure 4.16(c), F_{EP} initially increases, shows a maximum at -30 mC/m^2 and then decreases as the surface charge density value becomes more negative. According to the Coulomb's law, F_{EP} applied on the DNA surface depends on the electric field in the nanopore axis direction (*i.e.* z-axis in simulation model), E_z, by $F_{EP} = \oint qE_z$ around the DNA surface contour. While a constant external voltage of 1 V is applied between top and bottom sides of the nanopore, different surface charges on the device wall modify E_z, leading to a dependence of F_{EP} on the surface charge density. Figure 4.16(d) shows the horizontal distribution of E_z at z = -45 nm, which is 15 nm away from the front end of the DNA molecule. The direction of E_z near the tapered wall was reversed from the direction of the electric field by applied voltage due to the negative surface charge of the wall. The reversed electric field decays with the distance from the tapered wall. As the surface charge density becomes more negative, the magnitude of the reversed E_z near the tapered wall increases, resulting in a reduction of E_z at and near the DNA molecule

and thus F_{EP}. This accounts for the behavior of F_{EP} for the surface charge density ranging from -30 mC/m^2 to -80 mC/m^2.

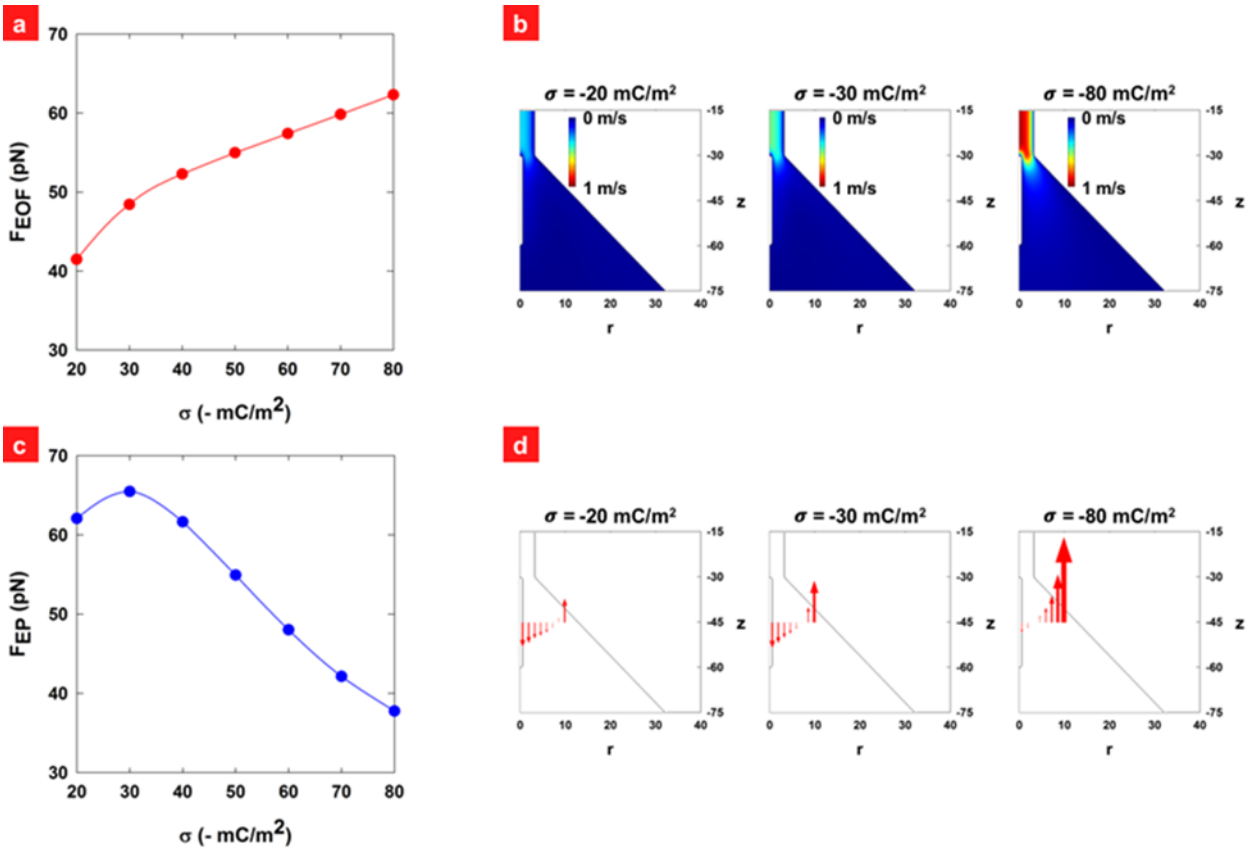

Figure 4.16. (a) F_{EOF} for a rod-like DNA placed at the mouth of a 10 nm diameter nanopore having various surface charge densities; (b) Spatial distribution the simulated EOF velocity in the direction of the nanopore axis for three representative surface charge density values of -20 mC/m^2, -30 mC/m^2 and -80 mC/m^2, respectively; higher surface charge density (absolute value) leads to a higher EOF velocity at or near the DNA molecule. (c) F_{EP} for a rod-like DNA placed at the mouth of a 10 nm diameter nanopore having various surface charge densities; (d) Horizontal distribution of electric field in nanopore axis direction, E_z, at z = -45 nm for three representative surface charge density values of -20 mC/m^2, -30 mC/m^2 and -80 mC/m^2, respectively. Higher surface charge (absolute value) density leads to stronger built up electric field near tapered wall and it has negative effect on E_z at DNA surface.

The behavior of F_{EP} for the surface charge density below -30 mC/m^2 can be explained by enhanced charge exclusion by the enlarged Debye length (or electric double layer) caused by the low surface charge density of the device wall. As shown in Figure 4.17, The nanopore device with more negative surface charge density has a higher number of charge carriers inside the nanopore.

The increased number of charge carriers inside the nanopore results in a decreased nanopore resistance and thus a lower E_z within nanopore, which subsequently leads to a higher E_z outside the nanopore. This explains the behavior of F_{EP} for the surface charge density below -30 mC/m^2.

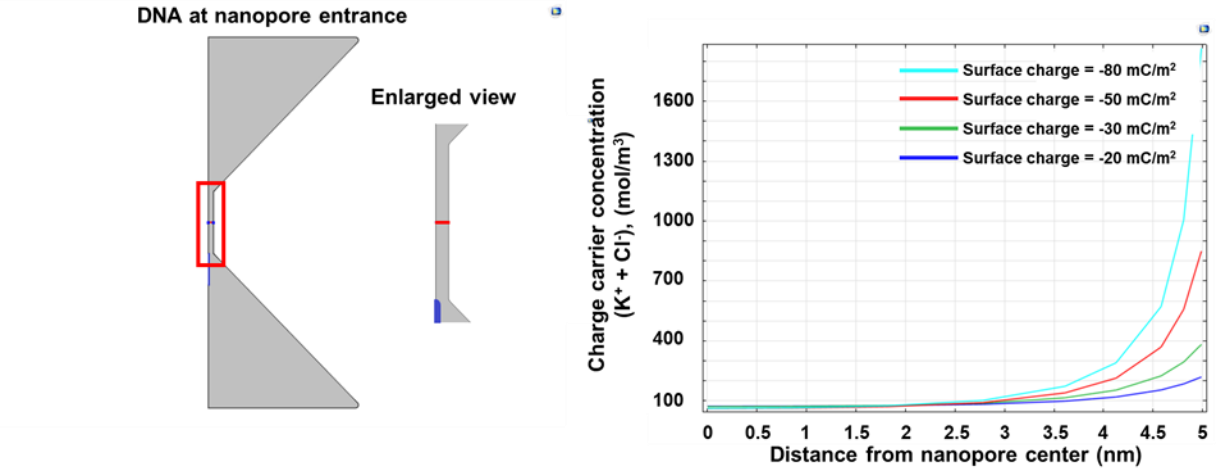

(a) (b)

Figure 4.17. (a) Simulation model with DNA at nanopore entrance; (b) Distribution of charge carriers within the nanopore along the red line indicated in the simulation model (from nanopore center to nanopore wall) for a 10 nm nanopore with -20 mC/m^2 (blue), -30 mC/m^2 (green), -50 mC/m^2 (red) and -80 mC/m^2 (light blue) surface charge density. Nanopore with more negative surface charge density has more charge carriers within nanopore, which leads to a decreased nanopore resistance and thus a lower E_z within the nanopore. This results in an increased E_z at the DNA surface outside the nanopore under the same applied voltage.

Figure 4.18(a) presents F_{eff} obtained from the simulated F_{EP} and F_{EOF} using Equation 4.25 as a function of surface charge density for different nanopore diameters. The solid triangle of Figure 4.18(a) presents F_{eff} for a 10 nm diameter nanopore obtained from Figure 4.16(a) and 4.16(c). Overall, F_{eff} decreases as the surface charge density becomes more negative. Interestingly, the sign of F_{eff} is reversed at a threshold surface charge density of -50 mC/m^2, indicating that the DNA molecule cannot be driven into the nanopore when the surface charge density is more negative than this threshold surface charge density value.

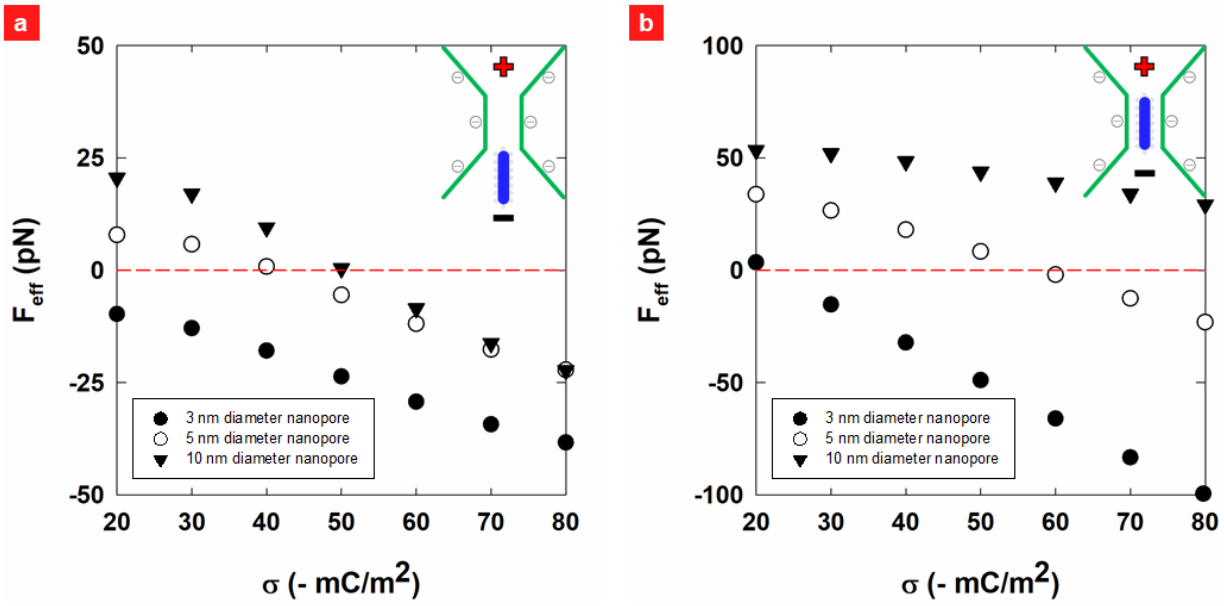

Figure 4.18. (a) F_{eff} for a rod-like DNA placed at the mouth nanopores with different pore sizes and various surface charge densities; (b) F_{eff} for a rod-like DNA placed inside nanopores with different pore sizes and various surface charge densities. Insets indicate DNA location in simulation model.

We further simulated F_{eff} versus surface charge density for different nanopore diameters of 3 nm and 5 nm which is also shown in Figure 4.18(a). For nanopores with the same surface charge density, F_{eff} decreases with decreasing the nanopore size, indicating that it is more difficult to drive the DNA molecule through smaller nanopores by electrophoretic motion. The negative effect of the tapered inlet structure on E_Z and F_{eff} becomes smaller for larger nanopores because the DNA is further away from the tapered wall. $\sigma_{threshold}$ is reduced from -50 mC/m^2 to -41 mC/m^2 as the pore diameter decreases from 10 nm to 5 nm. For the 3 nm pore, F_{eff} is always negative irrespective of the magnitude of the negative surface charge density, indicating that it is not possible to drive the DNA molecule through the pore with any nanopore devices with negative surface charge density (when 1× TE buffer is used).

Our results indicate that the negative effect from the tapered inlet structure on F_{eff} can be reduced with an abrupt inlet structure. Figure 4.19 shows the simulation model of the abrupt inlet

structure, and F_{EP}, F_{EOF} and F_{eff} versus surface charge density for a nanopore of 10 nm diameter. Both E_{EP} and E_{EOF} increase with surface charge density. While F_{eff} decreases with the surface charge density, the F_{eff} values are always positive irrespective of the surface charge density used for the simulation, indicating that DNA molecules reaching at the nanopore mouth are readily introduced into the nanopore. An interesting conclusion can be deduced from the simulation results; a tapered inlet structure built prior to a nanopore or nanochannel has been known to be helpful to reduce the entropic barrier to capture DNA molecules into a nanopore or nanochannel [33, 64, 65]. However, this merit is accompanied by the negative effect of reduced or even inverted F_{eff}. Therefore, this trade-off needs to be considered in the design of nanopore or nanochannel devices to improve the capture of the DNA molecules.

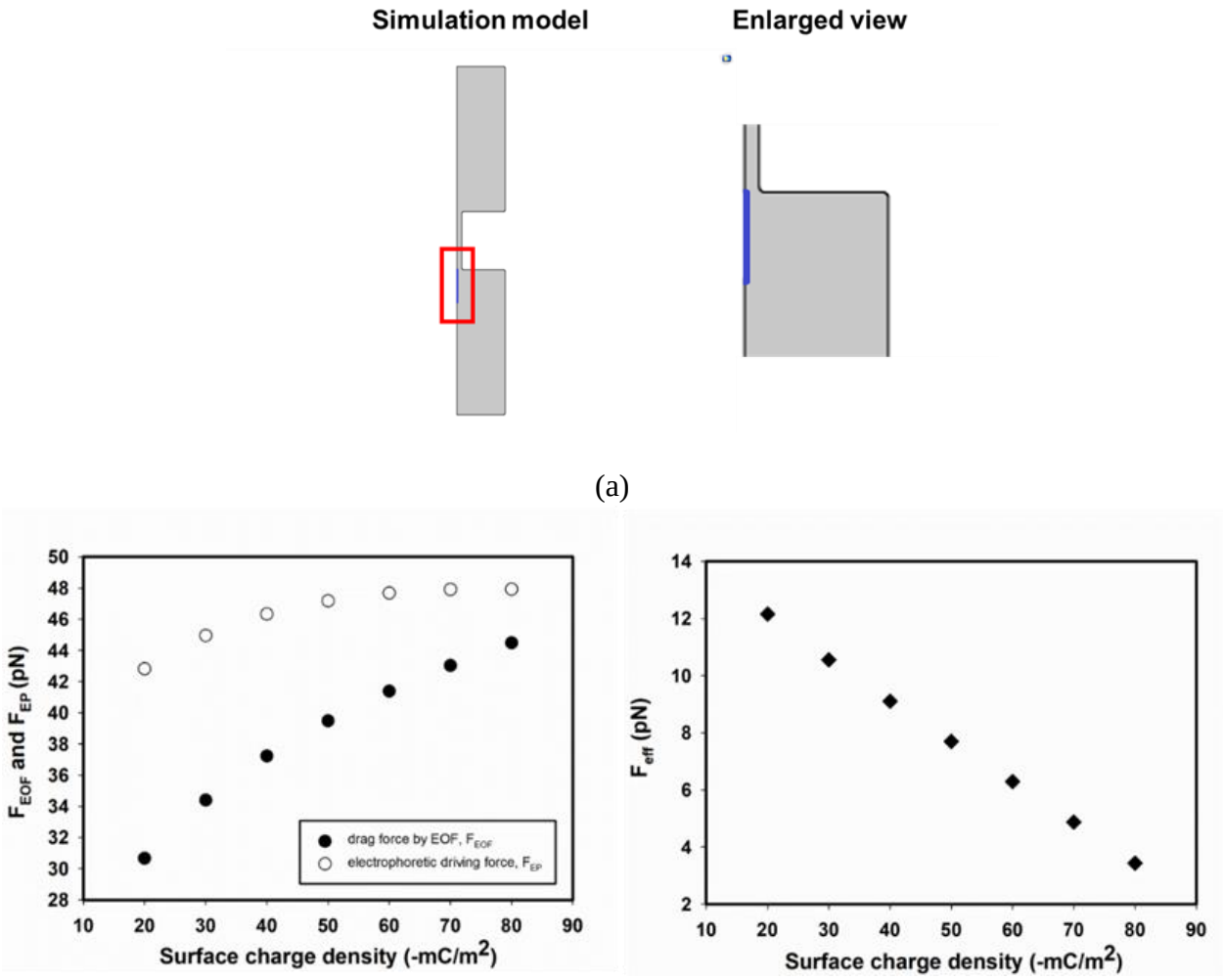

Figure 4.19. (a) COMSOL simulation model of a double-stranded DNA molecule at the nanopore mouth of a nanopore with an abrupt inlet. The DNA molecule is shown in color for illustration; (b) F_{EOF} and F_{EP} are plotted as a function of surface charge density. Unlike the nanopore with a tapered inlet, for an abrupt inlet F_{EP} increases slightly along with surface charge density. This is because of the enhancement of electric field z-axis component at the DNA surface. The number of charge carriers within nanopore increases as surface charge density increases, which leads to the enhancement for electric field z-axis component at DNA surface. F_{EOF} increases along with surface charge density because of stronger EOF. (c) As the difference of F_{EP} and F_{EOF}, F_{eff} decreases as surface charge density (absolute value) increases.

For comparison, we also simulated F_{eff} for a DNA molecule placed inside the nanopore of different diameters as shown in Figure 4.18(b). Similar to the previous case of DNA at nanopore mouth, F_{eff} decreases as the surface charge density becomes more negative and increases along

with the nanopore size. Because of the greater confinement in the nanopore, the contribution of E_Z by external applied voltage becomes larger, thus resulting in an overall increase in F_{eff}. The $\sigma_{threshold}$ values for 3 and 5 nm pores are -22 and -61 mC/m^2, respectively. For the 10 nm pore, F_{eff} show always positive values within the range of the surface charge density values investigated. The results clearly show that the location of the DNA molecule is critical to properly understand the capture behavior of the molecule from the nanopore mouth into the nanopore through the numerical simulation.

4.3.2 Surface charge density measurement

Prior to DNA translocation experiments, surface charge densities of PEGDA-COC, PMMA-COC and COC-COC devices were experimentally determined by measuring conductance through the nanochannel devices for different KCl concentration. When the KCl concentration is greater than 10^{-2} M, measured conductance fits linearly to the theoretical bulk conductance. At lower salt concentration, however, conductance saturates at a value which is dependent on the surface charge density and device geometry. From the transition point on the plot, the effective surface charge density, σ_s , can be calculated through Equation 4.25 [58, 62].

Figure 4.20 shows the nanochannel conductance as a function of salt concentrations for different hybrid devices. The effective surface charge densities obtained from Equation 4.25 were −24.1 mC/m², −51.7 mC/m², and −73.8 mC/m² for PEGDA-COC, PMMA-COC and COC-COC devices, respectively [62]. Surface charge density of O_2 plasma treated PMMA and COC are close to the values reported in the previous studies [58, 66]. It should be reminded that the simulated $\sigma_{threshold}$ of the 10 nm pore was -50 mC/m^2, from which we hypothesize that DNA molecules could only be driven through the nanopore made of PEGDA-COC, not devices made of PMMA-COC and COC-COC.

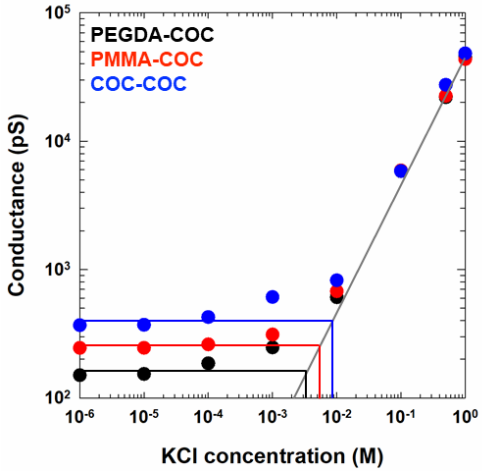

Figure 4.20. Nanochannel conductance for PEGDA-COC, PMMA-COC and COC-COC as a function of salt concentration.

4.3.3 Optical and electrical detection of λ-DNA translocation

In order to verify the surface charge dependent DNA capture behavior in nanopores, we conducted optical observation and electrical measurements for λ-DNA translocation through nanopore devices with tapered inlet/outlet made of different hybrid substrates. We used 1× TE buffer to ensure enough binding strength between YOYO-1 dye and λ-DNA backbones [41, 42]. Figure 4.21 shows fluorescence images when the stained λ-DNA molecules were driven towards the nanopore electrophoretically. For all the devices, fluorescence signals from λ-DNA molecules were seen in the nanopillar array region up the nanopore mouth, indicating that DNA molecules captured from the microchannels were accumulated in the nanopillar array region. However, their translocation behavior through the nanopore was different. For PEGDA-COC device, λ-DNA molecules translocated through the nanopore under bias voltage as low as 100-400 mV, which is similar to driving voltages reported for λ-DNA translocation through vertical nanopores [1, 32, 67]. We also observed that stretched λ-DNA molecules hesitated for a short time prior to entering into the nanopore, similar to a previous report for DNA translocation through an in-plane nanochannel [33]. When applying high driving voltage, this phenomenon became more obvious

as λ-DNA molecules piled up at the nanopore entrance region while the molecule can still enter into the nanopore. For PMMA-COC and COC-COC devices, on the other hand, λ-DNA molecules were stretched by pillar arrays and delivered to the nanopore mouth, but could not enter into the nanopore. We reversed the bias several times and also increased the driving voltage up to 10 V. However, no translocation events were observed while the molecules piled up prior to the nanopore.

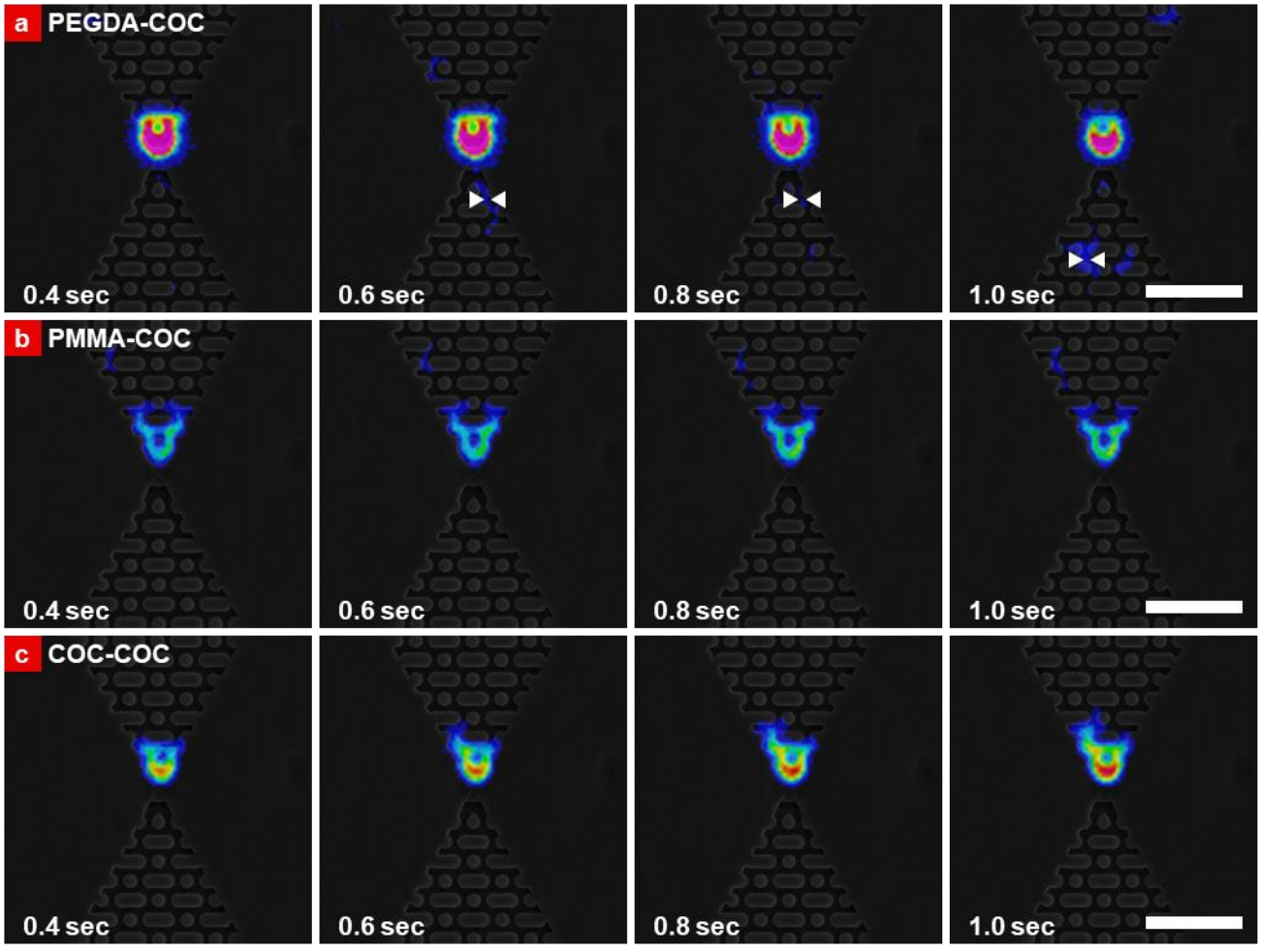

Figure 4.21. Sequential fluorescence images of stained λ-DNA translocation through in-plane single nanopore devices fabricated on (a) PEGDA, (b) PMMA and (c) COC. λ-DNA molecules passed through PEGDA nanopore under bias voltage as low as 100 mV but they could not do through PMMA and COC nanopore even under 10 V. The white arrows in Figure 4.21(a) indicate translocated λ-DNA molecules through PEGDA nanopore. Scale bar, 5 μm in white.

Immediately after fluorescence observation, we used the same nanopore devices for electrical detection of DNA translocation by using same 1× TE buffer as electrolyte. Figure 4.22 (a) shows ionic current traces measured from PEGDA-COC, PMMA-COC and COC-COC devices under a driving voltage of 1 V, which is the maximum value that can be applied with a commercial patch clamp used. Electrical measurement results were in an agreement with the optical observation. Current blockage events from translocated λ-DNA molecules occurred only for PEGDA-COC device, while no current blockage events were observed for PMMA-COC and COC-COC devices. Both the optical and electrical measurements support our hypothesis set based on the simulation results that λ-DNA molecules can be threaded into the in-plane nanopore only when the surface charge density of the device is less negative than $\sigma_{threshold}$. In other words, the simulated $\sigma_{threshold}$ value is the parameter that can be used to determine the translocation of biopolymers in the design of nanopore devices.

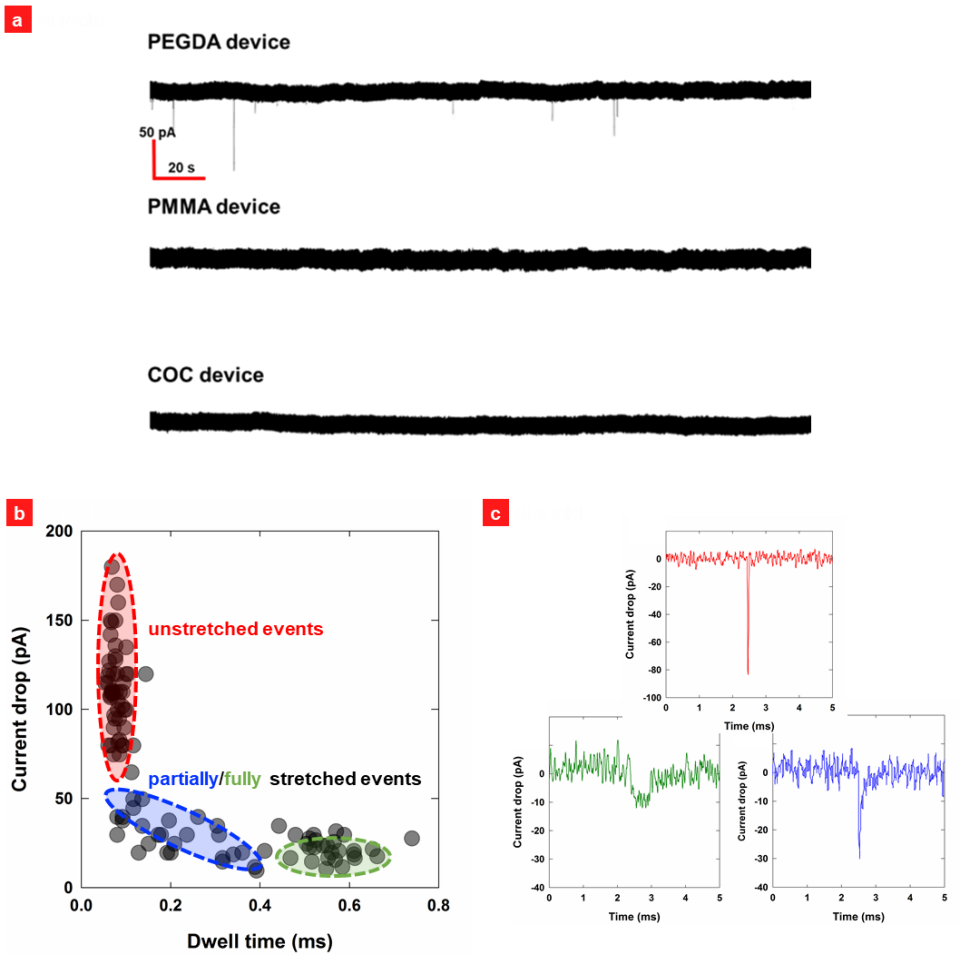

Figure 4.22. (a) Long duration current trace for stained λ-DNA translocation through PEGDA, PMMA and COC based in-plane nanopores; (b) Scatter plot of DNA translocation events in PEGDA device; (c) Typical unstretched, partially stretched and fully stretched current blockade events.

For vertical nanopore membranes, the blockade event of a nanopore by a DNA molecule at low salt concentration usually gives rise to an increased transient current peak due to the enhanced flow of counterions along the DNA molecular chain [5, 68, 69]. In our experiments, despite the use of 1× TE buffer with low salt concentration, all the transient current peaks were downward. The reason of decreased transient current peaks at low salt concentration is still not clear, but such opposite results have been reported for DNA translocation through transverse electrodes [43, 70] and carbon nanotubes [71]. Moreover, the event rate of λ-DNA translocation in PEGDA device was significantly low compared to that for vertical nanopores reported (> 1

event/ 10 s for 5 ng/μl λ-DNA under a 200 mV driving voltage) [2, 14]. Possible explanations for the low event rate maybe thicker EDLs at the DNA molecule and the nanopore surfaces that make DNA translocation more difficult [14, 72, 73].

We further analyzed the current transient peaks from λ-DNA translocation events in PEGDA-COC device. Figure 4.22(b) shows a scattered plot for the current drop and dwell time. Three regimes can be identified: (1) short dwell time regime, (2) short current drop regime, and (3) transition between (1) and (2) regimes. In Figure 4.22(c) is shown a representative current transient peak corresponding to each regime. Different current transient peaks indicate that λ-DNA molecules translocated through the nanopore in different translocation modes, *i.e.* unstretched, partially stretched, and fully stretched, which is similar to λ-DNA translocation observed in vertical solid-state nanopores.[1, 44] Generally speaking, fully stretched translocation events lead to a smaller current drop, longer dwelling time. Partially stretched or unstretched (*e.g.* single local folded, double local folded or fully folded) events show a larger current drop and shorter dwelling time. In addition to high rate fabrication modalities, polymer in-plane nanopores are advantageous in that both optical and electrical measurements can be performed in a single chip and that high throughput manufacturing modalities are readily available. Our results indicate that polymer in-plane nanopores can be an alternative platform to vertical nanopore membranes in obtaining biophysical information of biopolymers.

Since λ-DNA can be more easily translocated through PEGDA-based nanopore, we conducted more DNA translocation experiments using such devices with 1 M KCl as electrolyte. As discussed above, compared with low concentration electrolyte such as 1× TE, 1 M KCl is more ideal for electrical detection of λ-DNA due to thinner EDL and higher conductivity. Figure 4.23 shows simulated F_{eff} for the same model in Figure 4.14 with different concentration KCl as

electrolyte. Higher KCl concentration (ion strength) leads to thinner EDL and therefore less negative effect on F_{EP}, especially for nanopore with higher surface charge density (absolute value).Therefore, adding high concentration salt into buffer system could be one way to facilitate DNA translocation.

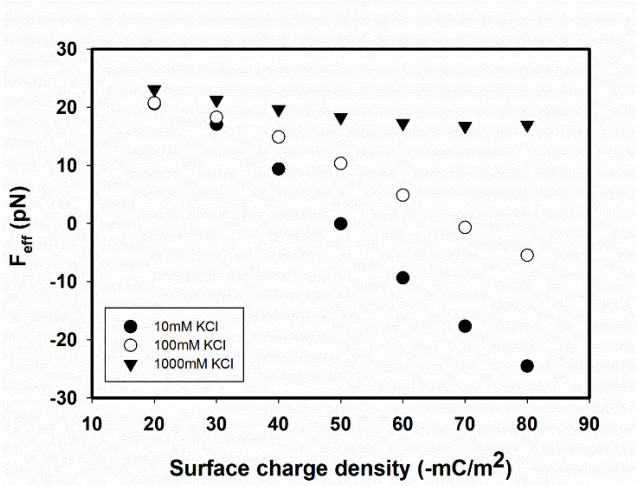

Figure 4.23. Effective driving force simulation for the same model with different concentration KCl as electrolyte.

Figure 4.24 shows current blockade vs. dwelling time for λ-DNA (without fluorescence label) translocation through a 18-nm diameter PEGDA nanopore filled with 1 M KCl under different driving voltages. Similar to the results summarized in section 4.1.2, current blockade decreases along with driving voltage while dwelling time responses in a opposite trend. Moreover, compared with λ-DNA translocation in 1× TE buffer, 1 M KCl leads to a higher event rate due to stronger F_{eff}.

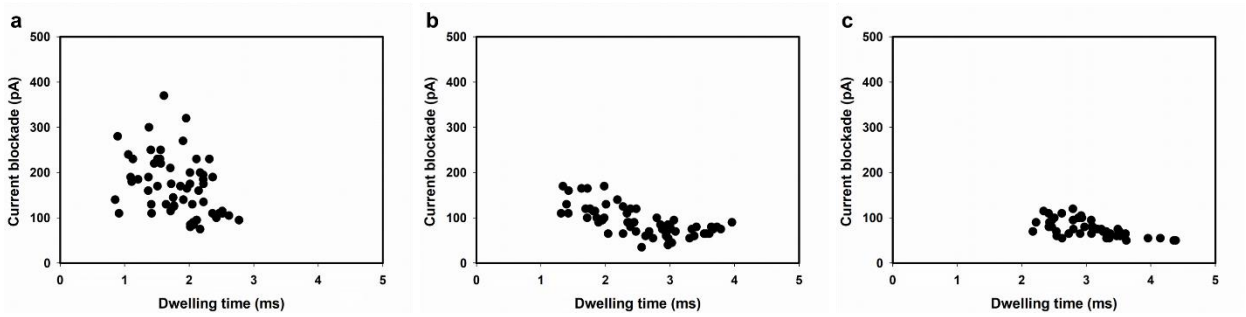

Figure 4.24. Current blockade vs dwelling time plots for λ-DNA translocation through PEGDA nanopore filled with 1 M KCl. (a) 1000 mV. (b) 800 mV. (c) 600 mV.

4.4 Conclusions

The effect of the surface charge density of in-plane nanopore devices with tapered inlet/outlet on the translocation of λ-DNA molecules was studied numerically and experimentally. The simulation results indicate that F_{eff} can be lowered or even reversed when the nanopore device is made of materials with highly negative surface charge, hindering DNA translocation by electrophoretic motion. This effect becomes more significant for smaller nanopores and nanopores with a tapered inlet structure. The simulated $\sigma_{threshold}$ at which the sign of F_{eff} is reversed can be used as an indicator to determine the molecular translocation through nanopore devices, as verified by DNA translocation experiments where devices with the measured surface charge density more negative than the simulated $\sigma_{threshold}$ did not allow translocation of λ-DNA translocation. Compared with PMMA and COC based devices, PEGDA based nanopore fabricated by UV-NIL has the potential to replace Si based solid-state nanopore in the future due to its low surface charge, hydrophilic nature and large-scale fabrication possibility.

4.5 References

1. Storm, A.J., et al., *Fast DNA translocation through a solid-state nanopore.* Nano Letters, 2005. **5**(7): p. 1193-1197.

2. Wanunu, M., et al., *Electrostatic focusing of unlabelled DNA into nanoscale pores using a salt gradient.* Nature nanotechnology, 2010. **5**(2): p. 160-165.

3. Carlsen, A.T., et al., *Selective detection and quantification of modified DNA with solid-state nanopores.* Nano letters, 2014. **14**(10): p. 5488-5492.

4. Mirsaidov, U., et al., *Nanoelectromechanics of methylated DNA in a synthetic nanopore.* Biophysical journal, 2009. **96**(4): p. L32-L34.

5. Smeets, R.M., et al., *Salt dependence of ion transport and DNA translocation through solid-state nanopores.* Nano Lett, 2006. **6**(1): p. 89-95.

6. Fologea, D., et al., *Detecting single stranded DNA with a solid state nanopore.* Nano letters, 2005. **5**(10): p. 1905-1909.

7. Dekker, C., *Solid-state nanopores.* Nat Nanotechnol, 2007. **2**(4): p. 209-15.

8. Wanunu, M., *Nanopores: A journey towards DNA sequencing.* Physics of life reviews, 2012. **9**(2): p. 125-158.

9. Miles, B.N., et al., *Single molecule sensing with solid-state nanopores: novel materials, methods, and applications.* Chemical Society Reviews, 2013. **42**(1): p. 15-28.

10. Levene, M.J., et al., *Zero-mode waveguides for single-molecule analysis at high concentrations.* Science, 2003. **299**(5607): p. 682-686.

11. He, Y., et al., *Gate manipulation of DNA capture into nanopores.* Acs Nano, 2011. **5**(10): p. 8391-8397.

12. Bayley, H., *Nanopore sequencing: from imagination to reality.* Clinical chemistry, 2015. **61**(1): p. 25-31.

13. Wong, C.T. and M. Muthukumar, *Polymer capture by electro-osmotic flow of oppositely charged nanopores.* J Chem Phys, 2007. **126**(16): p. 164903.

14. Chen, P., et al., *Atomic layer deposition to fine-tune the surface properties and diameters of fabricated nanopores.* Nano letters, 2004. **4**(7): p. 1333-1337.

15. Muthukumar, M., *Theory of capture rate in polymer translocation.* The Journal of chemical physics, 2010. **132**(19): p. 05B605.

16. Grosberg, A.Y. and Y. Rabin, *DNA capture into a nanopore: interplay of diffusion and electrohydrodynamics.* The Journal of chemical physics, 2010. **133**(16): p. 10B617.

17. Von Smoluchowski, M., *M. von Smoluchowski, Z. Phys. Chem. 92, 129 (1917).* Z. Phys. Chem., 1917. **92**: p. 129.

18. De Gennes, P., *Coil-stretch transition of dilute flexible polymers under ultrahigh velocity gradients.* The Journal of Chemical Physics, 1974. **60**(12): p. 5030-5042.

19. Doi, M. and S.F. Edwards, *The theory of polymer dynamics*. Vol. 73. 1988: oxford university press.

20. He, Y., et al., *DNA capture in nanopores for genome sequencing: challenges and opportunities.* Journal of Materials Chemistry, 2012. **22**(27): p. 13423-13427.

21. Hall, J.E., *Access resistance of a small circular pore.* The Journal of general physiology, 1975. **66**(4): p. 531-532.

22. Kowalczyk, S.W., et al., *Modeling the conductance and DNA blockade of solid-state nanopores.* Nanotechnology, 2011. **22**(31): p. 315101.

23. Venkatesan, B.M., et al., *DNA sensing using nanocrystalline surface-enhanced Al2O3 nanopore sensors.* Advanced functional materials, 2010. **20**(8): p. 1266-1275.

24. Maitra, R.D., J. Kim, and W.B. Dunbar, *Recent advances in nanopore sequencing.* Electrophoresis, 2012. **33**(23): p. 3418-3428.

25. Luan, B., G. Stolovitzky, and G. Martyna, *Slowing and controlling the translocation of DNA in a solid-state nanopore.* Nanoscale, 2012. **4**(4): p. 1068-1077.

26. Maglia, G., et al., *Enhanced translocation of single DNA molecules through alpha-hemolysin nanopores by manipulation of internal charge.* Proc Natl Acad Sci U S A, 2008. **105**(50): p. 19720-5.

27. Butler, T.Z., et al., *Single-molecule DNA detection with an engineered MspA protein nanopore.* Proc Natl Acad Sci U S A, 2008. **105**(52): p. 20647-52.

28. Wong, C.T.A. and M. Muthukumar, *Polymer capture by electro-osmotic flow of oppositely charged nanopores.* The Journal of chemical physics, 2007. **126**(16): p. 164903.

29. Ai, Y., et al., *Field effect regulation of DNA translocation through a nanopore.* Analytical chemistry, 2010. **82**(19): p. 8217-8225.

30. Paik, K.-H., et al., *Control of DNA capture by nanofluidic transistors.* ACS nano, 2012. **6**(8): p. 6767-6775.

31. Kumar, R. and M. Muthukumar, *Origin of translocation barriers for polyelectrolyte chains.* The Journal of chemical physics, 2009. **131**(19): p. 11B610.

32. Zhang, J. and B. Shklovskii, *Effective charge and free energy of DNA inside an ion channel.* Physical Review E, 2007. **75**(2): p. 021906.

33. Zhou, J., et al., *Enhanced nanochannel translocation and localization of genomic DNA molecules using three-dimensional nanofunnels.* Nature communications, 2017. **8**(1): p. 807.

34. Muthukumar, M., *Polymer escape through a nanopore.* The Journal of chemical physics, 2003. **118**(11): p. 5174-5184.

35. Chen, L. and A. Conlisk, *Forces affecting double-stranded DNA translocation through synthetic nanopores.* Biomedical microdevices, 2011. **13**(2): p. 403-414.

36. Keyser, U.F., et al., *Direct force measurements on DNA in a solid-state nanopore.* Nature Physics, 2006. **2**(7): p. 473.

37. van Dorp, S., et al., *Origin of the electrophoretic force on DNA in solid-state nanopores.* Nature Physics, 2009. **5**(5): p. 347-351.

38. Chen, L. and A. Conlisk. *Modeling of DNA Translocation in Nanopores*. in *47th AIAA Aerospace Sciences Meeting including The New Horizons Forum and Aerospace Exposition*. 2009.

39. Ghosal, S., *Electrokinetic-flow-induced viscous drag on a tethered DNA inside a nanopore.* Physical Review E, 2007. **76**(6): p. 061916.

40. Luan, B. and A. Aksimentiev, *Electro-osmotic screening of the DNA charge in a nanopore.* Physical Review E, 2008. **78**(2): p. 021912.

41. Günther, K., M. Mertig, and R. Seidel, *Mechanical and structural properties of YOYO-1 complexed DNA.* Nucleic acids research, 2010. **38**(19): p. 6526-6532.

42. Larsson, A., C. Carlsson, and M. Jonsson, *Characterization of the binding of YO to [poly (dA‐dT)] 2 and [poly (dG‐dC)] 2, and of the fluorescent properties of YO and YOYO complexed with the polynucleotides and double‐stranded DNA.* Biopolymers, 1995. **36**(2): p. 153-167.

43. Menard, L.D., et al., *A device for performing lateral conductance measurements on individual double-stranded DNA molecules.* ACS nano, 2012. **6**(10): p. 9087-9094.

44. Chen, P., et al., *Probing single DNA molecule transport using fabricated nanopores.* Nano letters, 2004. **4**(11): p. 2293-2298.

45. Astier, Y., O. Braha, and H. Bayley, *Toward single molecule DNA sequencing: direct identification of ribonucleoside and deoxyribonucleoside 5 '-monophosphates by using an engineered protein nanopore equipped with a molecular adapter.* Journal of the American Chemical Society, 2006. **128**(5): p. 1705-1710.

46. Clarke, J., et al., *Continuous base identification for single-molecule nanopore DNA sequencing.* Nat Nanotechnol, 2009. **4**(4): p. 265-70.

47. Feng, J., et al., *Identification of single nucleotides in MoS2 nanopores.* Nat Nanotechnol, 2015. **10**(12): p. 1070-6.

48. Fuller, C.W., et al., *Real-time single-molecule electronic DNA sequencing by synthesis using polymer-tagged nucleotides on a nanopore array.* Proceedings of the National Academy of Sciences, 2016. **113**(19): p. 5233-5238.

49. Hille, B., *Pharmacological modifications of the sodium channels of frog nerve.* The Journal of general physiology, 1968. **51**(2): p. 199-219.

50. Hille, B., *Ionic channels in nerve membranes.* Progress in biophysics and molecular biology, 1970. **21**: p. 1-32.

51. Li, J. and D.S. Talaga, *The distribution of DNA translocation times in solid-state nanopores.* J Phys Condens Matter, 2010. **22**(45): p. 454129.

52. Storm, A.J., et al., *Translocation of double-strand DNA through a silicon oxide nanopore.* Physical review E, 2005. **71**(5): p. 051903.

53. Fologea, D., et al., *Slowing DNA translocation in a solid-state nanopore.* Nano letters, 2005. **5**(9): p. 1734-1737.

54. Movahed, S. and D. Li, *Electrokinetic transport through nanochannels.* Electrophoresis, 2011. **32**(11): p. 1259-1267.

55. Grosberg, A.Y., T. Nguyen, and B. Shklovskii, *Colloquium: the physics of charge inversion in chemical and biological systems.* Reviews of modern physics, 2002. **74**(2): p. 329.

56. Movahed, S. and D. Li, *Electrokinetic motion of a rectangular nanoparticle in a nanochannel.* Journal of Nanoparticle Research, 2012. **14**(8): p. 1-15.

57. Liu, H., S. Qian, and H.H. Bau, *The effect of translocating cylindrical particles on the ionic current through a nanopore.* Biophysical journal, 2007. **92**(4): p. 1164-1177.

58. Uba, F.I., et al., *High process yield rates of thermoplastic nanofluidic devices using a hybrid thermal assembly technique.* Lab on a Chip, 2015. **15**(4): p. 1038-1049.

59. Uba, F.I., et al., *Surface charge, electroosmotic flow and DNA extension in chemically modified thermoplastic nanoslits and nanochannels.* Analyst, 2015. **140**(1): p. 113-26.

60. Stiufiuc, R., et al., *One-step synthesis of PEGylated gold nanoparticles with tunable surface charge.* Journal of Nanomaterials, 2013. **2013**: p. 88.

61. Lee, C.S., W.C. Blanchard, and C.T. Wu, *Direct control of the electroosmosis in capillary zone electrophoresis by using an external electric field.* Analytical Chemistry, 1990. **62**(14): p. 1550-1552.

62. Schoch, R.B. and P. Renaud, *Ion transport through nanoslits dominated by the effective surface charge.* Applied Physics Letters, 2005. **86**(25): p. 253111.

63. Stein, D., M. Kruithof, and C. Dekker, *Surface-charge-governed ion transport in nanofluidic channels.* Phys Rev Lett, 2004. **93**(3): p. 035901.

64. Wu, J., et al., *Complete plastic nanofluidic devices for DNA analysis via direct imprinting with polymer stamps.* Lab on a Chip, 2011. **11**(17): p. 2984-2989.

65. Cao, H., et al., *Gradient nanostructures for interfacing microfluidics and nanofluidics.* Applied Physics Letters, 2002. **81**(16): p. 3058-3060.

66. ONeil, C.E., et al., *Interrogating Surface Functional Group Heterogeneity of Activated Thermoplastics Using Super-Resolution Fluorescence Microscopy.* Analytical chemistry, 2016. **88**(7): p. 3686-3696.

67. Maglia, G., et al., *Enhanced translocation of single DNA molecules through α-hemolysin nanopores by manipulation of internal charge.* Proceedings of the National Academy of Sciences, 2008. **105**(50): p. 19720-19725.

68. Kowalczyk, S. and C. Dekker, *Measurement of the docking time of a DNA molecule onto a solid-state nanopore.* Nano Letters, 2012. **12**(8): p. 4159-4163.

69. Heng, J., et al., *Sizing DNA using a nanometer-diameter pore.* Biophysical Journal, 2004. **87**(4): p. 2905-2911.

70. Liang, X. and S.Y. Chou, *Nanogap detector inside nanofluidic channel for fast real-time label-free DNA analysis.* Nano letters, 2008. **8**(5): p. 1472-1476.

71. Liu, H., et al., *Translocation of single-stranded DNA through single-walled carbon nanotubes.* Science, 2010. **327**(5961): p. 64-67.

72. Zhou, K., M.L. Kovarik, and S.C. Jacobson, *Surface-charge induced ion depletion and sample stacking near single nanopores in microfluidic devices.* Journal of the American Chemical Society, 2008. **130**(27): p. 8614-8616.

73. Schoch, R.B., H. Van Lintel, and P. Renaud, *Effect of the surface charge on ion transport through nanoslits.* Physics of Fluids, 2005. **17**(10): p. 100604.

Chapter 5. Discrimination of dNMPs Through Polymer Dual-Nanopore

Since our final goal is to discriminate single nucleotides cleaved from dsDNA, after demonstrating single molecule detection ability of polymer in-plane nanopores, focus is given on the discrimination of mononucleotides by ToF measurement through polymer dual-nanopore devices. First, previous studies of mononucleotides detection via biological/solid-state nanopores and biomolecules sensing by dual-nanopore devices are summarized. Then mononucleotides discrimination was conducted using PEGDA dual-nanopore devices with various experimental conditions (including buffer pH, flight tube length and driving voltage), aiming to optimize discrimination resolution.

5.1 Introduction: Mononucleotides detection via biological/solid-state nanopores and biomolecules sensing by dual-nanopores

5.1.1 Mononucleotides detection via biological/solid-state nanopores

Mononucleotides identification was first explored for exonuclease-based DNA sequencing via biological nanopores by Bayley et al. in 2006 [1]. Physical properties of dNMPs are summarized in Table 5.1. Discrimination of four 2′- deoxyribonucleoside 5′-monophosphates (dNMP) was demonstrated by a mutant αHL nanopore with a positively charged transient adapter (cyclodextrin). The adapter can reduce the size of mutant nanopore further and at the same time assist dNMPs capture [1, 2]. dNMP translocation was conducted under 130 mV in 25 mM Tris·HCl, 1 M KCl, pH 8.0 at 22.5 °C [1]. As shown in Figure 5.1(a) and (b), the amplitudes of current blockade due to four dNMPs are in a decreasing order of dGMP> dTMP> dAMP > dCMP. Though the results from this work is promising, there are some problems preventing this method from real application: (1) the adapter was not covalently attached to nanopore; (2) the resolution of bases was not sufficient enough; and (3) the experimental conditions were not optimal for exonuclease activity (for example, salt concentration and temperature). In their later work published in 2009,

Bayley et al. presented dNMPs discrimination by mutant αHL nanopore with covalently attached adapter under various experimental conditions. Current blockade events were detected and analyzed using both individual nucleotides and mixture of nucleotides. As shown in Figure 5.1(c) and (d), residual current values for four dNMPs are in the same trend as their previous work but with more difference. Base-calling accuracy for four dNMPs and even DNA methylation (5-methylcytosine, m^5C) is as high as 99% (in 800 mM KCl). Dwell time for each dNMP was also reported and long dwell time was observed for dNMPs due to binding with adapter, especially for dTMP.

Table 5.1. Physical properties of dNMPs. Size of nucleotides (V_N) and DNA bases (V_B) in $Å^3$ and surface area of nucleotide (A_N) and DNA bases (A_B) in $Å^2$.

Base	MW (Da)	V_N (A_N) [3]	V_B (A_B)	Net charge at pH 8.3 [4]	Net charge at pH 10.3
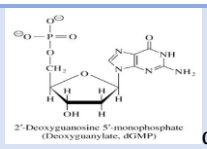 dGMP	347.3	359 (351)	168 (177)	-3	-4
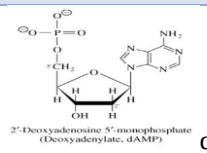 dAMP	331.2	349 (340)	157 (166)	-3	-3
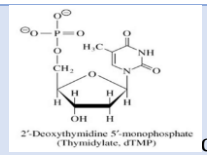 dTMP	322.2	339 (331)	150 (163)	-3	-4
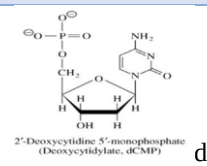 dCMP	307.2	324 (319)	133 (147)	-3	-3

One highlight of this work is that it presented preliminary results of exonuclease-sequencing by engineered mutant biological nanopore with sufficient discrimination accuracy, as illustrated in Figure 5.2. In consideration of the practical scenario for exonuclease-sequencing, several experimental conditions were optimized. For example, a asymmetric salt condition: 200 mM KCl at cis side to promote enzyme activity and 500 mM KCl at trans side to maintain high

conductance for good discrimination. Besides, the optimal driving voltage was studied in order to prevent dNMP's re-entering.

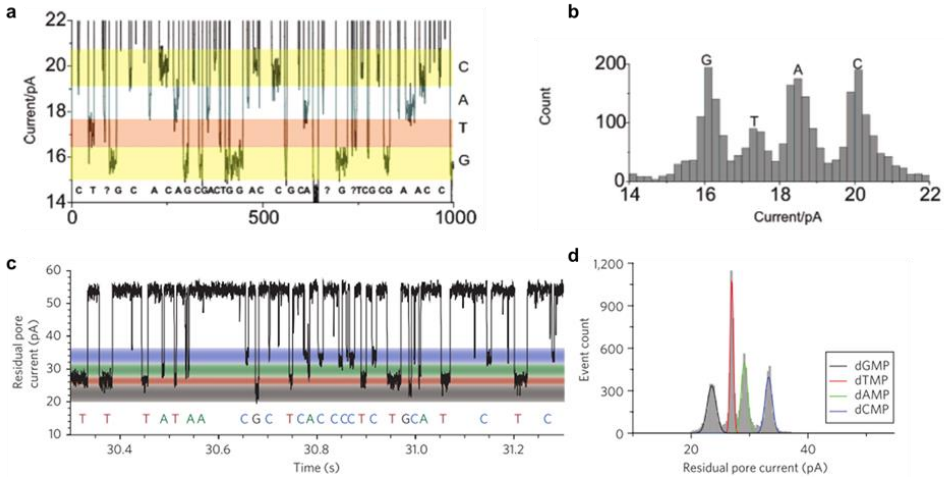

Figure 5.1. Top: mutant αHL nanopore with transient adapter. (a) Current trace for detection of mix dNMPs; (b) Histogram of residual current due to dNMPs translocation. Bottom: mutant αHL nanopore with permanent adapter. (c) Current trace for detection of mix dNMPs; (d) Histogram of residual current due to dNMPs translocation.

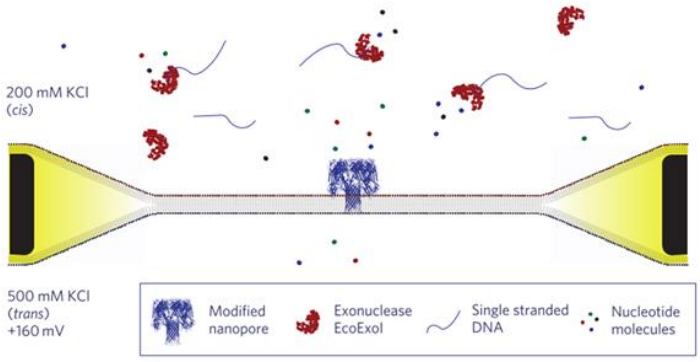

Figure 5.2. Detection of nucleotides cleaved from ssDNA by exonuclease.

Stimulated by biological nanopores, solid-state nanopores have been regarded as an ideal platform for biomolecules sensing due to better stability under various extreme experimental conditions. Biomolecules such as DNA [5], proteins [6], exosomes [7] have been successfully detected by solid-state nanopores, but it is still challenging for solid-state nanopore to achieve single nucleotide resolution for DNA sequencing (both strand-sequencing and exonuclease-

sequencing). Few results have been reported for single nucleotides discrimination by solid-state nanopores. There are two main reasons: (1) temporal resolution, fast translocation speed of nucleotides within solid-state nanopore and (2) spatial resolution, nanopore size variation during fabrication, which affects both signal-to-noise ratio and discrimination accuracy. Here we include three papers of single nucleotides detection by solid-state nanopores: one is by traditional Si_3N_4 nanopore [8], one is by MoS_2 monolayer nanopore [9] and the last one is by nanogap electrode [10].

Fabrication of Si based nanopores has been well developed since 2001 [11] but for a long time the application Si based nanopore was limited to the detection of dsDNA or ssDNA translocation. Recently Chen et al. reported the use of Si_3N_4 nanopore for single nucleotides discrimination [8]. A 1.8 nm-diameter nanopore was produced on 10 nm-thickness low-stress Si_3N_4 by FIB followed by TEM sculpting. For nucleotides sensing, the nanopore was filled with 1 M KCl containing 10 mM Tris-HCl and 1 mM EDTA. Unlike previous studies for DNA sensing, four nucleoside triphosphates (dNTPs) were introduced from trans side (positive electrode side) rather than cis side. Both their experimental results and molecular dynamic (MD) simulation (shown in Figure 5.3) confirmed that the dNTPs translocation were dominated by EOF due to the surface charges on nanopore walls. Compared with biological nanopore with positively charged adapter, the translocation mechanism in negatively solid-state nanopore is much more complicated and has not been well studied. Their work provides insights for solid-state nanopore researchers working on small biomolecules with less surface charges. The current blockades for dNTPs followed the same order of the volume of each nucleotide, i.e., dGTP > dATP > dTTP > dCTP. Besides, the mobility of four dNTPs was studied by comparing their dwell time. Due to strong EOF, the dwelling time for dNTPs can last to hundred microseconds, which is much longer than

translocation speed derived from DNA strand sensing. Interestingly, larger nucleotides were found to have higher mobility due to higher driving force resulting from more surface area exposed to EOF.

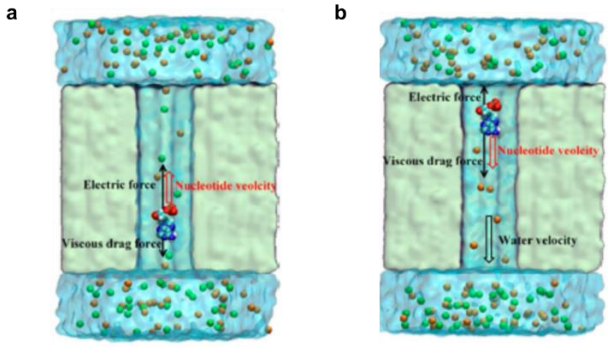

Figure 5.3. MD simulation of forces affecting nucleotides translocation. (a) Nanopore with zero surface charge density, electric force is dominant; (b) Nanopore with surface charge density of -53 mC/m^2, viscous drag force by EOF is dominant.

Compared with thick Si based nanopore, nanopores drilled on monolayers such as graphene[12-14], MoS_2 [15, 16] and boron nitride (BN) [17] have better longitudinal resolution for strand sequencing and provide an alternative way to monitor tunneling current change during biomolecules translocation. Feng et al. reported single nucleotides identification by 2.8 nm diameter MoS_2 nanopores (negatively charged). As illustrated in Figure 5.4(a), a gradient (in both viscosity and concentration) electrolyte system, BmimPF_6/ 2M KCl was used to slow down translocation speed. For example, the dwell time for λ-DNA was increased from 1.4 ms (in 2 M KCl) to 130 ms (in gradient system) without current amplitude reduction. Current blockade for dNMPs was shown in Figure 5.4(b) and it was in good agreement with previous studies by biological nanopores. However it is not easy to distinguish four nucleotides by their dwell time. They also explored the nanopore size effect on the differentiation of nucleotides and they found nanopores larger than 4 nm didn't allow a good differentiation. Their work proved monolayer

nanopores with gradient electrolyte system have the potential to be used for both strand sequencing and exonuclease-sequencing due to high spatial and temporal resolution.

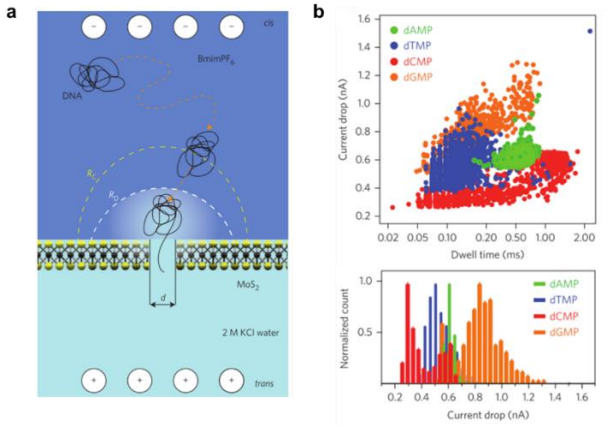

Figure 5.4. (a) Experiment configuration. Cis and trans chamber having gradient electrolyte are separated by MoS_2 nanopore. (b) Scatter plot and histogram of current blockade and dwell time of dNMPs.

As mentioned earlier, dNMPs can be discriminated by tunneling current measurement when translocated through graphene nanopore [13, 18] or nanogap electrode [10, 19]. Kawai et al. demonstrated single nucleotides identification by using gold electrodes with 1 nm inter gap [10]. Such electrodes was fabricated by bending gold nanoscale junctions shown in Figure 5.5(a) in a three-point bending configuration. Dissolved dNMPs were detected when diffused through the nanogap and tunneling current increase was observed during translocation. As presented in Figure 5.5(b), the current change was in a decreasing order of dGMP> dCMP > dTMP (dAMP was not presented due to specific binding to Au electrode). A mixture of dGMP and dTMP in solution can be discriminated by current change histogram as plotted in Figure 5.5(c). Besides, voltage dependent translocation event was also presented for dGMP. Tunneling current change increases along with applied voltage, while dwelling time has minor difference.

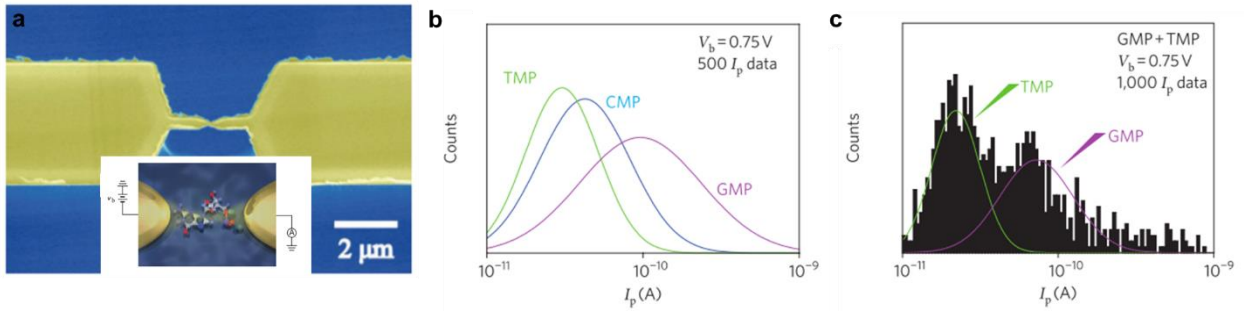

Figure 5.5. (a) Gold nanoscale conjunctions before bending [20]. Inset: schematic of tunneling current measurement of single nucleotide translocated through nanogap electrode in water. (b) Histogram of dNMPs tunneling current under 0.75 V (measured individually). (c) Histogram of current drop of nanogap electrode immersed into a solution containing equimolar amounts of dGMP and dTMP.

Table 5.2 summarizes the results and the critical experimental details of above mentioned methods. In summary, single nucleotides discriminating was well-studied in biological nanopores with high resolution and in consideration of practical application scenario. Solid-state nanopores (including nanogap electrodes) are still under developing: Si based nanopore and nanogap electrodes are suitable for exonuclease-sequencing; while monolayer nanopore can be used for both strand sequencing and exonuclease-sequencing. For solid-state nanopores, more efforts should be made on increasing discrimination resolution, molecule motion control and practical application issues, for example, optimal experimental conditions for enzyme activity.

Table 5.2. Summary of single nucleotides discrimination work.

Sensing modality	Schematic	Pore materials	Experimental conditions	Results
Ionic Current	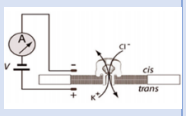	Mutant α-HL with covalently attached adapter [21]	400 mM KCl at pH 7.5; 180 mV, baseline current 54 pA, cis to trans; Individual/mix dNMPs (5 μM) and exonuclease-sequencing demonstrated	$I_G > I_T > I_A > I_C$ $T_T > T_C > T_G > T_A$
	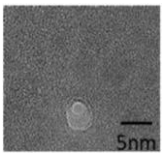	Si_3N_4 nanopore (1.8 nm diameter, 10 nm thick) [8]	1 M KCl at pH 7.5, trans to cis; Individual dNTPs (20 nM)	$I_G > I_A > I_T > I_C$ $T_T > T_C > T_A > T_G$
	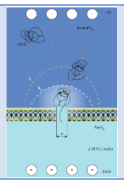	MoS_2 nanopore (2.8 nm diameter) [16]	$BmimPF_6$/ 100 mM KCl at pH 7.5 200 mV cis to tans Individual dNMPs (5 μg ml^{-1})	$I_G > I_A > I_T > I_C$ $T_A > T_G > T_T > T_C$
Tunneling current	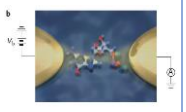	Gold electrodes with 1 nm gap [10]	dNMP dissolved in water, no driving voltage individual dNMPs and mix of dGMP/dCMP (5 μM)	$I_G > I_C > I_T$

5.1.2 Biomolecules sensing by dual-nanopores

Inspierd by biomolecules sensing via single nanopores, stacked nanopores in series were fabricated to provide more biological information and identification accuracy [22-24]. As illustrated in Figure 5.6(a), such structure was first built in Si_3N_4-Si to study the escape time of different analytes from the cavity by fluorescence observation [23]. Later on, the same device was used to study dsDNA mobility by analyzing the time-of-flight (TOF) during DNA translocation [25]. The schematic image in Figure 5.6(b) shows how does the device work: when DNA passed two pores with different sizes, it triggers two signals (paired peaks) with differenr amplitudes, and the time delay between two signals can be used to calculate DNA mobility. Compared with single nanopore experiment, the key issue for dual-nanopore experiment is how to correlate current change signals to paired peaks. As mentioned in their work, the experiment was conducted with

10 kbp dsDNA in low concentration (100 pM) to make sure they could observe isolated paired peaks. For data processing, they first define the maximum TOF (here 75 ms) as the "correlation range" to help assign current change signals to pore 1 and pore 2. Simply put, a moving window (75 ms width) was used identify the paied peaks on current recording trace (details can be found in supplementary information).

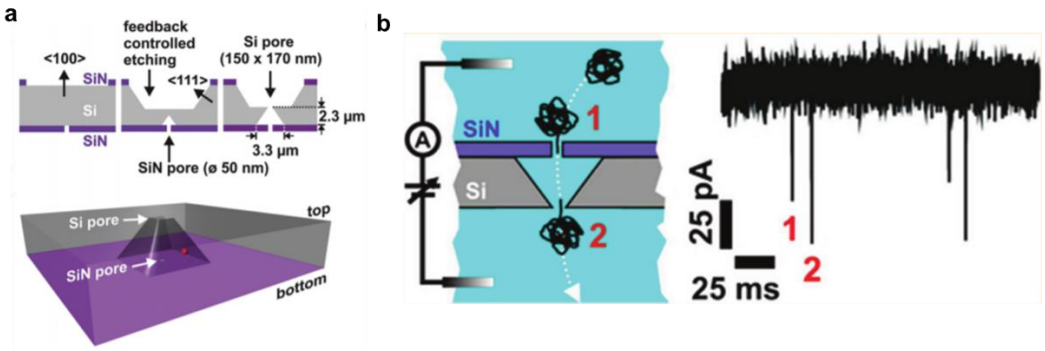

Figure 5.6. (a) How to fabricate stacked nanopores on Si_3N_4 coated Si; (b) How does the pore-cavity-cavity work and examples of paired peaks. Si_3N_4 pore 28 nm diameter, Si nanopore 23 nm by 23 nm. Data collected at pH 8.0 under 300 mV in 1 M KCl.

The same concept was realized by e-beam lithography in the format of in-plane nanopores by Jacobson et al., as shown in Figure 5.7(a). As discussed earlier, in-plane nanopores have several advantages over vertical nanopores, such as easy fabrication and the possibility of simultaneous observation of biomolecule translocation from fluorescence signals and ionic current change signals. Jacobson et al. used Si based in-plane dual-nanopore to detect single virus capsids, and the example of paired peaks is shown in Figure 5.7(b).

All these previous work on single nucleotides discrimination and biomolecules sensing by dual-nanopore devices provide insights for our research on mononucleotides sensing via polymer in-plane dual-nanopore. In the next section, dNMPs discrimination via polymer based dual-nanopore devices will be presented.

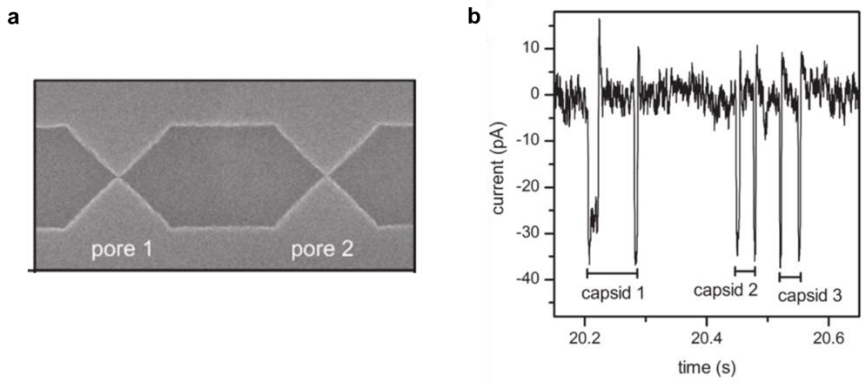

Figure 5.7 (a) SEM image of in-plane dual-nanopore, 50 nm wide, 50 nm deep and 40 nm long. (b) Examples of paired peaks, data was collected at pH 7.5 in 1 M NaCl.

5.2 Experiments

5.2.1 Device design and fabrication

As described in chapter 2 and chapter 3, polymer-based in-plane dual-nanopore devices were fabricated via NIL using UV-resin molds. An example of bitmap used for generating dual-nanopore, a Si master mold milled by FIB and a bonded PEGDA-PEGDA device are shown in Figure 5. 8. As presented in Figure 5.8(a) and (b), the channels connecting nanopores were defined in grey scale color with gradient to reduce the barrier for biomolecule translocation.

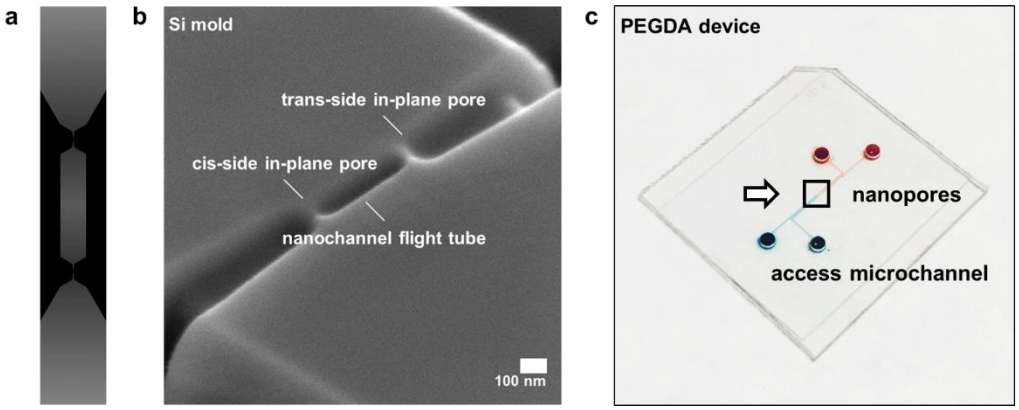

Figure 5.8. (a) Bitmap containing two nanopores with 500 nm flight tube. (b) Si master mold containing dual nanopores milled by FIB using bitmap in Figure 5.8 (a). (c) Bonded PEGDA-PEGDA device with access microchannels highlighted in food color and dual-nanopores indicated in a black box.

PMMA (ePlastics) and COC (COC6013, T_g=142 °C, TOPAS) based devices were imprinted using TPGDA resin molds at 135 °C, 3.5 MPa and 160 °C, 5 MPa for 15 min, respectively. PEGDA (MW = 200, Sigma-Aldrich) based devices were imprinted using MD 700 molds via UV-NIL. Prior to bonding, imprinted PMMA and COC substrates were treated with O_2 plasma under 450 mTorr, 50 W for 30 s to enhance solution wetting and assist bonding. A thin COC cover (COC8007, T_g=70 °C, TOPAS) was used to bond imprinted PMMA and COC at 70 °C, 1 MPa for 15 min. A 125 μm thickness PEGDA coated PMMA sheet was used for PEGDA device bonding at 70 °C, 1 MPa for 7.5 min. Dimensions of nanopore after thermal bonding were examined by coducting ionic current measurement on polymer devices filled with 1 M KCl (Sigma-Aldrich). For dual-nanopore devices with 500 nm flight tube and 1 μm flight tube, a ionic conductance of 50 nA and 40 nA (equal to the conductanc of a 10 nm diatemer nanopore, as shown in Figure 5.9) was applied as a creterion to determine whether a chip is suitable to use.

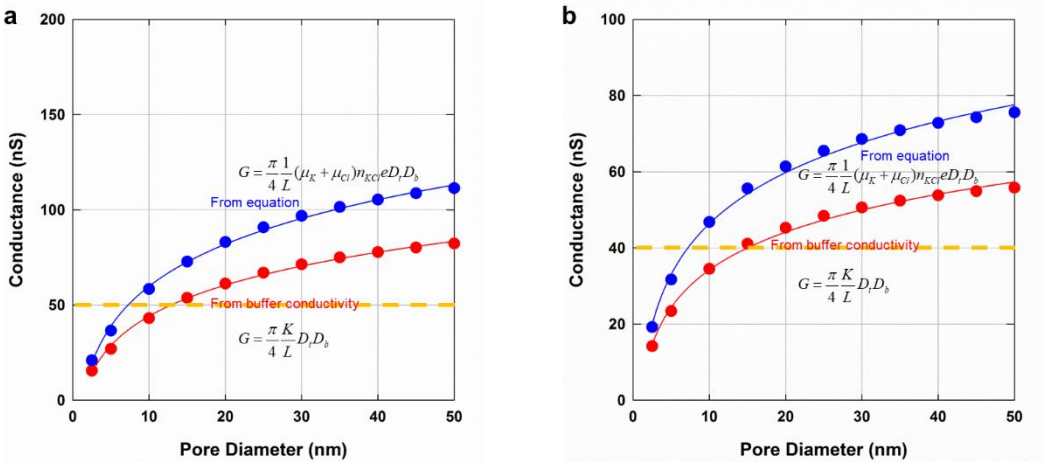

Figure 5.9. Conductance vs. nanopore size plot for dual nanopore size estimation (based on 1 M KCl as electrolyte). (a) Dual-nanopore with 500 nm flight tube; (b) Dual-nanopore with 1 μm flight tube.

5.2.2 Experiment set-up and data analysis

After filling with 1 M KCl, the device was checked under microscope to make sure the device was filled completely with no air bubbles trapped inside microchannels, especially at the

interface between microchannels and funnel inlet structure. In our experiment, we used both commercial patch-clamp, amplifier Axo-patch 200B with digitizer 1440A (Molecular Devices) shown in Figure 5.10 (a) and home-made amplifier (from our collaborator Dr. Collin Mckinney in UNC) with NI DAQ card (NI PXIe-1073, National Instruments) shown in Figure 5.10 (b) for data acquisition. Ionic current was then measured more than 10 min until the baseline current was stable, no any fake peaks were observed and the current reading was below the critical value. dNMP (Sigma-Aldrich) solution with certain concentration was introduced from cis or trans side reservoirs. After collecting enough data for one nucleotide, the device was washed (fill and withdraw by electric pump) with 1 M KCl several times and ionic current was measured more than 10 min to make sure no more peaks from previous nucleotide before introducting a new nucleotide.

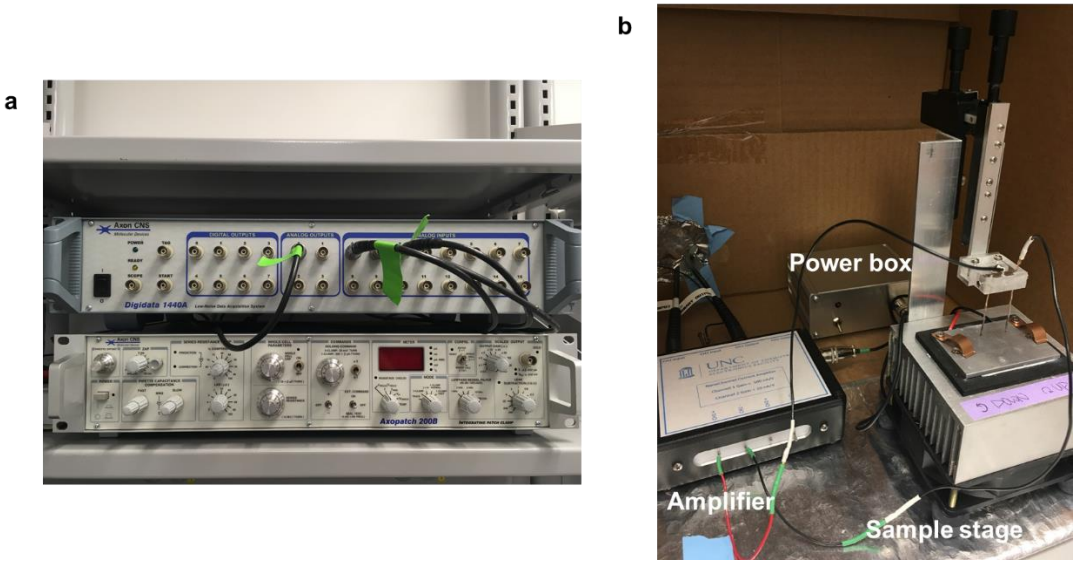

Figure 5.10. (a) Commercial patch-clamp. (b) Home-made patch-clamp by Dr. Collin Mckinney from UNC with sample stage in a home-made Faraday cage.

After collecting the ionic current data (current vs. time trace), we analyzed the data with the similar manner as described in Ref. [25]. The ideal case for ToF measurement is that after one molecule pass both two nanopores, the second molecule starts to approach to the first nanopore. Since we didn't use any enzyme to control the nucleotides feeding rate and even though we tried

to use dNMP solution with low concentration, it is challenging to avoid signal "cross-talk" between two nanopore sensors. Therefore, in this initial developing stage, we only collect ToF data from isolated peaks and we also have an estimated ToF value as "our corrolation range" based on the mobility measured from fluorescence labeled dNMPs in Ref. [4]. For 500 nm flight tube with 1 V as driving voltage, the estimated ToF for dNMPs is around 1 ms (Estimated ToF $= \frac{flight\ tube\ length}{electric\ field * apparent\ mobility} = \frac{500\ nm}{(2\times10^{5}\frac{V}{m})\times2\times10^{-5}\frac{cm^2}{Vs}}$) [4]. Thus we mannually selected pair peaks with time difference (from the end point of the first peak to the start point of the second peak) aroud 1 ms and at the same time there are no any other peaks before and after at least 10 ms (10 times of the estimated ToF) of the selected pairs. As shown in Figure 5.11(a), although peak pairs 1-2, 3-4 seems to be paired and have reasonable time interval, they are not isolated peaks. As for peak pair 5-6, they are isloated from other peaks but their time interval is much greater than the estimated ToF value. In Figure 5.11 (b), first three pairs are well isolated from each other and with reasonable ToF. It can be clearly seen that pair 4 ovelaps with unpaired signals due to poor feeding rate control, therefore in this case we still use its ToF information. For the final device, nucleotides feeding will be controlled by enzyme and ToF data analysis should be done by software. Some ideas for ToF data analyis software design based on above criterion are discussed in chapter 7.

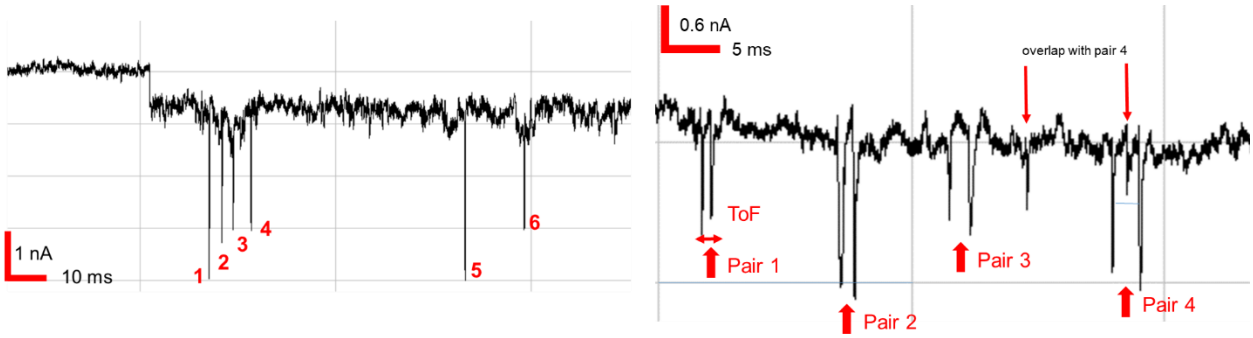

Figure 5.11. Example of paired peaks: (a) Current trace for 10 ng/µl dTMP detected by PEGDA-PEGDA device having 500 nm flight tube filled with 1 M KCl at pH 8.0 under 800 mV (driven by EP, baseline current 20 nA). (b) Current trace for 10 ng/µl dCMP detected by PEGDA-PEGDA

device having 500 nm flight tube filled with 1 M KCl at pH 10.0 under 3 V (driven by EOF, baseline current 11 nA).

5.3 Results and discussion

dNMPs discrimination experiment was initially conducted by using PMMA based devices replicated from Si mold shown in Figure 5.12. Based on SEM and AFM measurement, the nanopore at T side (24 nm in depth) is slightly smaller than the one at C side (25 nm in depth). 0.1 ng/μl dAMP was introduced from C side reservoir and a positive bias voltage ranging from 300 mV to 1000 mV was applied across two pores (C side ground/reference electrode, T side working electrode) as described in previous works [5, 9, 21]. Suprisingly, we have few current peaks detected at various driving voltages but they were all paired peaks. The snapshots of these peak pairs and ToF vs. driving voltage are shown in Figure 5.13. All the paired peaks follow the order of small-big, which conincides with dAMP's moving direction, from cis (smaller pore) to trans (larger pore). Moreover, as driving voltage increases, the ToF deceased due to enhanced electric field within flight tube. For a driving voltage more than 800 mV, we expect a ToF of less than 3 ms and with less variation , which provides hints for ToF values in the future work.

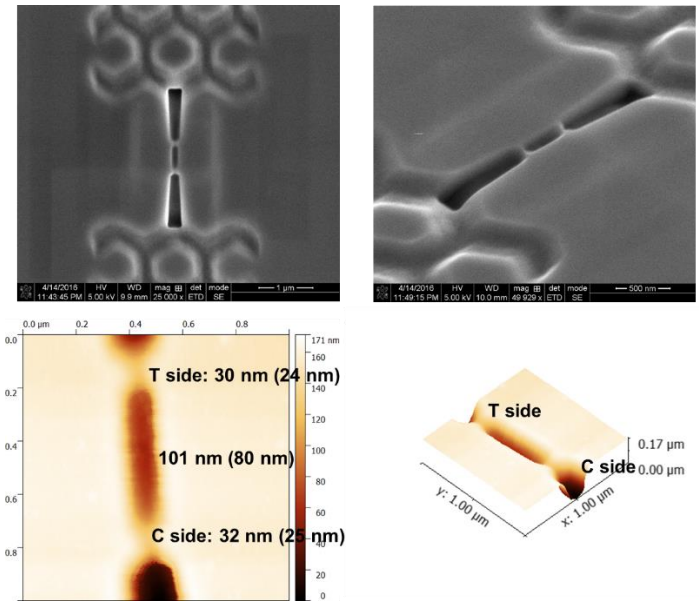

Figure 5.12. Si master mold (April 2nd) for dNMPs discrimination experiments at initial stage. Top: SEM images of Si mold; Bottom: AFM measurement of Si mold: values in brackets were nanopore/nanochannel depth measured by AFM and values outside brackets were measured by SEM. Both confirmed a smaller pore at cis (C) side and a larger pore at trans (T) side.

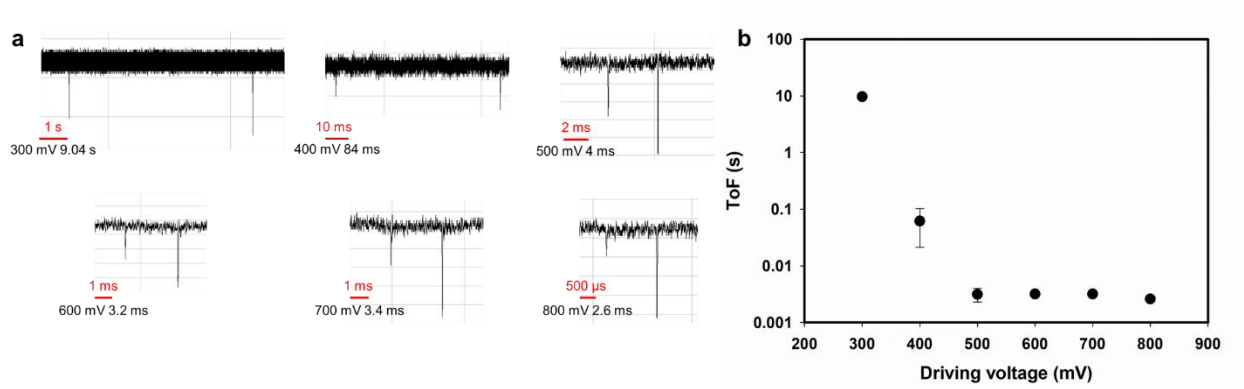

Figure 5.13. (a) Snapshots of paired peaks for dAMP translocation through PMMA based dual-nanopore device having 500 nm flight tube filled with 1 M KCl under various driving voltage. (b) ToF of dAMP vs. driving voltage. Error bars (standard variation) of ToF data at 600 mV, 700 mV and 800 mV were not shown due to limited data.

Initial experiments above proved the feasibility of using polymer dual-nanopore devices for nucleotides discrimination via ToF measurement. However, we couldn't get enough data (sometimes no events) from PMMA based devices after many trials. It was documented in previous

studies that small negatively charged biomolecules such as proteins and nucloetides sometimes can't be driven through negatively charged nanopore electrophoretically due to relatively low effective driving force, F_{eff}, resulting from less charges from shorter biomolecule chain [6, 8]. In order to study the translocation kinetic of nucleotides, we simulated F_{eff} for dsDNA with different length (2 nm, 5 nm, 10 nm, 15 nm, 30 nm) translocation through different size nanopore (3 nm, 5 nm and 10 nm in diameter) having various surface charge density (-20 mC/m^2, -40 mC/m^2 and -60 mC/m^2). dsDNA was choosen because they can be treated as 2 nm-diameter stiff cylinder when its length shorter than its persistence length, 50 nm. The simulation model is similar to the one used in chapter 4 and the biomolecules were located in front of nanopore with no initial velocity. The simulation results are presented in Figure 5.14. For certain nanopore size, F_{eff} decreases as surface charge density increases due to higher viscous drag force from stronger EOF. Moreover, longer biomolecules lead to higher F_{eff} because of more charges on biomolecule surface. In general, F_{eff} decreases as nanopore size decreases, which can be explained by the electric field strength reduction in front of nanopore. Overall, it is hard to drive small nucleotides electrophoretically througn tiny nanopores with high surface charge density, which is in agreement with experimental and MD simulation results from Ref. [8]. For biomolecules driven by electrophoretic motion, a nanopore with low surface charge density is preferred. Therefore, we replaced PMMA based devices with PEGDA based devices in order to assist nucleotides translocation as presented below.

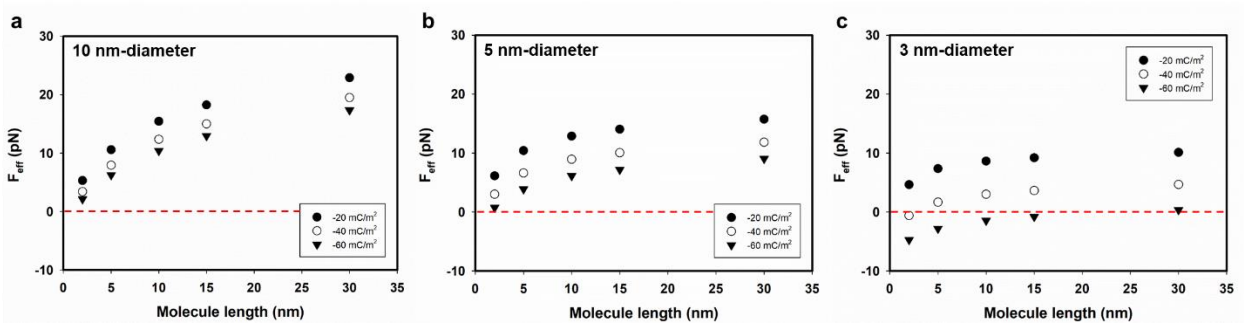

Figure 5.14. F_{eff} simulation for dsDNA with different length translocation through nanopore with different size having various surface charge density. 1 M KCl was used as electrolyte, the same as experimental conditions. (a) 10 nm-diameter nanopore. (b) 5 nm-diameter nanopore. (c) 3 nm-diameter nanopore.

Figure 5.15- Figure 5.17 show 10 ng/ µl dTMP translocation data (current blockade, dwell time and ToF) under different driving voltages through PEGDA based dual-nanopore devices. Compared with PMMA nanopores with higher surface charge density, it is easier to translocate dNMPs through PEGDA nanopores as indicated in Figure 5. 14 (c). Figure 5. 15 and Figure 5.16 show both current drop and dwell time increase with driving voltage. In this case, much more events can be detected (which can be contributed to a higher F_{eff} and a higher nucleotides concentration), therefore paired peaks were manually selected based on the criterion described above. ToF vs. driving voltages for dTMP is plotted in Figure 5.17, ToF of dTMP decrease as driving voltage increases, same as the ToF data of dAMP in Figure 5. 13(b). 1000 mV driving voltage leads to a ToF value less than 2 ms, which is also close to the one of dAMP. Moreover, the standard deviation of ToF reduces as driving voltage increases, which indicates a weakened interaction between dTMP and nanochannel walls. Therefore a slightly higher driving voltage is preferred to achieve high identification accuracy.

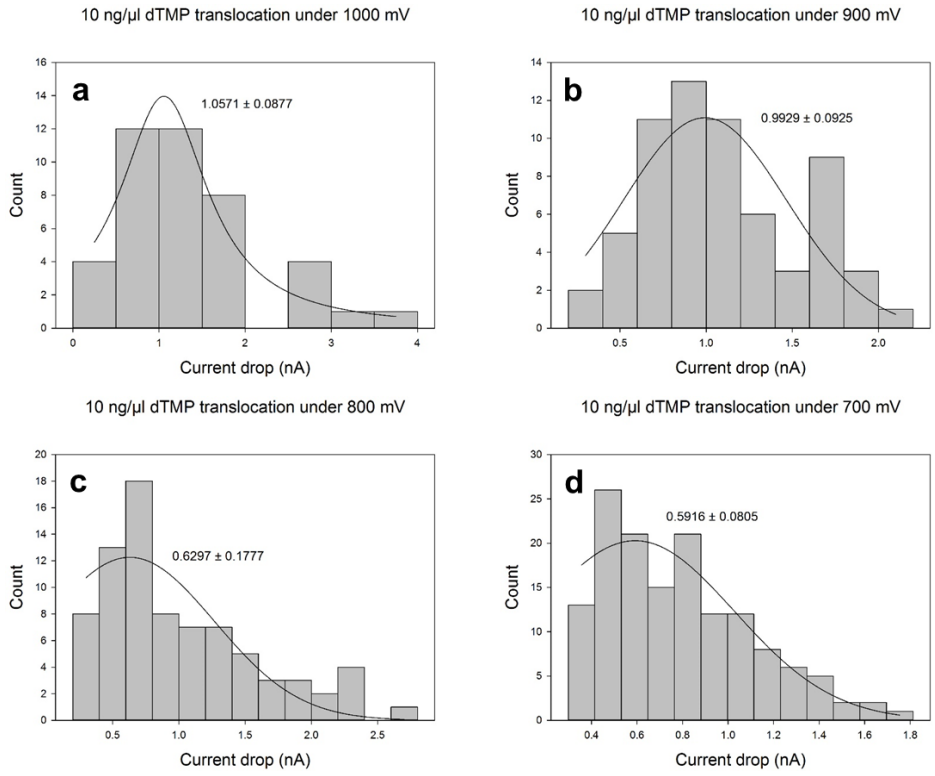

Figure 5.15. Histograms of the current blockade for dTMP transolation through PEGDA dual-nanopore device having 500 nm flight tube filled with 1 M KCl under different driving voltage. Current blockade values are extracted from manually selected paired peaks based on the criterion described above.

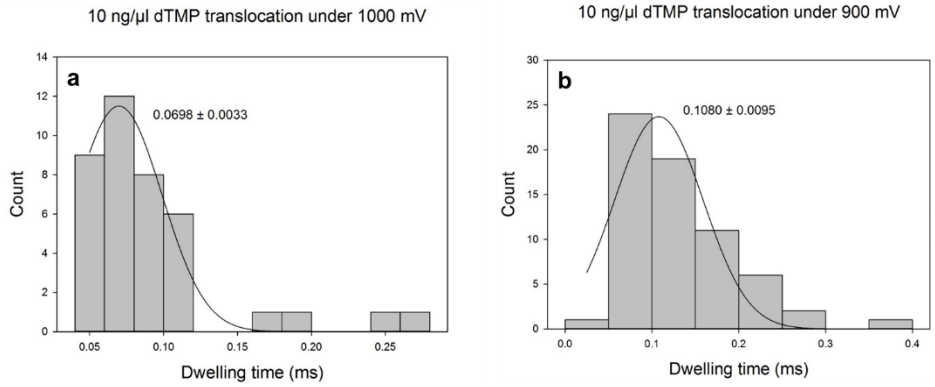

Figure 5.16. Histograms of dwell time for dTMP transolation through PEGDA dual-nanopore device having 500 nm flight tube filled with 1 M KCl under different driving voltage. Dwell time values are extracted from manually selected paired peaks based on the criterion described above. Standard variation of dwell time at 700 mV and 800 mV is high, therefore the histograms of dwell time distribution under 700 mV and 800 mV are shown here.

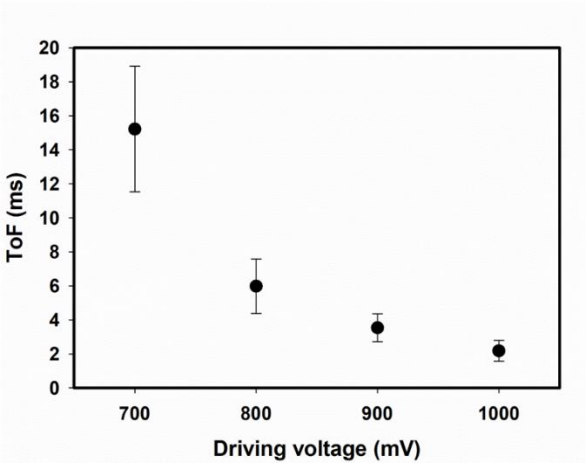

Figure 5.17. ToF vs. driving voltage for dTMP transolation through PEGDA dual-nanopore device having 500 nm flight tube filled with 1 M KCl under different driving voltage.

5.3.1 pH 8.0 vs. pH 10.0

After getting initial dTMP ToF data from PEGDA device, we tried to get ToF information of all dNMPs one after another through the same PEGDA device in order to avoid the variation factor from device fabrication. Same as dTMP translocation experiment, all dNMPs were driven through nanopore electrophoretically. While the electrolyte changed from 1 M KCl only to 1 M KCl containing 1× TE at pH 8.0. As shown in Figure 5.18, the ToF values for dNMPs are slightly smaller than the values shown above for dAMP and dTMP (around 2 ms), which can be attributed to the control of pH and the existence of TE buffer. More importantly, the ToF of dNMPs follows the order of dGMP > dAMP > dCMP > dTMP, which is in agreement with MD simulation except for dCMP and dTMP (smooth wall case) [26]. The slow motion of larger nucleotides in flight tube can be attributed to their larger surface area (higher viscous drag force) and larger mass (smaller acceleration). Besides, the interations between the nucleotides and nanochannel walls could be another reason for the flight time difference. Overall, by examing the ToF of the dNMPs, four nucleotides can be barely dicriminated at pH 8.0 under 1 V. Inspired by the work by O'Neil et al.,

we then tried to use electrolyte with higher pH to increase the resolution and the results are shown in Figure 5.19.

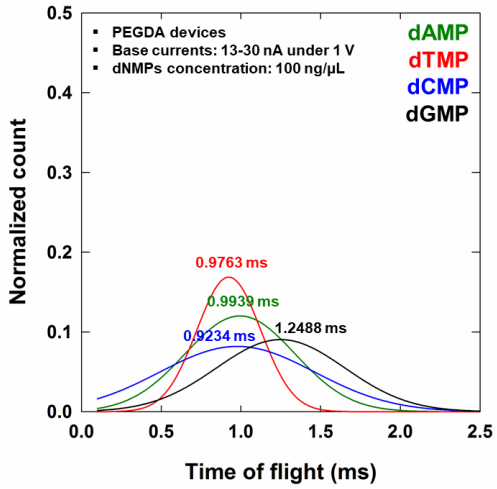

R (Resolution)	dAMP	dTMP	dCMP	dGMP
dAMP	-	0.1006	0.0647	0.0466
dTMP	0.1006	-	0.4490	0.1913
dCMP	0.0647	0.4490	-	0.0160
dGMP	0.0466	0.1913	0.0160	-

Identification Accuracy	
dAMP	-
dTMP	-
dCMP	-
dGMP	-

Figure 5.18. ToF values of dNMPs collecting from the same PEGDA dual-nanopore device having 500 nm flight tube filled with 1 M KCl containing 1× TE at pH 8.0 under 1 V (dNMPs were driven electrophoretically). At this condition, dNMPs can't be distingushed well and therefore identification accuracy was not calculated.

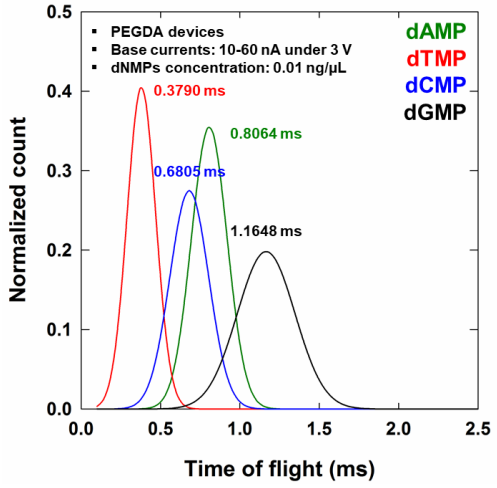

R (Resolution)	dAMP	dTMP	dCMP	dGMP
dAMP	-	1.0537	0.2680	0.6085
dTMP	1.0537	-	0.7101	1.4450
dCMP	0.2680	0.7101	-	0.7965
dGMP	0.6085	1.4450	0.7965	-

Identification Accuracy	
dAMP	35%
dTMP	85%
dCMP	24%
dGMP	78%

Figure 5.19. ToF values of dNMPs collecting from the same PEGDA dual-nanopore device having 500 nm flight tube filled with 1 M KCl containing 0.5× TBE at pH 10.0 under 3 V (dNMPs were driven electroosmotically). Compared with pH 8.0, dNMPs can be distinguished better with an average identification accuracy of 55%.

Interestingly, at pH 10.0 we couldn't detect any events when we tried to drive dNMPs electrophoretically in PEGDA devices as before. However, we can have events deteced when reversing the polarity of electrodes (electric field). This can be explained by the surface charge density enhancement of nanopore/nanochannel wall due to a higher pH. Though PEGDA has relatively low surface charge density, at pH 10.0 the stronger EOF is dominant over electrophoretic motion. Moreover, a higher driving voltage was required for dNMPs translocation at pH 10.0, which can also be attributed to the relatively lower F_{eff} due to stronger EOF. Therefore, we used the home-made patch-calmp system to collect data, which can provide driving voltage up to 9 V. Figure 5.19 shows the ToF data of dNMPs translocation through the same PEGDA device containing dual-nanopore. Though the translocation mechanism is different from pH 8.0, the ToF of dNMPs follows the same decreasing order of dGMP > dAMP > dCMP > dTMP at pH 8.0, which is same as the order of labeled dNMPs mobilitiy measured in nanochannel [4]. In order to explain this phenomenon, we can simply model the nucleotides translocation within nanochannel as linear motion with constant acceleration and no initial velocity (illustrated in Figure 5. 20),

$$\frac{1}{2}a \cdot ToF^2 = L \tag{1}$$

$$F_{eff} = |F_{EP}(E, \sigma_{nucleotide}) - F_{EOF}(E, A, \sigma_{nucleotide}, \sigma_{nanochannel})| = ma \tag{2}$$

$$\text{ToF} = \sqrt{\frac{2Lm}{|F_{EP} - F_{EOF}|}} \tag{3}$$

where a is the constant acceleration, L is flight tube length, E is electric field within nanochannel, $\sigma_{nucleotide}$ and $\sigma_{nanochannel}$ are surface charge density of nucleotide and naochannel, respectively, A is surface area of nucleotide and m is the mass of nucleotide.

Substituting Equation 5.2 to Equation 5.1, we get Equation 5.3, indicating ToF is affected by flight tube length, nucleotide mass, surface charge density of nucleotide and nanochannel wall, electric field inside nanochannel and nucleotide surface area. At pH 10.0, F_{EOF} is dominant over F_{EP}, however dGMP as the nucleotide with larger surface area has the longest travel time, which can be explained by its higher drag force F_{EP} by higher net charge and a larger mass value. In fact, the translocation process is quite complicated, therefore more study is required to explore the factors affecting nucleotides mobility within nanochannel. Overall, the average identification accuracy of dNMPs is 55%, much better than the results at pH 8.0.

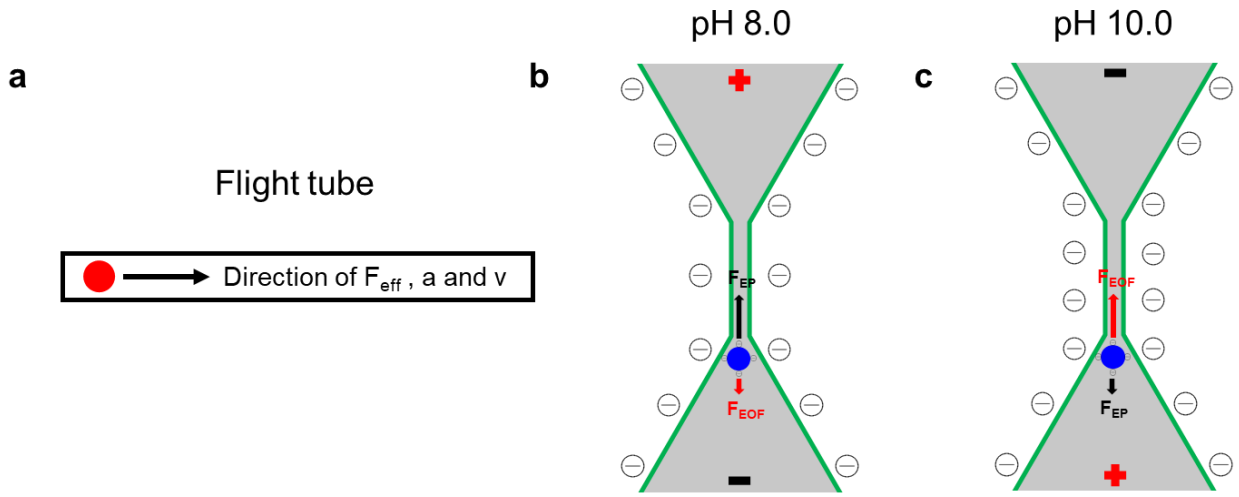

Figure 5.20. (a) Simple linear motion with constant acceleration model to calculate ToF. (b) Schematic image showing dNMPs translocation in PEGDA nanopore device at pH 8.0, where F_{EP} is donimant over F_{EOF} and F_{eff} is toward anode. (c) Schematic image showing dNMPs translocation in PEGDA nanopore device at pH 10.0, where F_{EOF} is donimant over F_{EP} and F_{eff} is toward cathode.

Histogram of current drop for dNMPs translocation through dual-nanopore is also presentented in Figure 5.21. Since the baseline current varied during dNMPs detection, the current drop (conductance drop) values were normalized by the total conductance. As shown below, the

trend of conductance drop follows a decreasing order of dAMP > dGMP > dCMP > dTMP, which is slightly different with previous studies and with poor identification accuracy.

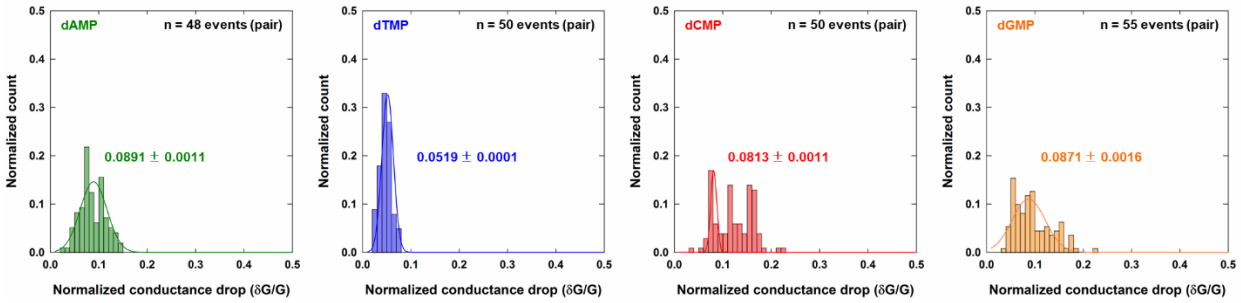

Figure 5.21. Histograms of the conductance drop for dNMPs transolation through the same PEGDA dual-nanopore device having 500 nm flight tube filled with 1 M KCl containing 0.5× TBE at pH 10.0 under 3 V. Conductance drop values are extracted from manually selected paired peaks based on the criterion described above.

5.3.2 500 nm flight tube vs. 1 μm flight tube

Based on Equation 5.3, by increasing flight tube length, the ToF values difference between four nucleotides can be increased, which could be helpful to improve the discrimination resolution. A Si master mold containing two nanopores with 1 μm flight tube was built for this purpose. The ToF values for dNMPs translocation through dual-nanopore with 1 μm flight tube filled with 1 M KCl containing 0.5× TBE at pH 10.0 under 3 V are presented in Figure 5.22. As flight tube length becomes double, the ToF values for all four dNMPs are more than two times larger than their values for 500 nm flight tube. This can be explained by the flight tube length increase and electric field strength reduction within longer flight tube. Again, the trend of ToF of dNMPs follows a decreasing order of dGMP > dAMP > dCMP > dTMP at pH 10.0 under 3 V for 1 μm flight tube. Although the distribution of flight time becomes broader, the average identification accuracy is improved to 75%. A longer flight tube can help to improve discrimination resolution and a higher driving voltage may be preferred to minimize the flight time variation.

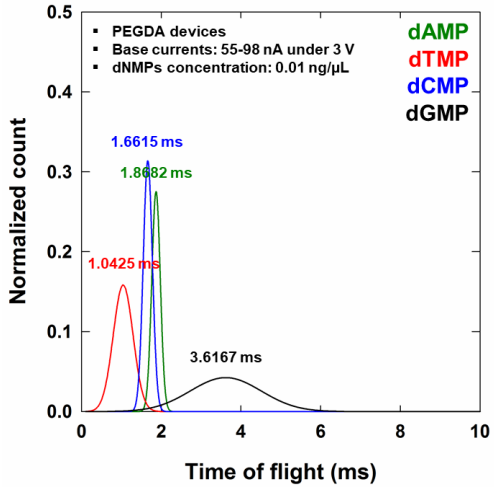

R (Resolution)	dAMP	dTMP	dCMP	dGMP
dAMP	-	1.1643	0.4685	0.8765
dTMP	1.1643	-	0.8536	1.1296
dCMP	0.4685	0.8536	-	0.9723
dGMP	0.8765	1.1296	0.9723	-

Identification Accuracy	
dAMP	59%
dTMP	92%
dCMP	53%
dGMP	95%

Figure 5.22. ToF values of dNMPs collecting from the PEGDA dual-nanopore device having 1μm flight tube filled with 1 M KCl containing 0.5× TBE at pH 10.0 under 3 V (dNMPs were driven electroosmotically). Compared with 500 nm flight tube device, dNMPs can be distinguished with an improved average identification accuracy of 75%.

5.3.3 ToF measurement of mix dGMP and dTMP under different driving voltage

Like previous studies with biological nanopores [21], a mix solution of dGMP/dTMP (volume ratio 7:3) was introduced in order to test the device performance. For mix solution, as shown in Figure 5.23, two distinct peaks can be identified at 1.5 V with a flight time of 0.8 ms and 3.0 m, respectively. Compared with ToF data from individual dNMPs at 3V, these two peaks (left to right) can be assigned to dTMP and dGMP. At 1 V, due to the broad distribution of ToF and limited data, we can barely assign two peaks with flight time of 4.3 ms and 9.5 ms to dTMP and dGMP, respectively. Compared with ToF values at 1.5 V and 3 V and in consideration of Equation 5.3, the long ToF at 1 V indicates that strong interaction between biomolecules and flight tube could be a problem at low driving voltage. Another interesting finding is, there are more paired peaks found for dTMP compared with dGMP although there are more dGMP in mix solution. This phenomenon can be attributed to the higher mobility for dTMP at pH 10.0, which is the same reason for dTMP's lowest ToF value.

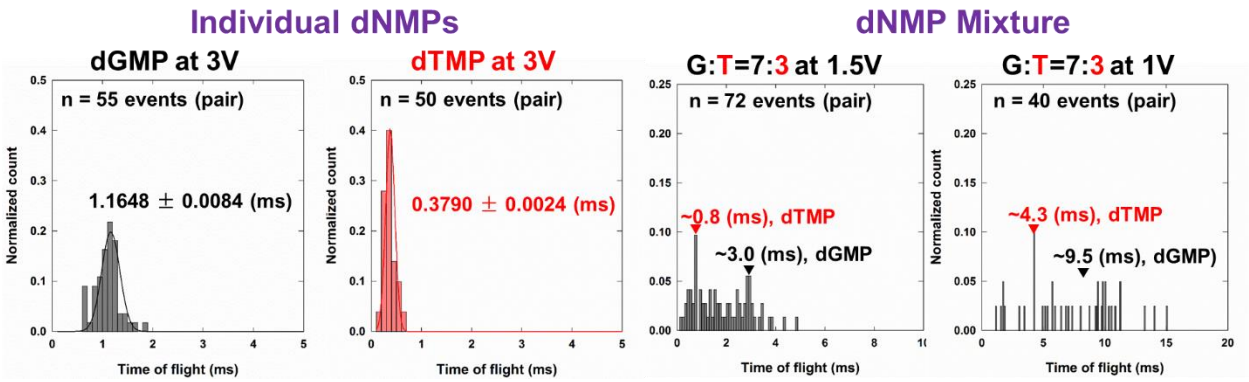

Figure 5.23. Left: ToF values for individual dGMP and dTMP from the PEGDA dual-nanopore device having 500 nm flight tube filled with 1 M KCl containing 0.5× TBE at pH 10.0 under 3 V. Right: ToF values for a mix solution of dGMP and dTMP from the PEGDA dual-nanopore device having 500 nm flight tube filled with 1 M KCl containing 0.5× TBE at pH 10.0 under 1.5 V and 1 V.

5.3.4 Reproducibility of ToF measurement

In order to avoid the variation from device difference, previous ToF data of four mononucleotides were collected under different experimental conditions from single devices. However, during the long-time ionic current recording, we observed an increase in baseline current especially for PEGDA device, which could affect the accuracy of ToF measurement. In order to demonstrate the reproducibility of ToF measurement, we collected ToF data of dGMP from two devices with 1μm flight tube at pH 10.0 with different baseline current values.

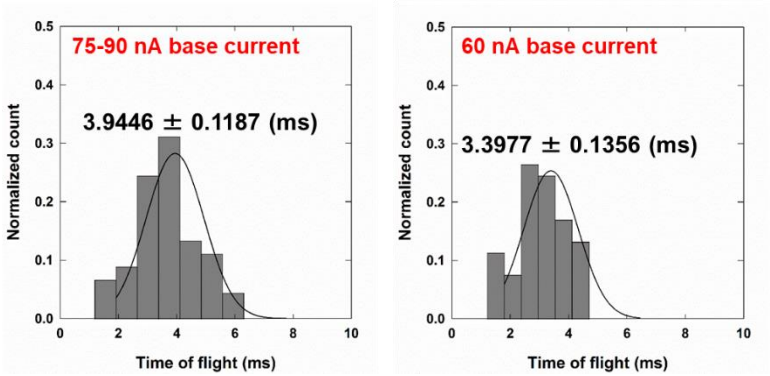

Figure 5.24. Histogram of dGMP ToF collected from dual-nanopore device with different baseline current.

As shown in Figure 5.24, ToF value collected from a nanopore device with lower baseline current is less than that from a device with higher baseline current. A lower baseline current indicates a smaller nanopore and a slightly smaller nanochannel after thermal bonding. Figure 5.25 presents the effective driving force, F_{eff}, of biomolecules inside nanopore with different sizes. For biomolecules driven by EOF, as nanopore size decreases, the absolute value of F_{eff} increases, which leads to a higher initial velocity entering the flight-tube. Such explanation was supported by the fact that the dwell time for lower baseline current device was 0.42 ms, which was less than that from a higher baseline current device of 1.02 ms.

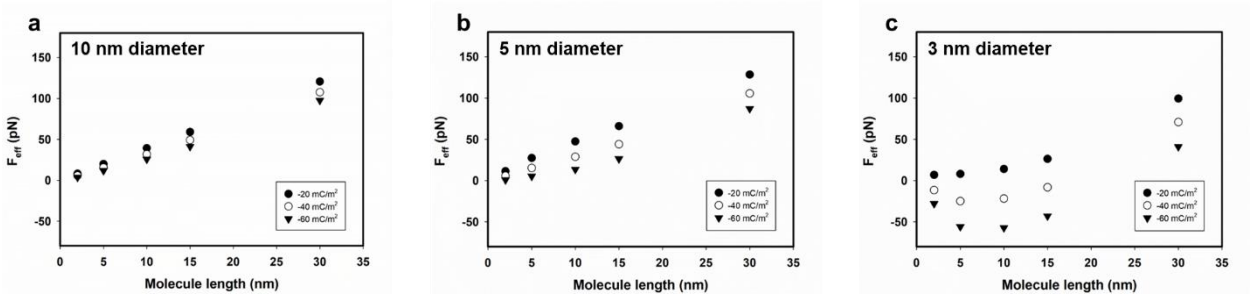

Figure 5.25. F_{eff} simulation for dsDNA with different length translocation inside nanopore with different size having various surface charge density. 1 M KCl was used as electrolyte, the same as experimental conditions. (a) 10 nm-diameter nanopore. (b) 5 nm-diameter nanopore. (c) 3 nm-diameter nanopore.

5.4 Conclusion

In this chapter, we present discrimination of dNMPs via ToF measurement using polymer dual-nanopore devices. At first, ToF of individual dNMP was measured using dual-nanopore devices having 500 nm flight tube with different surface charge density and pH values. At pH 8.0, nanopore with low surface charge density was preferred to drive small nucleotides electrophoretically. The ToF values for four dNMPs follow a decreasing order of dGMP > dAMP > dCMP > dTMP. But the discrimination resolution of four dNMPs was poor. Inspired by the work by O'Neil et al., which measured the mobilities of labeled dNMPs in nanochannel, a higher pH of

10.0 was tested to increase discrimination resolution. At pH 10.0, dNMPs translocation mechanism changes: even though PEGDA devices were used, F_{EOF} is dominant over F_{EP} due to increased surface charge density of nanopore/nanochannel walls at higher pH. Surprisingly, the ToF values follow the same decreasing order of dGMP > dAMP > dCMP > dTMP. At pH 10.0 under 3 V, an average identification accuracy of 55% was achieved. In order to improve resolution further, a device with longer flight tube of 1 μm was used to achieve an average identification accuracy of 75% at pH 10.0 under 3 V. At last, a mix solution of dGMP and dTMP was introduced and two distinct peaks were distinguished in a dual-nanopore device with 500 nm flight tube.

Overall, this work proves the idea of discrimination dNMPs using ToF measurement with dual-nanopore devices. A higher pH, a longer flight tube and a higher driving voltage are preferred to achieve better resolusion. Other factors affacting dNMP translocation within flight tube such as molecules mass, molecule/nanochannel surface charge density and molecule/nanochannel wall interaction should also be studied carefully in future work.

5.5 References

1. Astier, Y., O. Braha, and H. Bayley, *Toward single molecule DNA sequencing: direct identification of ribonucleoside and deoxyribonucleoside 5 '-monophosphates by using an engineered protein nanopore equipped with a molecular adapter*. Journal of the American Chemical Society, 2006. **128**(5): p. 1705-1710.

2. Maglia, G., et al., *Enhanced translocation of single DNA molecules through α-hemolysin nanopores by manipulation of internal charge.* Proceedings of the National Academy of Sciences, 2008. **105**(50): p. 19720-19725.

3. Zwolak, M. and M. Di Ventra, *Colloquium: Physical approaches to DNA sequencing and detection.* Reviews of Modern Physics, 2008. **80**(1): p. 141.

4. O'Neil, C., et al., *Electrokinetic transport properties of deoxynucleotide monophosphates (dNMPs) through thermoplastic nanochannels.* Analytica chimica acta, 2018. **1027**: p. 67-75.

5. Storm, A.J., et al., *Fast DNA translocation through a solid-state nanopore.* Nano Letters, 2005. **5**(7): p. 1193-1197.

6. Firnkes, M., et al., *Electrically facilitated translocations of proteins through silicon nitride nanopores: conjoint and competitive action of diffusion, electrophoresis, and electroosmosis.* Nano letters, 2010. **10**(6): p. 2162-2167.

7. Zhang, M., et al., *Methods and Technologies for Exosome Isolation and Characterization.* Small Methods, 2018: p. 1800021.

8. Yang, H., et al., *Identification of single nucleotides by a tiny charged solid-state nanopore.* The Journal of Physical Chemistry B, 2018.

9. Feng, J., et al., *Identification of single nucleotides in MoS2 nanopores.* Nat Nanotechnol, 2015. **10**(12): p. 1070-6.

10. Tsutsui, M., et al., *Identifying single nucleotides by tunnelling current.* Nat Nanotechnol, 2010. **5**(4): p. 286-90.

11. Li, J., et al., *Ion-beam sculpting at nanometre length scales.* Nature, 2001. **412**(6843): p. 166.

12. Merchant, C.A., et al., *DNA translocation through graphene nanopores.* Nano Lett, 2010. **10**(8): p. 2915-21.

13. Prasongkit, J., et al., *Transverse conductance of DNA nucleotides in a graphene nanogap from first principles.* Nano letters, 2011. **11**(5): p. 1941-1945.

14. Schneider, G.F., et al., *DNA translocation through graphene nanopores.* Nano letters, 2010. **10**(8): p. 3163-3167.

15. Liu, K., et al., *Atomically thin molybdenum disulfide nanopores with high sensitivity for DNA translocation.* ACS nano, 2014. **8**(3): p. 2504-2511.

16. Feng, J., et al., *Identification of single nucleotides in MoS2 nanopores.* arXiv preprint arXiv:1505.01608, 2015.

17. Shi, Y., et al., *Synthesis of few-layer hexagonal boron nitride thin film by chemical vapor deposition.* Nano letters, 2010. **10**(10): p. 4134-4139.

18. Prasongkit, J., et al., *Theoretical study of electronic transport through DNA nucleotides in a double-functionalized graphene nanogap.* The Journal of Physical Chemistry C, 2013. **117**(29): p. 15421-15428.

19. Chang, S., et al., *Electronic signatures of all four DNA nucleosides in a tunneling gap.* Nano letters, 2010. **10**(3): p. 1070-1075.

20. Tsutsui, M., et al., *Formation and self-breaking mechanism of stable atom-sized junctions.* Nano letters, 2008. **8**(1): p. 345-349.

21. Clarke, J., et al., *Continuous base identification for single-molecule nanopore DNA sequencing.* Nat Nanotechnol, 2009. **4**(4): p. 265-70.

22. Pedone, D., et al., *Fabrication and electrical characterization of a pore–cavity–pore device.* Journal of Physics: Condensed Matter, 2010. **22**(45): p. 454115.

23. Pedone, D., et al., *A pore− cavity− pore device to trap and investigate single nanoparticles and DNA molecules in a femtoliter compartment: confined diffusion and narrow escape.* Nano letters, 2011. **11**(4): p. 1561-1567.

24. Harms, Z.D., et al., *Nanofluidic devices with two pores in series for resistive-pulse sensing of single virus capsids.* Analytical chemistry, 2011. **83**(24): p. 9573-9578.

25. Langecker, M., et al., *Electrophoretic time-of-flight measurements of single DNA molecules with two stacked nanopores.* Nano letters, 2011. **11**(11): p. 5002-5007.

26. Xia, K., et al., *Electrophoretic transport of single DNA nucleotides through nanoslits: a molecular dynamics simulation study.* The Journal of Physical Chemistry B, 2015. **119**(35): p. 11443-11458.

Chapter 6. Surface Charge Density Manipulation Using Multivalent Salt

In chapter 5, we've demonstrated dNMPs discrimination using PEGDA based dual-nanopore devices with low surface charge density at various conditions. However, we noticed that molecules pile-up issue still occurred during dNMPs translocation, which could be troublesome for data analysis even with enzyme-assisted motion control. Unlike long chain DNA (such as λ-DNA), which has to overcome high entropy barrier by sufficient F_{eff} , the pile-up issue for particle-like nucleotides can be attributed to the ion selection property of nanopore, which has the same negatively charges as nucleotides. In order to assist nucleotides translocation, this chapter focuses on how to reduce the surface charge density of polymer surface further by using multivalent salt.

6.1 Introduction: Surface charge density of polymer surface and its modification

Unique transport phenomena and high sensitivity in nanoscale make nanofluidic devices such as nanochannels [1, 2] and nanopores [3, 4] ideal platforms for single molecule analysis. In recent years, nanofluidic devices made of thermoplastics such as poly(methylmethacrylate) (PMMA) [5], cyclic olefin copolymer (COC) [6] and polycarbonate (PC) [7] have drawn tremendous attention as the best candidate to replace silicon(Si) and glass based nanofluidic devices due to their low-cost and large-scale fabrication features. However, the hydrophobic nature of pristine polymer substrates prevents a good reagent filling into micro- and nanochannels and therefore proper surface modification of polymer substrates via O_2 plasma or UV/O_3 treatment is prerequisite [8-10]. When polymer substrates are treated with O_2 plasma or UV/O_3, polar functional groups (e.g. carboxyl groups) are normally formed on polymer surfaces [10, 11]. Such functional groups improve the wetting property of polymer substrate by increasing surface energy and the modified hydrophilic surface prevents non-specific binding to analytes such as DNA, RNA,

protein or cell. Upon contacting with aqueous solution, the modified polymer surface develops negative surface charges due to the dissociation of carboxyl groups given by:

$$COOH \rightleftharpoons COO^- + H^+ \quad (1)$$

These surface charges play an important role in manipulating biomolecules motion during electrophoresis within nanofluidic devices. For large biomolecules with negative surface charges, e.g. double-stranded (ds)DNA, negative charges on polymer surfaces prevent an efficient capture of DNA into nanofluidic devices. Since the negative charges on polymer substrates leads to a strong electroosmotic flow (EOF), which is opposite to DNA drift velocity by electrophoresis [12-14]. Such strong EOF leads to an insufficient effective driving force (F_{eff}) for folded long chain DNA to overcome entropy barrier [15, 16] or for pre-stretched long chain DNA [17, 18] to be threaded through nanochannel/nanopore. On the contrary to this, for small biomolecules with negative surface charges, e.g. proteins and mononucleotides, viscous force by EOF (F_{EOF}) is dominant over electrophoretic force (F_{EP}), working as the main driving force for biomolecules translocation [19, 20]. In this case, a stronger EOF may lead to high translocation speed, which is a challenging for the detection electronics with limited bandwidth [21-23]. Moreover, selective ions (analytes) transport [24] due to electrostatic repulsion is dominant especially for nanofluidic devices with extreme small length scale.

Because of aforementioned reasons, polymer nanofluidic devices with low and controllable surface charge density is desirable for single molecule analysis. There are several ways to manipulate surface charge density of nanofluidic devices. Poly(ethylene glycol) (PEG) has been successfully grafted on polymer substrates, such as PMMA [8, 25] and Polydimethylsiloxane (PDMS) [26], to suppress EOF and non-specific molecules binding. Compared with PEG coating, dynamic coating using surfactant such as polyvinylpyrrolidone (PVP) is more convenient and has

been used mostly for Si or glass based nanofluidics devices [27-29]. However, the existence of surfactant in buffer may affect the accuracy of biomolecule analysis based on resistive-pulse sensing and mass spectrometry [8]. A simpler way to manipulate the substrate surface charge is by introducing multivalent metal salts into buffer system [30, 31]. Unlike commonly used monovalent electrolytes (such as KCl [4], NaCl and LiCl [32]) for biomolecule sensing, both numerical and experimental studies demonstrated multivalent ions (such as Mg^{2+} and Al^{3+}) can reduce or even invert the negative surface charges on Si or glass based substrates [30, 31]. One drawback of introducing multivalent metal salt into buffer or using it directly as buffer [33] is that it may affect the fluorescence dye stability [2], unexpected noise or fake peaks during current measurement or even alter the polarity of biomolecules surface charge [34].

In this chapter, we present an easy method to manipulate surface charge density of polymer nanofluidic devices by using multivalent metal salts to facilitate biomolecule sensing. We mainly focus on a modification of COC substrate. Since it has excellent optical property and various glass transition temperature (T_g) for different applications [35] but has a higher surface charge density than other commonly used thermoplastic substrates based on literature [6] and our previous work. However, the method can be applicable for most polymer substrates even Si or glass substrates. Unlike previous studies, we expect to modify polymer surface charge density by the multivalent ions anchored to its surface, while keeping the original suitable buffer system for either fluorescence observation or ionic current measurement. Surface charge density change was determined by measuring the conductance of nanochannels imprinted on polymer substrates with and without modification. Then, the performance of modified device was tested by translocating biomolecules through polymer in-plane nanopore.

6.2 Experiments

6.2.1 Fabrication of polymer nanochannel devices and their surface modification

Surface charge density modification by using multivalent metal salts was conducted on three different polymer substrates with their surface charge density in a decreasing order of: COC > PMMA > PEGDA as shown in chapter 4. Polymer devices were fabricated via thermal- and UV-nanoimprint lithography (NIL) using UV-resin molds. First, a Si master mold containing two access microchannels and five nanochannels was fabricated by standard photolithography, wet etching and focused ion beam (FIB) milling. The patterns on the Si master mold were then transferred to UV-resin molds by UV-NIL. Finally, the mix-scale structure was imprinted on target substrates using the replicated UV-resin molds via thermal-NIL (COC and PMMA) and UV-NIL (PEGDA) at different imprinting conditions. Prior to bonding with a thin COC cover sheet, imprinted substrates (except for PEGDA) and the cover sheets were activated by O_2 plasma at 50 watt, 450 mTorr for 30 s. Substrates and cover sheets were then bonded at 70 °C, 1 MPa for 15 min. Bonded devices are denoted as COC-COC (substrate-cover), PMMA-COC and PEGDA-COC, respectively. Details and more information regarding device fabrication can be found in our previous chapters.

For manipulating surface charge density with multivalent metal salts, $MgCl_2$ (Sigma-Aldrich) and $AlCl_3$ (Sigma-Aldrich) were used as bivalent and trivalent metal salts, respectively. Protocol of conductance measurement before and after modification by multivalent metal salts is illustrated in Figure 6.1. We first measured the nanochannel conductance filled with 10^{-6} M KCl as a reference value. The KCl solution was then withdrawn from the nanochannels and replaced with different concentrations of $MgCl_2$ (e.g. 10 mM, 100 mM, 500 mM and 1M). After the nanochannel was filled with $MgCl_2$ having certain concentrations, we waited 20 min to allow a

sufficient time for Mg^{2+} ions binding on the negatively charged polymer surface. Then, $MgCl_2$ solution was withdrawn from the nanochannels and replaced with 10^{-6} M KCl solution by repeating withdraw-and-refill process. We measured the nanochannel conductance every four withdraw-and-refill cycles. Finally, we stopped the washing process until measured conductance is stable (which indicated the surface charge density of substrate after modification) and proceed to the next $MgCl_2$ concentration. The same procedure was applied to surface charge modification with $AlCl_3$.

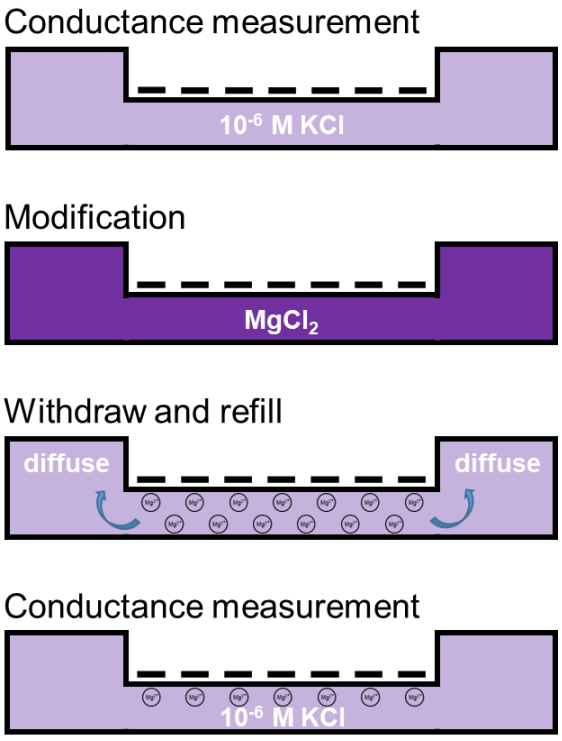

Figure 6.1. Schematic image illustrating the protocol of conductance measurement. Step 1: the nanochannels filled with 10^{-6} M KCl and conductance is measured as reference before modification; Step 2: KCl is withdrawn first, then the nanochannels are refilled with $MgCl_2$ or $AlCl_3$ with different concentration and wait for 20 min for "reaction"; Step 3: Withdraw-and-refill process are repeated several times to remove all the residual free multivalent ions in nanochannel; Step 4: conductance of modified nanochannels is measured when the nanochannel filled with 10^{-6} M KCl.

6.2.2 Translocation of λ-DNA through modified polymer nanopore

Before taking biomolecule translocation experiments, a binding behavior of negatively charged biomolecules to COC-COC device modified by $AlCl_3$ with different concentrations (0 M, 10 mM, 100 mM, 500 mM and 1M) was studied by introducing 5 ng/μL lambda-DNA (New England BioLabs) stained with YOYO-1 (ThermoFisher Scientific) into microchannels. DNA solution was withdrawn after 2 min and the device was washed twice with 1× TE buffer (Sigma-Aldrich). DNA molecules binding to microchannel walls was observed by a fluorescence microscope (Olympus IX70) with a 100× oil immersion objective (Olympus). Fluorescence images were captured by a CCD camera (Photon Max, Princeton Instruments) and the number of binding molecules on microchannel surface was determined by ImageJ (National Institutes of Health).

For biomolecule translocation experiments, 5 ng/μL stained lambda-DNA was driven into the same COC-COC single nanopore device filled with 1× TE buffer before and after 100 mM AlCl3 modification. DNA translocation was observed by fluorescence microscope and the images were captured by a CCD camera.

6.3 Results and Discussion

6.3.1 COC surface charge density modification by $MgCl_2$ and $AlCl_3$

In order to quantify surface charge density change after modification, we measured and monitored the conductance of nanochannel filled with a low salt concentration, e.g. 10^{-6} M KCl because the conductance depends on the surface charge density at a low salt concentration. Normally, the total conductance of nanochannel, G_T, can be expressed as the sum of bulk solution conductance, G_B, and surface conductance, G_S .

$$G_T = G_B + G_S \tag{2}$$

$$G_B = 10^3(\mu_{K^+} + \mu_{Cl^-})cN_A e\frac{nwh}{L} \quad (3)$$

$$G_S = 2\mu_{opp}\,\sigma_s n\frac{(w+h)}{L} \quad (4)$$

, where μ_{K^+} and μ_{Cl^-} are the ion mobilities of K^+ and Cl^- ions, c is the bulk electrolyte concentration, N_A is Avogadro's number, n is the number of nanochannels in the device and w, L and h are the nanochannel width, length and height, respectively, μ_{opp} is the mobility of the counterion, and σ_s is the effective surface charge density of polymer substrates. At high salt concentration, the number of charge carriers within nanochannel is determined by bulk solution concentration. Therefore, the second term in Equation 6.2, G_S, can be neglected and $G_T = G_B$, which is dependent on c. However, at low salt concentration, the number of charge carriers within nanochannel is determined by σ_s. The first term in Equation 6.2, G_B, can be neglected and $G_T = G_S$, which is dependent on σ_s.

COC-COC nanochannels were modified by $MgCl_2$ and $AlCl_3$ salt solutions with different concentrations. Figure 6.2 shows the conductance of nanochannels filled with 10^{-6} M KCl solution as a function of $MgCl_2$/$AlCl_3$ concentration. For both cases, nanochannel conductance decreases as salt concentration increases, which indicates a surface charge density reduction. Because of strong electrostatic attraction, the bare negative charges on COC surface were screened by multivalent ions, Mg^{2+} and Al^{3+}, leading to a net surface charge reduction. However, unlike previous studied on Si based [30] and glass based [31] nanofluidic devices, surface charge inversion was not observed for modified COC substrates with Mg^{2+} and Al^{3+} concentration up to 1 M. One possible reason is that when multivalent metal salt is used as buffer directly, multiple layers of counter ions are built against the negatively charged polymer surface, and all these counter ions help to neutralize substrate's bare charges [36]. While for our method, most Mg^{2+} and Al^{3+} ions left in nanochannel are anchored to polymer surface and form a thin layer of counter ions

with few counter ions in diffuse layer. Moreover, Figure 6.2 presents Al^{3+} can reduce COC surface charge density more efficiently than Mg^{2+} due to its stronger binding energy to negatively charged polymer surface [37], which is in good agreement with previous numerical [37, 38] and experimental [30, 31, 34, 39] studies.

Because of a similar manner, Al^{3+} can be more effectively anchored on more negatively charged polymer substrates, resulting in more efficient surface charge reduction. Figure 6.3 compares conductance of COC-COC, PMMA-COC and PEGDA-COC nanochannels after modification using $AlCl_3$. In chapter 4 we have shown PMMA and PEGDA have lower surface charge densities than COC. As $AlCl_3$ concentration increases, conductance of all three hybrid devices decrease. Though the surface charge density of $AlCl_3$ modified COC by is still higher than pristine PEGDA, considering its stability and broad T_g range, $AlCl_3$ modified COC is still an ideal candidate as nanofluidic devices substrate for biomolecules detection. And the performance of PEGDA device for nucleotides sensing could be improved due to surface charge reduction.

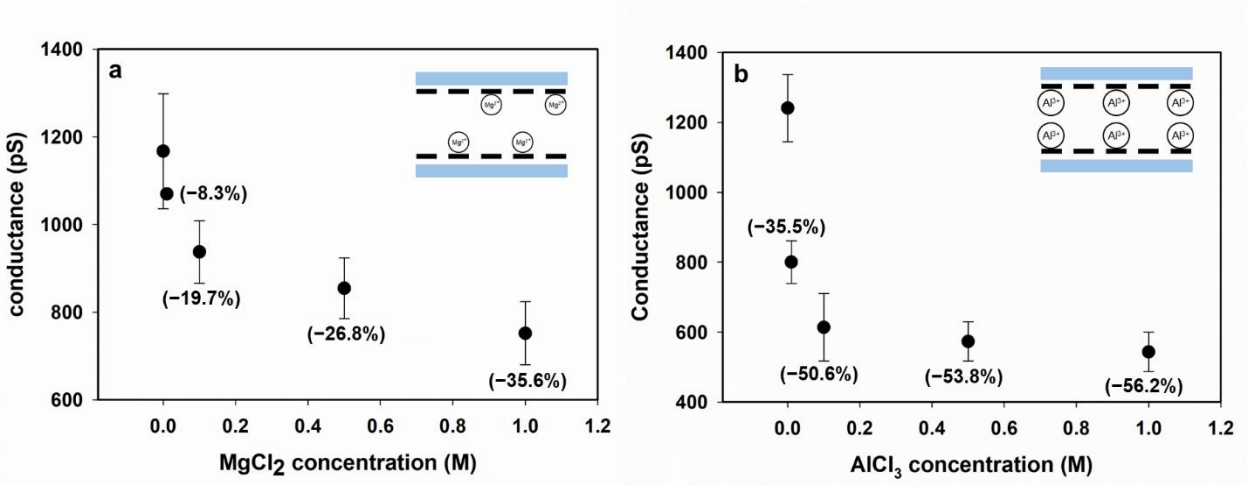

Figure 6.2. Conductance of nanochannels after modification with multivalent salt having different concentration. (a) COC-COC device modified by MgCl2 bivalent salt; (b) COC-COC device modified by $AlCl_3$ trivalent salt. The numbers in brackets indicate the reduction rate of conductance (surface charge density). 10 devices were measured for each modification method.

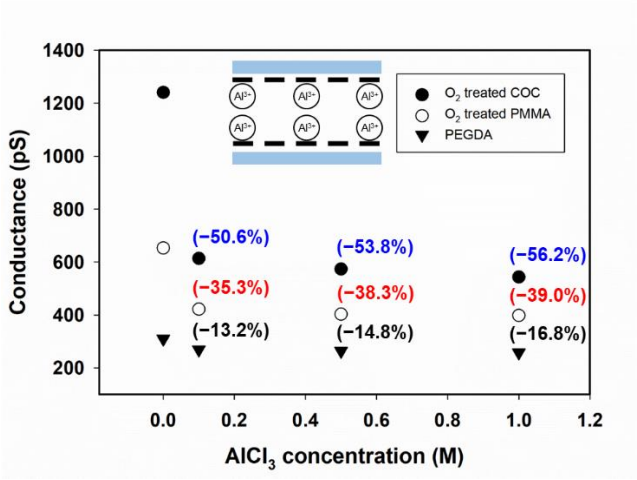

Figure 6.3. Conductance measurement of COC-COC, PMMA-COC and PEGDA-COC devices modified by $AlCl_3$ with different concentration. For all three devices, nanochannel conductance decrease as $AlCl_3$ concentration increases. Moreover, polymer substrates with higher surface charge density have more surface charge reduction due to a stronger electrostatic interaction with Al^{3+} ion. Error bar not shown for better illustration, 10 devices were examined for all data points.

Although surface charge reduction by multivalent ions has been reported in previous works [30, 31], meanwhile, few of them studied the stability of modification. When multivalent ions are present in nanofluidic device, negative charges on polymer surface attract multivalent ions to form a stern layer, while some multivalent ions within the diffuse layer can also be attracted close to polymer surface and form a loose layer [36]. During device filling or operation, multivalent ions close to polymer surface, especially in the diffuse layer can be removed by shear flow, leading to a surface charge density recovery, as illustrates in Figure 6.4(b). Besides, the O_2 plasma treated polymer surface also suffer from recovery [40], which may also affect the stability of surface charge modification. Figure 6.4(a) presents the conductance of nanochannel as a function of withdraw-and-refill cycles after treated with different concentration $AlCl_3$. In the first two cycles, conductance of modified nanochannel is even higher than its initial value because it is difficult to withdraw the $AlCl_3$ solution from nanochannels completely. After 4-6 cycles, nanochannel conductance saturates to a value which is lower than its initial value, indicating the remaining Al^{3+} ions in nanochannel are attached to polymer surfaces. We kept recording the conductance of

nanochannel modified by 500 mM $AlCl_3$ for 2 hours. Long time exposure to strong EOF may result in the removal of Al^{3+} ions in the loose layer or even from the stern layer. The conductance of modified COC nanochannel increases 9.3% but it is still much lower than its initial value.

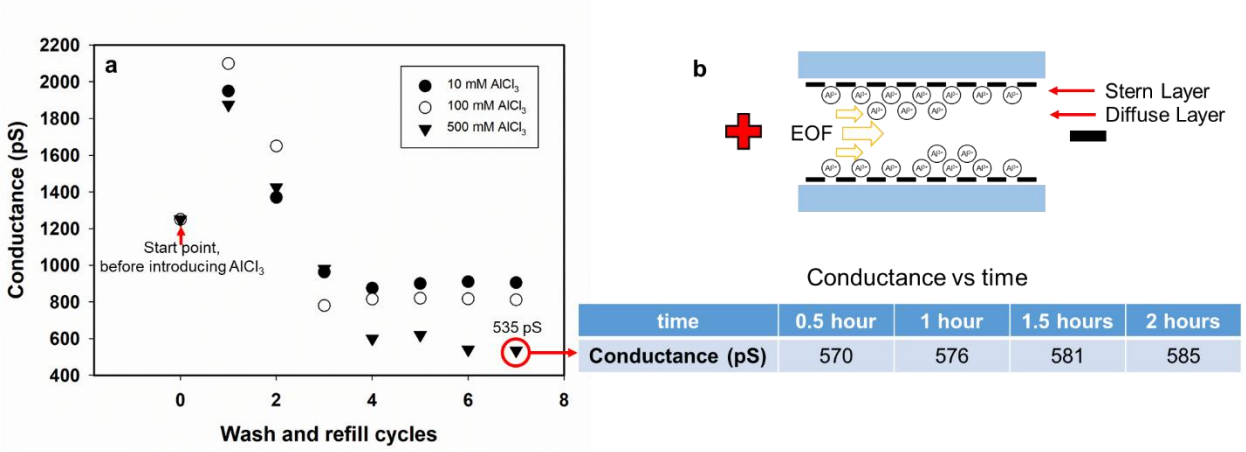

Conductance vs time

time	0.5 hour	1 hour	1.5 hours	2 hours
Conductance (pS)	570	576	581	585

Figure 6.4. Study on the modification stability. (a) Conductance vs. wash-and-refill cycles. For 500 mM AlCl3 modification, surface charge density recovers 9.3% after 2 hours continuous measurement (exposure to EOF). (b) Schematic image showing counter ions layers formed against surface charges. Shear flow can remove the counter ions in diffuse layer, leading to surface charge density recovery.

6.3.2 Translocation of λ-DNA through surface modified COC-COC nanopore

Prior to biomolecules translocation experiments, we studied biomolecules binding to multivalent metal salt modified COC surface. Figure 6.5(a) show fluorescence images of lambda-DNA molecules stuck on COC substrates modified by $AlCl_3$ with different concentration. The number of binding DNA increased by increasing $AlCl_3$ concentration, as shown in Figure 6.5(b). DNA binding to COC substrates can be explained by the strong electrostatic interaction between the Al^{3+} ions on polymer surface and the negatively charged dsDNA. Although COC surface charge density decrease as $AlCl_3$ concentration increases, too much Al^{3+} ions on COC surface may aggravate the specific binding of DNA on modified COC substrates. Therefore, for COC surface charge reduction, a moderate $AlCl_3$ concentration is preferred for actual nanochannel devices in order to translocate biomolecules, for example 100 mM.

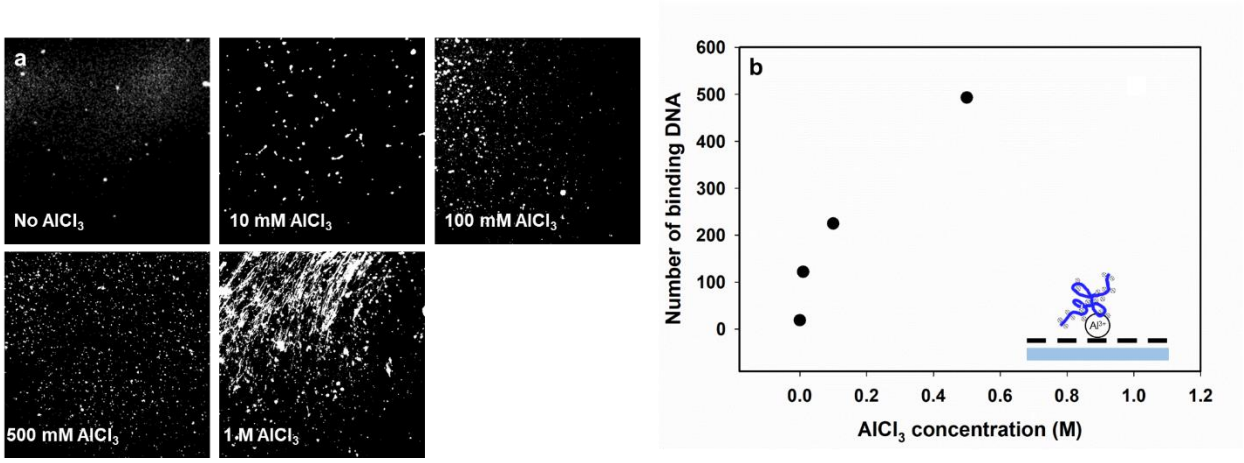

Figure 6.5. Negatively charged DNA binding to Al^{3+} modified COC surface. (a) Fluorescence images of stained DNA binding to COC surface after modified with different concentration $AlCl_3$. (b) Number of binding DNA vs. $AlCl_3$ concentration plot. 1 M data not shown due to many stretched DNA instead of point-like unstretched DNA.

Figure 6.6 shows fluorescence image of lambda-DNA translocation through in-plane nanopore made of COC. Before $AlCl_3$ modification, all incoming DNA molecules pile up in front of nanopore without translocation like previously shown in chapter 4. After treated with 100 mM $AlCl_3$, DNA molecules can pass through the nanopore due to lower surface charge density. Compared with fluorescence image of COC without modification, the image after AlCl3 modification is blurry, which can be attributed to DNA molecules stuck on COC surface due to electrostatic interaction.

Figure 6.6. λ-DNA translocation through COC-COC single nanopore device before and after modified by 100 mM $AlCl_3$, with 1× TE as buffer.

6.4 Conclusion

In this work, we present the manipulation of surface charge density of polymer nanofluidic devices using multivalent metal salts. Polymer surface charge density manipulation by multivalent salts is dependent on the valence of ions and the bare surface charge density of polymer substrates. Once introduced into nanofluidic device, multivalent ions bind to negatively charged COC substrate due to electrostatic attraction and thus neutralize COC substrate's bare charges. Compared with Mg^{2+}, Al^{3+} can reduce COC surface charge density more efficiently. Yet none of them can invert its surface charge, which is different from previous studied on Si- and glass-based nanofluidic devices. This modification method was also applied to PMMA and PEGDA with different surface charge densities. Conductance measurements revealed that surface charge reduction by Al^{3+} is more effective for polymer substrate with higher surface charge density.

Biomolecules translocation was also conducted to test the performance of Al^{3+} modified COC nanopore device. However, multivalent ions on polymer surface can bind negatively charged biomolecules because of strong electrostatic interactions. Therefore, a moderate multivalent salt concentration is preferred to modify polymer surface charge density. λ-DNA can be successfully translocated through COC-COC single nanopore after 100 mM $AlCl_3$ modification, which

confirmed the surface charge density reduction. Thus, modified COC has the potential to replace PEGDA for dNMPs detection due to its insoluble property. PEGDA device performance could be improved with Al^{3+} modification, minimizing the pile-up issue for nucleotides due to ion selective transport.

6.5 References

1. Foquet, M., et al., *DNA fragment sizing by single molecule detection in submicrometer-sized closed fluidic channels.* Analytical Chemistry, 2002. **74**(6): p. 1415-1422.

2. Menard, L.D., et al., *A device for performing lateral conductance measurements on individual double-stranded DNA molecules.* ACS nano, 2012. **6**(10): p. 9087-9094.

3. Harms, Z.D., et al., *Nanofluidic devices with two pores in series for resistive-pulse sensing of single virus capsids.* Anal Chem, 2011. **83**(24): p. 9573-8.

4. Storm, A.J., et al., *Fast DNA translocation through a solid-state nanopore.* Nano letters, 2005. **5**(7): p. 1193-1197.

5. Uba, F.I., et al., *Surface charge, electroosmotic flow and DNA extension in chemically modified thermoplastic nanoslits and nanochannels.* Analyst, 2015. **140**(1): p. 113-26.

6. Uba, F.I., et al., *High process yield rates of thermoplastic nanofluidic devices using a hybrid thermal assembly technique.* Lab on a Chip, 2015. **15**(4): p. 1038-1049.

7. Kawano, R., et al., *A Polymer-Based Nanopore-Integrated Microfluidic Device for Generating Stable Bilayer Lipid Membranes.* Small, 2010. **6**(19): p. 2100-2104.

8. Liu, J., et al., *Surface-modified poly (methyl methacrylate) capillary electrophoresis microchips for protein and peptide analysis.* Analytical chemistry, 2004. **76**(23): p. 6948-6955.

9. Wei, S., et al., *Photochemically patterned poly (methyl methacrylate) surfaces used in the fabrication of microanalytical devices.* The Journal of Physical Chemistry B, 2005. **109**(35): p. 16988-16996.

10. Chai, J., et al., *Wettability interpretation of oxygen plasma modified poly (methyl methacrylate).* Langmuir, 2004. **20**(25): p. 10919-10927.

11. ONeil, C.E., et al., *Interrogating Surface Functional Group Heterogeneity of Activated Thermoplastics Using Super-Resolution Fluorescence Microscopy.* Analytical chemistry, 2016. **88**(7): p. 3686-3696.

12. He, Y., et al., *DNA capture in nanopores for genome sequencing: challenges and opportunities.* Journal of Materials Chemistry, 2012. **22**(27): p. 13423-13427.

13. Wong, C.T. and M. Muthukumar, *Polymer capture by electro-osmotic flow of oppositely charged nanopores.* J Chem Phys, 2007. **126**(16): p. 164903.

14. Muthukumar, M., *Theory of capture rate in polymer translocation.* The Journal of chemical physics, 2010. **132**(19): p. 05B605.

15. Zhou, J., et al., *Enhanced nanochannel translocation and localization of genomic DNA molecules using three-dimensional nanofunnels.* Nature communications, 2017. **8**(1): p. 807.

16. Kumar, R. and M. Muthukumar, *Origin of translocation barriers for polyelectrolyte chains.* The Journal of chemical physics, 2009. **131**(19): p. 11B610.

17. Chen, L. and A. Conlisk. *Modeling of DNA Translocation in Nanopores*. in *47th AIAA Aerospace Sciences Meeting including The New Horizons Forum and Aerospace Exposition*. 2009.

18. van Dorp, S., et al., *Origin of the electrophoretic force on DNA in solid-state nanopores.* Nature Physics, 2009. **5**(5): p. 347-351.

19. Firnkes, M., et al., *Electrically facilitated translocations of proteins through silicon nitride nanopores: conjoint and competitive action of diffusion, electrophoresis, and electroosmosis.* Nano Lett, 2010. **10**(6): p. 2162-7.

20. Yang, H., et al., *Identification of single nucleotides by a tiny charged solid-state nanopore.* The Journal of Physical Chemistry B, 2018.

21. Ai, Y., et al., *Field effect regulation of DNA translocation through a nanopore.* Analytical chemistry, 2010. **82**(19): p. 8217-8225.

22. Sampath, G., *DNA sequencing with stacked nanopores and exonuclease: A simulation-based analysis.* Electrophoresis, 2016. **37**(17-18): p. 2429-2434.

23. Venkatesan, B.M., et al., *DNA Sensing using Nano-crystalline Surface Enhanced Al(2)O(3) Nanopore Sensors.* Adv Funct Mater, 2010. **20**(8): p. 1266-1275.

24. Yeh, L.-H., et al., *Ion concentration polarization in polyelectrolyte-modified nanopores.* The Journal of Physical Chemistry C, 2012. **116**(15): p. 8672-8677.

25. Bi, H., et al., *Deposition of PEG onto PMMA microchannel surface to minimize nonspecific adsorption.* Lab on a Chip, 2006. **6**(6): p. 769-775.

26. Kovach, K.M., et al., *The effects of PEG-based surface modification of PDMS microchannels on long-term hemocompatibility.* J Biomed Mater Res A, 2014. **102**(12): p. 4195-205.

27. Kaneta, T., et al., *Suppression of electroosmotic flow and its application to determination of electrophoretic mobilities in a poly(vinylpyrrolidone)-coated capillary.* J Chromatogr A, 2006. **1106**(1-2): p. 52-5.

28. Milanova, D., et al., *Effect of PVP on the electroosmotic mobility of wet-etched glass microchannels.* Electrophoresis, 2012. **33**(21): p. 3259-62.

29. Menard, L.D. and J.M. Ramsey, *Electrokinetically-driven transport of DNA through focused ion beam milled nanofluidic channels.* Analytical chemistry, 2012. **85**(2): p. 1146-1153.

30. Chou, K.-H., et al., *An Experimental Approach to Systematically Probe Charge Inversion in Nanofluidic Channels.* Nano letters, 2018. **18**(2): p. 1191-1195.

31. Brechtel, R., et al., *Control of the electroosmotic flow by metal-salt-containing buffers.* Journal of Chromatography A, 1995. **716**(1-2): p. 97-105.

32. Kowalczyk, S.W., et al., *Slowing down DNA translocation through a nanopore in lithium chloride.* Nano letters, 2012. **12**(2): p. 1038-1044.

33. Zhang, Y., et al., *Nanopore detection of DNA molecules in magnesium chloride solutions.* Nanoscale research letters, 2013. **8**(1): p. 245.

34. Besteman, K., K. Van Eijk, and S. Lemay, *Charge inversion accompanies DNA condensation by multivalent ions.* Nature Physics, 2007. **3**(9): p. 641.

35. Nunes, P.S., et al., *Cyclic olefin polymers: emerging materials for lab-on-a-chip applications.* Microfluidics and nanofluidics, 2010. **9**(2-3): p. 145-161.

36. Grosberg, A.Y., T. Nguyen, and B. Shklovskii, *Colloquium: the physics of charge inversion in chemical and biological systems.* Reviews of modern physics, 2002. **74**(2): p. 329.

37. Quesada-Pérez, M., et al., *Overcharging in colloids: beyond the Poisson–Boltzmann approach.* ChemPhysChem, 2003. **4**(3): p. 234-248.

38. Shklovskii, B.I., *Screening of a macroion by multivalent ions: correlation-induced inversion of charge.* Physical Review E, 1999. **60**(5): p. 5802.

39. Besteman, K., et al., *Direct observation of charge inversion by multivalent ions as a universal electrostatic phenomenon.* Physical review letters, 2004. **93**(17): p. 170802.

40. Lin, T.-Y., T.T. Pfeiffer, and P.B. Lillehoj, *Stability of UV/ozone-treated thermoplastics under different storage conditions for microfluidic analytical devices.* RSC advances, 2017. **7**(59): p. 37374-37379.

Chapter 7. Conclusion and Future Works

7.1 Conclusion

The goal of this study is to develop polymer dual-nanopore device for DNA sequencing and the focus is given on dNMPs discrimination assuming they have been cleaved from raw DNA. This goal has been achieved by accomplishing the following objectives: (1) fabrication of polymer dual-nanopore devices using high throughput nanoimprint lithography (NIL); (2) demonstration of single molecule sensing ability by conducting λ-DNA translocation experiments in polymer single nanopore devices with different surface charge density; (3) discrimination of dNMPs by ToF measurement using polymer dual-nanopore devices under various experimental conditions.

Chapter 3 focuses on the fabrication of polymer in-plane nanopore using NIL by investigating the whole fabrication process including Si master mold fabrication, UV-resin mold replication, polymer device imprinting and sealing. Nanopore dimensions, especially depth, in Si mater mold can be well controlled by milling time and proper bitmap design. Moreover, metal-assisted FIB milling was demonstrated to target sub-10 nm 2D nanopore. In order to achieve a sufficient replication fidelity for UV-resin mold fabrication and subsequent thermal-NIL, physical properties of UV-resin (monomer size, surface energy and Young's moduli) and geometry of master mold structure should be considered. With well copied UV-resin molds, nanopore patterns were successfully transferred to COC, PMMA and PEGDA via thermal- and UV- NIL, respectively.

Fabricated polymer single-nanopore devices were then used to studied the surface charge density effect on F_{eff} for DNA translocation and demonstrated single molecule sensing ability. COMSOL simulation predicted nanopore with a surface charge density higher than -50 mC/m^2 could prevent DNA translocation through nanopore filled with 1× TE, due to low F_{eff} resulting

from strong EOF. Simulation results were then validated by conducting λ-DNA translocation in 10 nm-diameter nanopore fabricated on three polymer substrates with their surface charge density in a decreasing order of COC (-73.8 mC/m^2) > PMMA (-51.7 mC/m^2) > PEGDA (-24.1 mC/m^2). Both fluorescence observation and ionic current measurement confirmed that λ-DNA translocation could only occur in PEGDA devices with the lowest surface charge density of -24.1 mC/m^2. Results in this chapter provide insights for device design and nanopore material selection, in order to increase event rate and facilitate biomolecule translocation. Besides, based on the current drop signals from λ-DNA we expected to detect nucleotides by using dual-nanopore devices with smaller pore size.

Chapter 5 demonstrates the discrimination of dNMPs via ToF measurement using polymer dual-nanopore devices under various experimental conditions. At pH 8.0, nanopore with low surface charge density was preferred to driving mononucleotides by electrophoretic motion. Four dNMPs can be barely discriminated by their ToF values, in a decreasing order of dGMP > dAMP > dCMP > dTMP. At pH 10.0, even with PEGDA nanopore, all dNMPs were driven through nanopore electroosmotically due to stronger EOF. Four dNMPs can be discriminated with an average identification accuracy of 55% in the same order as pH 8.0. Resolution can be improved further to 75 % by using 1 μm flight tube instead of 500 nm. Finally, a mix solution of dGMP and dTMP were introduced and identified based on their ToF difference.

Though dNMPs were translocated through PEGDA nanopores, we still observed dNMPs pile-up issue during translocation, which could be troublesome for subsequent ToF data analysis. In order to solve the pile-up issue for particle-like dNMPs resulting from ion selective transport, chapter 6 presents surface charge density reduction by using multivalent salt. $MgCl_2$ and $AlCl_3$ with different concentration were introduced to bonded polymer devices, aiming to neutralized

their surface charges after electrostatic binding. Due to stronger electrostatic interaction, Al^{3+} has better surface charge reduction effect over Mg^{2+}. Based on the same manner, COC has the highest surface charge reduction over PMMA and PEGDA. With 100 mM $AlCl_3$ modification (50.6% surface charge reduction), λ-DNA translocation was demonstrated in COC-COC device. The results indicated COC could replace PEGDA for dNMPs sensing due to its insoluble property.

7.2 Future works

7.2.1 DNA translocation kinetics through in-plane nanopores

DNA translocation kinetics through vertical nanopore has been extensively studied as summarized in chapter 4 [1-5]. As a new type of sensing platform, DNA translocation kinetics through in-plane nanochannel/nanopore has not been systematically studied. Unlike traditional vertical nanopore, DNA translocation kinetics through in-plane nanopore can be easily studied by fluorescence observation rather than electrical measurement. As shown in Figure 7.1(a), a simple in-plane nanochannel device usually consists of an inlet/outlet structure for DNA capture from microchannel and a nanochannel for DNA sensing.

Jiahao et al., studied the effect of inlet structure shape on DNA capture from microchannel to nanochannel and they found a funnel shape inlet could lead to an up to 5 times capture rate increase compared with rectangular shape inlet [6]. We applied the similar inlet structure design and we found that most time DNA molecules can be delivered easily to nanochannel/nanopore mouth however it took some time for captured DNA to be translocated through nanochannel/nanopore [7]. Thus DNA translocation through in-plane nanochannel/nanopore device is in entropy barrier limited regime. Entropy barrier for DNA translocation through vertical nanopore used to be studied in consideration of nanopore size and DNA chain length only. [1, 4, 8, 9]. However, for in-plane nanopores, DNA molecules are captured and confined by the

nanoscale inlet structures in front of the nanopore as illustrated in Figure 7.1(b). It causes that most part of the DNA molecule is exposed to the EOF and therefore EOF effect on entropy barrier cannot be neglected. For in-plane nanopores with EOF present, the DNA chain tends to stay away from nanopore mouth rather than get close. Bayley et al. found a threshold driving voltage decrease when the internal surface charges of biological nanopore change from negative to positive [10]. Therefore it is reasonable to conclude different surface charge density value can lead to different entropy barrier height. We have studied surface charge density effect on F_{eff} by assuming DNA molecules were fully stretched by pillar arrays in front of nanopore. It is worthy to study surface charge density effect on entropy barrier for in-plane nanofluidic devices to assist single molecule manipulation (such as sieving [11, 12] and trapping [13]).

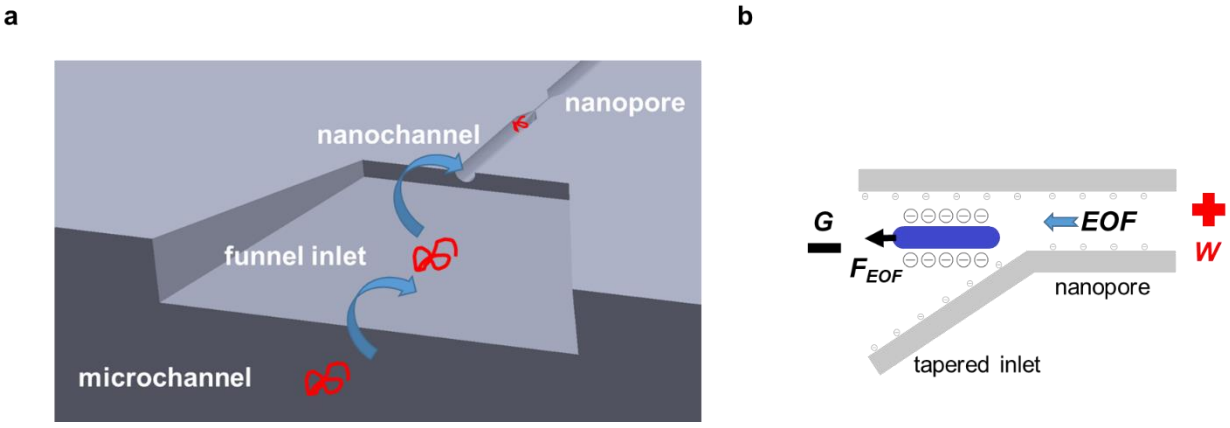

Figure 7.1. (a) Schematic image of a simple in-plane nanochannel device. Funnel inlet/outet are connected to microchannels and nanochannel. DNA molecules in microchannel are capture by inlet and delivered to naochannel mouth. (b) Captured DNA in front of nanochannel (cross-sectional view along nanochannel). Entropy barrier is dependent on EOF strength.

7.2.2 Signals correlation

In the developing stage, we didn't use enzyme to control the feeding of nucleotides to nanopore. Moreover, nucleotides pile-up issue could occur even with low analyte concentration. As shown in Figure 7.2(a), there could be multiple nucleotides passing one nanopore in a short time before the first nucleotide reaches the second nanopore. Such scenario could make trouble for data analysis when we trying to figure out which peak comes from which pore. There are two feasible ways to help assign current drop signals to their corresponding nanopore (1) by using three-electrode system, or (2) by designing dual-nanopore with different dimensions as described in chapter 3. Figure 7.2(b) shows a Si master containing two nanopores and an ionic channel which can be used as the third electrode. When analyte passes the first pore, it triggers a downwards current drop signal and it triggers a upwards signal when it passed the second pore. A special amplified needs to be built in order to fulfill this goal. In the similar manner, signals can be assigned to corresponding nanopores by using dual-nanopore having different dimensions. Compared with nanopore diameter (depth and width), it is easier to build dual nanopore with different length as illustrated in Figure 7.2(b). Longer nanopore leads to longer dwell time and shorter nanopore leads to shorter dwell time on current trace.

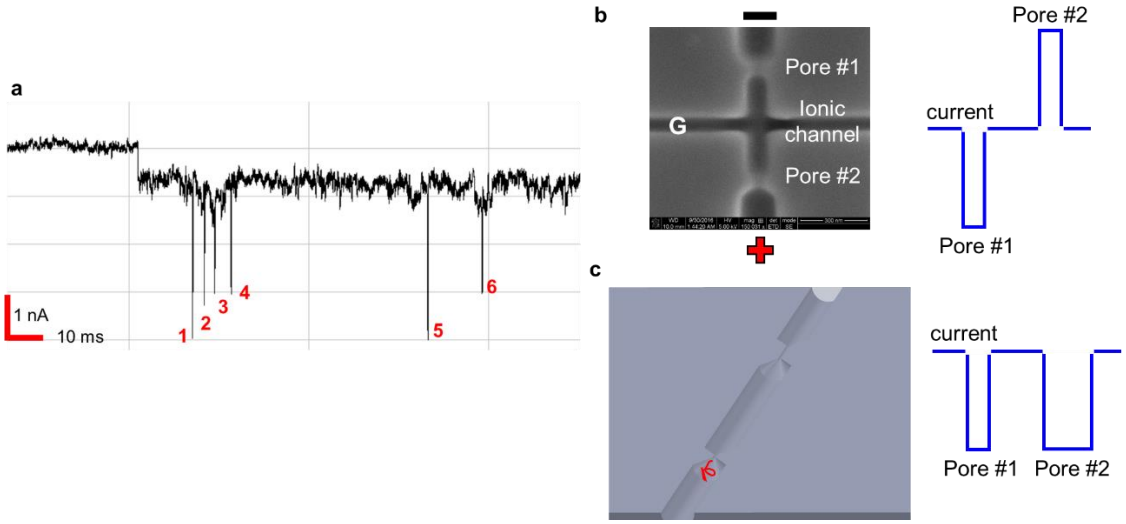

Figure 7.2. (a) Current trace example multiple peaks which can be attributed to multiple nucleotides pass nanopores. For current peak 1-4, it is difficult to determine which two peaks are paired, 1-2 and 3-4 or 1-3 and 2-4; (b) SEM image Si master mold with dual-nanopore and ionic channel as the third electrode, and corresponding current trace; (c) Schematic image of dual-nanopore with different nanopore length. Both Figure 7.2(b) and (c) assume biomolecules pass pore #1 first.

7.2.3 ToF data analysis

In this work, ToF data was collected manually based on certain criterion discussed in chapter 5. However, it is necessary to develop a software for data analysis in order to have consistent results. There are many well-developed softwares for peaks detection, for example OpenNanopore [14], which works well for detecting current blockade and dwell time from biomolecule translocation through single nanopore. The similar peak detection algorithm can be applied for processing data collected from dual-nanopore device. However, since the ultimate goal is to get ToF information from paired peaks, the challenging task is to define the paired peaks. A flow chart describing the ToF data analysis process is presented in Figure 7.3.

Assuming all events are detected by dual-nanopore and by peak detection software: start time, end time and current blockade are extracted from current trace. The first step is to assign detected peaks to the corresponding nanopores. The second step is to pair the assigned peaks based

on an estimated ToF. There are several ways to estimate ToF: (1) find isolated paired peaks and use their ToF as estimated ToF similar to the process described in chapter 5, or (2) use previous results as reference. If most assigned peaks can be paired using estimated ToF, then we can get the average of all the ToF value and save it for discrimination. If only a few peaks are paired, a new estimated ToF should be generated and repeat the pairing process again. Again, some complicated issues for example peak missing is not considered in this session. The software can be easily tested using data collected from nanoparticle translocation through dual-nanopore.

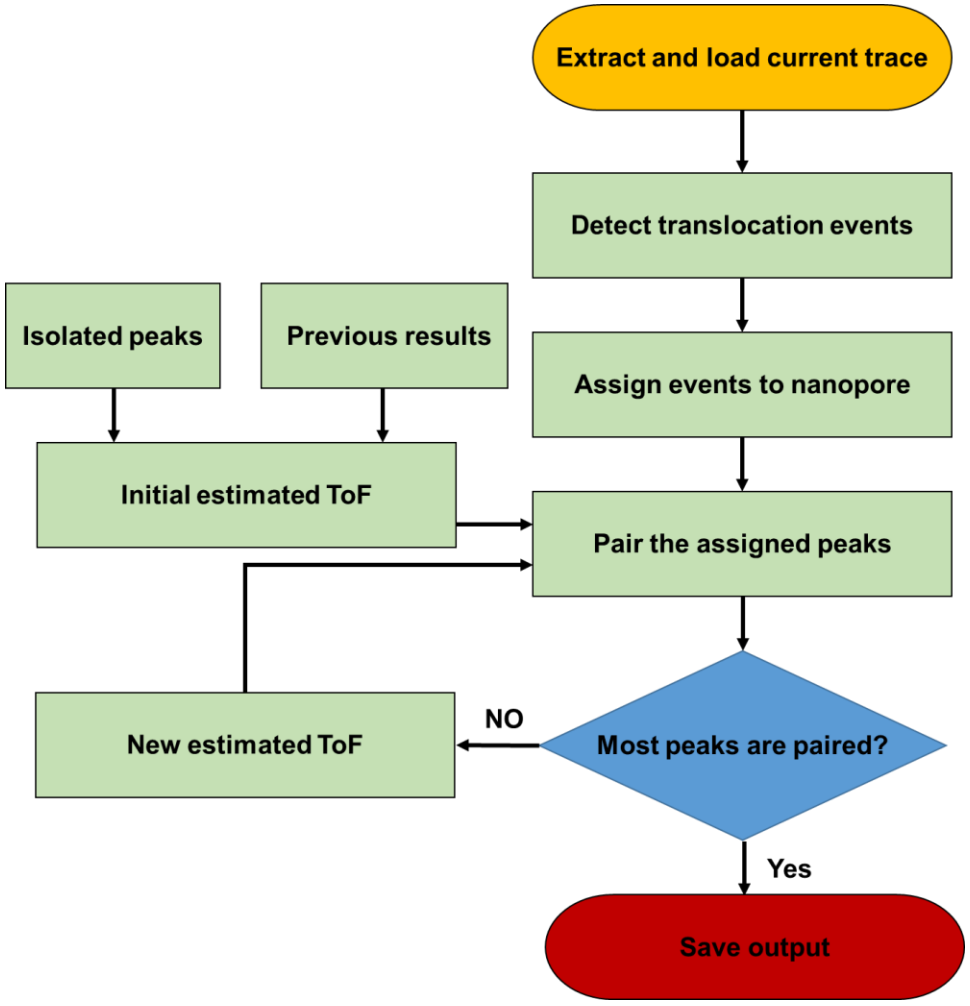

Figure 7.3. Flow chart of ToF data analysis.

7.3 References

1. Kumar, R. and M. Muthukumar, Origin of translocation barriers for polyelectrolyte chains. The Journal of chemical physics, 2009. 131(19): p. 11B610.

2. Grosberg, A.Y. and Y. Rabin, DNA capture into a nanopore: interplay of diffusion and electrohydrodynamics. The Journal of chemical physics, 2010. 133(16): p. 10B617.

3. Aksimentiev, A., et al., Microscopic Kinetics of DNA Translocation through synthetic nanopores. Biophys J, 2004. 87(3): p. 2086-97.

4. Muthukumar, M., Theory of capture rate in polymer translocation. The Journal of chemical physics, 2010. 132(19): p. 05B605.

5. Wanunu, M., et al., Electrostatic focusing of unlabelled DNA into nanoscale pores using a salt gradient. Nature nanotechnology, 2010. 5(2): p. 160-165.

6. Wu, J., et al. Influence of Nanochannel Inlet Structure Upon DNA Capture Ratio. in ASME 2011 International Mechanical Engineering Congress and Exposition. 2011. American Society of Mechanical Engineers.

7. Zhou, J., et al., Enhanced nanochannel translocation and localization of genomic DNA molecules using three-dimensional nanofunnels. Nature communications, 2017. 8(1): p. 807.

8. He, Y., et al., DNA capture in nanopores for genome sequencing: challenges and opportunities. Journal of Materials Chemistry, 2012. 22(27): p. 13423-13427.

9. Muthukumar, M., Polymer escape through a nanopore. The Journal of chemical physics, 2003. 118(11): p. 5174-5184.

10. Maglia, G., et al., Enhanced translocation of single DNA molecules through α-hemolysin nanopores by manipulation of internal charge. Proceedings of the National Academy of Sciences, 2008. 105(50): p. 19720-19725.

11. Cabodi, M., S.W. Turner, and H.G. Craighead, Entropic recoil separation of long DNA molecules. Analytical chemistry, 2002. 74(20): p. 5169-5174.

12. Kaji, N., et al., Separation of long DNA molecules by quartz nanopillar chips under a direct current electric field. Analytical chemistry, 2004. 76(1): p. 15-22.

13. Wu, L. and S. Levy, Fluctuations of DNA mobility in nanofluidic entropic traps. Biomicrofluidics, 2014. 8(4): p. 044103.

14. Raillon, C., et al., Fast and automatic processing of multi-level events in nanopore translocation experiments. Nanoscale, 2012. 4(16): p. 4916-4924.

Appendix. Copyright Information

IOP Publishing LICENSE
TERMS AND CONDITIONS

Oct 24, 2018

This is a License Agreement between Louisiana State University -- Zheng Jia ("You") and IOP Publishing ("IOP Publishing") provided by Copyright Clearance Center ("CCC"). The license consists of your order details, the terms and conditions provided by IOP Publishing, and the payment terms and conditions.

All payments must be made in full to CCC. For payment instructions, please see information listed at the bottom of this form.

License Number	4455370209375
License date	Oct 23, 2018
Licensed content publisher	IOP Publishing
Licensed content title	Nanotechnology
Licensed content date	Jan 1, 1990
Type of Use	Thesis/Dissertation
Requestor type	Author of requested content
Format	Electronic
Portion	chapter/article
The requesting person/organization is:	Zheng Jia/Louisiana State University
Title or numeric reference of the portion(s)	Selection of UV-resins for nanostructured molds for thermal-NIL
Title of the article or chapter the portion is from	Selection of UV-resins for nanostructured molds for thermal-NIL
Editor of portion(s)	Mark Reed
Author of portion(s)	Zheng Jia, Junseo Choi, Sunggook Park
Volume of serial or monograph.	Volume 29
Page range of the portion	
Publication date of portion	June 29, 2018
Rights for	Main product
Duration of use	Current edition and up to 5 years
Creation of copies for the disabled	yes
With minor editing privileges	yes
For distribution to	United States
In the following language(s)	Original language of publication
With incidental promotional use	no
The lifetime unit quantity of new product	Up to 499
Title	Development of polymer-based in-plane nanopore device for DNA

	sequencing
Institution name	Louisiana State University
Expected presentation date	Dec 2018
Billing Type	Invoice
Billing Address	Louisiana State University 2150 Elissalde Street, Unit 18 Baton Rouge, LA 70808 United States Attn: Zheng Jia
Total (may include CCC user fee)	0.00 USD
Terms and Conditions	

TERMS AND CONDITIONS

The following terms are individual to this publisher:

These special terms and conditions are in addition to the standard terms and conditions for CCC's Republication Service and, together with those standard terms and conditions, govern the use of the Works.

As the "User" you will make all reasonable efforts to contact the author(s) of the article which the Work is to be reused from, to seek consent for your intended use. Contacting one author who is acting expressly as authorised agent for their co-author(s) is acceptable.

User will reproduce the following wording prominently alongside the Work:

- the source of the Work, including author, article title, title of journal, volume number, issue number (if relevant), page range (or first page if this is the only information available) and date of first publication. This information can be contained in a footnote or reference note; and
- a link back to the article (via DOI); and
- if practicable, and IN ALL CASES for new works published under any of the Creative Commons licences, the words "© IOP Publishing. Reproduced with permission. All rights reserved"

Without the express permission of the author(s) and the Rightsholder of the article from which the Work is to be reused, User shall not use it in any way which, in the opinion of the Rightsholder, could: (i) distort or alter the author(s)' original intention(s) and meaning; (ii) be prejudicial to the honour or reputation of the author(s); and/or (iii) imply endorsement by the author(s) and/or the Rightsholder.

This licence does not apply to any article which is credited to another source and which does not have the copyright line '© IOP Publishing Ltd'. User must check the copyright line of the article from which the Work is to be reused to check that IOP Publishing Ltd has all the necessary rights to be able to grant permission. User is solely responsible for identifying and obtaining separate licences and permissions from the copyright owner for reuse of any such third party material/figures which the Rightsholder is not the copyright owner of. The Rightsholder shall not reimburse any fees which User pays for a republication license for such third party content.

This licence does not apply to any material/figure which is credited to another source in the Rightsholder's publication or has been obtained from a third party. User must check the Version of Record of the article from which the Work is to be reused, to check whether any of the material in the Work is third party material. Third party citations and/or copyright notices and/or permissions statements may not be included in any other version of the article from which the Work is to be reused and so cannot be relied upon by the User. User is solely responsible for identifying and obtaining separate licences and permissions from the

copyright owner for reuse of any such third party material/figures where the Rightsholder is not the copyright owner. The Rightsholder shall not reimburse any fees which User pays for a republication license for such third party content.

User and CCC acknowledge that the Rightsholder may, from time to time, make changes or additions to these special terms and conditions without express notification, provided that these shall not apply to permissions already secured and paid for by User prior to such change or addition.

User acknowledges that the Rightsholder (which includes companies within its group and third parties for whom it publishes its titles) may make use of personal data collected through the service in the course of their business.

If User is the author of the Work, User may automatically have the right to reuse it under the rights granted back when User transferred the copyright in the article to the Rightsholder. User should check the copyright form and the relevant author rights policy to check whether permission is required. If User is the author of the Work and does require permission for proposed reuse of the Work, User should select 'Author of requested content' as the Requestor Type. The Rightsholder shall not reimburse any fees which User pays for a republication license.

If User is the author of the article which User wishes to reuse in User's thesis or dissertation, the republication licence covers the right to include the Accepted Manuscript version (not the Version of Record) of the article. User must include citation details and, for online use, a link to the Version of Record of the article on the Rightsholder's website. User may need to obtain separate permission for any third party content included within the article. User must check this with the copyright owner of such third party content. User may not include the article in a thesis or dissertation which is published by ProQuest. Any other commercial use of User's thesis or dissertation containing the article would also need to be expressly notified in writing to the Rightsholder at the time of request and would require separate written permission from the Rightsholder.

User does not need to request permission for Work which has been published under a CC BY licence. User must check the Version of Record of the CC BY article from which the Work is to be reused, to check whether any of the material in the Work is third party material and so not published under the CC BY licence. User is solely responsible for identifying and obtaining separate licences and permissions from the copyright owner for reuse of any such third party material/figures. The Rightsholder shall not reimburse any fees which User pays for such licences and permissions.

As well as CCC, the Rightsholder shall have the right to bring any legal action that it deems necessary to enforce its rights should it consider that the Work infringes those rights in any way.

For STM Signatories ONLY (as agreed as part of the STM Guidelines)

Any licence granted for a particular edition of a Work will apply also to subsequent editions of it and for editions in other languages, provided such editions are for the Work as a whole in situ and do not involve the separate exploitation of the permitted illustrations or excerpts.

Other Terms and Conditions:

STANDARD TERMS AND CONDITIONS

1. Description of Service; Defined Terms. This Republication License enables the User to obtain licenses for republication of one or more copyrighted works as described in detail on the relevant Order Confirmation (the "Work(s)"). Copyright Clearance Center, Inc. ("CCC") grants licenses through the Service on behalf of the rightsholder identified on the Order Confirmation (the "Rightsholder"). "Republication", as used herein, generally means the inclusion of a Work, in whole or in part, in a new work or works, also as described on the Order Confirmation. "User", as used herein, means the person or entity making such republication.

2. The terms set forth in the relevant Order Confirmation, and any terms set by the Rightsholder with respect to a particular Work, govern the terms of use of Works in connection with the Service. By using the Service, the person transacting for a republication

license on behalf of the User represents and warrants that he/she/it (a) has been duly authorized by the User to accept, and hereby does accept, all such terms and conditions on behalf of User, and (b) shall inform User of all such terms and conditions. In the event such person is a “freelancer” or other third party independent of User and CCC, such party shall be deemed jointly a “User” for purposes of these terms and conditions. In any event, User shall be deemed to have accepted and agreed to all such terms and conditions if User republishes the Work in any fashion.

3. Scope of License; Limitations and Obligations.

3.1 All Works and all rights therein, including copyright rights, remain the sole and exclusive property of the Rightsholder. The license created by the exchange of an Order Confirmation (and/or any invoice) and payment by User of the full amount set forth on that document includes only those rights expressly set forth in the Order Confirmation and in these terms and conditions, and conveys no other rights in the Work(s) to User. All rights not expressly granted are hereby reserved.

3.2 General Payment Terms: You may pay by credit card or through an account with us payable at the end of the month. If you and we agree that you may establish a standing account with CCC, then the following terms apply: Remit Payment to: Copyright Clearance Center, 29118 Network Place, Chicago, IL 60673-1291. Payments Due: Invoices are payable upon their delivery to you (or upon our notice to you that they are available to you for downloading). After 30 days, outstanding amounts will be subject to a service charge of 1-1/2% per month or, if less, the maximum rate allowed by applicable law. Unless otherwise specifically set forth in the Order Confirmation or in a separate written agreement signed by CCC, invoices are due and payable on “net 30” terms. While User may exercise the rights licensed immediately upon issuance of the Order Confirmation, the license is automatically revoked and is null and void, as if it had never been issued, if complete payment for the license is not received on a timely basis either from User directly or through a payment agent, such as a credit card company.

3.3 Unless otherwise provided in the Order Confirmation, any grant of rights to User (i) is “one-time” (including the editions and product family specified in the license), (ii) is non-exclusive and non-transferable and (iii) is subject to any and all limitations and restrictions (such as, but not limited to, limitations on duration of use or circulation) included in the Order Confirmation or invoice and/or in these terms and conditions. Upon completion of the licensed use, User shall either secure a new permission for further use of the Work(s) or immediately cease any new use of the Work(s) and shall render inaccessible (such as by deleting or by removing or severing links or other locators) any further copies of the Work (except for copies printed on paper in accordance with this license and still in User's stock at the end of such period).

3.4 In the event that the material for which a republication license is sought includes third party materials (such as photographs, illustrations, graphs, inserts and similar materials) which are identified in such material as having been used by permission, User is responsible for identifying, and seeking separate licenses (under this Service or otherwise) for, any of such third party materials; without a separate license, such third party materials may not be used.

3.5 Use of proper copyright notice for a Work is required as a condition of any license granted under the Service. Unless otherwise provided in the Order Confirmation, a proper copyright notice will read substantially as follows: “Republished with permission of [Rightsholder’s name], from [Work's title, author, volume, edition number and year of copyright]; permission conveyed through Copyright Clearance Center, Inc. ” Such notice must be provided in a reasonably legible font size and must be placed either immediately adjacent to the Work as used (for example, as part of a by-line or footnote but not as a separate electronic link) or in the place where substantially all other credits or notices for the new work containing the republished Work are located. Failure to include the required notice results in loss to the Rightsholder and CCC, and the User shall be liable to pay liquidated

damages for each such failure equal to twice the use fee specified in the Order Confirmation, in addition to the use fee itself and any other fees and charges specified.

3.6 User may only make alterations to the Work if and as expressly set forth in the Order Confirmation. No Work may be used in any way that is defamatory, violates the rights of third parties (including such third parties' rights of copyright, privacy, publicity, or other tangible or intangible property), or is otherwise illegal, sexually explicit or obscene. In addition, User may not conjoin a Work with any other material that may result in damage to the reputation of the Rightsholder. User agrees to inform CCC if it becomes aware of any infringement of any rights in a Work and to cooperate with any reasonable request of CCC or the Rightsholder in connection therewith.

4. Indemnity. User hereby indemnifies and agrees to defend the Rightsholder and CCC, and their respective employees and directors, against all claims, liability, damages, costs and expenses, including legal fees and expenses, arising out of any use of a Work beyond the scope of the rights granted herein, or any use of a Work which has been altered in any unauthorized way by User, including claims of defamation or infringement of rights of copyright, publicity, privacy or other tangible or intangible property.

5. Limitation of Liability. UNDER NO CIRCUMSTANCES WILL CCC OR THE RIGHTSHOLDER BE LIABLE FOR ANY DIRECT, INDIRECT, CONSEQUENTIAL OR INCIDENTAL DAMAGES (INCLUDING WITHOUT LIMITATION DAMAGES FOR LOSS OF BUSINESS PROFITS OR INFORMATION, OR FOR BUSINESS INTERRUPTION) ARISING OUT OF THE USE OR INABILITY TO USE A WORK, EVEN IF ONE OF THEM HAS BEEN ADVISED OF THE POSSIBILITY OF SUCH DAMAGES. In any event, the total liability of the Rightsholder and CCC (including their respective employees and directors) shall not exceed the total amount actually paid by User for this license. User assumes full liability for the actions and omissions of its principals, employees, agents, affiliates, successors and assigns.

6. Limited Warranties. THE WORK(S) AND RIGHT(S) ARE PROVIDED “AS IS”. CCC HAS THE RIGHT TO GRANT TO USER THE RIGHTS GRANTED IN THE ORDER CONFIRMATION DOCUMENT. CCC AND THE RIGHTSHOLDER DISCLAIM ALL OTHER WARRANTIES RELATING TO THE WORK(S) AND RIGHT(S), EITHER EXPRESS OR IMPLIED, INCLUDING WITHOUT LIMITATION IMPLIED WARRANTIES OF MERCHANTABILITY OR FITNESS FOR A PARTICULAR PURPOSE. ADDITIONAL RIGHTS MAY BE REQUIRED TO USE ILLUSTRATIONS, GRAPHS, PHOTOGRAPHS, ABSTRACTS, INSERTS OR OTHER PORTIONS OF THE WORK (AS OPPOSED TO THE ENTIRE WORK) IN A MANNER CONTEMPLATED BY USER; USER UNDERSTANDS AND AGREES THAT NEITHER CCC NOR THE RIGHTSHOLDER MAY HAVE SUCH ADDITIONAL RIGHTS TO GRANT.

7. Effect of Breach. Any failure by User to pay any amount when due, or any use by User of a Work beyond the scope of the license set forth in the Order Confirmation and/or these terms and conditions, shall be a material breach of the license created by the Order Confirmation and these terms and conditions. Any breach not cured within 30 days of written notice thereof shall result in immediate termination of such license without further notice. Any unauthorized (but licensable) use of a Work that is terminated immediately upon notice thereof may be liquidated by payment of the Rightsholder's ordinary license price therefor; any unauthorized (and unlicensable) use that is not terminated immediately for any reason (including, for example, because materials containing the Work cannot reasonably be recalled) will be subject to all remedies available at law or in equity, but in no event to a payment of less than three times the Rightsholder's ordinary license price for the most closely analogous licensable use plus Rightsholder's and/or CCC's costs and expenses incurred in collecting such payment.

8. **Miscellaneous.**

8.1 User acknowledges that CCC may, from time to time, make changes or additions to the Service or to these terms and conditions, and CCC reserves the right to send notice to the User by electronic mail or otherwise for the purposes of notifying User of such changes or

additions; provided that any such changes or additions shall not apply to permissions already secured and paid for.

8.2 Use of User-related information collected through the Service is governed by CCC's privacy policy, available online here: http://www.copyright.com/content/cc3/en/tools/footer/privacypolicy.html.

8.3 The licensing transaction described in the Order Confirmation is personal to User. Therefore, User may not assign or transfer to any other person (whether a natural person or an organization of any kind) the license created by the Order Confirmation and these terms and conditions or any rights granted hereunder; provided, however, that User may assign such license in its entirety on written notice to CCC in the event of a transfer of all or substantially all of User's rights in the new material which includes the Work(s) licensed under this Service.

8.4 No amendment or waiver of any terms is binding unless set forth in writing and signed by the parties. The Rightsholder and CCC hereby object to any terms contained in any writing prepared by the User or its principals, employees, agents or affiliates and purporting to govern or otherwise relate to the licensing transaction described in the Order Confirmation, which terms are in any way inconsistent with any terms set forth in the Order Confirmation and/or in these terms and conditions or CCC's standard operating procedures, whether such writing is prepared prior to, simultaneously with or subsequent to the Order Confirmation, and whether such writing appears on a copy of the Order Confirmation or in a separate instrument.

8.5 The licensing transaction described in the Order Confirmation document shall be governed by and construed under the law of the State of New York, USA, without regard to the principles thereof of conflicts of law. Any case, controversy, suit, action, or proceeding arising out of, in connection with, or related to such licensing transaction shall be brought, at CCC's sole discretion, in any federal or state court located in the County of New York, State of New York, USA, or in any federal or state court whose geographical jurisdiction covers the location of the Rightsholder set forth in the Order Confirmation. The parties expressly submit to the personal jurisdiction and venue of each such federal or state court.If you have any comments or questions about the Service or Copyright Clearance Center, please contact us at 978-750-8400 or send an e-mail to info@copyright.com.

v 1.1

Questions? customercare@copyright.com or +1-855-239-3415 (toll free in the US) or +1-978-646-2777.

Vita

Zheng Jia was born in Changchun, Jilin Province, China. He received his Bachelor of Engineering in Airworthiness Science and Technology from Beihang University, Beijing, China, in 2013. He joined in Dr. Sunggook Park's group at Department of Mechanical Engineering in Louisiana State University, Baton Rouge, as a graduate student. He is expected to earn the degree of Doctor of Philosophy in December 2018.